

Selected Topics in the
Statistical Mechanics of Fluids

Lowri A. Davies

October 18, 1997

Department of Chemistry

University of Sheffield

Submitted for the degree of
Doctor of Philosophy

Selected Topics in the Statistical Mechanics of Fluids

Lowri A. Davies

Abstract

The phase behaviour and thermodynamic properties of simple model mixtures are examined using the statistical associating fluid theory as extended to chain molecules interacting with potentials of variable range (SAFT-VR), and by computer simulation. The SAFT-VR approach is based on an accurate and compact representation of the free energy of chain molecules. We present the SAFT-VR methodology as applied to mixtures of non-conformal molecules. A series of mixing rules are presented, beginning with the van der Waals one-fluid prescription and including more complex treatments. The vapour-liquid equilibria of a mixture consisting of hard spheres and square-well monomers is examined with the SAFT-VR equation of state, together with the liquid-liquid equilibria of a symmetrical square-well mixture with no unlike interactions. Additionally, we examine the vapour-liquid equilibria of a square-well monomer-dimer mixture, composed of equal-sized segments, both with the SAFT-VR approach and by Gibbs ensemble Monte Carlo simulation. The simulation data are used to determine the vapour-liquid critical line of the mixture. An extension of the SAFT-VR approach to describe the phase behaviour of chain molecules interacting with a soft repulsive potential and an attractive well of variable range is presented. We focus on the vapour-liquid properties of Lennard-Jones chains using a simple recipe for the evaluation of the chain free energy. We also perform a case study for a specific class of phase equilibria exhibited by binary mixtures, where systems are seen to possess a region of closed-loop immiscibility in their phase diagrams. We examine the nature of this type of phase behaviour using the SAFT-VR equation of state and Gibbs ensemble simulation for a simple model system with an anisotropic bonding site, which is seen to be the governing factor in the appearance of the region of low-temperature miscibility for this system. The model is chosen in order to mimic the physical features of real systems which exhibit this type of re-entrant phase behaviour. The critical regions of this model are examined using a finite-size scaling analysis performed in the semigrand canonical ensemble.

Acknowledgements

Within the array of people who have assisted, contributed and collaborated in this work the most influential has been Dr J. I need to thank him for his continuous support, enthusiasm and guidance. This thesis is a direct result of his uncomparable supervision. I am also indebted to him for the academic and social experiences gained during my time as his graduate student, most of which have been unforgettable for all the right reasons, and others which I'm sure you've all heard about!.

Special thanks must also be given to Dr Gil for his amazing ability to know the answer to every question and his willingness to explain the significance of these answers to those less knowledgeable than himself. Two other Dr. G's have also had a crucial role to play in the generation of this thesis; Dr. Galindo and Dr. Griffin. The combination the former's washing machines, the latter's hypochondria, together with their sense of humour and attitudes has entertained me throughout. A big kiss to you both.

The organisational skills and hospitality of Prof. Luis Rull have ensured that my visits to Sevilla have been perfect in every way; sincere thanks for everything. Enrique and Elvira should also be thanked for their scientific and cultural guidance during these visits.

I am grateful to Dr Steve Goodwin of BP for granting me such scientific freedom and for his sound advice, which has always proven to be worth following.

I would like to thank the remainder of the Jackson group (past and present) for showing me the way forward and occasionally the way back. Additionally, the other G-floor types especially Adrian, Paula, Denise and Julie, and the departmental netball and football teams all deserve a mention for being there for me as and when they were required. A big thank you to you all.

Finally, I doubt if this thesis would ever have been submitted without the wrath of Lorraine, for which I am (for once) grateful.

Contents

1	Introduction	6
2	The Statistical Associating Fluid Theory (SAFT-VR)	17
2.1	Introduction	17
2.2	SAFT-VR equation of state for mixtures.	20
2.2.1	The ideal mixture	21
2.2.2	Monomer contribution	21
2.2.3	Chain contribution	24
2.2.4	Association contribution	25
2.3	Mixing rules for conformal fluids	26
2.4	Mixing rules for non-conformal fluids	30
2.5	Combining rules	32
2.6	Conclusions	35
2.7	Appendix: Contact value of the radial distribution function	36
3	Molecular Simulation	48
3.1	Introduction	48

3.2	Statistical thermodynamics	49
3.3	Gibbs ensemble Monte Carlo simulations of mixtures	57
3.4	The semigrand canonical ensemble for mixtures	66
3.5	Concluding remarks	69
3.6	Appendix: Determination of chemical potential in the Gibbs ensemble	70
4	Prediction of phase equilibria of mixtures using the SAFT-VR approach	76
4.1	Introduction	76
4.2	SAFT-VR equation of state	78
4.3	Comparisons with simulation data	84
4.3.1	The hard-sphere and square-well mixture	85
4.3.2	The binary square-well mixture	88
4.3.3	The square-well monomer-dimer mixture	90
4.4	Conclusions	103
5	Examination of the the phase behaviour of Yukawa and soft-core fluids using the SAFT-VR approach	106
5.1	Introduction	106
5.2	SAFT-VR for pure fluids	107
5.3	Yukawa fluids	112
5.4	Lennard-Jones chains	119
5.5	Conclusions	132

6	Case Study: Closed-Loop Immiscibility in Fluids	135
6.1	Introduction	135
6.2	Theory of closed-loop behaviour	145
6.3	SAFT-VR prediction	150
6.4	Gibbs ensemble Monte Carlo simulation results	158
6.5	Critical behaviour and finite-size effects	171
6.6	Finite-size effects in the Gibbs ensemble	180
6.7	Finite-size scaling theory	186
6.8	Semigrand canonical ensemble simulation results	189
6.9	Conclusions	203
7	Concluding Remarks	210

Chapter 1

Introduction

One of the central concepts in the structure of physical science is the development of a theory for a particular model system. This general model is required to contain all the essential features of real substances and must also be simple enough to be examined within a theoretical framework. The theoretical prediction obtained can be compared with known experimental observations for the system. If the model proves to be successful it can be subsequently made more complete by including additional features of the real system. Familiar examples of such an approach include the kinetic model of gases, the nuclear model of atoms, and the ideal gas model which is used to describe the low-density gas phase of matter. We focus our attention here on the development of a theory to describe the liquid state using simplistic models.

The liquid state is that phase of matter which exists at pressures and temperatures bounded by the fusion curve and the vapour-pressure curve on the phase diagram of a pure substance. The well-known characteristics of the liquid state are that it is able to take the form of the container in which it is placed, as does the vapour phase, but the internal structure of a liquid is such that it has a higher degree of order than a vapour. This order is however not as long-ranged as the order observed in the structure of a solid phase. At high pressures and temperatures, above the vapour-liquid critical point, it is impossible to distinguish between the vapour and the liquid phases, so that it is common to refer to a single fluid phase at these conditions in phase behaviour studies.

As a result of the vast number of liquids encountered in everyday life, the study of the liquid state has been a source of interest to scientists for centuries. Currently

we have a general understanding of the interactions which govern the existence of such a phase of matter. Much of the present interest in the study of liquids exists due to the complexity of phase behaviour exhibited by liquids and their mixtures, and by the possibility of obtaining a theoretical description of the interactions responsible for such behaviour. A topical example is the liquid crystalline state, which exists as an intermediate state between a liquid and a solid, and displays an array of beautiful and interesting phase behaviour. Other diverse systems which are also being examined using theories of fluids are colloids, polymer solutions and complex biological molecules such as proteins and membranes. The study of liquids is obviously not limited to theoretical approaches. Most chemical processes are dominated by the interplay of the phases of matter, so that an understanding of the intermolecular interactions which govern phase coexistence and transitions between phases is vitally important to the experimentalist, regardless of the scale of the process in question.

The theoretical examination of a model system with a given interaction potential to obtain a prediction of the phase behaviour of real fluids which is valid over the entire range of pressure, temperature and density, was a concept first introduced in 1873 by van der Waals [1]. Here, an equation of state is proposed which is able to predict the existence of two fluid phases in a given model system. The deviations from ideality observed in real fluids are considered in terms of the structure of the system and of the intermolecular interactions present which are controlled by two coefficients. Molecules are considered as impenetrable hard spheres, so that the overall volume is reduced by the excluded volume of the spheres. The reduction of the pressure of the system is described in terms of the attractive interactions, which are responsible for reducing the frequency and the number of collisions between molecules in the fluid. An adjustment of the two parameters in the van der Waals equation enables us to predict the phase behaviour of fluids which is surprisingly acceptable given the simplicity of the model used. An important feature of the van der Waals equation of state is that it can be written in terms of a first order perturbation expansion of the free energy about a hard-sphere reference system [2, 3], thus incorporating the essential ideas of modern perturbation theory.

In this work we outline a particular route which can give a theoretical description of the fluid-phase behaviour of specific model systems by using both existing theories and certain new developments. This methodology can be used in turn to predict the phase behaviour of real systems over ranges of pressures and temperatures, some of which are difficult to examine experimentally. We also illustrate the value of molecular simulation techniques within a theoretical study of the phase behaviour of fluids. We pay particular attention to the use of perturbation theory in the theoretical description of the liquid state. Such an approach is valid since

it is well known experimentally that intermolecular repulsions between molecules in the fluid dominate the thermodynamic properties of the system. Hence, the attractive interactions are much less significant and can therefore be represented by a perturbation to a repulsive system in a theoretical description. A successful perturbation theory relies upon a relationship between the property of the fluid in question and a known property of the reference system. The simplest of such reference systems is that of a hard-sphere fluid, which has an interaction potential which is zero for intermolecular separations greater than the hard-core diameter and is infinite at separations smaller than the contact diameter of two spheres. The nature of the hard-sphere interaction is known from computer simulation studies to give rise to two states for such a system: a solid phase at high densities, and a fluid phase at lower densities. A sound theoretical knowledge of the properties of the hard-sphere fluid was first formulated in 1958 when Percus and Yevick [4] proposed an accurate equation of state from which the pressure and structure of the system could be obtained. This information was subsequently incorporated into the earlier work of Zwanzig [5, 6], where the formal expressions of modern perturbation theories are introduced. Within such a representation the change in physical properties resulting from the addition of an attractive interaction to a hard-sphere system are given in terms of a Taylor expansion of the Helmholtz free energy of the total system.

A solution of a perturbation expansion of the Helmholtz free energy can be obtained via expressions which are written in terms of known thermodynamic or structural properties of the reference system. Expressions for the first- and second-order perturbation terms in the free energy expansion in terms of the distribution functions of the hard-sphere fluid are first proposed in the work of Zwanzig [5]. An important advantage of this approach is that expressions for higher-order terms in the expansion can be obtained, however these higher terms contain higher-body distribution functions which are unknown, even for the hard-sphere system.

An accurate route to the first- and second-order contributions to the free energy of a fluid can be obtained using a method proposed by Barker and Henderson [7, 8] which involves an expansion which can be evaluated using known values of specific quantities for the hard-sphere reference system. The expansion is written in the inverse of temperature so that the series is rapidly convergent at high temperatures. The first-order term consists of an integral over the known hard-sphere radial distribution function for a system interacting via a pair-wise additive potential (e.g., see McQuarrie [9]). However, the expression for the second-order perturbation term includes the unknown three- and four-body distribution functions. Within the Barker and Henderson theory, two different approximations can be used to evaluate the second-order contribution, the macroscopic and local compressibility

approximations, MCA and LCA. Both these approaches can also be used to obtain values for the higher-order perturbative terms using fluctuation theory [10]. The LCA, where the compressibility is written in terms of the pressure derivative of the density at a particular distance from a given molecule, is found to give more accurate results than the MCA for the second-order term at low densities, but both methods fail to give a good description at high densities [7, 8]. An extension of the LCA to include higher-order terms in the expansion of the Helmholtz free energy illustrates that such terms do not give a significant contribution to the free energy, except at very low temperatures [11]. Additionally, a semi-empirical representation of these terms used to reproduce computer simulation results indicates that the first- and second-order terms give the the most significant contribution to the free energy [12].

A natural extension to these perturbation theories for hard-core potentials is their possible application to systems with more realistic interactions such as the Lennard-Jones potential, where the repulsive region of the potential is ‘softer’ than in the case of the hard-core systems. Introduction of this kind of potential into the perturbation approach of Zwanzig is not trivial since in this case, the diameter of the system is no longer fixed. Three different approaches exist, where a diameter for the reference system is defined differently in each case. This diameter is then incorporated into the definition of the equation of state for the reference system. The simplest of these methods is that proposed by Barker and Henderson [13, 14] where the system diameter depends only on the temperature of the system. The variational theory of Mansoori and Canfield [15]-[19] and the Weeks, Chandler and Anderson theory [20, 21], both propose reference system diameters which are temperature and density dependent. This dual dependence restricts their application to the description of mixtures due to the complex nature of the perturbation expressions when the diameter has a compositional dependence. The success of these soft-core approaches in obtaining a description of real systems is illustrated by the agreement between the melting curve of Argon obtained using the perturbation approaches of Barker and Henderson [22] and of Mansoori and Canfield [16] with the experimental results.

The nature of perturbation theories requires that the interaction potential of the model system in question must be known exactly. The pair potential for a specific system can be evaluated using *ab initio* quantum mechanics (see Ref. [23] for a review), but the complexity of such a calculation increases rapidly with the number of electrons in the system, becoming prohibitively slow even for small molecules, despite the available computer power. Hence it is currently impossible to use perturbation theories to obtain the thermodynamic properties of real systems, so that alternative routes must be found. These involve either the specification of

a model intermolecular potential which can be used within perturbation theories, and other related mathematical approaches, or by the construction of empirical correlations.

Such correlations consist of the construction of an equation of state for a system by fitting certain parameters in the equation to available experimental data for that system. The resulting expression cannot be used to extrapolate for the system's behaviour in regions of phase space outside of which the fitting was performed. Nevertheless, such correlation studies are widely used in industrial applications, since for a specific range of conditions they give acceptable results. Approaches such as the Wilson equation [24, 25], the NTRL equation [26, 27] and the UNIQUAC equation [28], relate the activity coefficients to the mole fraction of the system via expressions obtained from the excess Gibbs energy of solution. The values for the adjustable parameters which are included in these expressions are obtained via fitting to experimental data. The fact that such studies rely on the evaluation of the activity coefficients of systems result in the poor prediction of fluids which show a large amount of vapour-phase non-ideality [27].

As a result of the ability of the van der Waals equation of state to adequately predict the phase behaviour of a range of systems, much theoretical interest has been directed towards obtaining a van der Waals-like expression which gives a more accurate prediction of phase behaviour. The most accurate of these augmented van der Waals equations use an improved expression for the free energy of the hard-sphere reference system, such as that proposed by Carnahan and Starling [29]. Various empirical equations of state such as the Berthelot [30], Dieterici [31], Redlich-Kwong [32, 33] and the Peng-Robinson [34] equations have also been developed in order to give a better description of phase behaviour than is obtained with the van der Waals equation. These approaches involve the introduction of parameters into an equation of state which are derived from more complex routes than the van der Waals coefficients. For example, the constants in the Redlich-Kwong equation have a similar physical significance to the van der Waals constants [27]. Such equations have found widespread use in the prediction of the phase behaviour of both pure fluids and mixtures, despite the fact that they consider molecules as hard-spheres.

Extension of the original hard-sphere perturbation theories to account for the non-sphericity of real molecules has been the source of much theoretical interest (see Ref. [35] for a review). However, the adequacy of such approaches is seen to decrease rapidly as the elongation of the system increases. An alternative approach to an accurate equation of state for chain molecules is the a perturbed hard-chain theory (PHCT) [36]. The PHCT provides an equation which links the low density ideal gas limit and the high density Prigogine-Flory theory of polymer

fluids [27]. The ideas of the PHCT have been widely used in a number of related theories, such as the simplified perturbed hard-chain theory (SPHCT) [37, 38], where the nature of the attractive interaction is less complex than in the PHCT. The perturbed anisotropic chain theory (PACT) [39] is an extension of the PHCT approach which accounts for systems with anisotropic interactions, but is unable to describe the phase behaviour of associating systems. Such systems are found to be adequately described by the associated perturbed anisotropic hard-chain theory (APACT) [40]. The APACT approach is a modified perturbed hard-chain theory where simple chemical equilibria to account for association are also considered, following the approach of Heidemann and Prausnitz [41]. These PHCT-based approaches have been used in the prediction of mixtures containing chain molecules, mixtures of water and hydrocarbons and to examine the extent of association in supercritical water (see Ref. [42] for a review). However, these studies are not without their problems, which range from the empirical nature of the parameters in the APACT equation to the unphysical nature of the low temperature phase behaviour proposed by the SPHCT approach [43]-[45].

A molecular based equation of state which gives an excellent prediction of the full phase behaviour of a wide variety of systems is the statistical associating fluid theory (SAFT) [46, 47]. The approach is based on the thermodynamic perturbation theory proposed by Wertheim [48]-[53], in which the phase behaviour of associating systems is explicitly described. Within this perturbative approach the association between molecules via short-ranged interaction sites is described in terms of a graphical expansion of the densities of every species in the fluid. Since the singlet density dependent contribution to the free energy due to association is included in the perturbation expansion there is a slight difference between the perturbation approach of Wertheim and those discussed previously, however the essential principles are the same. The SAFT equation of state and its applications and extensions will be discussed in detail throughout this thesis. One of the important advantages of molecular based theories such as SAFT over empirical equations of state is that each term in the SAFT free energy expansion can be compared directly with computer simulation results. This provides an indication of the adequacy of the individual contributions in their ability to give an accurate description of the phase behaviour of the model system. This type of information is impossible to obtain when the terms in the equation of state are fitted to experimental data over a specific range.

The use of computer simulation techniques in theoretical studies is not limited to the determination of the effectiveness of different equations of state. The phase behaviour of model systems obtained by computer simulation can also be compared directly with experimental results. Simulation techniques can hence be considered

as a link between theoretical and experimental studies. The two-fold applicability of simulation methods has resulted in a wide range of studies in this area. The results obtained from computer simulations can be considered as ‘exact’ with respect to those obtained from other theoretical approaches since no approximations, other than some concerning the intermolecular interactions have to be made. This allows the comparison between theory and simulation to be similar to that of between theory and experiment, where molecular simulations are considered as computer experiments. The different types of simulation techniques available and the underlying statistical mechanics of such approaches are illustrated in Chapter 3. In this work we will use both aspects of computer simulation in order to obtain predictions of the phase behaviour of model systems directly and also as a means of testing the adequacy of equations of state. In order to examine the relative merits of the different approaches which can be used to determine the phase behaviour of a particular system, it is interesting to compare the cost and time associated with each approach. An estimation of such figures for a binary mixture liquid-vapour equilibrium calculation is given in Table 1.1 (taken from Ref. [54]). This allows an approximate comparison to be made between the various methods. The cost and time efficiency of theoretical approaches with respect to experimental studies is clearly illustrated. It is also important to note how both the financial and computational cost of molecular simulation methods rapidly increase with the complexity of the model studied.

Throughout this thesis we examine the phase behaviour of fluid mixtures using the SAFT-VR [57, 58] equation of state. This approach is known to give an accurate description of the properties of associating chain molecules with interaction potentials of variable attractive range. In order to be able to describe mixtures within the SAFT-VR approach it is necessary to define suitable mixing rules for the cross-component parameters. We discuss the nature and complexity of possible mixing rules. A series of studies of simple model systems are presented as a means of testing the adequacy of the SAFT-VR description for mixtures. The model systems examined in this context interact via simple hard-core attractive potentials. An extension of the SAFT-VR approach to describe systems which interact via soft-core potentials is also presented. The ability of any equation of state to accurately describe the phase behaviour of systems interacting with realistic potentials is clearly advantageous.

In the final chapter of this work particular attention is focused on a specific class of phase equilibria, characterised by phase diagrams with ‘closed-loop’ regions of immiscibility. The SAFT-VR approach and computer simulation methods are employed to describe this type of behaviour using a model system which contains the physical features responsible for the appearance of closed-loop immiscibility in

Table 1.1: Approximate costs of a binary mixture vapour-liquid phase equilibria calculation for a single state point for a fluid interacting via the Lennard-Jones (LJ) potential using experiment, theoretical techniques and Gibbs ensemble Monte Carlo simulation. The empirical correlation is performed using the Redlich-Kwong-Soave equation [55] and the perturbation theory is a second order Barker and Henderson expansion. The estimates for the simulation cost are performed for a system of $N=500$ particles for 10,000 cycles on a Dec 5000 workstation. The figures are expected to be slightly lower if current cost-effective supercomputers are used [56]. All estimations are for calculations made in 1992, so an adjustment for inflation must be made in order to bring the prices into current context.

Method	Cost (\$)	Time
Experiment	2600	2 days
Empirical correlation	2.4×10^{-6}	10^{-2} s
Perturbation theory	1.2×10^{-5}	5×10^{-2} s
Molecular Simulation		
Spherical LJ	4.5	5 h
Two-site LJ	31.2	35 h
n -site LJ	$> 4.5n^2$	$> 5n^2$ h

real fluids. Such a study illustrates the the motivation behind this thesis, where the combination of a powerful theoretical method and computer simulation techniques are used to to describe the phase behaviour and thermodynamic properties of real systems which are of industrial interest.

Bibliography

- [1] J. D. van der Waals, Ph.D. Thesis, University of Leiden (1873); English translation edited by J. S. Rowlinson in *Studies in Statistical Mechanics*, Vol. 14, North Holland (1988).
- [2] M. Rigby, *Quart. Rev.*, **24**, 416 (1970).
- [3] J. A. Barker and D. Henderson, *J. Chem. Educ.*, **45**, 2 (1968).
- [4] J. K. Percus and G. J. Yevick, *Phys. Rev.*, **110**, 1 (1958).
- [5] R. W. Zwanzig, *J. Chem. Phys.*, **22**, 1420 (1954).
- [6] L. Landau and E. Lifchitz, *Statistical Physics*, Pergamon Press, (1969).
- [7] J. A. Barker and D. Henderson, *J. Chem. Phys.*, **47**, 2856 (1967).
- [8] J. A. Barker and D. Henderson, *J. Chem. Phys.*, **47**, 4714 (1967).
- [9] D. A. McQuarrie, *Statistical Mechanics*, Harper Collins, (1976).
- [10] A. Münster, *Statistical Thermodynamics*, Academic Press (1969).
- [11] E. Praestgaard and S. Toxvaerd, *J. Chem. Phys.*, **53**, 2389 (1970).
- [12] A. Gil-Villegas, F. del Rífo, and A. L. Benavides, *Fluid Phase Equilib.*, **119**, 97 (1996).
- [13] J. A. Barker and D. Henderson, *Phys. Rev. A.*, **1**, 1266 (1970).
- [14] R. O. Watts and D. Henderson, *J. Chem. Phys.*, **50**, 1651 (1969).
- [15] G. A. Mansoori and F. B. Canfield, *J. Chem. Phys.*, **51**, 4958 (1969).
- [16] G. A. Mansoori and F. B. Canfield, *J. Chem. Phys.*, **51**, 4967 (1969).
- [17] G. A. Mansoori and F. B. Canfield, *J. Chem. Phys.*, **51**, 5295 (1969).
- [18] G. A. Mansoori and F. B. Canfield, *J. Chem. Phys.*, **53**, 1618 (1970).
- [19] G. A. Mansoori and F. B. Canfield, *Ind. Eng. Chem.*, **62**, 12 (1970).

- [20] D. Chandler and J. D. Weeks, *Phys. Rev. Letters*, **25**, 149 (1970).
- [21] J. D. Weeks, D. Chandler, and H. C. Andersen, *J. Chem. Phys.*, **54**, 5237 (1971).
- [22] J. A. Barker and D. Henderson, *Mol. Phys.*, **14**, 587 (1968).
- [23] R. A. Freisner, *Ann. Rev. Phys. Chem.* **42**, 341 (1991).
- [24] G. M. Wilson, *J. Am. Chem. Soc.*, **86**, 127 (1964).
- [25] R. V. Orye and J. M. Prausnitz, *Ind. Eng. Chem.*, **57**, 19 (1965).
- [26] H. Renon and J. M. Prausnitz, *AIChE J.*, **14**, 135 (1968).
- [27] J. M. Prausnitz, R. N. Lichtenthaler, and E. G. de Azevedo, *Molecular Thermodynamics of Fluid-Phase Equilibria*, 2nd. Edition, Prentice-Hall, (1986).
- [28] D. Abrams and J. M. Prausnitz, *AIChE J.*, **21**, 116 (1975).
- [29] N. S. Carnahan and K. E. Starling, *J. Chem. Phys.*, **51**, 635 (1969).
- [30] D. Berthelot, *Trav. Bur. Int. Poids. Mes.*, **13**, 113 (1907).
- [31] C. Dieterici, *Ann. Physik*, **69**, 685 (1899).
- [32] O. Redlich and J. N. S. Kwong, *Chem. Rev.*, **44**, 233 (1949).
- [33] O. Redlich, J. N. S. Kwong, and A. K. Dunlop, *Chem. Eng. Prog. Symp. Series*, **59**, 95 (1963).
- [34] D. -Y. Peng and D.B. Robinson, *Ind. Eng. Chem. Fundam.*, **15**, 59 (1976).
- [35] C. G. Gray and K. E. Gubbins, *Theory of Molecular Fluids* Clarendon Press, (1984).
- [36] S. Beret and J. M. Prausnitz, *AIChE J.*, **21**, 1123 (1975).
- [37] C. -H. Kim, P. Vimalchand, M. D. Donohue, and S. I. Sandler, *AIChE J.*, **32**, 1726 (1986).
- [38] K. H. Lee, M. Lombardo, and S. I. Sandler, *Fluid Phase Equilib.*, **21**, 177 (1985).
- [39] P. Vimalchand and M. D. Donohue, *Ind. Eng. Chem. Fundam.*, **24**, 246 (1985).
- [40] G. D. Ikononou and M. D. Donohue, *AIChE J.*, **32**, 1716 (1986).
- [41] R. A. Heidemann and J. M. Prausnitz, *Proc. Natl. Acad. Sci. U.S.A.*, **73**, 1773 (1976).

- [42] A. Galindo, P. J. Whitehead, G. Jackson, G., and A. N. Burgess, *J. Phys. Chem.*, **100**, 6781 (1996).
- [43] A. van Pelt, C. J. Peters, and J. de Swaan Arons, *J. Chem. Phys.*, **95**, 7569 (1991).
- [44] D. G. Green and G. Jackson, *J. Chem. Phys.*, **97**, 8672 (1992).
- [45] A. van Pelt, C. J. Peters, and J. de Swaan Arons, *J. Chem. Phys.*, **102**, 3361 (1985).
- [46] W. G. Chapman, K. E. Gubbins, G. Jackson, G., and M. Radosz, *Fluid Phase Equilib.*, **52**, 31 (1989)
- [47] W. G. Chapman, K. E. Gubbins, G. Jackson, G., and M. Radosz, *Ind. Eng. Chem. Res.*, **29**, 1709 (1990).
- [48] M. S. Wertheim, *J. Stat. Phys.*, **35**, 19 (1984).
- [49] M. S. Wertheim, *J. Stat. Phys.*, **35**, 35 (1984).
- [50] M. S. Wertheim, *J. Stat. Phys.*, **42**, 459 (1986).
- [51] M. S. Wertheim, *J. Stat. Phys.*, **42**, 477 (1986).
- [52] M. S. Wertheim, *J. Chem. Phys.*, **85**, 2929 (1986).
- [53] M. S. Wertheim, *J. Chem. Phys.*, **87**, 7323 (1987).
- [54] K. E. Gubbins, *Models for Thermodynamic and Phase Equilibria Calculations*, Edited by S. I. Sandler, Dekker (1994).
- [55] G. Soave, *Chem. Eng. Sci.*, **27**, 1197 (1972).
- [56] G. Bell, *Science*, **256**, 64 (1992).
- [57] A. Gil-Villegas, A. Galindo, P. J. Whitehead, S. J. Mills, G. Jackson, and A. N. Burgess, *J. Chem. Phys.*, **106**, 4186 (1997).
- [58] A. Galindo, L. A. Davies, A. Gil-Villegas, and G. Jackson, *Mol. Phys.*, in press (1997).

Chapter 2

The Statistical Associating Fluid Theory (SAFT-VR)

2.1 Introduction

The thermodynamic perturbation theory for fluids consisting of associating chain molecules proposed by Wertheim [1]-[6], provides the basis for the SAFT equation of state [7, 8]. Within the SAFT approach the individual molecular contributions to the macroscopic behaviour are accounted for by expanding the free energy into a sum of the different energies involved. Hence the equation of state for a mixture of associating chain molecules is written in terms of four separate contributions to the Helmholtz free energy A

$$\frac{A}{NkT} = \frac{A^{IDEAL}}{NkT} + \frac{A^{MONO.}}{NkT} + \frac{A^{CHAIN}}{NkT} + \frac{A^{ASSOC.}}{NkT}, \quad (2.1)$$

where N is the number of chain molecules in the mixture, k is the Boltzmann constant, and T is the temperature. In the above equation A^{IDEAL} is the ideal free energy, $A^{MONO.}$ is the excess free energy due to the monomer segments, A^{CHAIN} is the contribution due to the formation of chains of monomers, and $A^{ASSOC.}$ is the term that describes the contribution to the free energy due to intermolecular association. A major advantage of the SAFT approach is that only the monomer Helmholtz free energy and the contact value of the monomer cavity function are required to describe the equation of state of chain molecules.

The success of this approach lies in its ability to provide an accurate prediction of the thermodynamics and hence the phase behaviour of systems where molecular shape and associating phenomena are dominant characteristics. The SAFT equation of state has been used to correlate the phase equilibria data for sets of pure components [9], binary mixtures [10, 11], and ternary mixtures [11] (where the phase equilibria is obtained from the corresponding binary data [12]). Specific examples of other mixtures which have been studied within the SAFT framework include carbon dioxide with bitumen [13], carbon dioxide with methylnaphthalene [14], aromatics in ethene and ethane [15], binary and ternary systems of n-alkanes containing ethene and 1-butene [16], methanol and ethene mixtures [17], systems containing alcohols [18], and recently mixtures of carbon dioxide with acetonitrile and acrylic acid [19]. In all the above examples the SAFT approach gives an excellent description of the thermodynamic properties. The theory is also being used to correlate and predict the phase behaviour of a wide variety of complex polymer systems (e.g., see Ref. [20]).

The original SAFT equation of state [7, 8], was proposed for a system of Lennard-Jones segments, where the monomer contribution is described by a perturbation expansion and the chain contribution by the radial distribution function for the hard sphere reference system. The simplest version of current SAFT approaches is the SAFT-HS equation of state, where the segments are treated as hard spheres (HS) and a mean-field (van der Waals) attractive interaction is included in the potential model. This simple treatment of the intermolecular interaction gives an accurate prediction of phase equilibria of a variety of systems. Examples include the critical behaviour of n-alkanes [21], the upper critical solution temperatures of mixtures of alkanes and perfluoroalkanes [22], the high-pressure critical lines of mixtures of alkanes and water [23], mixtures containing hydrogen fluoride [24], and aqueous mixtures of alcohols and alkylpolyoxethylene surfactants [25]. The SAFT-HS approach is found to give an accurate description of the thermodynamic properties of systems in which association (such as hydrogen bonding) are the dominant interactions, so that the mean field description of the dispersion forces does not have a significant effect on the accuracy of the overall phase equilibria obtained using such a fundamental representation. A related simplified SAFT approach is used in Ref. [26] where the simplified perturbed hard chain theory (SPHCT) is used as in place of the hard spheres of the SAFT-HS approach.

The SAFT methodology, as well as the closely related ideas of Wertheim, have been extended to varying degrees; to include a more accurate representation of the monomer-monomer distribution function [27]-[33], to include higher body interactions in the dimer versions of the theory [34, 35]. The nature of the bonding described within the SAFT approach has also been extended, so that double bond-

ing [36], ring formation [37]-[40], and bond co-operativity [41] can be treated within the equation of state. Furthermore the isotropic-nematic transition for associating rod-like molecules has also been characterised using the Wertheim theory of association [42, 43].

The SAFT-VR equation of state is a version of SAFT that considers non-conformal properties of fluids [44, 45], within the framework of a very general perturbation theory for hard-sphere monomers interacting with attractive interactions of variable range (VR). The use of the Barker and Henderson perturbation theory [46]-[49], together with a simple method for evaluating the first perturbation term, the mean-attractive energy, leads to a theory with the van der Waals form but which is applicable to a wide variety of potentials. More specifically, chains formed from square-well (SW), Sutherland (S) and Yukawa (Y) segments with varying attractive range have been examined [44]. The SAFT-VR approach provides an excellent representation of the properties of simple, non-associating, mixtures such as alkanes and perfluoroalkanes [44, 50, 51] but also more complex fluid mixtures, e.g., those comprising replacement refrigerants [52]. The application of SAFT-VR to describe the phase behaviour of three specific model mixtures is presented in Chapter 4 [45, 53], and the extension of the theory to systems interacting via soft-core potentials is given in Chapter 5 [54]. The beauty of the SAFT approach lies in its versatility and in the means in which the results obtained can be compared directly with molecular simulation results. It offers the ideal framework to study complex fluid phenomena, the phase behaviour of liquid-crystalline colloids being a particularly topical example.

Here we review the SAFT-VR expressions for mixtures of chain molecules formed from segments interacting via a square-well potential, following references [44] and [45]. Since the SAFT-VR approach for the calculation of the mean-attractive energy requires a knowledge of the van der Waals constant and the radial distribution function of a mixture of hard spheres, simple expressions for the mixing rules can be formulated. We then discuss the use of a variety of possible mixing rules from the simple van der Waals one-fluid description to the full SAFT-VR second-order expressions. The mixing rules for the free energy of conformal and non-conformal mixtures are presented, as are the combining rules for the un-like interaction parameters.

2.2 SAFT-VR equation of state for mixtures.

The SAFT-VR equation of state for an n -component mixture of associating chain molecules takes the form of Eq. (2.1), where each of the individual terms will be subsequently discussed in turn. Within the SAFT framework molecules are described as chains consisting of spherical segments with diameter σ , where the general form of the interaction potential between two particles i and j a distance r_{ij} apart is given by

$$u^M(r_{ij}) = u^{HS}(r_{ij}; \sigma_{ij}) - \varepsilon_{ij}\phi(r_{ij}; \lambda_{ij}). \quad (2.2)$$

The monomer-monomer interaction potential $u^M(r_{ij})$ consists of a hard sphere repulsive contribution u^{HS} , defined by

$$u^{HS}(r_{ij}; \sigma_{ij}) = \begin{cases} \infty & \text{if } r_{ij} < \sigma_{ij} \\ 0 & \text{if } r_{ij} > \sigma_{ij}, \end{cases} \quad (2.3)$$

where σ_{ij} is the contact distance, and an attractive interaction of depth $-\varepsilon_{ij}$ and shape $\phi(r_{ij}; \lambda_{ij})$, where λ_{ij} is a parameter associated with the range of the attractive forces. By including the range parameter λ_{ij} in Eq. (2.2), the system's non-conformal properties can be described. A variation of the parameters σ_{ij} and ε_{ij} has no effect on the corresponding states behaviour of two particular systems, but a variation in λ_{ij} leads to the breakdown of this correspondence for a given potential.

Here we will introduce initially the SAFT-VR expressions for systems interacting via the square-well potential, the shape of which is governed by:

$$\phi^{SW}(r_{ij}; \lambda_{ij}) = \begin{cases} 1 & \text{if } \sigma_{ij} < r_{ij} < \lambda_{ij}\sigma_{ij} \\ 0 & \text{if } r_{ij} > \lambda_{ij}\sigma_{ij}, \end{cases} \quad (2.4)$$

so that the energy is constant over the range of interaction.

Although hard-core potentials of this kind are simplifications of the true interactions between molecules, they allow a highly accurate description of the properties of real substances. An additional advantage is that the statistical mechanics of such hard-core attractive models is very well known, the analytical solutions which exist for the square-well potential [55]-[61] provide a useful guide for the development of an accurate equation of state.

Since the SAFT equation of state consists of an expression in term of the Helmholtz free energy A of fluids, it is important to specify the relationships between A and

the fundamental thermodynamic variables of phase equilibria. In order for two or more phases to be in equilibrium with one another the pressures, temperatures, and chemical potentials of each component species must be equal in the coexisting phases. The chemical potential, μ_i , of species i can be written in terms of the free energy:

$$\frac{\mu_i}{kT} = \left(\frac{\partial A/kT}{\partial N_i} \right)_{T,V,N_{j \neq i}}, \quad (2.5)$$

where N_i is the number of chain molecules of species i . The overall pressure, p , may be calculated through the compressibility factor, Z , as

$$\begin{aligned} Z &= \frac{pV}{NkT} \\ &= \sum_i^n x_i \frac{\mu_i}{kT} + \frac{A}{NkT}, \end{aligned} \quad (2.6)$$

where n is the total number of components in the mixture and $x_i = N_i/N$ is the mole fraction of component i .

Each of the individual contributions to the SAFT-VR Helmholtz free energy in Eq. (2.1) are now examined.

2.2.1 The ideal mixture

The free energy of the ideal mixture is given by [62]

$$\frac{A^{IDEAL}}{NkT} = \sum_{i=1}^n x_i \ln \rho_i \Lambda_i - 1, \quad (2.7)$$

where $\rho_i = N_i/V$ is the number density and Λ_i is the thermal de Broglie wavelength, of species i .

2.2.2 Monomer contribution

The monomer free energy is

$$\begin{aligned} \frac{A^{MONO.}}{NkT} &= \left(\sum_{i=1}^n x_i m_i \right) \frac{A^M}{N_s kT} \\ &= \left(\sum_{i=1}^n x_i m_i \right) a^M, \end{aligned} \quad (2.8)$$

where m_i is the number of spherical segments in each chain i , and N_s is the total number of segments. The monomer free energy per segment of the mixture $a^M = A/(N_s kT)$ is obtained from the Barker and Henderson high temperature expansion [46]- [49]:

$$a^M = a^{HS} + \beta a_1 + \beta^2 a_2 + \dots, \quad (2.9)$$

where a_{HS} is the free energy for a mixture of hard-spheres, $\beta = 1/kT$; a_1 and a_2 are the first two perturbation terms associated with the attractive energy $-\varepsilon_{ij}$.

The free energy of the reference hard-sphere mixture is obtained from the expression of Boublík [63] and Mansoori *et al.* [64] as

$$a^{HS} = \frac{6}{\pi \rho_s} \left[\left(\frac{\zeta_2^3}{\zeta_3^2} - \zeta_0 \right) \ln(1 - \zeta_3) + \frac{3\zeta_1 \zeta_2}{1 - \zeta_3} + \frac{\zeta_2^3}{\zeta_3(1 - \zeta_3)^2} \right]. \quad (2.10)$$

In this expression $\rho_s = N_s/V$ is the number density of spherical segments, where $\rho_s = \rho(\sum_i x_i m_i)$, ρ being the total number density of the mixture. The reduced densities ζ_l are defined as

$$\zeta_l = \frac{\pi}{6} \rho_s \left[\sum_{i=1}^n x_{s,i} (\sigma_i)^l \right], \quad (2.11)$$

where σ_i is the diameter of spherical segments of chain i , and $x_{s,i}$ is the mole fraction of segments of type i in the mixture, given by

$$x_{s,i} = \frac{m_i x_i}{\sum_{j=1}^n m_j x_j}. \quad (2.12)$$

The overall packing fraction of the mixture is thus given by ζ_3 .

The mean-attractive term a_1 is given by

$$a_1 = \sum_{i=1}^n \sum_{j=1}^n x_{s,i} x_{s,j} a_1^{ij}, \quad (2.13)$$

where

$$\begin{aligned} a_1^{ij} &= -2\pi \rho_s \varepsilon_{ij} \int_{\sigma_{ij}}^{\infty} r_{ij}^2 g_{ij}^{HS}[r_{ij}; \zeta_{ij}] dr_{ij} \\ &= -3\rho_s b_{ij}^{VDW} \varepsilon_{ij} \int_1^{\infty} x^2 \phi_{ij}(x) g_{ij}^{HS}(x) dx \end{aligned} \quad (2.14)$$

where $b_{ij}^{VDW} = 2\pi \sigma_{ij}^3/3$, and $g_{ij}^{HS}[r_{ij}; \zeta_{ij}]$ is the radial distribution function for a mixture of hard-spheres. The integral is factorised by applying the mean-value theorem [44] which gives an expression for a_1 in terms of the contact value of

g_{ij}^{HS} :

$$a_1^{ij} = -\rho_s \sum_{i=1}^n \sum_{j=1}^n x_{s,i} x_{s,j} \alpha_{ij}^{VDW} g_{ij}^{HS}[\sigma_{ij}; \zeta_3^{eff}], \quad (2.15)$$

where

$$\alpha_{ij}^{VDW} = 2\pi \varepsilon_{ij} \sigma_{ij}^3 (\lambda_{ij}^3 - 1)/3 \quad (2.16)$$

is the van der Waals attractive constant for the $i - j$ square-well interaction, and ζ_3^{eff} is an effective packing fraction, the exact nature of which will be discussed in the next section. The contact value $g_{ij}^{HS}[\sigma_{ij}; \zeta_3^{eff}]$ is obtained from the Boublík [63] expression for the contact value $g_{ij}^{HS}[\sigma_{ij}; \zeta_3]$, which is evaluated at the overall packing fraction of the mixture ζ_3 . The mapping procedure used for obtaining ζ_3^{eff} from ζ_3 depends on the interaction potential and on the actual mixing rule used. Since the chemical potential is obtained as the derivative of the free energy with respect to the number of chain molecules care must be taken to ensure that the correct number of species are counted. For the square-well potential of range $1.1 \leq \lambda_{ij} \leq 1.8$, the mean-attractive energy is given by

$$a_1^{ij} = a_1^{ijVDW} g_{ij}^{HS}[1; \zeta_{eff}], \quad (2.17)$$

where the van der Waals mean-field parameter is

$$a_1^{ijVDW} = -4\zeta \varepsilon_{ij} (\lambda_{ij}^3 - 1). \quad (2.18)$$

The parameterisation for the effective packing fraction $\zeta_{eff}[\zeta, \lambda_{ij}]$ depends on the particular mixing rules used and will be discussed in the next section.

The fluctuation term of the free energy is given by

$$a_2 = \sum_{i=1}^n \sum_{j=1}^n x_{s,i} x_{s,j} a_2^{ij}, \quad (2.19)$$

where each of the terms a_2^{ij} are obtained with the local compressibility approximation (LCA) [46, 47], which is once again specific for each interaction potential, stating:

$$a_2^{i,j} = \frac{1}{2} K^{HS} \varepsilon_{ij} \rho_s \frac{\partial a_1^{*ij}}{\partial \rho_s}, \quad (2.20)$$

where K^{HS} is the isothermal compressibility for a mixture of hard-spheres, given by the Percus-Yevick expression [65],

$$K^{HS} = \frac{\zeta_0(1 - \zeta_3)^4}{\zeta_0(1 - \zeta_3)^2 + 6\zeta_1\zeta_2(1 - \zeta_3) + 9\zeta_2^3}, \quad (2.21)$$

and

$$\begin{aligned}
a_1^{*ij} &= -2\pi\rho_s\sigma_{ij}^3\varepsilon_{ij}\int_{\sigma_{ij}}^{\infty}r_{ij}^2\phi_{ij}^2(r_{ij})g_{ij}^{HS}(r_{ij})dr_{ij} \\
&= -3\rho_sb_{ij}^{VDW}\varepsilon_{ij}\int_1^{\infty}x^2\phi_{ij}^2(x)g_{ij}^{HS}(x)dx
\end{aligned}
\tag{2.22}$$

is the mean-attractive energy associated with a potential ϕ_{ij}^2 . The explicit dependence of the second order term on the mean-attractive energy is clearly shown in the above expression, indicating that evaluation of the first order term is the crucial step in the SAFT-VR approach. The fluctuation term a_2^{ij} for square-well fluids is given directly from the first density derivative of a_1^{ij} , since $a_1^{*ij} = a_1^{ij}$, giving

$$a_2^{ij} = \frac{1}{2}\varepsilon_{ij}K^{HS}\rho_s\frac{\partial a_1^{ij}}{\partial\rho_s}.\tag{2.23}$$

2.2.3 Chain contribution

The contribution to the free energy due to the formation of chains of monomeric segments is given by

$$\frac{A^{chain}}{NkT} = -\sum_{i=1}^n x_i(m_i - 1)\ln y_{ii}^M(\sigma_{ii}),\tag{2.24}$$

where $y_{ii}^M = \exp(-\beta\varepsilon_{ii})g^M(\sigma_{ii})$ is the background correlation function. Since the Boltzmann factor $\exp(-\beta\varepsilon_{ii})$ is not required in the determination of the phase equilibria we can write

$$\frac{A^{chain}}{NkT} = -\sum_{i=1}^n x_i(m_i - 1)\ln g_{ii}^{SW}(\sigma_{ii}),\tag{2.25}$$

without loss of generality. An $(n - 1)$ th order perturbation theory in a fluid's structure is equivalent to a n th order perturbation in the free energy. Since the SAFT-VR approach consists of a second-order perturbation theory in the monomer free energy, the contact value of the radial distribution function for segments of species i and j can be therefore be written as a first-order expansion:

$$g_{ij}(\sigma_{ij}) = g_{ij}^{HS}(\sigma_{ij}) + \beta\varepsilon_{ij}g_1^{ij}(\sigma_{ij}).\tag{2.26}$$

The term $g_1(\sigma_{ij})$ is obtained from a self-consistent calculation of the pressure by equating the expressions obtained from the Clausius virial theorem and from the density derivative of the Helmholtz free energy [44], giving an expression for g_1^{ij} which depends on the mean-attractive energy a_1 , so it is hence specific for each

interaction potential. The contact value of the radial distribution function for the reference system of a mixture of hard-spheres at the actual packing fraction ζ_3 of the mixture is given by [63]

$$g_{ij}^{HS}(\sigma_{ij}; \zeta_3) = \frac{1}{1 - \zeta_3} + 3 \frac{D_{ij}\zeta_3}{(1 - \zeta_3)^2} + 2 \frac{(D_{ij}\zeta_3)^2}{(1 - \zeta_3)^3}, \quad (2.27)$$

where D_{ij} is defined

$$D_{ij} = \frac{\sigma_{ii}\sigma_{jj}}{\sigma_{ii} + \sigma_{jj}} \frac{\sum_{i=1}^n x_{s,i} \sigma_{ii}^2}{\sum_{i=1}^n x_{s,i} \sigma_{ii}^3}. \quad (2.28)$$

It is important to note that the contact value at the effective packing fraction ζ_3^{eff} is required for the expression of g_1^{ij} (second term in Eq. (2.26)) which also depends on a_1^{ij} ; $g_{ij}^{HS}[\sigma_{ij}, \zeta_3^{eff}]$ is obtained from Eq. (2.27) with the appropriate value of the effective packing fraction ζ_3^{eff} . For a mixture of square wells, g_1^{ij} is given by [44] (see appendix for a full derivation)

$$g_1^{ij}(\sigma_{ij}) = \frac{1}{2\pi\epsilon_{ij}\sigma_{ij}^3} \left[3 \left(\frac{\partial a_1^{ij}}{\partial \rho_s} \right) - \frac{\lambda_{ij}}{\rho_s} \frac{\partial a_1^{ij}}{\partial \lambda_{ij}} \right], \quad (2.29)$$

so that upon substituting in Eq. (2.26) we have

$$\begin{aligned} g_{ij}^{SW}(\sigma_{ij}, \zeta_3) &= g_{ii}^{HS}(\sigma_{ij}, \zeta_3) \\ &+ \beta\epsilon_{ii} \left[g_{ij}^{HS}[\sigma_{ij}, \zeta_3^{eff}] \right. \\ &\left. + (\lambda_{ij}^3 - 1) \frac{\partial g_{ij}^{HS}[\sigma_{ij}, \zeta_3^{eff}]}{\partial \zeta_3^{eff}} \left(\frac{\lambda_{ij}}{3} \frac{\partial \zeta_3^{eff}}{\partial \lambda_{ij}} - \zeta_3 \frac{\partial \zeta_3^{eff}}{\partial \zeta_3} \right) \right]. \end{aligned} \quad (2.30)$$

2.2.4 Association contribution

The contribution to the free energy due to association of s_i square-well interaction sites on chain molecules of species i , is obtained from the theory of Wertheim [66] as:

$$\frac{A^{ASSOC.}}{NkT} = \sum_{i=1}^n x_i \left[\sum_{a=1}^{s_i} \left(\ln X_{a,i} - \frac{X_{a,i}}{2} \right) + \frac{s_i}{2} \right], \quad (2.31)$$

where first sum is over the species i , and the second over all s_i sites a on a molecule of species i . $X_{a,i}$ is the fraction of molecules of type i not bonded at site a , given by the mass action equation as [8, 66]:

$$X_{a,i} = \frac{1}{1 + \sum_{j=1}^n \sum_{b=1}^{s_j} \rho x_j X_{b,j} \Delta_{a,b,i,j}}, \quad (2.32)$$

where

$$\Delta_{a,b,i,j} = K_{a,b,i,j} F_{a,b,i,j} g^{SW}(\sigma_{ij}). \quad (2.33)$$

$K_{a,b,i,j}$ is the volume available for bonding [8, 66], $F_{a,b,i,j}$ is the Mayer f -function $F_{a,b,i,j} = \exp(-\phi_{a,b,i,j}/kT) - 1$ of the $a - b$ square-well site-site interaction $\epsilon_{a,b,i,j}$, and $g^{SW}(\sigma_{ij})$ is given by Eq. (2.30)

We have now presented the formal expressions for each contribution to the free energy in the SAFT-VR approach, both in general and for the specific case of the square-well interaction potential. The precise expressions for the perturbation terms a_1 and a_2 , and for the contact value $g_{ij}^{SW}(\sigma_{ij})$ of the monomer reference depend on the type of mixing rule that is used to describe the mixture. A number of possibilities are discussed in the following section.

2.3 Mixing rules for conformal fluids

The extension to multicomponent mixtures of any equation of state developed for pure component systems requires the use of appropriate mixing rules for both the thermodynamic variables and the parameters of the equation of state. These mixing rules introduce an implicit composition dependence into the equation of state. In the van der Waals (vdW) n -fluid theories [62, 67] the aim is to simplify the complex dependence on composition by assuming simple relationships between the pair correlation functions of the mixture and those for the pure components. The simplest case is the vdW one-fluid approximation, which can be defined in terms of the standard van der Waals mixing rules for the size and energy parameters:

$$\sigma_x^3 = \sum_{i=1}^n \sum_{j=1}^n x_{s,i} x_{s,j} \sigma_{ij}^3, \quad (2.34)$$

and

$$\alpha_x^{VDW} = \sum_{i=1}^n \sum_{j=1}^n x_{s,i} x_{s,j} \alpha_{ij}^{VDW}, \quad (2.35)$$

respectively. For monomer-monomer interactions consisting of a repulsive hard-sphere plus an arbitrary attractive well, the van der Waals attractive constant α_{ij}^{VDW} has the general form

$$\alpha_{ij}^{VDW} = \Phi(\lambda_{ij}) \epsilon_{ij} \sigma_{ij}^3, \quad (2.36)$$

where $\Phi(\lambda_{ij})$ is a shape factor that depends only on the range parameter λ_{ij} of the potential; from Eq. (2.16) it follows that for square-well interactions $\Phi(\lambda_{ij}) = 2\pi(\lambda_{ij}^3 - 1)/3$.

For mixtures of conformal fluids λ_{ij} has the same value for all species since $\lambda_{ij} = \lambda$, and Φ becomes a constant. The mixing rule given by Eq. (2.35) is then transformed into a definition of a mean-energy parameter:

$$\varepsilon_x \sigma_x^3 = \sum_{i=1}^n \sum_{j=1}^n x_{s,i} x_{s,j} \varepsilon_{ij} \sigma_{ij}^3. \quad (2.37)$$

The mixing rule for the effective size parameter σ_x (Eq. (2.34)) gives a vdW one-fluid definition of the packing fraction ζ_x for the mixture as (cf. Eq. (2.11))

$$\begin{aligned} \zeta_x &= \frac{\pi}{6} \rho_s \sum_{i=1}^n \sum_{j=1}^n x_{s,i} x_{s,j} \sigma_{ij}^3 \\ &= \frac{\pi}{6} \rho_s \sigma_x^3. \end{aligned} \quad (2.38)$$

In the context of mixtures of conformal fluids, the vdW one-fluid approximation is completed by approximating the pair distribution function for the mixture by the radial distribution function for a single fluid, using the parameters σ_x and ε_x defined previously in Eqs. (2.34 and 2.35):

$$g_{ij}(r_{ij}/\sigma_{ij}; \rho, T, x_i, x_j) = g_0(r_{ij}/\sigma_x; \rho \sigma_x^3, kT/\varepsilon_x), \quad (2.39)$$

where g_0 is the one-fluid radial distribution function.

The van der Waals two- and three-fluid theories use mixing rules with two and three size and energy parameters, respectively, and with g_{ij} still given by the pure component pair correlation function. One of the drawbacks of the higher order vdW n -fluid theories, apart from their increased complexity with respect to the one-fluid model, is that they introduce inconsistencies into the determination of coexistence properties and critical behaviour [67]. A closely related approximation to the vdW one-fluid approach is the mean-density approximation (MDA) [62, 68], in which σ_x is given by the vdW one-fluid approximation Eq. (2.34), but where the temperature scales with the individual energy parameters ε_{ij} :

$$g_{ij}(r_{ij}/\sigma_{ij}; \rho, T, x_i, x_j) = g_0(r_{ij}/\sigma_x, \rho \sigma_x^3, kT/\varepsilon_{ij}). \quad (2.40)$$

Although the one-fluid approximation can be used at all levels in the equation of state [29], it is desirable to maintain the accuracy of the description of the structure of the reference system given by Eq. (2.27). In order to achieve this, we only need to introduce the mixing rules at the level of the perturbative terms of the monomer free energy. Since the mean-attractive energy a_1 is the basic quantity which is used for the evaluation of all the other perturbative terms in the SAFT-VR approach,

we focus our discussion on the approximations obtained for a_1 .

In both the vdW one-fluid and mean-density approaches the mean-attractive energy is given by (cf. Eq. (2.15))

$$\begin{aligned} a_1 &= -\rho_s \sum_i \sum_j x_{s,i} x_{s,j} \alpha_{ij}^{VDW} g_0^{HS}[\sigma_x; \zeta_x^{eff}(\lambda)] \\ &= -\rho_s \alpha_x^{VDW} g_0^{HS}[\sigma_x; \zeta_x^{eff}(\lambda)]. \end{aligned} \quad (2.41)$$

The contact value of g_0 is obtained from the Carnahan and Starling expression for pure fluids [69, 62] as

$$g_0^{HS}[\sigma_x; \zeta_x^{eff}(\lambda)] = \frac{1 - \zeta_x^{eff}/2}{(1 - \zeta_x^{eff})^3}. \quad (2.42)$$

The effective packing fraction ζ_x^{eff} within the vdW one-fluid approximation is obtained from the corresponding packing fraction of the pure component (see Ref. [44] for the pure square-well system):

$$\zeta_x^{eff}(\zeta_x, \lambda) = c_1(\lambda)\zeta_x + c_2(\lambda)\zeta_x^2 + c_3(\lambda)\zeta_x^3, \quad (2.43)$$

where the coefficients c_1 , c_2 and c_3 are approximated by those of the pure fluid [44]:

$$\begin{pmatrix} c_1 \\ c_2 \\ c_3 \end{pmatrix} = \begin{pmatrix} 2.25855 & -1.50349 & 0.249434 \\ -0.669270 & 1.40049 & -0.827739 \\ 10.1576 & -15.0427 & 5.30827 \end{pmatrix} \begin{pmatrix} 1 \\ \lambda \\ \lambda^2 \end{pmatrix}. \quad (2.44)$$

One should note that in this case the range is the same for all components, and thus enters the expressions in a trivial manner.

A step beyond the vdW n-fluid and the MDA approaches is to calculate a_1 with the hard-sphere contact value g_{ij}^{HS} of the mixture given by Eq. (2.27), rather than that of the one-fluid expression, Eq. (2.42):

$$a_1 = -\rho_s \sum_{i=1}^n \sum_{j=1}^n x_{s,i} x_{s,j} \alpha_{ij}^{VDW} g_{ij}^{HS}[\sigma_{ij}; \zeta_3^{eff}(\lambda)]. \quad (2.45)$$

An advantage of such an approach is that Eq. (2.27) explicitly accounts for the different sizes of the spherical segments. We obtain the contact value of the pair distribution function for the mixture at the effective packing fraction ζ_3^{eff} from Eq. (2.27), with ζ_3^{eff} replacing ζ_3 :

$$g_{ij}^{HS}[\sigma_{ij}; \zeta_3^{eff}(\lambda)] = \frac{1}{1 - \zeta_3^{eff}} + 3 \frac{D_{ij} \zeta_3^{eff}}{(1 - \zeta_3^{eff})^2} + 2 \frac{(D_{ij} \zeta_3^{eff})^2}{(1 - \zeta_3^{eff})^3}. \quad (2.46)$$

Note that $g_{ij}^{HS}[\sigma_{ij}; \zeta_3^{eff}(\lambda)]$ is a functional of the function $\zeta_3^{eff}(\lambda)$.

There are three obvious ways of calculating the effective packing fraction ζ_3^{eff} . The first involves the use of the vdW one-fluid value, where (from Eq. (2.43))

$$\zeta_3^{eff}(\zeta_x, \lambda) = \zeta_x^{eff}(\zeta_x, \lambda). \quad (2.47)$$

The second involves the use of the individual packing fractions for each species, and the total packing fraction of the mixture is then obtained from the sum

$$\zeta_3^{eff}(\zeta_{3,i}, \lambda) = \sum_{i=1}^n \zeta_{3,i}^{eff}(\zeta_{3,i}, \lambda), \quad (2.48)$$

where

$$\zeta_{3,i}^{eff}(\zeta_{3,i}, \lambda) = c_1(\lambda)\zeta_{3,i} + c_2(\lambda)\zeta_{3,i}^2 + c_3(\lambda)\zeta_{3,i}^3, \quad (2.49)$$

and

$$\zeta_{3,i} = \frac{\pi}{6} x_{s,i} \rho_s \sigma_{ii}^3. \quad (2.50)$$

The dependence of the coefficients c_1 , c_2 and c_3 on the range λ is again obtained from the pure square-well fluid (cf. Eq. (2.44)). Finally, we can use the total packing fraction ζ_3 together with an expression similar to Eq. (2.43):

$$\zeta_3^{eff}(\zeta_3, \lambda) = c_1(\lambda)\zeta_3 + c_2(\lambda)\zeta_3^2 + c_3(\lambda)\zeta_3^3. \quad (2.51)$$

We end this section by reviewing the mixing rules (MXC) that we propose for conformal fluids within the SAFT-VR approach; note that this is essentially an exercise since SAFT-VR explicitly takes into account the range of the potential and hence the fluid's non-conformal nature. The possibilities discussed earlier are summarised in Table 2.1.

Table 2.1: The mixing rules (MXC) for the conformal mixtures within the SAFT-VR approach. The precise equations for a_1 , $g_{ij}^{HS}(\sigma_{ij}; \zeta_3^{eff})$ and ζ_3^{eff} are given for each mixing rule; the rest of the SAFT-VR expressions can be obtained from these expressions. The numbers refer to the equations given in the text.

Mixing Rule	a_1	$g_{ij}^{HS}(\sigma_{ij})$	ζ_3^{eff}
MXC1	(2.41)	(2.42)	(2.43)
MXC2	(2.45)	(2.46)	(2.48)
MXC3	(2.45)	(2.46)	(2.51)

The numbering of the mixing rule (MXC) refers to the representation of the effective packing fraction: MXC1 for Eq. (2.43), MXC2 Eq. (2.48), or MXC3 for Eq. (2.51). The MXC1 rule is basically the van der Waals one-fluid representation of the perturbation term for the monomer mixture. One should note that due to

the use of the mean-value theorem in the expression for a_1 , the separate energy contributions for each pair interaction factorise out of the integral giving the van der Waals constant. Furthermore, the total free energy for the reference monomer mixture also includes each pair interaction $g_{ij}^{HS}(\sigma_{ij})$ and $g_{ij}^{SW}(\sigma_{ij})$. This means that MXC1 as used in our theory is similar to the MDA approach. The prescriptions given by MXC2 and MXC3 for the partial and total packing fractions both go beyond the VDW one-fluid level. The simplest and probably the most accurate mixing rule is MXC3 although, as will be discussed later, there are some problems associated with the critical region of the phase diagram when this mixing rule is used in practice. In all of these MXC expressions the range λ plays a trivial role, since for conformal fluids the range is the same for all species. This is not the case for the non-conformal fluids which we discuss next.

2.4 Mixing rules for non-conformal fluids

A central feature of the SAFT-VR approach is that it incorporates the non-conformal properties of the fluid by using different values of the range λ_{ij} for each species. The factorisation of the radial distribution function g_{ij}^{HS} in the expression for the mean-attractive energy (using the mean-value theorem) Eq. (2.14) together with the contact value of g_{ij}^{HS} , allows a straightforward description of the mixture.

The vdW one-fluid mixing rules, Eqs. (2.34) and (2.35) are still valid for non-conformal fluids. We can derive two mixing rules from Eq. (2.35), one for the energy,

$$\varepsilon_x = \frac{\sum_{i=1}^n \sum_{j=1}^n x_{s,i} x_{s,j} \varepsilon_{ij} \lambda_{ij}^3 \sigma_{ij}^3}{\sum_{i=1}^n \sum_{j=1}^n x_{s,i} x_{s,j} \lambda_{ij}^3 \sigma_{ij}^3}, \quad (2.52)$$

and another for the range of the potential,

$$\lambda_x^3 = \frac{\sum_{i=1}^n \sum_{j=1}^n x_{s,i} x_{s,j} \varepsilon_{ij} \lambda_{ij}^3 \sigma_{ij}^3}{\sum_{i=1}^n \sum_{j=1}^n x_{s,i} x_{s,j} \varepsilon_{ij} \sigma_{ij}^3}. \quad (2.53)$$

As for the conformal fluid described in the previous section, the corresponding mixing rules (MX) for the non-conformal systems can be obtained via the three possibilities which exist for the determination of the effective packing fraction (which we will denote as MX1, MX2, or MX3), but now using one of two possibilities for the range of the interaction potential of the mixture: a) as the simplest option one can use the vdW one-fluid rule for λ_x given by Eq. (2.53); b) alternatively, a more accurate representation can be obtained by using the individual

range λ_{ij} for each pair interaction. The vdW one-fluid mixing rule for a_1 in the case of our non-conformal square-well mixture (MX1a) is

$$\begin{aligned} a_1 &= -\rho_s \sum_{i=1}^n \sum_{j=1}^n x_{s,i} x_{s,j} \alpha_{ij}^{VDW} g_0^{HS}[\sigma_x; \zeta_x^{eff}(\lambda_x)] \\ &= -\rho_s \alpha_x^{VDW} g_0^{HS}[\sigma_x; \zeta_x^{eff}(\lambda_x)] \end{aligned} \quad (2.54)$$

where $g_0^{HS}[\sigma_x; \zeta_x^{eff}(\lambda_x)]$ is obtained from the pure-fluid Carnahan and Starling expression (Eq. (2.42)). The effective packing fraction is obtained from the one-fluid expressions for the packing fraction ζ_x (Eq. (2.43)) and range λ_x (Eq. (2.53)):

$$\zeta_x^{eff}(\zeta_x, \lambda_x) = c_1(\lambda_x) \zeta_x + c_2(\lambda_x) \zeta_x^2 + c_3(\lambda_x) \zeta_x^3. \quad (2.55)$$

When the individual ranges λ_{ij} are used one can no longer factorise the pair distribution function out of the sum, and the corresponding mixing rule MX1b is given by

$$a_1 = -\rho_s \sum_{i=1}^n \sum_{j=1}^n x_{s,i} x_{s,j} \alpha_{ij}^{VDW} g_0^{HS}[\sigma_x; \zeta_x^{eff}(\lambda_{ij})] \quad (2.56)$$

where now $g_0^{HS}[\sigma_x; \zeta_x^{eff}(\lambda_{ij})]$ depends explicitly on the range of the pair interaction via the expression for the effective packing fraction:

$$\zeta_x^{eff}(\zeta_x, \lambda_{ij}) = c_1(\lambda_{ij}) \zeta_x + c_2(\lambda_{ij}) \zeta_x^2 + c_3(\lambda_{ij}) \zeta_x^3. \quad (2.57)$$

Note that as for the conformal mixture we approximate the coefficients c_1 , c_2 , and c_3 by the values obtained for the pure fluid Eq. (2.44) (see Ref. [44]).

In the second class of mixing rule we use the packing fraction obtained from the individual species (cf. Eqs. (2.48) and (2.49)) but with the two distinct treatments of its dependence on the range of the potential. When we use the value of λ_x given by Eq. (2.53) we obtain the mixing rule MX2a, where

$$a_1 = -\rho_s \sum_{i=1}^n \sum_{j=1}^n x_{s,i} x_{s,j} \alpha_{ij}^{VDW} g_{ij}^{HS}[\sigma_{ij}; \zeta_3^{eff}(\lambda_x)], \quad (2.58)$$

with

$$\zeta_3^{eff}(\zeta_{3,i}, \lambda_x) = \sum_{i=1}^n \zeta_{3,i}^{eff}(\zeta_{3,i}, \lambda_x) \quad (2.59)$$

and

$$\zeta_{3,i}^{eff}(\zeta_{3,i}, \lambda_x) = c_1(\lambda_x) \zeta_{3,i} + c_2(\lambda_x) \zeta_{3,i}^2 + c_3(\lambda_x) \zeta_{3,i}^3. \quad (2.60)$$

The mixing rule MX2b is given in terms of the range of each pair interaction as

$$a_1 = -\rho_s \sum_{i=1}^n \sum_{j=1}^n x_{s,i} x_{s,j} \alpha_{ij}^{VDW} g_{ij}^{HS}[\sigma_{ij}; \zeta_3^{eff}(\lambda_{ij})], \quad (2.61)$$

where the effective packing fraction is now

$$\zeta_3^{eff}(\zeta_{3,i}, \lambda_{ij}) = \sum_{i=1}^n \zeta_{3,i}^{eff}(\zeta_{3,i}, \lambda_{ij}) \quad (2.62)$$

with

$$\zeta_{3,i}^{eff}(\zeta_{3,i}, \lambda_{ij}) = c_1(\lambda_{ij})\zeta_{3,i} + c_2(\lambda_{ij})\zeta_{3,i}^2 + c_3(\lambda_{ij})\zeta_{3,i}^3. \quad (2.63)$$

The third class of mixing rule MX3 uses a direct mapping of the packing fraction of the mixture with that of the pure fluid to give an expression for the effective packing fraction, as in the MXC3 rule for conformal fluids. When λ_x is given by Eq. (2.53), the mixing rule MX3a is obtained as

$$a_1 = -\rho_s \sum_{i=1}^n \sum_{j=1}^n x_{s,i} x_{s,j} \alpha_{ij}^{VDW} g_{ij}^{HS}[\sigma_{ij}; \zeta_3^{eff}(\lambda_x)], \quad (2.64)$$

where

$$\zeta_3^{eff}(\zeta_3, \lambda_x) = c_1(\lambda_x)\zeta_3 + c_2(\lambda_x)\zeta_3^2 + c_3(\lambda_x)\zeta_3^3. \quad (2.65)$$

Finally, using the individual values of the interaction potential range, we obtain the mixing rule MX3b as

$$a_1 = -\rho_s \sum_{i=1}^n \sum_{j=1}^n x_{s,i} x_{s,j} \alpha_{ij}^{VDW} g_{ij}^{HS}[\sigma_{ij}; \zeta_3^{eff}(\lambda_{ij})], \quad (2.66)$$

with

$$\zeta_3^{eff}(\zeta_3, \lambda_{ij}) = c_1(\lambda_{ij})\zeta_3 + c_2(\lambda_{ij})\zeta_3^2 + c_3(\lambda_{ij})\zeta_3^3. \quad (2.67)$$

The mixing rules for non-conformal fluid are summarised in Table 2.2. The simplest rule MX1a is similar to that of MXC1 for conformal fluids and essentially represents a vdW one-fluid treatment. The most rigorous is probably the full MX3b representation; this prescription was first suggested in the original SAFT-VR paper Ref. ([44]). Its simplicity is a particularly attractive feature of the approach.

2.5 Combining rules

In order to evaluate the parameters for the unlike interactions (the so-called cross parameters) for the mixtures one can use the standard Lorentz-Berthelot (LB)

Table 2.2: The mixing rules (MX) for the non-conformal mixtures within the SAFT-VR approach. The precise representation for a_1 , $g_{ij}^{HS}[\sigma_{ij}; \zeta_3^{eff}]$ and ζ_3^{eff} are given for each mixing rule; the rest of the SAFT-VR expressions can be obtained from these expressions. The numbers refer to the equations given in the text.

Mixing Rule	a_1	$g_{ij}^{HS}(\sigma_{ij})$	ζ_3^{eff}
MX1a	(2.54)	(2.42)	(2.55)
MX1b	(2.56)	(2.42)	(2.57)
MX2a	(2.58)	(2.46)	(2.59)
MX2b	(2.61)	(2.46)	(2.62)
MX3a	(2.64)	(2.46)	(2.65)
MX3b	(2.66)	(2.46)	(2.67)

combining rules, which are derived for conformal fluids [67]:

$$\sigma_{ij} = \frac{\sigma_{ii} + \sigma_{jj}}{2} \quad (2.68)$$

$$\varepsilon_{ij} = \sqrt{\varepsilon_{ii}\varepsilon_{jj}}. \quad (2.69)$$

Equation (2.69) is a particular case of the more general combining rule [67]:

$$\varepsilon_{ij} = \xi_{ij}\sqrt{\varepsilon_{ii}\varepsilon_{jj}}. \quad (2.70)$$

It is well known [67] that real substances depart from the LB rules to varying degrees depending on the particular interactions involved; in many cases mixtures are characterised by values of $\xi_{ij} < 1$. The value of ε_{ij} for real fluid mixtures is usually obtained by an appropriate fit to the experimental properties of the specific mixture.

A combining rule for the van der Waals attractive constant α_{ij}^{VDW} follows from the LB rule for the energy, Eq. (2.69),

$$\alpha_{ij}^{VDW} = \Gamma_{ij}\sqrt{\alpha_{ii}^{VDW}\alpha_{jj}^{VDW}}, \quad (2.71)$$

where Γ_{ij} depends on the form of the potential. For square-well mixtures Γ_{ij} is given by

$$\Gamma_{ij} = \frac{(\lambda_{ij}^3 - 1)\sigma_{ij}^3}{\sqrt{(\lambda_{ii}^3 - 1)(\lambda_{jj}^3 - 1)\sigma_{ii}^3\sigma_{jj}^3}}. \quad (2.72)$$

An alternative combining rule to Eq. (2.69) corresponds to the geometric mean for α_{ij}^{VDW} :

$$\alpha_{ij}^{VDW} = \sqrt{\alpha_{ii}^{VDW}\alpha_{jj}^{VDW}}. \quad (2.73)$$

This is equivalent to the general rule given by Eq. (2.70) with $\xi_{ij} = 1/\Gamma_{ij}$. It is

clear that, for conformal fluids, the three rules given by Eqs. (2.68), (2.69) and (2.73) are inconsistent unless the particles in the mixture are of the equal size.

However, for non-conformal fluids, the three combining rules, Eqs. (2.68), (2.69) and (2.73), can be used if λ_{ij} is chosen in such a way so that they are self-consistent, i.e. by assuming $\Gamma_{ij} = 1$ in Eq. (2.72). This leads to an expression for λ_{ij} of the form

$$\lambda_{ij}^3 = 1 + \frac{1}{\sigma_{ij}^3} \sqrt{(\lambda_{ii}^3 - 1)(\lambda_{jj}^3 - 1)\sigma_{ii}^3 \sigma_{jj}^3}. \quad (2.74)$$

It is possible to relax this criterion for λ_{ij} and to use either Eq. (2.69) or Eq. (2.73), together with a specific combining rule for λ_{ij} . A simple arithmetic-mean combining rule may be used, analogous to that for the particle diameters (cf. Eq. (2.68)):

$$\lambda_{ij} = \frac{\lambda_{ii}\sigma_{ii} + \lambda_{jj}\sigma_{jj}}{\sigma_{ii} + \sigma_{jj}}. \quad (2.75)$$

Another option for the evaluation of λ_{ij} is by optimising its value from a fit to experimental data for the mixture.

In the case of the association contribution to the SAFT-VR free energy similar combining rules can be used for the energy of the site-site interaction $\varepsilon_{a,b,i,j}$ in the mixture and the bonding volume $K_{a,b,i,j}$ in Eq. (2.33). The Berthelot rule for the unlike site-site interaction is

$$\varepsilon_{a,b,i,j} = \sqrt{(\varepsilon_{a,b,i,i}\varepsilon_{a,b,j,j})}, \quad (2.76)$$

and the combining rule for the bonding volume is

$$K_{a,b,i,j} = \left[\frac{K_{a,b,i,i}^{1/3} + K_{a,b,j,j}^{1/3}}{2} \right]. \quad (2.77)$$

This completes our description of the combining rules. One should, of course, note that the combining rules are a convenient first representation of the unlike interactions, but real substances show large deviations in practice, especially when the components of the mixture are chemically very different. It is usually necessary to fit the cross parameters to experimental data. In most cases the phase equilibria of real mixtures is most sensitive to the variation in the energy parameters.

2.6 Conclusions

In this chapter we provide a detailed analysis of the SAFT-VR approach to mixtures of fluids consisting of chain molecules with attractive interactions of variable range. The resulting SAFT-VR equation of state has a van der Waals form where the monomer properties are evaluated using a standard high-temperature perturbation expansion. The mean-value theorem is used to give a compact expression for the mean-attractive energy a_1 , and the contact value of the radial distribution function is given by a self-consistent method, which combines two routes for the evaluation of the pressure of the fluid [44]. This simple representation of a_1 allows us to propose a number of straightforward mixing rules which range from the simplest van der Waals one-fluid expressions to the full second-order description. It is important to mention that although the SAFT-VR expressions and the corresponding mixing rules have been presented here in the context of square-well mixtures, this is solely for convenience and the analysis can be easily applied to other types of hard-core attractive potential (see Ref. [44]). To our knowledge, we present the first in-depth analysis of mixing rules for non-conformal fluids.

The main motivation of the SAFT-VR approach is to obtain a description of the phase behaviour of real fluid mixtures. The implicit dependence on the variable range of the intermolecular potential makes the equation of state extremely versatile, and allows for an accurate representation of the thermodynamics of fluid systems [44]. The approach is currently being used to examine the vapour-liquid and liquid-liquid equilibria of a number of mixtures. Use of the SAFT-VR methodology with the full MX3b mixing rule is seen to provide an excellent description of the vapour-liquid equilibria for mixtures of n-alkanes [50], and for mixtures of replacement refrigerants [52]. However, further studies of mixtures which exhibit large regions of liquid-liquid immiscibility, such as mixtures of alkanes and perfluoroalkanes [51], have shown that there are large inconsistencies in the description of the UCST when the MX3b mixing rule is used. This inability to describe mixture properties is not surprising, and is common in 'two-fluid' equations of state for mixtures which use parameters defined for pure fluids [67, 70]; in the SAFT-VR approach the range dependence of the effective density for the mixture is obtained from the pure fluid system. The use of the vdW one-fluid packing fraction ζ_x^{eff} together with the MX3b mixing rule does not remove the inconsistency, and one has to resort to using the vdW one-fluid MX1 mixing rules in order to obtain an adequate description. The MX1b mixing rule has been found to give an excellent representation of both the vapour-liquid and the liquid-liquid critical behaviour in binary mixtures of perfluoromethane with a series of n-alkanes [51].

2.7 Appendix: Contact value of the radial distribution function

Here we illustrate how a closed expression for the radial distribution function at contact for a square-well fluid is derived within the SAFT-VR approach. The method involves the use of two independent routes to evaluate the compressibility factor (or pressure) of the fluid. The Clausius virial for the compressibility factor can be written as

$$Z^V = 1 - \frac{2\pi\beta}{3}\rho_s \sum_{i=1}^n \sum_{j=1}^n x_i x_j \int_0^\infty r^2 r \left(\frac{\partial U_{ij}}{\partial r} \right) g_{ij}(r) dr, \quad (2.78)$$

where $r(\partial U_{ij}/\partial r)$ is the virial contribution. An equivalent expression can be obtained from the density derivative of the Helmholtz free energy as

$$Z^T = \rho_s \frac{\partial a}{\partial \rho_s}, \quad (2.79)$$

which upon application of a high temperature expansion gives

$$Z^T = Z^{HS} + \beta \sum_{i=1}^n \sum_{j=1}^n x_i x_j Z_{ij}. \quad (2.80)$$

We first focus on the virial route to the compressibility factor of Eq. (2.78). For discontinuous potentials such as the hard-core square-well of Eq. (2.4), it is advantageous to examine the behaviour of the background correlation function $y_{ij}(r) = \exp(\beta U_{ij})g_{ij}(r)$ in Eq. (2.78) rather than $g_{ij}(r)$ itself, since $y_{ij}(r)$ it is a continuous function of r . In order to be able to express the compressibility factor of Eq. (2.78) in terms of $y_{ij}(r)$, we must first obtain the derivative

$$\frac{\partial \exp(-\beta U_{ij})}{\partial r} = -\beta \frac{\partial U_{ij}}{\partial r} \exp(-\beta U_{ij}), \quad (2.81)$$

which can be re-arranged to give

$$\frac{\partial U_{ij}}{\partial r} = -\frac{1}{\beta} \frac{\partial \exp(-\beta U_{ij})}{\partial r} \exp(\beta U_{ij}). \quad (2.82)$$

Substituting this expression into the integral of Eq. (2.78) gives

$$\begin{aligned} \int_0^\infty r^3 \frac{\partial U_{ij}}{\partial r} g_{ij}(r) dr &= -\int_0^\infty r^3 \frac{1}{\beta} \frac{\partial \exp(-\beta U_{ij})}{\partial r} \exp(\beta U_{ij}) g_{ij}(r) dr \\ &= -\frac{1}{\beta} \int_0^\infty r^3 \frac{\partial \exp(-\beta U_{ij})}{\partial r} y_{ij}(r) dr, \end{aligned} \quad (2.83)$$

so that Eq. (2.78) becomes

$$Z^V = 1 + \frac{2\pi}{3} \rho_s \sum_{i=1}^n \sum_{j=1}^n x_i x_j \int_0^\infty r^3 \frac{\partial \exp(-\beta U_{ij})}{\partial r} y_{ij}(r) dr. \quad (2.84)$$

In order to simplify this integral the properties of the Heaviside function inside the integral of Eq. (2.84) must be examined; these are summarised by

$$\frac{\partial \exp(-\beta U_{ij})}{\partial r} = \begin{cases} 0 & \text{if } r < \sigma_{ij} \\ A\delta(r - \sigma_{ij}) & \text{if } r = \sigma_{ij} \\ 0 & \text{if } \sigma_{ij} < r < \lambda_{ij}\sigma_{ij} \\ -B\delta(r - \lambda_{ij}\sigma_{ij}) & \text{if } r = \lambda_{ij}\sigma_{ij} \\ 0 & \text{if } r > \lambda_{ij}\sigma_{ij} \end{cases}, \quad (2.85)$$

where δ is the Dirac delta function, and A and B are constants which have to be evaluated. The properties of the Dirac delta function can be written as

$$\int_{-\infty}^{\infty} \delta(x) dx = 1, \quad (2.86)$$

where

$$\int_a^b f(x) \delta(x - x_0) = \begin{cases} f(x_0) & \text{if } x_0 \in [a, b] \\ 0 & \text{if } x_0 \notin [a, b]. \end{cases} \quad (2.87)$$

The integral of Eq. (2.84) can be split as follows

$$\begin{aligned} \int_0^\infty \frac{\partial \exp(-\beta U_{ij})}{\partial r} dr &= \int_0^{\sigma_{ij}^-} \frac{\partial \exp(-\beta U_{ij})}{\partial r} dr + \int_{\sigma_{ij}^-}^{\sigma_{ij}^+} \frac{\partial \exp(-\beta U_{ij})}{\partial r} dr \\ &+ \int_{\sigma_{ij}^+}^{\lambda_{ij}\sigma_{ij}^-} \frac{\partial \exp(-\beta U_{ij})}{\partial r} dr + \int_{\lambda_{ij}\sigma_{ij}^-}^{\lambda_{ij}\sigma_{ij}^+} \frac{\partial \exp(-\beta U_{ij})}{\partial r} dr \\ &+ \int_{\lambda_{ij}\sigma_{ij}^+}^\infty \frac{\partial \exp(-\beta U_{ij})}{\partial r} dr. \end{aligned} \quad (2.88)$$

For the square-well potential this reduces to

$$\begin{aligned} \int_0^\infty \frac{\partial \exp(-\beta U_{ij})}{\partial r} dr &= \int_{\sigma_{ij}^-}^{\sigma_{ij}^+} \frac{\partial \exp(-\beta U_{ij})}{\partial r} dr \\ &+ \int_{\lambda_{ij}\sigma_{ij}^-}^{\lambda_{ij}\sigma_{ij}^+} \frac{\partial \exp(-\beta U_{ij})}{\partial r} dr, \end{aligned} \quad (2.89)$$

which upon substitution of Eq. (2.85) becomes

$$\begin{aligned} \int_0^\infty \frac{\partial \exp(-\beta U_{ij})}{\partial r} dr &= \int_{\sigma_{ij}^-}^{\sigma_{ij}^+} A\delta(r - \sigma_{ij}) dr \\ &- \int_{\lambda_{ij}\sigma_{ij}^-}^{\lambda_{ij}\sigma_{ij}^+} B\delta(r - \lambda_{ij}\sigma_{ij}) dr. \end{aligned} \quad (2.90)$$

From Eq. (2.87), we know that the properties of the Dirac delta function can result in an expression of the form

$$\int_0^{\infty} \frac{\partial \exp(-\beta U_{ij})}{\partial r} dr = A - B. \quad (2.91)$$

The LHS of the above expression can also be evaluated in full by integrating over the full range of the interaction potential

$$\begin{aligned} \int_0^{\infty} \frac{\partial \exp(-\beta U_{ij})}{\partial r} dr &= [\exp(-\beta U_{ij})]_0^{\infty} \\ &= 1, \end{aligned} \quad (2.92)$$

so that we can write

$$1 = A - B. \quad (2.93)$$

In order to evaluate the constants A and B we examine the second integral in Eq. (2.88)

$$\begin{aligned} \int_{\sigma_{ij}^-}^{\sigma_{ij}^+} \frac{\partial \exp(-\beta U_{ij})}{\partial r} dr &= [\exp(-\beta U_{ij})]_{\sigma_{ij}^-}^{\sigma_{ij}^+} \\ &= \exp(-\beta U_{ij}(\sigma_{ij}^+)) - \exp(-\beta U_{ij}(\sigma_{ij}^-)) \\ &= \exp(-\beta \varepsilon_{ij}) - 0, \end{aligned} \quad (2.94)$$

we also know that from Eq. (2.90) that

$$\int_{\sigma_{ij}^-}^{\sigma_{ij}^+} \frac{\partial \exp(-\beta U_{ij})}{\partial r} dr = \int_{\sigma_{ij}^-}^{\sigma_{ij}^+} A \delta(r - \sigma_{ij}) dr, \quad (2.95)$$

enabling us to write

$$A = \exp(-\beta \varepsilon_{ij}), \quad (2.96)$$

and

$$B = \exp(-\beta \varepsilon_{ij}) - 1. \quad (2.97)$$

Substituting these values of A and B into Eq. (2.85) we can obtain an expression for the integral in the virial compressibility factor of Eq. (2.78) of the form

$$\begin{aligned} \int_0^{\infty} r^3 \frac{\partial \exp(-\beta U_{ij})}{\partial r} y_{ij}(r) dr &= \int_{\sigma_{ij}^-}^{\sigma_{ij}^+} r^3 \exp(\beta \varepsilon_{ij}) \delta(r - \sigma_{ij}) y_{ij}(r) dr \\ &\quad - \int_{\lambda_{ij} \sigma_{ij}^-}^{\lambda_{ij} \sigma_{ij}^+} r^3 [\exp(\beta \varepsilon_{ij}) - 1] \delta(r - \lambda_{ij} \sigma_{ij}) y_{ij}(r) dr. \end{aligned} \quad (2.98)$$

Using the property of the Dirac delta given in Eq. (2.87) we can re-write the Clausius virial Eq. (2.78) as

$$Z^V = 1 + \frac{2\pi}{3}\rho_s \sum_{i=1}^n \sum_{j=1}^n x_i x_j \{ \exp(\beta\varepsilon_{ij}) \sigma_{ij}^3 y_{ij}(\sigma_{ij}) - [\exp(\beta\varepsilon_{ij}) - 1] \lambda_{ij}^3 \sigma_{ij}^3 y_{ij}(\lambda_{ij}\sigma_{ij}) \}, \quad (2.99)$$

which simplifies further to

$$Z^V = 1 + \frac{2\pi}{3}\rho_s \sum_{i=1}^n \sum_{j=1}^n x_i x_j \{ \sigma_{ij}^3 g_{ij}(\sigma_{ij}) - [\exp(\beta\varepsilon_{ij}) - 1] \lambda_{ij}^3 \sigma_{ij}^3 y_{ij}(\lambda_{ij}\sigma_{ij}) \}. \quad (2.100)$$

In order to express the compressibility factor as a series in β , so that it is consistent with the perturbation expansion used for the mean-attractive energy in the SAFT-VR methodology, we utilise a property of the exponential series, which gives

$$\exp(\beta\varepsilon_{ij}) \simeq 1 + \beta\varepsilon_{ij} \quad (2.101)$$

and hence

$$\exp(\beta\varepsilon_{ij}) - 1 \simeq \beta\varepsilon_{ij}. \quad (2.102)$$

The compressibility factor of Eq. (2.100) then becomes

$$Z^V = 1 + \frac{2\pi}{3}\rho_s \sum_{i=1}^n \sum_{j=1}^n x_i x_j \sigma_{ij}^3 \{ g_{ij}(\sigma_{ij}) - \exp(\beta\varepsilon_{ij}) \lambda_{ij}^3 \sigma_{ij}^3 y_{ij}(\lambda_{ij}\sigma_{ij}) \}. \quad (2.103)$$

Recalling that within the SAFT-VR perturbation expansions we can truncate the high-temperature expansion for the radial distribution function at first order

$$g_{ij}(r) = g_{ij}^{HS}(r) + \beta\varepsilon_{ij} g_{ij}^1(r), \quad (2.104)$$

so that the expression for the background correlation function becomes

$$y_{ij}(\lambda_{ij}\sigma_{ij}) = \exp(-\beta\varepsilon_{ij}) [g_{ij}^{HS}(\lambda_{ij}\sigma_{ij}) + \beta\varepsilon_{ij} g_{ij}^1(\lambda_{ij}\sigma_{ij})]. \quad (2.105)$$

Expansion of the exponential function in the above expression gives

$$y_{ij}(\lambda_{ij}\sigma_{ij}) \simeq (1 - \beta\varepsilon_{ij}) [g_{ij}^{HS}(\lambda_{ij}\sigma_{ij}) + \beta\varepsilon_{ij} g_{ij}^1(\lambda_{ij}\sigma_{ij})], \quad (2.106)$$

which can be simplified to

$$y_{ij}(\lambda_{ij}\sigma_{ij}) \simeq g_{ij}^{HS}(\lambda_{ij}\sigma_{ij}) + \beta\varepsilon_{ij} g_{ij}^1(\lambda_{ij}\sigma_{ij}) - \beta\varepsilon_{ij} g_{ij}^{HS}(\lambda_{ij}\sigma_{ij}). \quad (2.107)$$

Substituting this expression for $y_{ij}(\lambda_{ij}\sigma_{ij})$ into Eq. (2.103) gives an expression for the virial compressibility of the form

$$\begin{aligned} Z^V &= 1 + \frac{2\pi}{3}\rho_s \sum_{i=1}^n \sum_{j=1}^n x_i x_j \sigma_{ij}^3 \{g_{ij}^{HS}(\sigma_{ij}) + \beta \varepsilon_{ij} g_{ij}^1(\sigma_{ij})\} \\ &\quad - \frac{2\pi}{3}\rho_s \beta \sum_{i=1}^n \sum_{j=1}^n x_i x_j \sigma_{ij}^3 \varepsilon_{ij} \lambda_{ij}^3 g_{ij}^{HS}(\lambda_{ij}\sigma_{ij}). \end{aligned} \quad (2.108)$$

Since we know that

$$Z^{HS} = 1 + \frac{2\pi}{3}\rho_s \sum_{i=1}^n \sum_{j=1}^n x_i x_j \sigma_{ij}^3 g_{ij}^{HS}(\sigma_{ij}), \quad (2.109)$$

we can re-write Eq. (2.108) for the compressibility factor as

$$Z^V = Z^{HS} + \frac{2\pi}{3}\rho_s \beta \sum_{i=1}^n \sum_{j=1}^n x_i x_j \sigma_{ij}^3 \varepsilon_{ij} [g_{ij}^1(\sigma_{ij}) - \lambda_{ij}^3 g_{ij}^{HS}(\lambda_{ij}\sigma_{ij})]. \quad (2.110)$$

We can obtain a similar expression for the compressibility factor from the Helmholtz free energy, Eq. (2.79) as

$$Z^T = Z^{HS} + \beta \rho_s \sum_{i=1}^n \sum_{j=1}^n x_i x_j \frac{\partial a_1^{ij}}{\partial \rho_s}. \quad (2.111)$$

Equating these two expressions for the compressibility factor we obtain

$$\frac{\partial a_1^{ij}}{\partial \rho_s} = \frac{2\pi}{3}\sigma_{ij}^3 \varepsilon_{ij} [g_{ij}^1(\sigma_{ij}) - \lambda_{ij}^3 g_{ij}^{HS}(\lambda_{ij}\sigma_{ij})], \quad (2.112)$$

which can be re-arranged to give an expression for g_{ij}^1

$$g_{ij}^1(\sigma_{ij}) = \frac{3}{2\pi\sigma_{ij}^3 \varepsilon_{ij}} \frac{\partial a_1^{ij}}{\partial \rho_s} + \lambda_{ij}^3 g_{ij}^{HS}(\lambda_{ij}\sigma_{ij}). \quad (2.113)$$

In order to evaluate $g_{ij}^{HS}(\lambda_{ij}\sigma_{ij})$ we examine the definition of the mean-attractive energy for the square-well potential within the SAFT-VR framework (Eq. 2.13), over a particular region of the potential, so that

$$a_1^{ij} = -2\pi\rho_s \varepsilon_{ij} \int_{\sigma_{ij}}^{\lambda_{ij}\sigma_{ij}} r_{ij}^2 g_{ij}^{HS}(r_{ij}) dr_{ij}. \quad (2.114)$$

The Leibniz rule [71] states that

$$\frac{d}{d\lambda} \int_{a(\lambda)}^{b(\lambda)} f(\lambda, x) dx = \int_{a(\lambda)}^{b(\lambda)} \frac{\partial f}{\partial \lambda} dx + f(\lambda, b) \frac{db}{d\lambda} - f(\lambda, a) \frac{da}{d\lambda}, \quad (2.115)$$

in our case, $a = \sigma_{ij}$ and $f = r_{ij}^2 g_{ij}^{HS}(r_{ij})$ are independent of $\lambda_{ij} \sigma_{ij}$, so that the rule reduces to

$$\int_{\sigma_{ij}}^{\lambda_{ij} \sigma_{ij}} = r_{ij}^2 g_{ij}^{HS}(r_{ij}) dr_{ij} = (\lambda_{ij} \sigma_{ij})^2 g_{ij}^{HS}(\lambda_{ij} \sigma_{ij}). \quad (2.116)$$

Hence the the derivative in the expression for the mean-attractive energy, Eq. (2.114) becomes

$$\frac{\partial a_1^{ij}}{\partial(\lambda_{ij} \sigma_{ij})} = -2\pi \rho_s \varepsilon_{ij} \lambda_{ij}^2 \sigma_{ij}^2 g_{ij}^{HS}(\lambda_{ij} \sigma_{ij}). \quad (2.117)$$

This simplifies to

$$\frac{1}{\sigma_{ij}} \frac{\partial a_1^{ij}}{\partial \lambda_{ij}} = -2\pi \rho_s \varepsilon_{ij} \lambda_{ij}^2 \sigma_{ij}^2 g_{ij}^{HS}(\lambda_{ij} \sigma_{ij}), \quad (2.118)$$

which rearranges to give

$$g_{ij}^{HS}(\lambda_{ij} \sigma_{ij}) = -\frac{1}{2\pi \rho_s \varepsilon_{ij} \lambda_{ij}^2 \sigma_{ij}^3} \frac{\partial a_1^{ij}}{\partial \lambda_{ij}}. \quad (2.119)$$

Substituting into Eq. (2.113) we obtain

$$g_{ij}^1(\sigma_{ij}) = \frac{3}{2\pi \sigma_{ij}^3 \varepsilon_{ij}} \frac{\partial a_1^{ij}}{\partial \rho_s} - \frac{\lambda_{ij}}{2\pi \rho_s \varepsilon_{ij} \sigma_{ij}^3} \frac{\partial a_1^{ij}}{\partial \lambda_{ij}}, \quad (2.120)$$

which can be used in the expansion for the radial distribution function of Eq. (2.104) to give

$$g_{ij}(\sigma_{ij}) = g_{ij}^{HS}(\sigma_{ij}) + \frac{\beta}{2\pi \sigma_{ij}^3} \left[3 \frac{\partial a_1^{ij}}{\partial \rho_s} - \frac{\lambda_{ij}}{\rho_s} \frac{\partial a_1^{ij}}{\partial \lambda_{ij}} \right]. \quad (2.121)$$

The derivatives of the mean-attractive energy required in the above expression for the square-well potential can be obtained from the SAFT-VR expressions for a_1^{ij}

$$a_1^{ij} = -\alpha_{ij}^{VDW} \rho_s g_{ij}^{HS}(\sigma_{ij}; \zeta_3^{eff}), \quad (2.122)$$

where

$$\alpha_{ij}^{VDW} = \frac{2\pi}{3} \varepsilon_{ij} \sigma_{ij}^3 (\lambda_{ij}^3 - 1), \quad (2.123)$$

and ζ_3^{eff} is the effective packing fraction, which depends on the overall system packing fraction ζ_3 and on the range of the interaction potential λ_{ij} .

The derivative of a_1^{ij} with respect to ρ_s is given by

$$\frac{\partial a_1^{ij}}{\partial \rho_s} = -\alpha_{ij}^{VDW} g_{ij}^{HS}(\sigma_{ij}; \zeta_3^{eff}) - \alpha_{ij}^{VDW} \rho_s \frac{\partial g_{ij}^{HS}(\sigma_{ij}; \zeta_3^{eff})}{\partial \rho_s}, \quad (2.124)$$

which can be re-written in terms of the packing fraction ζ_3 as

$$\frac{\partial a_1^{ij}}{\partial \rho_s} = -\alpha_{ij}^{VDW} g_{ij}^{HS}(\sigma_{ij}; \zeta_3^{eff}) - \alpha_{ij}^{VDW} \zeta_3 \frac{\partial g_{ij}^{HS}(\sigma_{ij}; \zeta_3^{eff})}{\partial \zeta_3}. \quad (2.125)$$

The derivative of g_{ij}^{HS} with respect to ζ_3 is given by

$$\frac{\partial g_{ij}^{HS}}{\partial \zeta_3} = \frac{\partial g_{ij}^{HS}}{\partial \zeta_3^{eff}} \frac{\partial \zeta_3^{eff}}{\partial \zeta_3}. \quad (2.126)$$

Both the partial derivatives on the RHS of this equation can be easily evaluated since the dependency of the hard-sphere radial distribution function on the overall packing fraction and the dependency of the effective packing fraction on the overall packing fraction are both known in the SAFT-VR approach. This gives a final expression for Eq. (2.125) of the form

$$\frac{\partial a_1^{ij}}{\partial \rho_s} = -\alpha_{ij}^{VDW} g_{ij}^{HS}(\sigma_{ij}; \zeta_3^{eff}) - \alpha_{ij}^{VDW} \zeta_3 \frac{\partial g_{ij}^{HS}}{\partial \zeta_3^{eff}} \frac{\partial \zeta_3^{eff}}{\partial \zeta_3}. \quad (2.127)$$

The derivative of the mean-attractive energy a_1^{ij} with respect to the potential range λ_{ij} is obtained through

$$\frac{\partial a_1^{ij}}{\partial \lambda_{ij}} = -\frac{\partial \alpha_{ij}^{VDW}}{\partial \lambda_{ij}} \rho_s g_{ij}^{HS}(\sigma_{ij}; \zeta_3^{eff}) - \alpha_{ij}^{VDW} \rho_s \frac{\partial g_{ij}^{HS}(\sigma_{ij}; \zeta_3^{eff})}{\partial \lambda_{ij}}, \quad (2.128)$$

where the derivative of α_{ij}^{VDW} is given by

$$\frac{\partial \alpha_{ij}^{VDW}}{\partial \lambda_{ij}} = 2\pi \varepsilon_{ij} \sigma_{ij}^3 \lambda_{ij}^2. \quad (2.129)$$

The derivative of g_{ij}^{HS} can be written

$$\frac{\partial g_{ij}^{HS}}{\partial \lambda_{ij}} = \frac{\partial g_{ij}^{HS}}{\partial \zeta_3^{eff}} \frac{\partial \zeta_3^{eff}}{\partial \lambda_{ij}}, \quad (2.130)$$

where the dependency of the effective packing fraction on the range of the potential is known. Hence Eq. (2.128) becomes

$$\frac{\partial a_1^{ij}}{\partial \lambda_{ij}} = -2\pi \varepsilon_{ij} \sigma_{ij}^3 \lambda_{ij}^2 \rho_s g_{ij}^{HS}(\sigma_{ij}; \zeta_3^{eff}) - \alpha_{ij}^{VDW} \rho_s \frac{\partial g_{ij}^{HS}}{\partial \zeta_3^{eff}} \frac{\partial \zeta_3^{eff}}{\partial \lambda_{ij}}. \quad (2.131)$$

Substituting the expressions for the density and range derivatives (Eqs. 2.127 and 2.131) of the mean-attractive energy into Eq. (2.121) we obtain the radial distribution function within the SAFT-VR approach in terms of known parameters for the square-well potential, as

$$\begin{aligned} g_{ij}(\sigma_{ij}) &= g_{ij}^{HS}(\sigma_{ij}) \\ &+ \frac{\beta}{2\pi \sigma_{ij}^3} \left[3(-\alpha_{ij}^{VDW} g_{ij}^{HS}(\sigma_{ij}; \zeta_3^{eff}) - \alpha_{ij}^{VDW} \zeta_3 \frac{\partial g_{ij}^{HS}}{\partial \zeta_3^{eff}} \frac{\partial \zeta_3^{eff}}{\partial \zeta_3}) \right] \end{aligned} \quad (2.132)$$

$$- \frac{\lambda_{ij}}{\rho_s} \left(-2\pi \varepsilon_{ij} \sigma_{ij}^3 \lambda_{ij}^2 \rho_s g_{ij}^{HS}(\sigma_{ij}; \zeta_3^{eff}) - \alpha_{ij}^{VDW} \rho_s \frac{\partial g_{ij}^{HS}}{\partial \zeta_3^{eff}} \frac{\partial \zeta_3^{eff}}{\partial \lambda_{ij}} \right).$$

This simplifies to give a final expression for the radial distribution function for chains of molecules interacting via the square-well potential, which can be incorporated into the contributions to the SAFT-VR Helmholtz free energy due to chain formation and association of molecules,

$$g_{ij}(\sigma_{ij}) = g_{ij}^{HS}(\sigma_{ij}) \tag{2.133}$$

$$+ \beta \varepsilon_{ij} \left[g_{ij}^{HS}(\sigma_{ij}; \zeta_3^{eff}) + (\lambda_{ij}^3 - 1) \frac{\partial g_{ij}^{HS}}{\partial \zeta_3^{eff}} \left(\frac{\lambda_{ij}}{3} \frac{\partial \zeta_3^{eff}}{\partial \lambda_{ij}} - \zeta_3 \frac{\partial \zeta_3^{eff}}{\partial \zeta_3} \right) \right].$$

Bibliography

- [1] M. S. Wertheim, *J. Stat. Phys.*, **35**, 19 (1984).
- [2] M. S. Wertheim, *J. Stat. Phys.*, **35**, 35 (1984).
- [3] M. S. Wertheim, *J. Stat. Phys.*, **42**, 459 (1986).
- [4] M. S. Wertheim, *J. Stat. Phys.*, **42**, 477 (1986).
- [5] M. S. Wertheim, *J. Chem. Phys.*, **85**, 2929 (1986).
- [6] M. S. Wertheim, *J. Chem. Phys.*, **87**, 7323 (1987).
- [7] W. G. Chapman, K. E. Gubbins, G. Jackson, and M. Radosz, *Fluid Phase Equilib.*, **52**, 31 (1989)
- [8] W. G. Chapman, K. E. Gubbins, G. Jackson, and M. Radosz, *Ind. Eng. Chem. Res.*, **29**, 1709 (1990).
- [9] S. H. Huang and M. Radosz, *Ind. Eng. Chem. Res.*, **29**, 2284 (1990).
- [10] S. H. Huang and M. Radosz, *Ind. Eng. Chem. Res.*, **30**, 1994 (1991).
- [11] M. L. Yu and Y. P. Chen, *Fluid Phase Equilib.*, **94**, 149 (1994).
- [12] S. J. Suresh and E. J. Beckman, *Fluid Phase Equilib.*, **99**, 219 (1994).
- [13] S. H. Huang and M. Radosz, *Fluid Phase Equilib.*, **70**, 33 (1991).
- [14] C. J. Gregg and M. Radosz, *Fluid Phase Equilib.*, **86**, 211 (1993).
- [15] I. G. Economou, C. J. Gregg, and M. Radosz, *Ind. Eng. Chem. Res.*, **31**, 2620 (1992).
- [16] C. J. Gregg, F. P. Stein, S. J. Chen, and M. Radosz, *Ind. Eng. Chem. Res.*, **32**, 1442 (1993).
- [17] B. M. Hasch, E. J. Maurer, L. F. Ansanelli, and M. A. McHugh, *J. Chem. Thermodynamics*, **26**, 625 (1994).

- [18] S. W. Campbell, *Fluid Phase Equilib.*, **102**, 61 (1994).
- [19] H. S. Byun, B. M. Hasch, and M. A. McHugh, *Fluid Phase Equilib.*, **115**, 179 (1996).
- [20] S. -J. Chen, I. G. Economou, and M. Radosz, *Macromolecules*, **25**, 4987 (1992); C. J. Gregg, S. -J. Chen, F. P. Stein, and M. Radosz, *Fluid Phase Equilib.*, **83**, 375 (1993); C. J., Chen, I. G. Economou, and M. Radosz, *Fluid Phase Equilib.*, **83**, 391 (1993); C. K. Chen, M. A. Duran, and M. Radosz, *Ind. Eng. Chem. Res.*, **32**, 3123 (1993); S. J. Suresh, R. M. Enik, and E. J. Beckman, *Macromolecules*, **27**, 348 (1994); C. K. Chen, M. A. Duran, and M. Radosz, *Ind. Eng. Chem. Res.*, **33**, 306 (1994); S. J. Chen, Y. C. Chiew, J. A. Gardecki, S. Nilsen, and M. Radosz, *J. Polymer Science B.*, **32**, 1791 (1994); D. Pradhan, C. K. Chen, and M. Radosz, *Ind. Eng. Chem. Res.*, **33**, 1984 (1994); S. H. Lee, M. A. Lostracco, and M. A. McHugh, *Macromolecules*, **27**, 4652 (1994); C. J. Gregg, F. P. Stein, and M. Radosz, *Macromolecules*, **27**, 4972 (1994); *ibid.*, 4981; *J. Phys. Chem.*, **98**, 10634 (1994); C. S. Wu, and Y. P. Chen, *Fluid Phase Equilib.*, **100**, 103 (1994); B. M. Hasch and M. A. McHugh, *J. Polymer Science B.*, **33**, 715 (1995); Y. Xiong and E. Kiran, *J. Applied Polymer Science*, **55**, 1805 (1995); J. S. Chen, M. Banaszak, and M. Radosz, *Macromolecules*, **28**, 1812 (1995); B. M. Hasch, S. H. Lee, and M. A. McHugh, *J. Applied Polymer Science*, **59**, 1107 (1996); S. H. Lee, M. A. Lostracco, and M. A. McHugh, *Macromolecules*, **29**, 1349 (1996); H. S. Byun, B. M. Hasch, M. A. McHugh, F. O. Mahling, M. Busch, and M. Buback, *Macromolecules*, **29**, 1625 (1996).
- [21] G. Jackson and K. E. Gubbins, *Pure Appl. Chem.*, **61**, 1021 (1989).
- [22] A. L. Archer, M. D. Amos, G. Jackson, and I. A. McLure, *Int. J. Thermophys.*, **17**, 201 (1996).
- [23] A. Galindo, P. J. Whitehead, G. Jackson, and A. N. Burgess, *J. Phys. Chem.*, **100**, 6781 (1996).
- [24] A. Galindo, P. J. Whitehead, G. Jackson, and A. N. Burgess, *J. Phys. Chem. B*, **101**, 2082 (1997).
- [25] M. N. García-Lisbona, A. Galindo, G. Jackson, and A. N. Burgess, *Mol. Phys.*, in press (1997).
- [26] Y. H. Fu and S. I. Sandler, *Ind. Eng. Chem. Res.*, **34**, 1897 (1995).
- [27] W. G. Chapman, *J. Chem. Phys.*, **93**, 4299 (1990).
- [28] S. H. Huang and M. Radosz, *Ind. Eng. Chem. Res.*, **29**, 2284 (1990).
- [29] S. H. Huang and M. Radosz, *Ind. Eng. Chem. Res.*, **30**, 1994 (1991).

- [30] D. Ghonasgi and W. G. Chapman, *Mol. Phys.*, **80**, 161 (1993).
- [31] J. K. Johnson, E. A. Müller, and K. E. Gubbins, *J. Phys. Chem.*, **98**, 6413 (1994).
- [32] M. Banaszak, Y. C. Chiew, R. Olenick, and M. Radosz, *J. Chem. Phys.*, **100**, 3803 (1994).
- [33] M. Banaszak, Y. C. Chiew, and M. Radosz, *Phys. Rev. E*, **48**, 3760 (1993).
- [34] D. Ghonasgi and W. G. Chapman, *J. Chem. Phys.*, **100**, 6633 (1994).
- [35] F. W. Tavares, J. Chang, and S. I. Sandler, *Mol. Phys.*, **86**, 1451 (1995).
- [36] R. P. Sear and G. Jackson, *Mol. Phys.*, **82**, 1033 (1994).
- [37] D. Ghonasgi, V. Perez, and W. G. Chapman, *J. Chem. Phys.*, **101**, 6880 (1994).
- [38] D. Ghonasgi and W. G. Chapman, *J. Chem. Phys.*, **102**, 2585 (1995).
- [39] R. P. Sear and G. Jackson, *Phys. Rev. E*, **50**, 386 (1994).
- [40] R. P. Sear and G. Jackson, *Mol. Phys.*, **87**, 517 (1996).
- [41] R. P. Sear and G. Jackson, *J. Chem. Phys.*, **105**, 1113 (1996).
- [42] R. P. Sear and G. Jackson, *Mol. Phys.*, **82**, 473, (1994).
- [43] S. C. McGrother, R. P. Sear and G. Jackson, *J. Chem. Phys.*, **106**, 7315, (1997).
- [44] A. Gil-Villegas, A. Galindo, P. J. Whitehead, S. J. Mills, G. Jackson, and A. N. Burgess, *J. Chem. Phys.*, **106**, 4186 (1997).
- [45] A. Galindo, L. A. Davies, A. Gil-Villegas, and G. Jackson, *Mol. Phys.*, in press (1997).
- [46] J. A. Barker and D. Henderson, *J. Chem. Phys.*, **47**, 2856 (1967).
- [47] J. A. Barker and D. Henderson, *J. Chem. Phys.*, **47**, 4714 (1967).
- [48] P. J. Leonard, J. A. Barker and D. Henderson, *Trans. Faraday Soc.*, **66**, 2439 (1970).
- [49] J. A. Barker and D. Henderson, *Rev. Mod. Phys.*, **48**, 587 (1975).
- [50] C. M. McCabe, A. Galindo, A. Gil-Villegas, and G. Jackson, *Int. J. Thermophys.*, submitted (1997).
- [51] C. M. McCabe, A. Galindo, A. Gil-Villegas, and G. Jackson, in preparation (1997).

- [52] A. Galindo, A. Gil-Villegas, P. J. Whitehead, G. Jackson, and A. N. Burgess, *J. Phys. Chem.*, submitted (1997).
- [53] L. A. Davies, A. Gil-Villegas, G. Jackson, S. Calero, and S. Lago, *Phys. Rev. E*, submitted (1997).
- [54] L. A. Davies, A. Gil-Villegas, and G. Jackson, *Int. J. Thermophys.*, submitted (1997).
- [55] F. del R o, and L. Lira, *Mol. Phys.*, **61**, 275 (1987).
- [56] A. L. Benavides and F. del R o, *Mol. Phys.*, **68**, 983 (1989).
- [57] A. Gil-Villegas and F. del R o, *Rev. Mex. Fis.*, **39**, 526 (1993).
- [58] Y. P. Tang and B. C. Y. Lu, *J. Chem. Phys.*, **99**, 9828 (1993).
- [59] Y. P. Tang and B. C. Y. Lu, *J. Chem. Phys.*, **100**, 3079 (1994).
- [60] J. Chang and S. I. Sandler, *Mol. Phys.*, **81**, 745 (1994).
- [61] A. Gil-Villegas, F. del R o, and A. L. Benavides, *Fluid Phase Equilib.*, **119**, 97 (1996).
- [62] L. L. Lee, *Molecular Thermodynamics of Nonideal Fluids*, Butterworth Publishers, (1988).
- [63] T. Boubl k, *J. Chem. Phys.*, **53**, 471 (1970).
- [64] G. A. Mansoori, N. F. Carnahan, K. E. Starling, and T. W. Leland, *J. Chem. Phys.*, **54**, 1523 (1971).
- [65] T. M. Reed and K. E. Gubbins, *Applied Statistical Mechanics*, McGraw-Hill, (1973).
- [66] W. G. Chapman, G. Jackson, and K. E. Gubbins, *Mol. Phys.*, **65**, 1057 (1988).
- [67] J. S. Rowlinson and F. L. Swinton, *Liquids and Liquid Mixtures*, 3rd ed., Butterworth Scientific, (1982).
- [68] G. A. Mansoori and T. W. Leland, *J. Chem. Soc. Faraday Trans. II*, **8**, 320 1972.
- [69] N. F. Carnahan and K. E. Starling, *J. Chem. Phys.*, **51**, 635 (1969).
- [70] C. P. Hicks and C. L. Young, *Chem. Revs.*, **75**, 119 (1975).
- [71] M. Abramowitz and I. A. Stegun (Editors), *Handbook of Mathematical Functions*, Dover (1972).

Chapter 3

Molecular Simulation

3.1 Introduction

Molecular simulation techniques provide an alternative approach to the theoretical study of fluids. The results obtained can be used firstly to formulate a direct comparison with experimental data and secondly to complement other theoretical studies by providing means of testing the postulates used in these procedures. The main advantage of molecular simulation techniques over theory in the prediction of the thermodynamic and transport properties of fluids, is that no approximations other than the initial assumptions about the intermolecular interactions have to be made. This allows a highly accurate study of the thermodynamics of fluid systems to be performed. In order to be able to compare computer simulation results with those obtained experimentally, simulations of complex model interactions are required, which mimic the behaviour of real systems as accurately as possible. However, the use of simulation techniques to examine the nature of particular phenomena only requires that the essential physics of the system is contained within the model studied, thus eliminating the need for a complex model system. In this work we exploit this feature of computer simulation where the phase behaviour of simple model systems, obtained by simulation methods is used to determine the adequacy of a molecular based equation of state.

Computer simulation methods can be sub-divided into two general classes; Monte Carlo (MC) [1], where a random sampling technique is used as a basis to describe

the fluid's properties; and molecular dynamics (MD) [2, 3], where the fluid is analysed by solving Newton's equations of motion. Additionally, a number of recently developed simulation techniques exist which use a combination of both MC and MD methods, such as Brownian dynamics. We will be interested only in MC techniques, and more specifically in particular ensembles, the Gibbs ensemble and the semigrand canonical ensemble, which will be discussed in some detail in the following sections. As a direct consequence of the ability of computer simulation to yield 'exact' microscopic properties which can be used to give a macroscopic description of the fluid, the technique has become an integral part of the modern study of fluids and their mixtures, for theoreticians and industrialists alike. In the next sections we will introduce the statistical thermodynamics which forms the basis of Monte Carlo simulations, and also illustrate the underlying concepts of the technique.

3.2 Statistical thermodynamics

The basic assumption made in statistical mechanics is that the ensemble average of a mechanical property, such as the pressure P , the energy E , the volume V or the number of particles N , is equivalent to the value of that property at the macroscopic (or thermodynamic) level. A statistical ensemble is defined as the assembly of all possible microstates, or configurations, of a system. A particular microstate can be considered as an exact replica of the overall system at a thermodynamic level which differs from other microstates at a molecular level. Such microstates exist since a particular system can occupy several different energy levels whilst remaining in the same thermodynamic state. By calculating the ensemble average of a thermodynamic property we obtain an average over all the microstates of the system. Each of these configurations is assumed to occur with equal probability in an isolated system with fixed total energy and of a fixed size at thermodynamic equilibrium. Each microstate is thus assumed to have an equal weight within the distribution of configurations, so that the macroscopic system can evolve by sampling from any combination of the available microstates, i.e., the microstates are said to be ergodic. The probability that a macroscopic system lies in a state ν with N particles, a volume V , and energy E , is given by

$$P_\nu = \frac{1}{\Omega_{NVE}}, \quad (3.1)$$

where Ω_{NVE} is the number of microscopic states with N particles, a volume V and an energy of between E and $E - \Delta E$. ΔE represents the finite uncertainty which exists in the specification of the actual value of the energy for a given energy level;

it arises as a consequence of the Heisenberg uncertainty principle [4, 5]. For a finite value of ΔE , Ω_{NVE} is a finite function upon which standard mathematical analysis can be performed. The link to thermodynamics within this ensemble is made via the entropy S , which is related to Ω_{NVE} by the equation

$$S = k \ln \Omega_{NVE}, \quad (3.2)$$

where k is Boltzmann's constant. The conditions of fixed number of particles, system volume and energy define a system in the microcanonical ensemble, which can be considered as a closed isolated system. Other ensembles exist which are defined by the fixed thermodynamic conditions particular to that ensemble.

The canonical ensemble is an important example of an alternative ensemble, where the individual microstates have fixed number of particles and volume, but their energy is permitted to fluctuate, and the system is kept at a fixed temperature T in order to maintain thermal equilibrium. The canonical ensemble can hence be visualised in the same manner as the microcanonical ensemble, as a closed system which is in contact with a heat bath of temperature T . Within the canonical ensemble the probability that the macroscopic system is in a state ν with fixed N , V and T can be shown to be given by [6]

$$P_\nu = \frac{1}{Q_{NVT}} \exp(-E_\nu/kT), \quad (3.3)$$

where the Boltzmann factor is introduced from the definition of entropy S in the microcanonical ensemble Eq. (3.2). Q_{NVT} is the canonical partition function which is defined as a discrete sum over all the possible microstates ν of a system

$$Q_{NVT} = \sum_\nu \exp(-E_\nu/kT). \quad (3.4)$$

The partition function is the key quantity used for obtaining macroscopic properties from microscopic averages, since it appears in the expression for the configurational (or ensemble) average of a thermodynamic function. For a given function \mathcal{A} the configurational average is given by

$$\begin{aligned} \langle \mathcal{A} \rangle_{NVT} &= \langle \mathcal{A}_\nu \rangle = \sum_\nu P_\nu \mathcal{A}_\nu \\ &= \frac{\sum_\nu \mathcal{A}_\nu \exp(-E_\nu/kT)}{Q_{NVT}} \\ &= \frac{\sum_\nu \mathcal{A}_\nu \exp(-E_\nu/kT)}{\sum_\nu \exp(-E_\nu/kT)}. \end{aligned} \quad (3.5)$$

Within the canonical ensemble the Helmholtz free energy is related to the partition

function by

$$A = -kT \ln Q_{NVT}, \quad (3.6)$$

where A is the thermodynamic potential with independent variables equal to those of the canonical ensemble, which is equivalent to the role of entropy in the microcanonical ensemble. The other thermodynamic properties of a system in the canonical ensemble are given by standard relations, for example, the pressure as

$$P = - \left(\frac{\partial A}{\partial V} \right)_{T,N} = kT \left(\frac{\partial \ln Q_{NVT}}{\partial V} \right)_{T,N}, \quad (3.7)$$

the average energy as

$$E = -T^2 \left(\frac{\partial A/T}{\partial T} \right)_{V,N} = kT^2 \left(\frac{\partial \ln Q_{NVT}}{\partial T} \right)_{V,N}, \quad (3.8)$$

and the chemical potential of species i as

$$\mu_i = \left(\frac{\partial A}{\partial N_i} \right)_{T,V,N_j \neq i} = -kT \left(\frac{\partial \ln Q_{NVT}}{\partial N_i} \right)_{T,V,N_j \neq i}. \quad (3.9)$$

The partition function in other common ensembles, such as the isothermal-isobaric ensemble (constant NPT) and the grand canonical ensemble (constant μVT) can be written in terms of the partition function for the canonical ensemble. For example, in the NPT ensemble the partition function is given by

$$\begin{aligned} Q_{NPT} &= \sum_{\nu} \int_{V=0}^{\infty} \exp(-[E_{\nu} + PV]/kT) \\ &= \sum_{V} \exp(-PV/kT) Q_{NVT}, \end{aligned} \quad (3.10)$$

and in the μVT ensemble by,

$$\begin{aligned} Q_{\mu VT} &= \sum_{\nu} \sum_N \exp(-[E_{\nu} - \mu N]/kT) \\ &= \sum_N \exp(\mu N/kT) Q_{NVT}. \end{aligned} \quad (3.11)$$

In the thermodynamic limit, when $N \rightarrow \infty$, away from the critical region, the averages obtained using the common statistical ensembles are equivalent [7, 8].

The aim of Monte Carlo simulation is to provide a means of obtaining configurational averages of thermodynamic properties by performing virtual experiments in which a series of microstates are generated, over which averages are taken. Thus the concept of an ensemble average is approximated by performing a large number of computer generated states, or trials τ . It is possible to write the configurational

average of Eq. (3.5) as

$$\langle \mathcal{A} \rangle_{NVT} \approx \frac{\sum_{\tau=1}^{\tau_{max}} \mathcal{A}(\tau) \exp(-E(\tau)/kT)}{\sum_{\tau=1}^{\tau_{max}} \exp(-E(\tau)/kT)}, \quad (3.12)$$

where τ_{max} is the total number of trials performed. The number of trials τ can be increased until a suitably accurate value of \mathcal{A} is obtained by means of a simple mean sample method, which involves sampling from all the permitted values of \mathcal{A} . However, a large proportion of the trials performed in such a process would only give a negligible contribution to the ensemble average in Eq. (3.12), so that in order for even a crude estimate of the property \mathcal{A} to be obtained, the number of trials required is prohibitively large.

The Metropolis method permits configurational averages to be obtained in a much more efficient manner, via the use of importance sampling techniques. Here random numbers are selected from a given distribution (or density) of states ρ which allows the average to be calculated only in regions where it gives a significant contribution to the numerator of Eq. (3.5).

Sampling configurations from a random distribution, leads to an expression for the configurational average of the form

$$\langle \mathcal{A} \rangle_{NVT} = \langle \mathcal{A} \rho_{NVT} / \rho \rangle_{trials}, \quad (3.13)$$

where ρ_{NVT} is the density of states in the canonical ensemble which is given by

$$\rho_{NVT} = \frac{1}{Q_{NVT}} \exp(-E_{\nu}/kT) \quad (3.14)$$

which differs from Eq. (3.3) in that here we are considering a continuous distribution of states, and the partition function is now written as an integral over all states. For most thermodynamic functions (the free energy being the most notable exception), the contribution to the ensemble average will be significant when the distribution of states in the NVT ensemble ρ_{NVT} is significant. Hence an estimate of the average of \mathcal{A} can be obtained by setting $\rho = \rho_{NVT}$, so that

$$\langle \mathcal{A} \rangle_{NVT} = \langle \mathcal{A} \rangle_{trials}. \quad (3.15)$$

The generation of such a sequence of states during a simulation, where all states occur with equal probability, which also has to be equal to the probability of microstates in the canonical ensemble, is the basis of the Monte Carlo method. The Metropolis algorithm provides a solution to this problem by the construction of a Markov chain for the fluid which has a limiting distribution equal to ρ_{NVT} .

A Markov chain is a sequence of trials where the outcome of each trial belongs to a finite set of possible outcomes, and depends only on the result of the previous trial. Two states m and n in the chain are linked by a transition probability \mathcal{P}_{mn} , which is the probability that the system moves from state m to state n . The limiting distribution of a Markov chain, the vector ρ , must satisfy the condition

$$\rho \mathcal{P} = \rho \quad (3.16)$$

where the transition matrix \mathcal{P} is made up of the elements \mathcal{P}_{mn} such that

$$\sum_m \rho_m \mathcal{P}_{mn} = \rho_n, \quad (3.17)$$

and is stochastic, since all its rows add to one

$$\sum_n \mathcal{P}_{mn} = 1. \quad (3.18)$$

For fluids in the NVT Metropolis scheme the transition matrix must be both stochastic and ergodic, that is each of the individual states is equally likely to be ‘visited’ by the overall system during the simulation. The elements of the matrix must be generated from a knowledge of the limiting distribution of a Markov chain which has elements $\rho_m = \rho_{NVT}(\Gamma_m)$, for each Γ_m point in phase space. A further constraint on the transition matrix of a fluid is that its elements should be independent of the corresponding partition function, in this case the canonical partition function Q_{NVT} . Application of the condition of microscopic reversibility

$$\rho_m \mathcal{P}_{mn} = \rho_n \mathcal{P}_{nm}, \quad (3.19)$$

so that the probability of moving from m to n is equal to the probability of moving in the reverse direction, i.e. from n to m , is sufficient to ensure that the transition matrix for the generation of liquid configurations obeys all the required criteria. Hence, providing that the different configurations in a given simulation ensemble are microscopically reversible they can be considered as being elements of a Markov chain of configurations, equivalent to those used in the original Metropolis Monte Carlo formalism [1]. An additional advantage of the use of the Markov chain in the simulation is that configurations can be generated without having to evaluate the normalisation factor of the distribution of microstates, i.e. the canonical ensemble partition function.

The transition between neighbouring states m and n in the MC method is governed by the difference in energy ΔU_{mn} of the two states, ΔU_{mn} . If the new configuration has a lower (or equal) energy to that of the initial configuration, the transition is accepted, if the energy of the new configuration is greater than that of the old

state, the transition is not necessarily rejected. Such moves are accepted with a probability proportional to

$$\exp(-\Delta U_{mn}/kT). \quad (3.20)$$

This selective acceptance of Monte Carlo moves which are ‘uphill’ in energy prevents the simulation from becoming trapped in local energy minima on the phase space, hence ensuring that the thermodynamic properties obtained from the simulation take the correct value for the system studied. In order to accept a Monte Carlo move with a probability given by Eq. (3.20) the ratio of probabilities of neighbouring states is compared with a random number between zero and unity. If the ratio in Eq. (3.20) is greater than the random number the move from m to n is accepted (see [8] for full details).

The scope of the Monte Carlo technique has expanded dramatically since its introduction in 1953, becoming “the most powerful and commonly used technique for analysing complex problems” [9]. The first Monte Carlo studies resulted in the mechanical and structural properties of simple hard-sphere fluids. However, the nature of the model systems to which the MC method can be applied has rapidly progressed via the use of different inter-molecular interactions; for example the Lennard-Jones potential was first used in a MC simulation in 1957 [10]. Further sophistication of the models used has led to the study of realistic systems using the Monte Carlo method, a particularly relevant example being that of water, which has been extensively studied using the TIP4P model [11, 12], the TIPS2 model [13, 14] and the SPC model [15, 16]. Other systems which have been studied using MC techniques range from n -alkanes [17]-[19], methanol [20], complex fluids such as surfactants [21], [22] to the examination of the swelling of clay systems with the addition of aqueous solutions [23].

The nature of the information which can be obtained from MC simulation studies has also advanced from the early work of Metropolis *et al.* New techniques such as the grand canonical ensemble [24] and the Widom test particle method [25, 26] have been developed which permit the evaluation of properties such as the free energy and entropy. These quantities are difficult to obtain from standard MC methods since the Metropolis algorithm is designed so that it samples configurations with small or negative energies, which have a small effect on the configurational average in Eq. (3.12). Such techniques, together with the development of realistic models for fluids, allow the evaluation of the full phase behaviour of a complex model system using computer simulation.

We focus on the use of Monte Carlo methods in the study of phase coexistence of simple model fluids, which can be achieved by using either direct or indirect simu-

lation techniques. Direct simulations yield phase equilibria data by simultaneously examining the two coexisting phases. Indirect MC methods involve the calculation of the chemical potential or free energy within a simulation for a series of state points; the region of phase coexistence is determined by the location of points in the phase space with equal temperature, pressure and chemical potential. A range of special techniques have been developed in order to obtain thermal properties, such as the free energy and entropy, some of which will be briefly discussed here (see Refs. [8] and [27] for a review).

Use of the grand canonical ensemble [24], in which chemical potential, volume and temperature are fixed during the simulation, is a direct simulation method which has been widely used. Density is allowed to fluctuate over the course of the simulation, and the average density is calculated as an ensemble average. Within the grand canonical ensemble two Monte Carlo moves are performed in order to generate states, particle displacements and particle insertions/deletions (see Ref. [8]). The disadvantage of such an approach is that it relies upon successful insertions in order to obtain an adequate sampling of the density fluctuations, which become less likely as the density of the system increases. A related ensemble which does not rely upon particle insertions is the semigrand canonical ensemble which is discussed later.

An alternative route to the determination of chemical potential in standard simulation ensembles is the use of the test particle method [25, 26], which consists of the introduction of a virtual or test particle into the simulation. This molecule measures the intermolecular interactions at that point, but it does not influence the other molecules in the system in any way. This method and variations of it have been used extensively to obtain chemical potentials in both MC and MD simulations (see Ref. [28] for a review). The approach as adapted for the Gibbs ensemble (see later) is given in the appendix. Application of the test particle method in the NPT ensemble is particularly useful, since the density is permitted to fluctuate, which is useful in studies close to the critical region, as will be shown in Chapter 6.

A range of modified sampling techniques which facilitate the insertion of particles have been developed (see Ref. [28] and references therein), an example of which is the so-called ‘umbrella’ sampling method [29, 30, 8] which samples configurations which are important in the determination of the chemical potential. Another such technique is density scaling Monte Carlo [29, 30], where simulations are performed on a non-Boltzmann distribution in order to evaluate the Helmholtz free energy between two states of different density along an isotherm. The position variables are scaled by density so that the generated configurations are also density depen-

dent; the simulation results in the free energy difference between any two given densities. It is also important to note that it is possible to exploit the standard thermodynamic identities between the free energy or the chemical potential and the internal energy or pressure of a system in order to obtain values for such quantities. Such a route is termed thermodynamic integration, and has seen a wide range of applications (see Ref. [28]). One of the most applicable of such approaches is the Gibbs-Duhem integration method proposed by Kofke [31]-[33]. The method consists of the numerical integration of the Clausius-Clapeyron equation, and its main advantage lies in the fact that it is not limited to systems with coexistence curves in the pressure-temperature plane. For example, it can be used to locate phase transitions as a function of the interaction potential of a system (see Ref. [34] for a recent review).

A more intuitive route to the simulation of phase behaviour is the use of direct techniques, where the coexistence between two phases is simulated 'directly'. Interfacial techniques, where two phases are simulated within a single subsystem separated by an interface, are an example of such methods. These studies lead to the description of the interfacial properties of the two fluids but can also yield bulk system properties. The common problems of direct MC simulation methods include long equilibration times and that the stability of the two phase region is very sensitive to the density difference of the two fluids. Additionally, confining the two fluids between parallel walls leads to the simulation of a confined fluid rather than that of coexisting phases. These limitations and the possible means by which their effect can be minimised are discussed in Refs. [35, 27] and [28]. Accurate evaluation of phase coexistence by MC simulation thus appears only to be possible by means of indirect techniques coupled with a bias sampling scheme, or by using a direct method with long simulation runs, taking care with the method used to confine the fluid. An alternative direct simulation technique is the Gibbs ensemble Monte Carlo (GEMC) method, where the phase equilibria of model systems can be readily obtained without any of the problems associated with the two-phase interface. Within the Gibbs ensemble the coexisting phases are simulated in two separate subsystems which are in thermodynamic equilibrium but not in physical contact.

3.3 Gibbs ensemble Monte Carlo simulations of mixtures

Since its introduction 10 years ago by Panagiotopoulos [36], the GEMC simulation technique has become one of the most widely used simulation methods for the determination of phase equilibria. The technique and its advantages and limitations, together with its applications has been extensively reviewed in Refs. [27, 37]-[39]. As a simulation method it is particularly well suited to the study of coexisting phases since it consists of two separate subsystems, or boxes, each of which can be assigned to one of the individual phases. These two boxes are examined simultaneously and are not in physical contact, but can be imagined to be embedded within the bulk of each phase. Hence the thermodynamic properties which are evolved have no interfacial contributions associated with them. However, these two subsystems, are not completely isolated from one another, at least in the thermodynamic sense, since they are maintained in such a way that they are in equilibrium with one another. This requires that equality of pressure, temperature and chemical potential exists between the two boxes, and hence between the two phases. This equilibrium is sustained via three kinds of Monte Carlo move, particle displacement to maintain thermal equilibrium, volume changes, to maintain mechanical equilibrium, and interchange between the two boxes, to maintain chemical equilibrium. The GEMC technique was first proposed for the study of pure fluids at a constant number of particles, volume and temperature, that is constant NVT overall, so that a coupled volume change of $+\Delta V$ in one box and $-\Delta V$ in the other maintains the overall volume. This form of the Gibbs ensemble has seen many applications, a few examples being the simulation of the Lennard-Jones fluid both for monomers [36, 40] and higher chain molecules [41, 42], the square-well fluid [43]-[45], the Stockmayer fluid [46], the Yukawa fluid [47, 48], the Gay-Berne fluid [49], and of the Buckingham exp-6 fluid [50].

The Gibbs ensemble technique can also be applied to studies of coexisting mixtures [51], and it is this aspect of the method which is of interest here. In this case the method can be implemented at constant NPT overall, since by increasing the number of components of the system the number of variables which can be specified in the simulation also increases. Hence, for a two component system, the temperature and pressure of the two coexisting phases can be specified, whilst for the case of the pure component, only the temperature can be specified. Use of the constant NPT Gibbs ensemble also results in smaller uncertainties in the coexisting densities (or compositions) than for the constant NVT case. As one would expect, many different mixtures have been examined using the Gibbs ensemble technique, some examples are Lennard-Jones mixtures [51, 52], square-well

mixtures [53, 54], Stockmayer mixtures [55], alkane mixtures [12, 56, 57], associating mixtures [58], water/methanol/salt mixtures [59], polydisperse fluids [60], and surfactant solutions [61].

The GEMC technique has recently been extended to simulate multiphase equilibria [62], where the original GEMC two box partition function is written in terms of two canonical ensemble partition functions. For simulation of an n -phase system, n canonical partition functions are used in the overall Gibbs ensemble partition function. Results are presented in Ref. [62] for mixtures of Lennard-Jones atoms, including binary mixtures exhibiting two and three phase coexistence, and ternary mixtures exhibiting three and four phase coexistence. The ability to perform direct simulations of multiphase, multicomponent mixtures using the Gibbs ensemble is likely to become one of the fundamental advantages of the technique over other simulation methods in the near future.

In this work we are interested only in the application of the Gibbs ensemble simulation method as a means of obtaining the phase coexistence of simple model systems. The GEMC simulation results for a binary mixture of square-well monomers and dimers are presented in Chapter 4 and the simulation of a symmetrical square-well associating mixture is discussed in Chapter 6. We present the general expressions of the GEMC partition function for a binary mixture at constant NPT , together with the other related functions which are used in the estimation of the thermodynamic properties of the fluid. The means by which the chemical potential can be obtained within a Gibbs ensemble is detailed in the appendix. We also discuss three possible algorithms for the particle transfer step in terms of their significance in the expression for the acceptance criterion of the move.

Within the Gibbs ensemble a binary mixture of $N = N_1 + N_2$ particles, N_1 of type 1 and N_2 of type 2, at a constant temperature T and a constant pressure P is divided into two subsystems, labelled a and b , with volumes V^a and V^b , and numbers of particles $N^a = N_1^a + N_2^a$ and $N^b = N_1^b + N_2^b$, respectively, where N_i^j is the number of particles of type i in subsystem j . The partition function for such a mixture is

$$\begin{aligned}
 Q_{NPT}^{\text{Gibbs}} &= \frac{1}{N_1! \Lambda_1^{3N_1} V_0} \frac{1}{N_2! \Lambda_2^{3N_2} V_0} \sum_{N_1^a=0}^{N_1} \frac{N_1!}{N_1^a! N_1^b!} \sum_{N_2^a=0}^{N_2} \frac{N_2!}{N_2^a! N_2^b!} \\
 &\times \int_0^\infty dV^a \exp\left(-\frac{PV^a}{kT}\right) \int_0^\infty dV^b \exp\left(-\frac{PV^b}{kT}\right) \\
 &\times \int d(\mathbf{r}_1^a)^{N_1^a} \int d(\mathbf{r}_2^a)^{N_2^a} \exp\left(-\frac{U^a(N^a)}{kT}\right)
 \end{aligned}$$

$$\times \int d(\mathbf{r}_1^b)^{N_1^b} \int d(\mathbf{r}_2^b)^{N_2^b} \exp\left(-\frac{U^b(N^b)}{kT}\right), \quad (3.21)$$

where Λ_i is the thermal de Broglie wavelength of particle i , V_0 is a basic unit of volume chosen to render the partition function dimensionless [63], $(\mathbf{r}_i^j)^{N_j}$ represents the positions of particles of type i in subsystem j , and $U^j(N^j)$ is the energy of subsystem j . Note that in the case of non-spherical particles the orientations of particles also have to be specified. After introducing the re-scaled co-ordinates $\xi_i^j = \mathbf{r}_i^j/L^j$, where L^j is the box length of the simulated subsystem j , the partition function can be written as

$$\begin{aligned} Q_{NPT}^{\text{Gibbs}} &= \frac{1}{N_1! \Lambda_1^{3N_1} V_0} \frac{1}{N_2! \Lambda_2^{3N_2} V_0} \sum_{N_1^a=0}^{N_1} \frac{N_1!}{N_1^a! N_1^b!} \sum_{N_2^a=0}^{N_2} \frac{N_2!}{N_2^a! N_2^b!} \\ &\times \int_0^\infty dV^a \exp\left(-\frac{PV^a}{kT}\right) (V^a)^{N^a} \int_0^\infty dV^b \exp\left(-\frac{PV^b}{kT}\right) (V^b)^{N^b} \\ &\times \int d(\xi_1^a)^{N_1^a} \int d(\xi_2^a)^{N_2^a} \exp\left(-\frac{U^a(N^a)}{kT}\right) \\ &\times \int d(\xi_1^b)^{N_1^b} \int d(\xi_2^b)^{N_2^b} \exp\left(-\frac{U^b(N^b)}{kT}\right). \end{aligned} \quad (3.22)$$

Hence, the configurational average of a function \mathcal{A} in the NPT version of the Gibbs ensemble is given by (cf. Eq. (3.5)),

$$\begin{aligned} \langle \mathcal{A} \rangle_{NPT}^{\text{Gibbs}} &= \frac{1}{Q_{NPT}^{\text{Gibbs}}} \frac{1}{N_1! \Lambda_1^{3N_1} V_0} \frac{1}{N_2! \Lambda_2^{3N_2} V_0} \sum_{N_1^a=0}^{N_1} \frac{N_1!}{N_1^a! N_1^b!} \sum_{N_2^a=0}^{N_2} \frac{N_2!}{N_2^a! N_2^b!} \\ &\times \int_0^\infty dV^a \exp\left(-\frac{PV^a}{kT}\right) (V^a)^{N^a} \int_0^\infty dV^b \exp\left(-\frac{PV^b}{kT}\right) (V^b)^{N^b} \\ &\times \int d(\xi_1^a)^{N_1^a} \int d(\xi_2^a)^{N_2^a} \exp\left(-\frac{U^a(N^a)}{kT}\right) \\ &\times \int d(\xi_1^b)^{N_1^b} \int d(\xi_2^b)^{N_2^b} \exp\left(-\frac{U^b(N^b)}{kT}\right) \mathcal{A}. \end{aligned} \quad (3.23)$$

An inspection of Eq. (3.23) indicates that it represents an ensemble average with a probability distribution proportional to a pseudo-Boltzmann factor

$$\begin{aligned} \mathcal{P}^{\text{Gibbs}} &= \exp\left[\ln\left(\frac{N_1!}{N_1^a! N_1^b!}\right) + \ln\left(\frac{N_2!}{N_2^a! N_2^b!}\right) + N^a \ln V^a + N^b \ln V^b\right. \\ &\left. - \frac{PV^a}{kT} - \frac{PV^b}{kT} - \frac{U^a(N^a)}{kT} - \frac{U^b(N^b)}{kT}\right]. \end{aligned} \quad (3.24)$$

The acceptance criterion for each of the individual MC steps performed in the Gibbs ensemble can be derived from Eq. (3.24).

For a particle displacement in subsystem j , new configurations are accepted with a probability proportional to

$$\mathcal{P}^d{}^j = \exp\left(-\frac{\Delta U^j}{kT}\right), \quad (3.25)$$

which is equivalent to the original canonical NVT Metropolis scheme of Eq. (3.20) [1].

A volume change at constant pressure generates new configurations which are accepted with a probability proportional to

$$\begin{aligned} \mathcal{P}^v = & \exp\left[N^a \ln\left(\frac{V^a + \Delta V^a}{V^a}\right) + N^b \ln\left(\frac{V^b + \Delta V^b}{V^b}\right)\right. \\ & \left. - \frac{P\Delta V^a}{kT} - \frac{P\Delta V^b}{kT} - \frac{\Delta U^a}{kT} - \frac{\Delta U^b}{kT}\right]. \end{aligned} \quad (3.26)$$

This is identical to the original isothermal-isobaric, NPT , Monte Carlo prescription, proposed by Wood [64], written for a volume change in two identical subsystems. Overall convergence in the NPT Gibbs ensemble is found to be faster if the volume of only one subsystem is changed per simulation cycle (defined later) [51]. Selection of which subsystem is to undergo a volume change is carried out at random, so that the acceptance criterion given in Eq. (3.26), only depends on the terms which involve the chosen subsystem, for example, for a volume change of ΔV^a in a , the pseudo-Boltzmann factor is given by

$$\mathcal{P}^v = \exp\left[N^a \ln\left(\frac{V^a + \Delta V^a}{V^a}\right) - \frac{P\Delta V^a}{kT} - \frac{\Delta U^a}{kT}\right]. \quad (3.27)$$

Interchange of particles between the two subsystems has an acceptance probability, for transfer of a particle of type i from subsystem a to subsystem b , proportional to

$$\mathcal{P}^t{}_i = \exp\left[\ln\left(\frac{N_i^a V^b}{(N_i^b + 1)V^a}\right) - \frac{\Delta U^a}{kT} - \frac{\Delta U^b}{kT}\right]. \quad (3.28)$$

In the thermodynamic limit, each subsystem thus corresponds to the generalised μVT canonical ensemble [65]. It is important to note that the method employed to select the transferred particle affects the expressions involved in the above acceptance criterion. We now illustrate, for three transfer step algorithms, why this is the case, and also explain why the three algorithms are equivalent by means of their microscopic reversibility.

The condition of microscopic reversibility is an essential feature of all Monte Carlo simulation methods, it requires that the probability of transforming a configu-

ration m into a configuration n must be equal to the probability of performing the reverse step. The roots of such a requirement lie in the fundamentals of the Metropolis Monte Carlo technique [1] as shown earlier. The Gibbs ensemble (and all the other MC ensembles) use the Metropolis algorithm, which requires that the Gibbs ensemble transition matrix must satisfy the same conditions as those for the Metropolis case. The microscopic reversibility of the individual steps in the Gibbs ensemble, for the case of the particle displacement and volume change steps, is easily recognised [8], since they correspond to the usual canonical and isothermal-isobaric ensembles, and hence are known to be microscopically reversible. However, in the case of the particle transfer step, the reversibility of the process is not so apparent. Here, we outline the route involved in establishing the reversibility of the transfer step, by using three different particle transfer algorithms. We borrow heavily from the language of Rull *et al.* in Ref. [66] where the condition of microscopic reversibility in the Gibbs ensemble was first discussed in any detail.

We examine the same binary mixture as earlier, consisting of $N^a = N_1^a + N_2^a$ and $N^b = N_1^b + N_2^b$ particles, where N_i^j is the number of particles of type i in subsystem j . The probability of moving from an overall state m to an overall state n by transferring a particle of type 1 from subsystem a to subsystem b is proportional to

$$\begin{aligned} \mathcal{P}_{mn} = & N_1^a!N_1^b!N_2^a!N_2^b! \times \mathcal{P}^{\text{subsystem } a} \times \mathcal{P}^{\text{type } 1} \times \mathcal{P}_m^{\text{particle } 1, a} \\ & \times \mathcal{P}^{\text{position } b} \times \mathcal{P}_m^{\text{Gibbs}} \times \mathcal{P}_{mn}^{\text{criterion}}, \end{aligned} \quad (3.29)$$

where each of the terms in the above equation will be considered in turn. The factor $N_1^a!N_1^b!N_2^a!N_2^b!$ corresponds to the number of permutations of the labels used to describe the configuration m . $\mathcal{P}^{\text{subsystem } a}$ is the probability of choosing subsystem a as the donor subsystem for the transfer, $\mathcal{P}^{\text{type } 1}$ is the probability of choosing a given particle of type 1 to be transferred, and $\mathcal{P}_m^{\text{particle } 1, a}$ is the probability of choosing a particle of type 1 in subsystem a . $\mathcal{P}^{\text{position } b}$ is the probability of selecting a particular position for insertion in subsystem b , $\mathcal{P}_m^{\text{Gibbs}}$ is the probability that the overall system is in the configuration n given in Eq. (3.24), and $\mathcal{P}_{mn}^{\text{criterion}}$ is the acceptance criterion for the particle transfer step in the Gibbs ensemble, given in Eq. (3.28). The probabilities of choosing either a particle of type 1 or of type 2 to be transferred are equal, $\mathcal{P}^{\text{type } 1} = \mathcal{P}^{\text{type } 2} = 1/2$, similarly, the probability of choosing subsystem a or b as the donor subsystem are equal, so that $\mathcal{P}^{\text{subsystem } a} = \mathcal{P}^{\text{subsystem } b} = 1/2$. The probabilities for selecting a particular position for insertion in subsystem a and b are also equal, $\mathcal{P}^{\text{position } a} = \mathcal{P}^{\text{position } b}$, so that these three terms will not appear in the overall acceptance criteria, which is a ratio of the probability of transfers from state m to n and from n to m . The probability of choosing a given particle of type 1 in subsystem a , $\mathcal{P}_m^{\text{particle } 1, a}$ depends on the algorithm used in the particle transfer step.

In order that a particular transfer algorithm yields microscopically reversible configurations, and hence be considered as a true Metropolis algorithm, the probabilities of the forward and reverse transfers must be equal, that is

$$\mathcal{P}_{mn} = \mathcal{P}_{nm}. \quad (3.30)$$

The first transfer step algorithm (1) proposed in the original prescription of the Gibbs ensemble technique for mixtures [51], follows the methodology:

- random selection of the recipient subsystem
- random selection of particle type i
- random selection of a particle of that type in the donor subsystem
- transfer of the selected particle to a random position in the recipient subsystem

The probability that a particle of type 1 is transferred from a to b is given by Eq. (3.29), where the probability of choosing a particle of type 1 in subsystem a in configuration m is

$$\mathcal{P}_m^{\text{particle } 1, a} = \frac{1}{N_1^a}, \quad (3.31)$$

and $\mathcal{P}_m^{\text{Gibbs}}$ is given by Eq. (3.24). The probability of the reverse step, the transfer of a particle of type 1 from subsystem b to subsystem a is proportional to

$$\begin{aligned} \mathcal{P}_{nm} &= (N_1^a - 1)!(N_1^b + 1)!N_2^a!N_2^b! \times \mathcal{P}^{\text{subsystem } b} \times \mathcal{P}^{\text{type } 1} \times \mathcal{P}_n^{\text{particle } 1, b} \\ &\times \mathcal{P}^{\text{position } a} \times \mathcal{P}_n^{\text{Gibbs}} \times \mathcal{P}_{nm}^{\text{criterion}}. \end{aligned} \quad (3.32)$$

For the configuration n , the factor $(N_1^a - 1)!(N_1^b + 1)!N_2^a!N_2^b!$ corresponds to the number of permutations of the labels, $\mathcal{P}_n^{\text{particle } 1, b}$ is the probability of choosing a particle of type 1 in subsystem b , given by

$$\mathcal{P}_n^{\text{particle } 1, b} = \frac{1}{N_1^b + 1}. \quad (3.33)$$

The probability that the overall system is in configuration n is, cf. Eq. (3.24),

$$\begin{aligned} \mathcal{P}_n^{\text{Gibbs}} &= \exp \left[\ln \left(\frac{N_1!}{(N_1^a - 1)!(N_1^b + 1)!} \right) + \ln \left(\frac{N_2!}{N_2^a!N_2^b!} \right) \right. \\ &+ (N^a - 1) \ln V^a + (N^b + 1) \ln V^b \\ &\left. - \frac{PV^a}{kT} - \frac{PV^b}{kT} - \frac{U^a(N^a - 1)}{kT} - \frac{U^b(N^b + 1)}{kT} \right]. \end{aligned} \quad (3.34)$$

Equating the forward and reverse probabilities for this transfer step algorithm, Eqs. (3.29) and (3.32), gives

$$\begin{aligned}
\mathcal{P}_1^t &= \frac{\mathcal{P}_{mn}^{\text{criterion}}}{\mathcal{P}_{nm}^{\text{criterion}}} \\
&= \frac{(N_1^a - 1)!(N_1^b + 1)!N_2^a!N_2^b!}{N_1^a!N_1^b!N_2^a!N_2^b!} \times \frac{\mathcal{P}^{\text{subsystem } b}}{\mathcal{P}^{\text{subsystem } a}} \times \frac{\mathcal{P}^{\text{type } 1}}{\mathcal{P}^{\text{type } 1}} \times \frac{\mathcal{P}_n^{\text{particle } 1, b}}{\mathcal{P}_m^{\text{particle } 1, a}} \\
&\times \frac{\mathcal{P}^{\text{position } a}}{\mathcal{P}^{\text{position } b}} \times \frac{\mathcal{P}_m^{\text{Gibbs}}}{\mathcal{P}_n^{\text{Gibbs}}} \\
&= \exp \left[\ln \left(\frac{N_1^a V^b}{(N_1^b + 1) V^a} \right) - \frac{\Delta U^a}{kT} - \frac{\Delta U^b}{kT} \right]. \tag{3.35}
\end{aligned}$$

This is identical to the general particle transfer step acceptance criterion given by Eq. (3.28). An identical expression can be obtained for component 2 in terms of N_2^a and N_2^b .

The second transfer step algorithm (2) [53] is less specific in its method of particle selection, it proceeds by:

- random selection of the recipient subsystem
- random selection of a particle in the donor subsystem, regardless of type
- transfer of the selected particle to a random position in the recipient subsystem.

Here, the particle to be transferred is selected from the total N^i particles in the selected subsystem i , so that $\mathcal{P}^{\text{type } 1}$ is not included in the transfer step probability. The species subscripts are dropped from the expressions for the probabilities of selecting a particle of a given type in a specific subsystem, $\mathcal{P}_n^{\text{particle}, a}$ and $\mathcal{P}_m^{\text{particle}, b}$, so that they become $1/N^a$ and $1/(N^b + 1)$, respectively. The reversible transfer criterion for this algorithm can hence be written

$$\begin{aligned}
\mathcal{P}_2^t &= \frac{\mathcal{P}_{mn}^{\text{criterion}}}{\mathcal{P}_{nm}^{\text{criterion}}} \\
&= \frac{(N_1^a - 1)!(N_1^b + 1)!N_2^a!N_2^b!}{N_1^a!N_1^b!N_2^a!N_2^b!} \times \frac{\mathcal{P}^{\text{subsystem } b}}{\mathcal{P}^{\text{subsystem } a}} \times \frac{\mathcal{P}_n^{\text{particle}, b}}{\mathcal{P}_m^{\text{particle}, a}} \times \frac{\mathcal{P}^{\text{position } a}}{\mathcal{P}^{\text{position } b}} \times \frac{\mathcal{P}_n^{\text{Gibbs}}}{\mathcal{P}_m^{\text{Gibbs}}} \\
&= \left(\frac{N_1^b + 1}{N_1^a} \right) \left(\frac{N^a}{N^b + 1} \right) \exp \left[\ln \left(\frac{N_1^a V^b}{(N_1^b + 1) V^a} \right) - \frac{\Delta U^a}{kT} - \frac{\Delta U^b}{kT} \right], \\
&= \exp \left[\ln \left(\frac{N^a V^b}{(N^b + 1) V^a} \right) - \frac{\Delta U^a}{kT} - \frac{\Delta U^b}{kT} \right]. \tag{3.36}
\end{aligned}$$

In this case the acceptance criterion is identical to that for the pure component NVT Gibbs ensemble simulation [36].

The third transfer step algorithm (3) [66] is the most general of the three algorithms examined here, it proceeds by:

- random selection of a particle from the total N particles, regardless of subsystem and type
- transfer of that selected particle to a random position in the other subsystem.

The particle which is to be transferred is hence selected from the total N particles, so that $\mathcal{P}_{\text{subsystem } a}$, $\mathcal{P}_{\text{subsystem } b}$ and $\mathcal{P}_{\text{type } 1}$ are not included in the expressions for $\mathcal{P}_{mn}^{\text{criterion}}$ and $\mathcal{P}_{nm}^{\text{criterion}}$. The probability of choosing a particle of a particular type in a given subsystem, for both the forward and reverse steps, $\mathcal{P}_m^{\text{particle}}$ and $\mathcal{P}_n^{\text{particle}}$ are now equal, and given by $1/N$, and hence cancel from the transfer step criterion, which is now given by

$$\begin{aligned}
 \mathcal{P}_3^t &= \frac{\mathcal{P}_{mn}^{\text{criterion}}}{\mathcal{P}_{nm}^{\text{criterion}}} \\
 &= \frac{(N_1^a - 1)!(N_1^b + 1)!N_2^a!N_2^b!}{N_1^a!N_1^b!N_2^a!N_2^b!} \times \frac{\mathcal{P}_m^{\text{particle}}}{\mathcal{P}_n^{\text{particle}}} \times \frac{\mathcal{P}_{\text{position } a}}{\mathcal{P}_{\text{position } b}} \times \frac{\mathcal{P}_n^{\text{Gibbs}}}{\mathcal{P}_m^{\text{Gibbs}}} \\
 &= \left(\frac{N_1^b + 1}{N_1^a} \right) \exp \left[\ln \left(\frac{N_1^a V^b}{(N_1^b + 1) V^a} \right) - \frac{\Delta U^a}{kT} - \frac{\Delta U^b}{kT} \right], \\
 &= \exp \left[\ln \left(\frac{V^b}{V^a} \right) - \frac{\Delta U^a}{kT} - \frac{\Delta U^b}{kT} \right]. \tag{3.37}
 \end{aligned}$$

This is identical to the criterion obtained when the equivalent algorithm is applied to pure systems in the Gibbs ensemble [66].

In order to compare these three algorithms a NPT Gibbs ensemble Monte Carlo simulation of a binary mixture consisting of equal sized spheres, $\sigma_{11} = \sigma_{12} = \sigma_{22}$, interacting via a square-well potential of fixed range $\lambda = \lambda_{11} = \lambda_{22} = 1.5$, and $\lambda_{12} = 1$ is performed. The attractive interactions are given the values $\varepsilon_{11} = \varepsilon_{22} > 0$ and $\varepsilon_{12} = 0$. This mixture has been studied previously via the GEMC technique [53], the particular choice of intermolecular interaction parameters result in a phase diagram for the mixture which is dominated by regions of liquid-liquid immiscibility. Results obtained using the different transfer step algorithms are summarised in Table 3.1. All three algorithms are seen to give very similar results for the phase coexistence of the mixture, but the first algorithm (1), is found to require the fewest particle interchanges per simulation cycle, so that it is the most computationally efficient.

Table 3.1: Liquid-liquid coexistence data obtained from NPT Gibbs ensemble Monte Carlo simulations for a symmetrical mixture of square wells with a range $\lambda = 1.5$, performed using the various algorithms in the particle transfer step. The fixed variables during the simulation are the number of particles $N = 512$, the reduced pressure $P^* = P\sigma^3/\varepsilon = 1.08$ and the reduced temperature $T^* = kT/\varepsilon = 1.829$. The reduced densities $\rho^* = N\sigma^3/V$ and compositions x_2 , in the two coexisting liquid phases are labeled l_1 and l_2 , respectively; the uncertainties correspond to one standard deviation. The time corresponds to the cpu time required (in hours) to perform 100,000 simulation cycles on a 150 MHz, IP22 processor R4400 Silicon Graphics workstation. One simulation cycle consists of N MC displacements, one volume change and a fixed number of particle insertions (N_{inset}). The number of insertions is controlled so that 1% of the N particles are interchanged per cycle. Data marked with a † correspond to the equivalent data for the symmetrical square-well mixture of Ref. [53].

algorithm	$\rho_{l_1}^*$	$\rho_{l_2}^*$	x_{2,l_1}	x_{2,l_2}	time	N_{inset}
1	0.474 ± 0.016	0.474 ± 0.017	0.945 ± 0.020	0.055 ± 0.020	7.14	200
2	0.482 ± 0.020	0.466 ± 0.017	0.953 ± 0.020	0.066 ± 0.023	9.39	1200
3	0.469 ± 0.024	0.465 ± 0.021	0.940 ± 0.026	0.065 ± 0.028	9.41	1200
2†	0.481 ± 0.014	0.478 ± 0.013	0.948 ± 0.016	0.049 ± 0.017	-	-

3.4 The semigrand canonical ensemble for mixtures

Another Monte Carlo simulation ensemble used in this work is the semigrand canonical ensemble (SGC) [67, 68], which is an analogue of the grand canonical ensemble. Within the grand canonical ensemble simulations are performed at constant chemical potential μ , volume and temperature (μVT) using MC displacements and particle insertions/deletions to maintain the equality of the thermodynamic variables. The main difference between the the grand canonical (and the semigrand canonical) ensemble and the Gibbs ensemble is that the simulation is performed in a single subsystem. In the semigrand canonical ensemble particle identity changes are performed rather than the particle insertions of the grand canonical ensemble [69]. The total number of particles, N is kept constant in the SGC ensemble, but the concentration of the individual species is allowed to fluctuate by enforcing that the difference in chemical potentials $\Delta\mu = \mu_1 - \mu_2$ is kept constant in addition to the number of particles, the volume and the temperature.

In order to obtain the partition function for a binary mixture in the semigrand canonical ensemble, it is first necessary to present the expressions for the grand canonical ensemble. The partition function for a binary mixture of $N = N_1 + N_2$ particles, N_1 of type 1 and N_2 of type 2, at a constant volume V and a constant temperature T in the grand canonical ensemble is given by

$$\begin{aligned}
 Q_{\mu_1, \mu_2, V, T} &= \sum_{N_1, N_2}^{\infty} \frac{1}{N_1! \Lambda_1^{3N_1}} \frac{1}{N_2! \Lambda_2^{3N_2}} \\
 &\times \exp\left(\frac{N_1 \mu_1}{kT}\right) \exp\left(\frac{N_2 \mu_2}{kT}\right) V^{N_1 + N_2} \\
 &\times \int d\zeta^{N_1 + N_2} \exp\left[-\frac{U(N_1 + N_2)}{kT}\right], \quad (3.38)
 \end{aligned}$$

where μ_i is the chemical potential of particle i . $U(N_1 + N_2)$ is the configurational energy of the system of $N_1 + N_2$ particles which have scaled coordinates $\zeta_i = \mathbf{r}_i/L$, where \mathbf{r}_i corresponds to the positions and momenta of species i , and L is the linear simulation box length. It is common to re-write the partition function in terms of its configurational contribution, $Z_{N_1, N_2, V, T}$

$$\begin{aligned}
 Q_{\mu_1, \mu_2, V, T} &= \sum_{N_1, N_2}^{\infty} \frac{1}{N_1! \Lambda_1^{3N_1}} \frac{1}{N_2! \Lambda_2^{3N_2}} \\
 &\times \exp\left(\frac{N_1 \mu_1}{kT}\right) \exp\left(\frac{N_2 \mu_2}{kT}\right) Z_{N_1, N_2, V, T}, \quad (3.39)
 \end{aligned}$$

where $Z_{N_1, N_2, V, T}$ is defined

$$Z_{N_1, N_2, V, T} = V^{N_1 + N_2} \int d\zeta^{N_1 + N_2} \exp \left[-\frac{U(N_1 + N_2)}{kT} \right]. \quad (3.40)$$

In order to arrive at the partition function for the semigrand ensemble, we re-write Eq. (3.39) by fixing the chemical potential of one component (μ_2 for example) and defining the difference in chemical potential $\Delta\mu = \mu_2 - \mu_1$. This confines us to only allowing μ_1 and N_2 to vary, whilst μ_2 and N_1 are fixed. Eq. (3.39) thus becomes

$$\begin{aligned} Q_{\mu_1, \Delta\mu, V, T} &= \sum_{N=0}^{\infty} \frac{1}{\Lambda_1^{3N}} \exp \left(\frac{N\mu_1}{kT} \right) \left[\sum_{N_2=0}^N \frac{1}{N_2!(N-N_2)!} \right. \\ &\times \left(\frac{\Lambda_1}{\Lambda_2} \right)^{3N_2} \exp \left(\frac{N_2\Delta\mu}{kT} \right) \\ &\times Z_{N-N_2, N_2, V, T} \Big] \\ &= \sum_{N=0}^{\infty} \frac{1}{\Lambda_1^{3N}} \exp \left(\frac{N\mu_1}{kT} \right) Y_{N, V, T, \Delta\mu}, \end{aligned} \quad (3.41)$$

where $Y_{N, V, T, \Delta\mu}$ is defined

$$\begin{aligned} Y_{N, V, T, \Delta\mu} &= \sum_{N_2=0}^N \frac{1}{N_2!(N-N_2)!} \left(\frac{\Lambda_1}{\Lambda_2} \right)^{3N_2} \\ &\times \exp \left(\frac{N_2\Delta\mu}{kT} \right) Z_{N-N_2, N_2, V, T}. \end{aligned} \quad (3.42)$$

Note the similarities between the semigrand canonical partition function Eq. (3.41) and the grand canonical partition function Eq. (3.39), particularly in the way in which they can both be written as an exponential factor multiplied by a configurational part. The configurational average of a function \mathcal{A} in the semigrand canonical ensemble can be written

$$\begin{aligned} \langle \mathcal{A} \rangle_{N, V, T, \Delta\mu} &= \frac{1}{Y_{N, V, T, \Delta\mu}} \\ &\times \sum_{N_2=0}^N \frac{1}{N_2!(N-N_2)!} \left(\frac{\Lambda_1}{\Lambda_2} \right)^{3N_2} \\ &\times \exp \left(\frac{N_2\Delta\mu}{kT} \right) Z_{N-N_2, N_2, V, T} \mathcal{A}. \end{aligned} \quad (3.43)$$

The above expression corresponds to an ensemble average which has a probability distribution, which is proportional to

$$\mathcal{P}^{\text{semigrand}} = \exp \left\{ \ln \left[\frac{1}{N_2!(N-N_2)!} \right] + \left(\frac{N_2\Delta\mu^0}{kT} \right) + N \ln V - \left(\frac{U(N)}{kT} \right) \right\}, \quad (3.44)$$

where $\Delta\mu^0 = \mu_2^0 - \mu_1^0$ and $\mu_i^0 = \mu_i - \ln \Lambda_i^3$. New configurations in the semigrand canonical ensemble are generated by performing both particle displacements and

particle identity changes. Random displacement of particles leads to configurations which are generated with a probability proportional to

$$\mathcal{P}^d = \exp\left(-\frac{\Delta U}{kT}\right). \quad (3.45)$$

The identity change step is implemented by first selecting a species at random, then selecting a particle of that type from the total N particles and changing its identity. For the identity change of a particle of type 1 to a particle of type 2 configurations are generated with a probability proportional to

$$\mathcal{P}^{id} = \exp\left[\ln\left(\frac{N_1}{N_2 + 1}\right) + \left(\frac{\Delta\mu^0}{kT}\right) - \left(\frac{\Delta U}{kT}\right)\right]. \quad (3.46)$$

For the reverse process, when a particle of type 2 is changed into a particle of type 1, we find

$$\mathcal{P}^{id} = \exp\left[\ln\left(\frac{N_2}{N_1 + 1}\right) - \left(\frac{\Delta\mu^0}{kT}\right) - \left(\frac{\Delta U}{kT}\right)\right]. \quad (3.47)$$

An alternative algorithm for the particle identity change step exists [67], where a particle is chosen at random from the total N particles and its identity subsequently changed. In this case the new configurations are generated with a probability proportional to

$$\mathcal{P}^{id} = \exp\left[\left(\frac{\Delta\mu^0}{kT}\right) - \left(\frac{\Delta U}{kT}\right)\right], \quad (3.48)$$

in the case when type 1 \rightarrow type 2, and

$$\mathcal{P}^{id} = \exp\left[-\left(\frac{\Delta\mu^0}{kT}\right) - \left(\frac{\Delta U}{kT}\right)\right], \quad (3.49)$$

in the case when type 2 \rightarrow type 1.

The advantage of the semigrand ensemble over other simulation ensembles such as the Gibbs or the grand canonical ensembles is that it does not rely on particle insertions to achieve equilibrium. The convergence of the simulation is not limited by the density of the the system studied, so that it direct simulation of solid-liquid equilibria is theoretically possible [68]. The semigrand ensemble can also be applied to multicomponent systems where the chemical potential of only one species at a given state has to be evaluated regardless of the number of components present in the simulation. The phase behaviour of the symmetrical square-well mixture of Ref. [53] has recently been examined within the SGC ensemble [70]. The symmetry of the system examined in Ref. [70] permits the direct simulation of two-phase coexistence as in the Gibbs ensemble, but the simulation is performed in a single subsystem. The similarity between the SGC and the grand canonical ensembles is also exploited in Ref. [70], where a finite-size scaling (FSS) analysis of the crit-

ical region for the system is presented. In FSS studies the infinite system size critical properties are obtained from a series of finite-system simulations, usually performed in the GC ensemble, due to the density and energy fluctuations. The greater efficiency of semigrand canonical simulations than the corresponding grand canonical simulations hence make it a favourable ensemble for use in finite-size scaling studies. In this work, we follow an approach similar to that of Ref. [70] where the critical region of a specific model system is examined using FSS techniques in the SGC ensemble.

3.5 Concluding remarks

In this chapter we have introduced the concept of molecular simulation as a means of obtaining phase coexistence data for simple model systems. In particular, we show how simulations can be performed in the Gibbs and semigrand canonical ensembles. The Gibbs ensemble technique is the most widely used direct simulation technique currently available for the study of fluid mixtures. It consists of simulations which are performed in two subsystems which are in thermodynamic equilibrium but not in physical contact. The advantage of this approach is that it eliminates the problems associated with the interface, which is the main disadvantage of two-phase simulation methods. The GEMC simulation results presented in this work are used as a means of testing the adequacy of the theoretical representation of model fluids obtained using the SAFT-VR equation of state. Additionally, we perform Gibbs ensemble simulations as a means of testing the effect of including specific features in the model on the phase behaviour exhibited by the system.

The semigrand canonical ensemble is an indirect simulation technique, where the difference in chemical potential of the component species is fixed. Since particle identity changes are performed rather than insertions, the technique is applicable to high density fluids and even solids. In this work we use the semigrand ensemble to examine a specific model, which due to its symmetry can be simulated in a single subsystem. The critical region of this model is also examined using a finite size scaling analysis of the simulation results.

3.6 Appendix: Determination of chemical potential in the Gibbs ensemble

A feature of the Gibbs ensemble technique is that the chemical potential of the individual species does not have to be calculated during the simulation, since the particle interchange step maintains equality of chemical potential between the two phases. A disadvantage of the Metropolis algorithm is its difficulty in obtaining non-mechanical properties such as the free energy, the entropy and the chemical potential during the simulation. It is however a useful test of the GEMC algorithm to actually determine the chemical potentials of the individual species present in the simulation. This can be achieved, within the GEMC transfer step, following Widom's particle insertion method [25]. Here, a virtual or test particle is inserted into the simulation box, and its energy with respect to all the other particles is calculated, enabling the excess chemical potential of the system to be obtained from

$$\mu^{\text{ex}} = -kT \ln \left(\left\langle \exp \left[-\frac{U^{\text{test}}}{kT} \right] \right\rangle_{NVT} \right), \quad (3.50)$$

where U^{test} is the interaction energy of the test particle with the other N particles, and the angular brackets represent an average in the canonical ensemble. The full chemical potential is thus given by

$$\mu = \mu^0 + kT \ln \rho - kT \ln \left(\left\langle \exp \left[-\frac{U^{\text{test}}}{kT} \right] \right\rangle_{NVT} \right), \quad (3.51)$$

where $\mu^0 = kT \ln \Lambda^{-3}$.

However, it has been noted [71] that this test insertion technique is strictly only valid for the NVT ensemble, as derived in the original Metropolis scheme [1]. In order to use the same technique in the Gibbs ensemble it is important to account for the fluctuations in the number of particles and in the volume of the subsystems, which arise in the Gibbs ensemble, both at constant NVT and at constant NPT . These fluctuations only become important close to the critical point, and when the number of particles is small. At temperatures away from the critical temperature, when the particle number is stable, the chemical potential of a species i in subsystem s in the NPT Gibbs ensemble is given by

$$\mu_i^j = \mu_i^0 - kT \ln \left(\left\langle \frac{V^j}{N_i^j + 1} \exp \left[-\frac{U_i^{\text{test},j}}{kT} \right] \right\rangle_{NPT}^{\text{Gibbs}} \right). \quad (3.52)$$

The chemical potentials obtained by Eq. (3.51) and by Eq. (3.52) are found to differ by less than the simulation uncertainties for pure component species, except

when the number of particles in one of the subsystems is very small [71]. In order to prevent poor sampling in the case of GEMC simulations of mixtures, where one subsystem can conceivably have a very small number of particles of a given component, the chemical potential of the mixture is evaluated both during the particle transfer step and in a separate subroutine using the Widom insertion technique, as governed by Eq. (3.52).

Bibliography

- [1] N. Metropolis, A. Rosenbluth, M. Rosenbluth, A. Teller, and E. Teller, *J. Chem. Phys.*, **21**, 1087 (1953).
- [2] B. J. Alder and T. E. Wainwright, *J. Chem. Phys.*, **27**, 1208 (1957).
- [3] B. J. Alder and T. E. Wainwright, *J. Chem. Phys.*, **31**, 459 (1959).
- [4] L. Landau and E. Lifchitz, *Physique Statistique*, Editions MIR, (1967).
- [5] D. A. McQuarrie, *Statistical Mechanics*, Harper Collins, (1976).
- [6] D. Chandler, *Introduction to Modern Statistical Mechanics*, Oxford University, (1987).
- [7] M. E. Fisher, *Arch. Rat. Mech. Anal.*, **17**, 377 (1964).
- [8] M. P. Allen and D. J. Tildesley, *Computer Simulation of Liquids*, Clarendon, (1987).
- [9] R. Y. Rubinstein, *Simulation and Monte Carlo Methods*, Wiley (1981).
- [10] W. W. Wood and F. R. Parker, *J. Chem. Phys.*, **27**, 720 (1957).
- [11] W. L. Jorgensen, F. Chandrachekhar, J. D. Madura, R. W. Impey, and M. L. Klein, *J. Chem. Phys.*, **79**, 926 (1983).
- [12] J. J. de Pablo and J. M. Prausnitz, *Fluid Phase Equilib.*, **53**, 177 (1989).
- [13] W. L. Jorgensen, *J. Chem. Phys.*, **77**, 4156 (1982).
- [14] R. F. Cracknell, D. Nicholson, N. G. Parsonage, and H. Evans, *Mol. Phys.*, **71**, 931 (1990).
- [15] H. J. C. Berendsen, J. M. P. Postma, W. F. von Gustersen, and J. Hermans, *Jerusalem Symp. Quantum Chem. Biochem.*, **14**, 331 (1981).
- [16] J. J. de Pablo, J. M. Prausnitz, H. J. Strauch, and P. T. Cummings, *J. Chem. Phys.*, **93**, 7355 (1990).

- [17] B. Smit, S. Karaborni, and J. I. Siepmann, *J. Chem. Phys.*, **105**, 2126 (1995).
- [18] B. Smit, *Mol. Phys.*, **85**, 153 (1995).
- [19] B. Smit, *Ind. Eng. Chem. Res.*, **35**, 4166 (1995).
- [20] M. E. van Leeuwen and B. Smit, *J. Phys. Chem.*, **99**, 1831 (1995).
- [21] B. Smit, *Mol. Simul.*, **14**, 259 (1995).
- [22] S. Karaborni and B. Smit, *Curr. Op. Coll. Int. Sci.*, **1**, 411 (1996).
- [23] S. Karaborni, B. Smit, W. Heidug, J. Urai, and E. van Oort, *Science*, **271**, 1102 (1996).
- [24] G. E. Norman and V. S. Filinov, *High Temp.*, **7**, 216 (1969).
- [25] B. Widom, *J. Chem. Phys.*, **39**, 2802 (1963).
- [26] K. S. Shing and K. E. Gubbins, *Mol. Phys.*, **49**, 1121 (1983).
- [27] K. E. Gubbins, *Mol. Simul.*, **2**, 223 (1989).
- [28] K. E. Gubbins, *Models for Thermodynamic and Phase Equilibria Calculations*, Edited by S. I. Sandler, Dekker (1994).
- [29] J. P. Valleau, *J. Computational Phys.*, **95**, 584 (1991).
- [30] J. P. Valleau, *J. Chem. Phys.*, **99**, 4718 (1993).
- [31] D. A. Kofke, *Mol. Phys.*, **78**, 1331 (1993).
- [32] D. A. Kofke, *J. Chem. Phys.*, **98**, 4149 (1993).
- [33] R. Agrawal, M. Mehta, and D. A. Kofke, *Int. J. Thermophys.*, **15**, 1073 (1994).
- [34] D. Frenkel, *Observation and Prediction of Phase Transitions in Complex Fluids*, edited by M. Baus, L. F. Rull, and J. P. Ryckaert, Kluwer Academic, (1995).
- [35] J. S. Rowlinson and B. Widom, *Molecular Theory of Capillarity*, Clarendon, (1986).
- [36] A. Z. Panagiotopoulos, *Mol. Phys.*, **61**, 813 (1987).
- [37] A. Z. Panagiotopoulos, *Mol. Simul.*, **9**, 1 (1992).
- [38] B. Smit, *Computer Simulation in Chemical Physics*, edited by M. P. Allen and D. J. Tildesley Kluwer Academic, (1993), pp. 173-209.
- [39] A. Z. Panagiotopoulos, *Observation and Prediction of Phase Transitions in Complex Fluids*, edited by M. Baus, L. F. Rull, and J. P. Ryckaert, Kluwer Academic, (1995).

- [40] B. Smit, Ph. de Smedt, and D. Frenkel, *Mol. Phys.*, **68**, 931 (1989).
- [41] G. S. Dubey, S. F. O'Shea, and P. A. Monson, *Mol. Phys.*, **80**, 997 (1993).
- [42] F. A. Escobedo and J. J. de Pablo, *Mol. Phys.*, **87**, 347 (1996).
- [43] L. Vega, E. de Miguel, L. F. Rull, G. Jackson, and I. A. McLure, *J. Chem. Phys.*, **96**, 2296 (1992).
- [44] J. R. Recht and A. Z. Panagiotopoulos, *Mol. Phys.*, **80**, 843 (1993).
- [45] E. de Miguel, *Phys. Rev. E*, **55**, 1347 (1997).
- [46] B. Smit, C. P. Williams, E. M. Hendriks, and S. W. de Leeuw, *Mol. Phys.*, **68**, 765 (1989).
- [47] B. Smit and D. Frenkel, *Mol. Phys.*, **74**, 35 (1991).
- [48] E. Lomba and N. G. Almarza, *J. Chem. Phys.*, **100**, 8367 (1994).
- [49] E. de Miguel, L. F. Rull, M. K. Chalam, and K. E. Gubbins, *Mol. Phys.*, **71**, 1223 (1990).
- [50] F. W. Tavares and S. I. Sandler, *Mol. Phys.*, **87**, 1471 (1996).
- [51] A. Z. Panagiotopoulos, N. Quirke, M. R. Stapleton, and D. J. Tildesley, *Mol. Phys.*, **63**, 527 (1988).
- [52] R. J. Sadus, *Fluid Phase Equilib.*, **116**, 289 (1996).
- [53] D. G. Green, G. Jackson, E. de Miguel, and L. F. Rull, *J. Chem. Phys.*, **101**, 3190 (1994).
- [54] L. A. Davies, A. Gil-Villegas, G. Jackson, S. Calero, and S. Lago, *Phys. Rev. E*, submitted (1997).
- [55] R. J. Sadus, *Mol. Phys.*, **87**, 979 (1996).
- [56] J. J. de Pablo, M. Bonnin, and J. M. Prausnitz, *Fluid Phase Equilib.*, **73**, 187 (1992).
- [57] M. G. Martin and J. I. Siepmann, *Abs. Am. Chem. Soc.*, **212**, 242 (1996).
- [58] J. K. Johnson and K. E. Gubbins, *Mol. Phys.*, **77**, 1033 (1992).
- [59] H. J. Strauch and P. T. Cummings, *Fluid Phase Equilib.*, **83**, 213 (1993).
- [60] M. R. Stapleton, D. J. Tildesley, and N. Quirke, *J. Chem. Phys.*, **92**, 4456 (1990).
- [61] A. D. Mackie, E. A. O'Toole, D. A. Hammer, and A. Z. Panagiotopoulos, *Fluid Phase Equilib.*, **82**, 251 (1993).

- [62] J. N. Canongia Lopes and D. J. Tildesley, *Mol. Phys.*, in press (1997).
- [63] W. W. Wood, *Physics of Simple Liquids*, edited by H.N.V.Temperley, J.S.Rowlinson, and G.S.Rushbrooke, North Holland, (1981) pp. 115-230.
- [64] W. W. Wood, *J. Chem. Phys.*, **48**, 415 (1968).
- [65] T. L. Hill, *Statistical Mechanics* McGraw-Hill (1956).
- [66] L. F. Rull, G. Jackson, and B. Smit, *Mol. Phys.*, **85**, 435 (1995).
- [67] D. A. Kofke and E. D. Glandt, *Mol. Phys.* **64**, 1105 (1988).
- [68] D. Frenkel, *Computer Simulation in Chemical Physics*, edited by M. P. Allen and D. J. Tildesley Kluwer Academic, (1993) pp. 93 -152.
- [69] A. Z. Panagiotopoulos, *Int. J. Thermophys.*, **10**, 447 (1989).
- [70] E. de Miguel, E. M. del Río, and M. M. Telo da Gamma, *J. Chem. Phys.*, **103**, 6188 (1995).
- [71] B. Smit and D. Frenkel, *Mol. Phys.*, **68**, 951 (1989).

Chapter 4

Prediction of phase equilibria of mixtures using the SAFT-VR approach

4.1 Introduction

An important advantage of molecular based theories such as SAFT-VR [1, 2], is that each of the individual contributions to the Helmholtz free energy can be compared directly with computer simulation data. Here we examine three binary mixtures using the SAFT-VR equation of state (as described in Chapter 2). A mixture of hard-sphere and square-well monomers, a mixture consisting of only square-well monomers, and a square-well monomer-dimer mixture. The adequacy of the SAFT-VR expressions in describing phase behaviour of mixtures in general can be established via a study of these three important prototype systems. All the particles which are examined here have the same segment diameter and square-well interaction range. The dimers of the third mixture are formed from two tangentially bonded square-well monomers, so that the monomer and dimer segments have the same range and strength of square-well interaction. This simplifies the actual expressions involved in the equation of state.

The two monomer mixtures can be used to determine the adequacy of the con-

tribution to the SAFT-VR free energy due to monomers via an examination of their vapour-liquid equilibria, in the case of the hard-sphere and square-well mixture and of the liquid-liquid phase equilibria of the binary square-well mixture. The coexistence region for both these mixtures has been examined previously by Gibbs ensemble Monte Carlo simulation [3]-[5]. Thus it is possible to formulate a direct comparison between the SAFT-VR prediction and the simulation data of the mixtures.

The square-well monomer-dimer mixture is perhaps the most interesting of the three mixtures studied here, since it allows one to quantify the effect of chain length on fluid phase equilibria. Although the phase equilibria of systems with increasing chain length have been studied experimentally (e.g., mixtures of homologous series such as alkanes, perfluoroalkanes, dimethylsiloxanes etc.), the complexity of real intermolecular interactions makes it difficult to establish the precise effect of molecular extension. Computer simulation methods are ideally suited to the study of such systems, since the nature of the intermolecular interactions can be controlled within a simulation, and the results obtained can be considered as exact, particularly in the context of comparisons with equations of state. Simulation studies have been previously performed on both the pure component square-well monomer [6, 7, 5] and dimer [8], but no simulation data has been reported for the binary monomer-dimer mixture. In this chapter we present Gibbs ensemble Monte Carlo simulation data for this mixture, which are used to examine the accuracy of the SAFT-VR equation of state in predicting the phase equilibria of chain molecules.

The SAFT-VR formalism is described in Chapter 2, so that here we will only briefly present the main elements of the theory as applied to the three binary mixtures of interest; the hard-sphere and square-well monomer mixture; the binary square-well monomer mixture; the square-well monomer-dimer mixture. Comparisons between the SAFT-VR predictions and computer simulation data are made for each of these mixtures in turn. For the monomer-dimer mixture we also report new GEMC simulation data and illustrate how this can be used to obtain the phase diagram of the pure components.

4.2 SAFT-VR equation of state

The SAFT-VR equation of state for a mixture of associating chain molecules is written in terms of four separate contributions to the Helmholtz free energy, A [1, 2]

$$\frac{A}{NkT} = \frac{A^{IDEAL}}{NkT} + \frac{A^{MONO.}}{NkT} + \frac{A^{CHAIN}}{NkT} + \frac{A^{ASSOC.}}{NkT}, \quad (4.1)$$

where N is the number of chain molecules in the mixture, k is Boltzmann's constant, and T is the temperature. In this equation A^{IDEAL} is the ideal free energy, $A^{MONO.}$ is the residual free energy due to the monomer segments, A^{CHAIN} is the contribution due to the formation of chains of monomers, and $A^{ASSOC.}$ is the term that describes the contribution to the free energy due to intermolecular association. Here, we focus on systems interacting with a square-well potential:

$$u_{ij}(r_{ij}) = \begin{cases} +\infty & \text{if } r_{ij} < \sigma_{ij}, \\ -\varepsilon_{ij} & \text{if } \sigma_{ij} \leq r_{ij} < \lambda_{ij}\sigma_{ij}, \\ 0 & \text{if } r_{ij} \geq \lambda_{ij}\sigma_{ij}, \end{cases} \quad (4.2)$$

where r_{ij} is the distance between two particles i and j . The contact distance is σ_{ij} and the parameters λ_{ij} and ε_{ij} are the range and depth of the potential well for the i - j interaction, respectively. For all three mixtures, the molecular diameters and the range of the square-well interaction are equal for each component, so that $\sigma = \sigma_{11} = \sigma_{12} = \sigma_{22}$, and $\lambda = \lambda_{11} = \lambda_{12} = \lambda_{22}$. The nature of the i - j interaction, ε_{ij} must be defined individually for the three mixtures. For the hard-sphere and square-well mixture, with the hard sphere as component 1, the mixture interactions are given by $\varepsilon_{11} = \varepsilon_{12} = 0$ and $\varepsilon_{22} = \varepsilon$. For the binary square-well mixture both components have equal like interactions, so that $\varepsilon_{11} = \varepsilon_{22} = \varepsilon$, but we specify that there is no attraction between unlike components, so $\varepsilon_{12} = 0$. In the case of the monomer-dimer square-well mixture, all the interactions between unlike and like components are equal, so that here $\varepsilon_{11} = \varepsilon_{12} = \varepsilon_{22} = \varepsilon$. We present the general SAFT-VR expressions for each contribution to the free energy in Eq. (4.1) together with those which are specific for each of the three binary mixtures examined here here.

The free energy of the ideal n -component mixture is given by [9]

$$\frac{A^{IDEAL}}{NkT} = \sum_{i=1}^n x_i \ln \rho_i \Lambda_i - 1 \quad (4.3)$$

where $x_i = N_i/N$ is the mole fraction, $\rho_i = N_i/V$ is the number density and Λ_i is the thermal de Broglie wavelength of species i , for a binary mixture this reduces

to

$$\frac{A^{IDEAL}}{NkT} = x_1 \ln \rho_1 \Lambda_1^3 + x_2 \ln \rho_2 \Lambda_2^3 - 1. \quad (4.4)$$

The monomer free energy is

$$\begin{aligned} \frac{A^{MONO.}}{NkT} &= \left(\sum_{i=1}^n x_i m_i \right) \frac{A^M}{N_s kT} \\ &= \left(\sum_{i=1}^n x_i m_i \right) a^M, \end{aligned} \quad (4.5)$$

where m_i is the number of spherical segments in each chain i . For a binary mixture consisting of only monomers, where $m_i = 1$, we have

$$\frac{A^{MONO.}}{NkT} = a^M, \quad (4.6)$$

and for a binary mixture of monomers (component 1) and dimers (component 2) with $m_2 = 2$ we have

$$\frac{A^{MONO.}}{NkT} = (x_1 + 2x_2) a^M. \quad (4.7)$$

The monomer free energy per segment of the mixture $a^M = A/(N_s kT)$ is obtained from the Barker and Henderson high-temperature expansion up to second order [10]- [12]:

$$a^M = a^{HS} + \beta a_1 + \beta^2 a_2, \quad (4.8)$$

where a^{HS} is the free energy for a mixture of hard-spheres, $\beta = 1/kT$, a_1 and a_2 are the first two perturbation terms associated with the attractive energy.

The free energy of the reference hard-sphere mixture is obtained from the expression of Boublík [13] and Mansoori *et al.* [14]:

$$a^{HS} = \frac{6}{\pi \rho_s} \left[\left(\frac{\zeta_2^3}{\zeta_3^2} - \zeta_0 \right) \ln(1 - \zeta_3) + \frac{3\zeta_1 \zeta_2}{1 - \zeta_3} + \frac{\zeta_2^3}{\zeta_3(1 - \zeta_3)^2} \right]. \quad (4.9)$$

In this expression $\rho_s = N_s/V$ is the number density of the mixture in terms of the number of spherical segments. Note that $\rho_s = \rho(\sum_i x_i m_i)$, where ρ is the total number density of the mixture. The reduced densities ζ_l are defined as

$$\zeta_l = \frac{\pi}{6} \rho_s \left[\sum_{i=1}^n x_{s,i} (\sigma_i)^l \right], \quad (4.10)$$

where σ_i the diameter of spherical segments of chain i , and $x_{s,i}$ is the mole fraction

of segments of type i in the mixture, given by

$$x_{s,i} = \frac{m_i x_i}{\sum_{k=1}^n m_k x_k}. \quad (4.11)$$

When $m_i = 1$ for both components, $x_{s,i} = x_i$, but for monomers in a monomer-dimer mixture we have

$$x_{s,1} = \frac{x_1}{x_1 + 2x_2} \quad (4.12)$$

and for dimers in the same mixture,

$$x_{s,2} = \frac{2x_2}{x_1 + 2x_2}. \quad (4.13)$$

The overall packing fraction of the mixture is given by ζ_3 , which is equivalent to $\eta = \pi\rho\sigma^3/6$ for the pure component. In all of the binary mixtures of interest here, since $\sigma = \sigma_{11} = \sigma_{22}$, the free energy of the reference hard-sphere mixture reduces to the Carnahan and Starling expression [15, 9]

$$a^{HS} = \frac{4\eta - 3\eta^2}{(1 - \eta)^2}. \quad (4.14)$$

The mean-attractive energy a_1 in the perturbation expansion is given by

$$a_1 = \sum_{i=1}^n \sum_{j=1}^n x_{s,i} x_{s,j} a_1^{ij} \quad (4.15)$$

where

$$a_1^{ij} = -2\pi\rho_s \varepsilon_{ij} \int_{\sigma_{ij}}^{\infty} r_{ij}^2 g_{ij}^{HS}(r_{ij}; \zeta_3) dr_{ij}, \quad (4.16)$$

and g_{ij}^{HS} is the radial distribution function for a mixture of hard spheres. The integral is transformed by applying the mean-value theorem [1] which gives an expression for a_1 in terms of the contact value of g_{ij}^{HS} :

$$a_1^{SW} = -\rho_s \sum_{i=1}^n \sum_{j=1}^n x_{s,i} x_{s,j} \alpha_{ij}^{VDW} g_{ij}^{HS}[\sigma_{ij}; \zeta_3^{eff}], \quad (4.17)$$

where

$$\alpha_{ij}^{VDW} = 2\pi\varepsilon_{ij}\sigma_{ij}^3(\lambda_{ij}^3 - 1)/3 \quad (4.18)$$

is the van der Waals attractive constant for the $i - j$ square-well interaction. The contact value of the radial distribution function for the hard-sphere reference system, $g_{ij}^{HS}[\sigma_{ij}; \zeta_3^{eff}]$ is evaluated at an effective packing fraction ζ_3^{eff} , given by the expression of Boublík [13] and Mansoori *et al.* [14]

$$g_{ij}^{HS}[\sigma_{ij}; \zeta_3^{eff}] = \frac{1}{1 - \zeta_3^{eff}} + 3 \frac{\sigma_{ii}\sigma_{jj}}{\sigma_{ii} + \sigma_{jj}} \frac{\zeta_2^{eff}}{(1 - \zeta_3^{eff})^2} \quad (4.19)$$

$$+ 2 \left(\frac{\sigma_{ii}\sigma_{jj}}{\sigma_{ii} + \sigma_{jj}} \right)^2 \frac{\zeta_2^{eff2}}{(1 - \zeta_3^{eff})^3}.$$

For the three systems of interest here the nature of the interactions and the fact that all the segments are of equal diameter leads to the simplification of the mean-attractive energy expressions for these mixtures. For the hard-sphere and square-well mixture, Eq. (4.15) becomes

$$\begin{aligned} a_1 &= x_2^2 a_1^{22} \\ &= x_2^2 a_1^{SW}, \end{aligned} \quad (4.20)$$

since $a_1^{11} = a_1^{12} = 0$. Similarly for the binary square-well mixture the expression for a_1 is given by

$$\begin{aligned} a_1 &= x_1^2 a_1^{11} + x_2^2 a_1^{22} \\ &= (x_1^2 + x_2^2) a_1^{SW}, \end{aligned} \quad (4.21)$$

since $a_1^{12} = 0$. For the monomer-dimer square-well mixture all the interactions are non-zero, so we obtain an expression for the mean-attractive energy of the form

$$\begin{aligned} a_1 &= x_1^2 a_1^{11} + x_1 x_2 a_1^{12} + x_2^2 a_1^{22} \\ &= (x_1 + x_2)^2 a_1^{SW} \\ &= a_1^{SW}. \end{aligned} \quad (4.22)$$

In each of these cases a_1^{SW} is given by

$$a_1^{SW} = -\rho_s \alpha^{VDW} g^{HS}[\sigma; \eta^{eff}] \quad (4.23)$$

where

$$\alpha^{VDW} = 2\pi\epsilon\sigma^3(\lambda^3 - 1)/3 \quad (4.24)$$

and the contact value of the radial distribution function is given by the Carnahan and Starling expression [15, 9]

$$g^{HS}[\sigma; \eta^{eff}] = \frac{1 - \eta^{eff}/2}{(1 - \eta^{eff})^3}, \quad (4.25)$$

with $\eta^{eff} = \zeta_3^{eff}$. The parameterisation for η^{eff} obtained for the pure square-well fluid in Ref. [1] is used, where

$$\eta^{eff}(\eta, \lambda) = c_1(\lambda)\eta + c_2(\lambda)\eta^2 + c_3(\lambda)\eta^3, \quad (4.26)$$

the coefficients c_1 , c_2 and c_3 are given by:

$$\begin{pmatrix} c_1 \\ c_2 \\ c_3 \end{pmatrix} = \begin{pmatrix} 2.25855 & -1.50349 & 0.249434 \\ -0.669270 & 1.40049 & -0.827739 \\ 10.1576 & -15.0427 & 5.30827 \end{pmatrix} \begin{pmatrix} 1 \\ \lambda \\ \lambda^2 \end{pmatrix}. \quad (4.27)$$

This corresponds to the MX1 or MX3 mixing rule of Chapter 2 and Ref. [2].

The fluctuation term of the free energy is given by

$$a_2 = \sum_{i=1}^n \sum_{j=1}^n x_{s,i} x_{s,j} a_2^{ij}, \quad (4.28)$$

where each of the terms a_2^{ij} are obtained with the local compressibility approximation (LCA) [10, 11] as

$$a_2^{ij} = \frac{1}{2} K^{HS} \varepsilon_{ij} \rho_s \frac{\partial a_1^{ij}}{\partial \rho_s}, \quad (4.29)$$

where K^{HS} is the isothermal compressibility for a mixture of hard-spheres, given by the Percus-Yevick expression [16]

$$K^{HS} = \frac{\zeta_0(1 - \zeta_3)^4}{\zeta_0(1 - \zeta_3)^2 + 6\zeta_1\zeta_2(1 - \zeta_3) + 9\zeta_2^3}. \quad (4.30)$$

Since all segments have equal diameter we have

$$a_2 = \frac{1}{2} K^{HS} \varepsilon \rho_s \frac{\partial a_1}{\partial \rho_s}, \quad (4.31)$$

where K^{HS} is now the pure component expression given by

$$\begin{aligned} K^{HS} &= \frac{(1 - \eta)^4}{(1 - \eta)^2 + 6\eta(1 - \eta) + 9\eta^2} \\ &= \frac{(1 - \eta)^4}{(1 + 2\eta)}. \end{aligned} \quad (4.32)$$

The contribution to the SAFT-VR Helmholtz free energy due to the formation of chains is given by

$$\frac{A^{chain}}{NkT} = - \sum_{i=1}^n x_i (m_i - 1) \ln y^{SW}(\sigma_{ii}), \quad (4.33)$$

where $y^{SW}(\sigma_{ii}) = \exp(-\beta\varepsilon_{ii})g^{SW}(\sigma_{ii})$ is the background correlation function, and $g^{SW}(\sigma_{ii})$ is the radial distribution function for the square well system, both evaluated at contact. The term corresponding to the Boltzmann factor $\exp(-\beta\varepsilon_{ii})$ is

not required in the phase equilibria calculations, which permits us to write:

$$\frac{A^{chain}}{NkT} = - \sum_{i=1}^n x_i(m_i - 1) \ln g_{ii}^{SW}(\sigma_{ii}). \quad (4.34)$$

The contact value of the radial distribution function between segments i and j is obtained in the SAFT-VR approach from a first order perturbation expansion

$$g_{ij}^{SW}(\sigma_{ij}) = g_{ij}^{HS}(\sigma_{ij}) + \beta \epsilon_{ij} g_1(\sigma_{ij}), \quad (4.35)$$

where $g_1(\sigma_{ij})$ is obtained from a self-consistent calculation of the pressure using the Clausius virial theorem [1], as was explained in Chapter 2:

$$\begin{aligned} g_{ij}^{SW}[\sigma_{ij}; \zeta_3] &= g_{ij}^{HS}[\sigma_{ij}; \zeta_3] \\ &+ \beta \epsilon_{ij} \left[g_{ij}^{HS}[\sigma_{ij}; \zeta_3^{eff}] \right. \\ &\left. + (\lambda_{ij}^3 - 1) \left(\frac{\lambda_{ij}}{3} \frac{\partial g_{ij}^{HS}[\sigma_{ij}; \zeta_3^{eff}]}{\partial \lambda_{ij}} - \rho_s \frac{\partial g_{ij}^{HS}[\sigma_{ij}; \zeta_3^{eff}]}{\partial \rho_s} \right) \right]. \end{aligned} \quad (4.36)$$

Since both the hard-sphere and square-well mixture and the binary square-well mixture consist only of monomeric segments, the contribution due to the formation of chains in Eq. (4.1) is only present in the monomer-dimer mixture, where

$$\frac{A^{chain}}{NkT} = x_2 \ln g^{SW}(\sigma). \quad (4.37)$$

Additionally, since all of the square-well segments have equal diameter the contact value of the square-well radial distribution function of Eq. (4.36) reduces to

$$\begin{aligned} g^{SW}[\sigma; \eta] &= g^{HS}[\sigma; \eta] \\ &+ \beta \epsilon \left[g^{HS}[\sigma; \eta^{eff}] + (\lambda^3 - 1) \frac{\partial g^{HS}[\sigma; \eta^{eff}]}{\partial \eta^{eff}} \left(\frac{\lambda}{3} \frac{\partial \eta^{eff}}{\partial \lambda} - \eta \frac{\partial \eta^{eff}}{\partial \eta} \right) \right]. \end{aligned} \quad (4.38)$$

None of the three binary mixtures examined here are permitted to associate, so that the contribution to Eq. (4.1) due to association is zero, hence we now have a complete description of the SAFT-VR equations of state for the three mixtures.

For all mixtures, in order to determine the conditions of phase equilibria for two coexisting phases a and b the temperature, pressure and chemical potential are required to satisfy the equations

$$T^a = T^b, P^a = P^b, \mu_i^a = \mu_i^b. \quad (4.39)$$

The chemical potential, μ_i , of species i can be obtained from the Helmholtz free

energy of the SAFT-VR equation of state using the standard relation:

$$\frac{\mu_i}{kT} = \left(\frac{\partial A/kT}{\partial N_i} \right)_{T,V,N_j \neq i}, \quad (4.40)$$

where N_i is the number of chain molecules of species i . The overall pressure P may be calculated through the compressibility factor Z as:

$$\begin{aligned} Z &= \frac{PV}{NkT} \\ &= \sum_{i=1}^n x_i \frac{\mu_i}{kT} + \frac{A}{NkT}, \end{aligned} \quad (4.41)$$

where n is the total number of components in the mixture and $x_i = N_i/N$ is the mole fraction of component i . These functions are used in the numerical determination of the phase behaviour of the mixture, using a simplex method [17].

4.3 Comparisons with simulation data

In the previous section we have discussed details of the application of the SAFT-VR equation of state to three different mixtures consisting of hard-sphere and square-well molecules (in both monomer and dimer forms). The principal motivation of the SAFT-VR approach lies in the description of the phase equilibria of real mixtures, it is important to first examine the adequacy of the equation of state used by comparing the theoretical predictions with exact data obtained by computer simulation. Here, we present appropriate comparisons with Gibbs Ensemble Monte Carlo (GEMC) [18, 19] data for the vapour-liquid and liquid-liquid phase equilibria of specifically chosen square-well mixtures. We initially study mixtures of monomeric segments of the same size, with attractive interactions of equal range but with extreme values of the attractive energies, which essentially is a test of the Barker and Henderson perturbation theory used to describe the monomer contribution in the SAFT-VR free energy. These comparisons allow us to assess the adequacy of the pure-fluid range dependence which is used to determine the effective packing fraction of the mixture. Simulation data for the vapour-liquid and liquid-liquid equilibria of these mixtures have already been reported [3].

By specifying that the segments of the mixture are of equal size and that the square-well interaction is of equal strength and range for both components, the phase equilibria of the monomer-dimer mixture examined here is governed by the difference in length of the two components. Comparison of the SAFT-VR pre-

diction with GEMC data for this mixture allows us to test the adequacy of the term which describes the contribution to the Helmholtz free energy due to chain formation. Since the mixtures examined here all consist of square-well segments of equal diameter and interaction range, we are unable to present a stringent test of the mixing rules described in Chapter 2 and in Ref. [2], however further GEMC simulations are currently being performed for mixtures with components of different size and with energy parameters so that a more detailed analysis of the mixing rules can be obtained.

4.3.1 The hard-sphere and square-well mixture

The vapour-liquid phase equilibria of a binary mixture consisting of hard-sphere (1) and square-well (2) monomers is examined. Both components are of equal diameter with $\sigma = \sigma_{11} = \sigma_{12} = \sigma_{22}$, and the mixture interactions are characterised $\epsilon_{11} = \epsilon_{12} = 0$, $\epsilon = \epsilon_{22} > 0$, $\lambda_{11} = \lambda_{12} = 1$ and $\lambda = \lambda_{22} = 1.5$. Constant pressure slices of the vapour-liquid phase diagrams for the mixture are shown in Figures 4.1 and 4.2.

The SAFT-VR predictions for the vapour-liquid equilibria are compared with the GEMC data of Ref. [3] for both the temperature-density ($T\rho$) and temperature-composition (Tx) coexistence curves. The phase behaviour of this mixture has been examined before [20, 21, 3]: the critical temperature and pressure of the square-well fluid is seen to increase upon the addition of the hard spheres, and as expected the vapour phase is richer in hard spheres than the coexisting liquid phase which is composed almost entirely of square-well monomers. The phase diagrams given in Fig. 4.1 are at a constant reduced pressure of $P^* = P\sigma^3/\epsilon = 0.1$ which is very close to the critical pressure of the pure square well: where the reduced critical temperature, pressure and density for the pure square-well fluid with a range of $\lambda = 1.5$ are give in Ref. [7] as $T_c^* = kT_c/\epsilon = 1.219$, $P_c^* = P_c\sigma^3/\epsilon = 0.108$, and $\rho_c^* = \rho_c\sigma^3 = 0.299$, respectively. Results are presented for the SAFT-VR theory including only the a_1 term in the contribution to the free energy due to monomers, and for the theory including both a_1 and a_2 . These first- and second-order versions of the SAFT-VR expressions are both found to give an excellent description of the vapour-liquid phase equilibria for the coexisting densities (Fig. 4.1 (a)) and the compositions (Fig. 4.1 (b)). Inclusion of the second-order term a_2 leads to a better description of the liquid densities and of the vapour compositions. The vapour-liquid coexistence curves for a supercritical pressure slice of $P^* = P\sigma^3/\epsilon = 1.0$ are shown in Fig. 4.2; this state corresponds to about ten times the critical pressure of the pure square-well fluid. The first- and second-order predictions obtained with

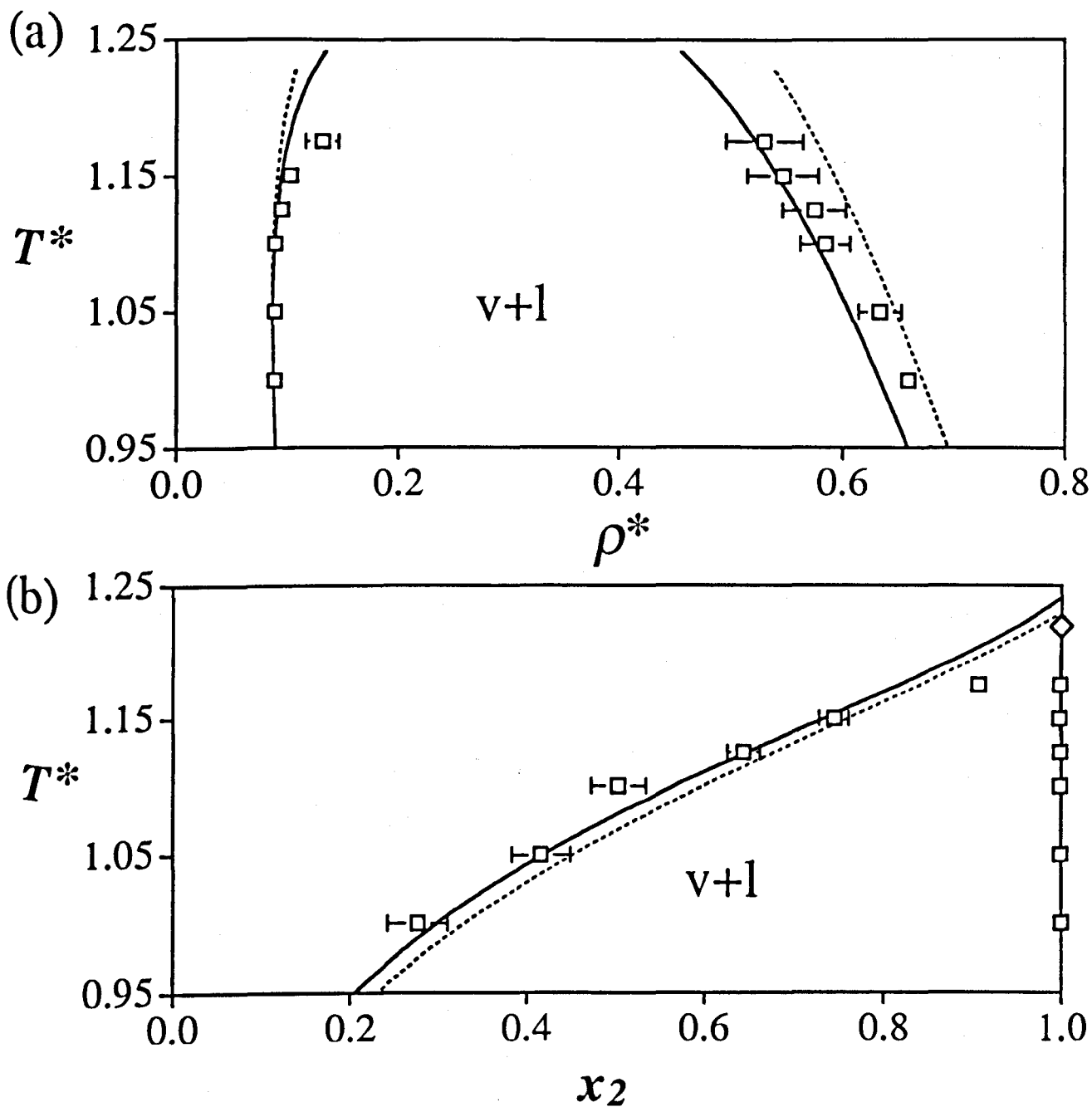


Figure 4.1: (a) Temperature-density and (b) temperature-composition slices of the vapour-liquid coexistence for the mixture of hard spheres (1) and square wells (2) with $\lambda = 1.5$ at a reduced pressure of $P^* = P\sigma^3/\epsilon = 0.1$; the reduced temperature is defined as $T^* = kT/\epsilon$, the reduced density as $\rho^* = \rho\sigma^3$, and x_2 refers to the mole fraction of square wells. The dotted and solid curves correspond to the first-order (a_1 term) and second-order (a_1 and a_2 terms) SAFT-VR predictions, respectively. The data points represent the results of the GEMC simulations [3]; the diamond in (b) corresponds to the critical point [7].

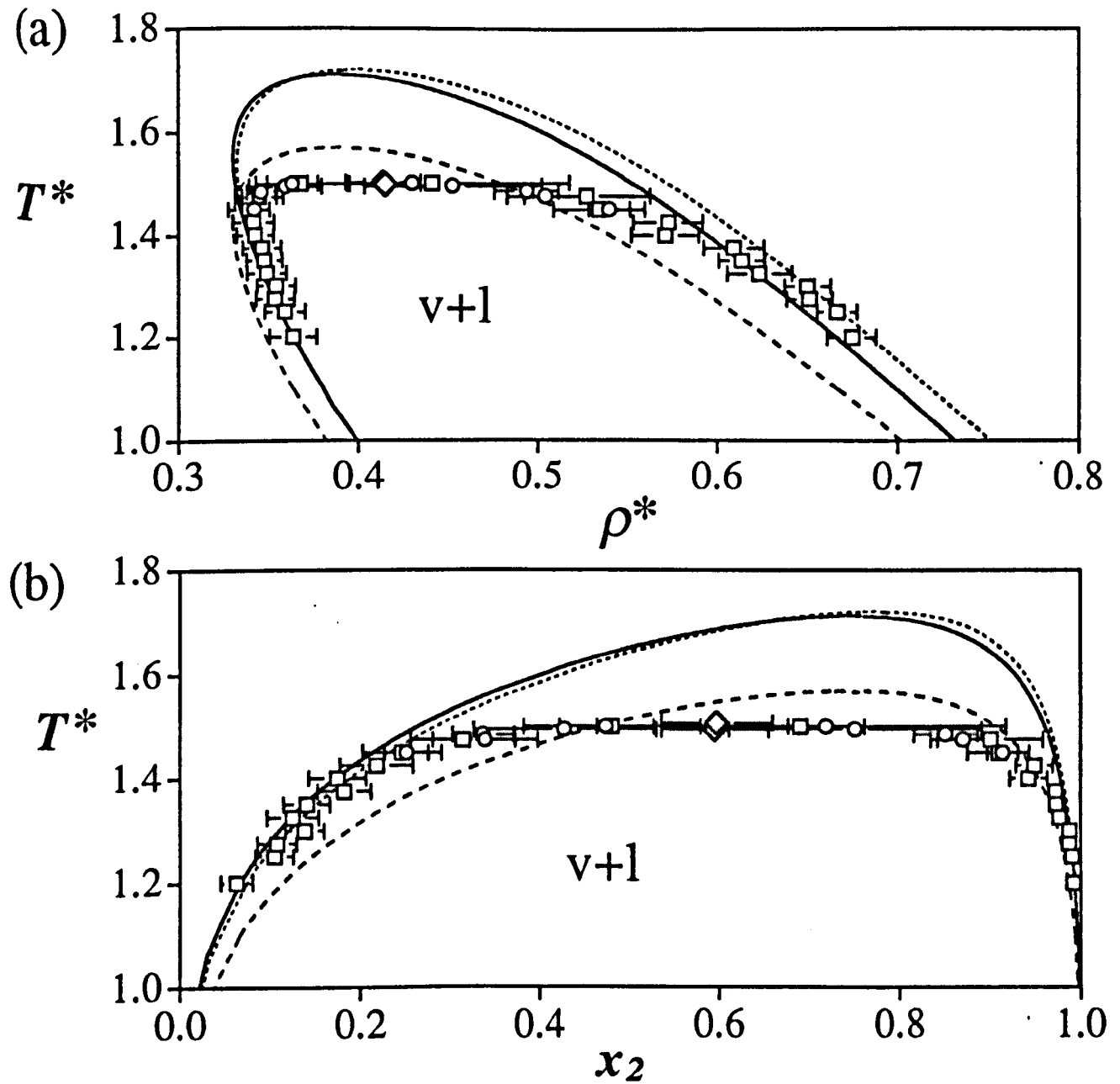


Figure 4.2: (a) Temperature-density and (b) temperature-composition slices of the vapour-liquid coexistence for the mixture of hard spheres (1) and square wells (2) with $\lambda = 1.5$ at a reduced pressure of $P^* = P\sigma^3/\epsilon = 1.0$. See Fig. 4.1 for details. The dashed curves represents the rescaled second-order SAFT-VR coexistence curves.

the SAFT-VR approach are again compared with the corresponding GEMC data. The SAFT-VR expressions provide an excellent representation of the coexisting densities and compositions for temperatures below the critical point. However, the theory leads to an overestimate of the critical temperature, a feature that it has in common with other analytical equations of state which possess classical critical exponents [23]. The SAFT-VR equation of state also leads to an overestimate of the vapour-liquid critical point of the pure component square-well fluid with $\lambda = 1.5$ [1]. In order to illustrate that the overestimate in the critical point of the mixture can be attributed almost entirely to that of the pure component, we rescale the second-order coexistence curves with the critical temperature of the pure fluid obtained from GEMC data (as $T_c^* = 1.219$ in Ref. [7]). From Figs. 4.2 (a) and (b) it is clear that this leads to a much improved representation of the critical region for the mixture at the detriment of the prediction of the coexistence curve at lower temperatures.

4.3.2 The binary square-well mixture

The liquid-liquid phase equilibria of a symmetrical binary mixture of square-well monomers is also examined. The segments are of equal diameter, $\sigma = \sigma_{11} = \sigma_{12} = \sigma_{22}$, the square-well interaction is of equal strength and range for both components, and no unlike interactions exist; $\varepsilon = \varepsilon_{11} = \varepsilon_{22} > 0$, $\varepsilon_{12} = 0$, $\lambda = \lambda_{11} = \lambda_{22} = 1.5$, and $\lambda_{12} = 1$. The phase behaviour of such a system has already been characterised [22, 4, 3, 5]: the principal feature of the phase behaviour is the large extent of liquid-liquid immiscibility at high pressures due to the absence of any unlike attractive interactions; at low pressures the phase equilibria is complicated by vapour-liquid-liquid three-phase coexistence. A temperature-composition Tx slice of the mixture at a pressure of $P^* = P\sigma^3/\varepsilon = 1.08$ is shown in Fig. 4.3; at this high pressure this system only exhibits liquid-liquid phase separation. The theoretical predictions obtained using the SAFT-VR approach with both the first- and second-order representation are compared with the corresponding GEMC simulation data [3]. The theory is seen to provide a good representation of the coexisting compositions for the liquid-liquid phase equilibria below the upper critical solution temperature (UCST). As with the vapour-liquid equilibria of the mixture of hard spheres and square wells, the SAFT-VR approach overestimates the critical point of the system due to the classical representation of the coexistence curve (quadratic rather than the flatter cubic dependence). We observe that by rescaling the second-order coexistence curve with respect to the pure component vapour-liquid critical point, a much better representation of the critical region is obtained. This again indicates that the principal inadequacy of our theoretical approach lies in the description of the critical point of the pure component rather than by any

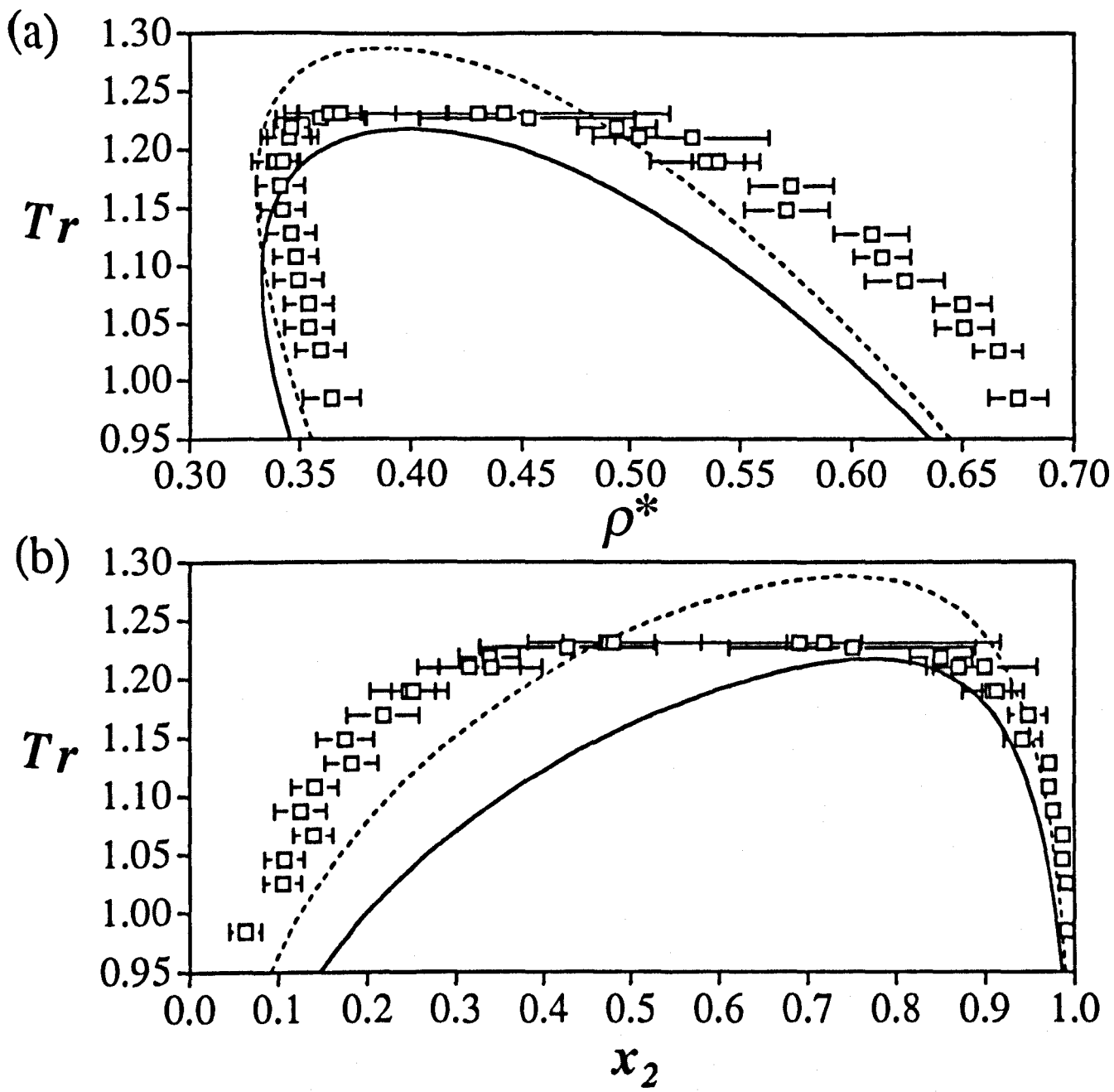


Figure 4.3: Temperature-composition slice of the liquid-liquid coexistence for the symmetrical mixture of square wells with $\lambda = 1.5$ at a reduced pressure of $P^* = P\sigma^3/\epsilon = 1.08$. See Fig. 4.1 for details. The dashed curve represents the rescaled second-order SAFT-VR coexistence curve.

incorrect representation of the mixture within the equation of state.

4.3.3 The square-well monomer-dimer mixture

The vapour-liquid equilibria of a binary square-well mixture of monomers (1) and dimers (2) with equal spherical diameters $\sigma = \sigma_{11} = \sigma_{12} = \sigma_{22}$ is the third system studied. The square-well interactions are defined, $\lambda = \lambda_{11} = \lambda_{12} = \lambda_{22} = 1.5$ and $\epsilon = \epsilon_{11} = \epsilon_{12} = \epsilon_{22}$. We use the same reduced variables as in the previous mixtures, $T^* = kT/\epsilon$ for the temperature and $P^* = P\sigma^3/\epsilon$ for the pressure. The mole fraction of monomers is $x_1 = N_1/N$ and of dimers is $x_2 = N_2/N$. No simulation data has been previously reported for the monomer-dimer mixture, so that it was necessary to undertake isothermal-isobaric NPT Gibbs ensemble Monte Carlo simulations [18, 19] in order to have data with which to compare the theoretical prediction.

The GEMC method is described in Chapter 3, so only brief details are presented here. Simulations are performed in cubic boxes, the particles in the vapour subsystem are initially arranged on a face-centred-cubic (fcc) lattice, while the higher density liquid configurations are obtained by compressing a single subsystem with a standard NPT Monte Carlo technique [24, 25]. The usual periodic boundary conditions and minimum image convention are used [25]. Initial guesses for the coexisting densities and compositions at each pressure and temperature state point are made by using the corresponding SAFT-VR solutions; one must always ensure that the overall composition of the system lies somewhere between the compositions of the two coexisting phases. The chemical potential was determined with the Widom test particle technique [26] as adapted to the GEMC approach [27], in order to ensure that phase equilibria is achieved during the simulation. The use of the NPT version of the Gibbs ensemble technique yields constant pressure slices of the phase diagram of the mixture by performing a series of simulation cycles. One cycle consists of N displacements/reorientations of a randomly selected particle in each subsystem (see Ref. [28]), one volume change for either subsystem, and a specific number of particle interchanges between subsystems (using the transfer algorithm of Ref. [18]). The maximum displacement and volume change are adjusted to give an acceptance ratio of between 30 and 40%, and the number of insertions is controlled so that between 1 and 3% of particles are interchanged each cycle. The majority of the simulations are performed with systems of $N = 512$ particles, but it is necessary to use $N = 1728$ particles in order to get closer to the critical line of the mixture. An initial simulation of 50,000 cycles is performed to equilibrate the subsystems, before averaging for between 100,000 and 250,000

cycles.

The phase behaviour of the mixture is summarised in Figs. 4.4 and 4.5, and the corresponding Gibbs ensemble data are reported in Tables 4.1 to 4.8

As will become clear later the simulation data obtained for the mixture can be used to estimate the vapour-liquid equilibria of each pure component fluid: the phase diagram of the square-well monomer is shown in Fig. 4.6 and that of the square-well dimer in Fig. 4.7, with the corresponding data given in Tables 4.9 and 4.10. A pressure-temperature projection of the full phase behaviour, including the pure component data is given in Fig. 4.8.

Table 4.1: Vapour-liquid coexistence data obtained from NPT Gibbs ensemble Monte Carlo simulations for a mixture of square-well monomers and dimers with a range $\lambda = 1.5$. The fixed variables during the simulation are the number of particles $N = 512$, the reduced pressure $P^* = P\sigma^3/\varepsilon$ and the reduced temperature $T^* = kT/\varepsilon = 1.00$. The packing fractions η , dimer mole fractions x_2 , and the reduced energies per segment $E^* = E/\varepsilon N_s$ in the coexisting vapour and liquid phases are labeled v and l , respectively; the uncertainties correspond to one standard deviation.

P^*	η_v	η_l	$x_{2,v}$	$x_{2,l}$	E_v^*	E_l^*
0.004	0.003±0.0002	0.395±0.004	0.313±0.015	0.873±0.015	-0.10±0.03	-5.29±0.06
0.007	0.004±0.0004	0.389±0.004	0.112±0.020	0.708±0.017	-0.13±0.03	-5.27±0.07
0.011	0.006±0.001	0.383±0.004	0.051±0.019	0.544±0.012	-0.09±0.04	-5.26±0.07
0.013	0.008±0.001	0.379±0.004	0.017±0.016	0.476±0.012	-0.14±0.04	-5.25±0.07
0.019	0.012±0.001	0.376±0.006	0.032±0.012	0.339±0.017	-0.30±0.06	-5.29±0.08
0.027	0.015±0.002	0.374±0.008	0.007±0.009	0.132±0.007	-0.19±0.06	-5.44±0.11
0.031	0.021±0.002	0.366±0.008	0.007±0.006	0.090±0.005	-0.44±0.09	-5.36±0.12

Pressure-composition (Px) constant temperature slices of the vapour-liquid phase diagram for the monomer-dimer mixture are shown in Figs. 4.4 and 4.5. The square-well dimer is the less volatile of the two components, and a slight negative deviation from Raoult's law can be detected. As the temperature is increased above the critical point of the pure monomer square-well fluid, vapour-liquid critical points are observed for the mixture. The SAFT-VR predictions are compared with the GEMC simulation data for a series of temperatures: four sub-critical with respect to the pure monomer fluid, one at the estimated vapour-liquid critical temperature of the monomer ($T_{c,1}^* = 1.22$ and $P_{c,1}^* = 0.108$) [7]; and three temperatures above the monomer critical point. Very good agreement between the

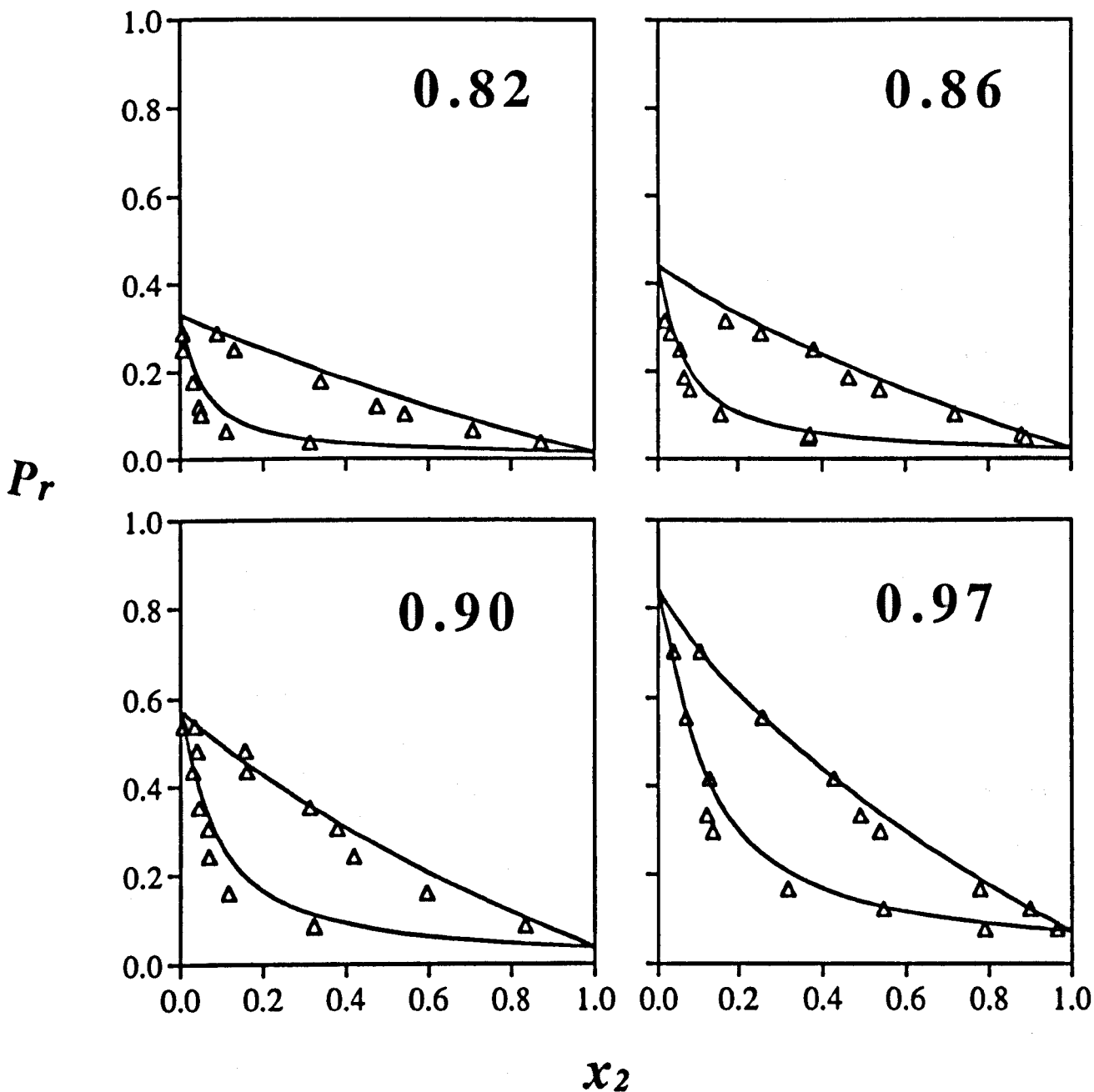


Figure 4.4: Pressure-composition slices of the vapour-liquid coexistence for the square-well mixture of monomers (1) and dimers (2) with $\lambda = 1.5$ for temperatures below the critical point of the pure monomer system. The reduced pressure $P_r = P^*/P_{c,1}^*$ is defined in terms of the critical point of the monomer, and x_2 is the mole fraction of dimers. The curves are labelled with their corresponding values of the reduced temperature $T_r = T^*/T_{c,1}^*$. The data points represent the results of the GEMC simulations for systems of $N = 512$ particles, and the continuous curves correspond to the SAFT-VR prediction.

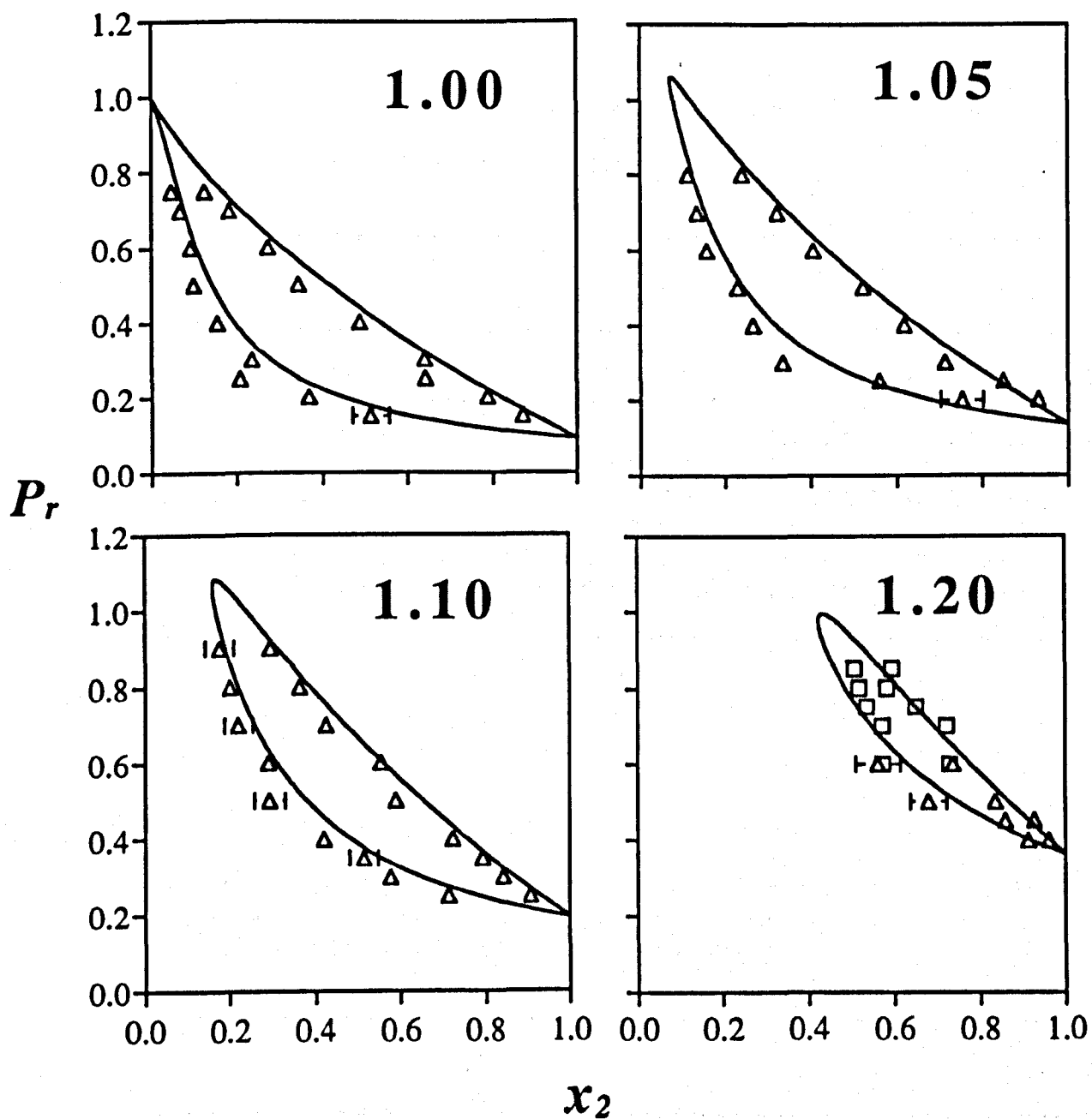


Figure 4.5: Pressure-composition slices of the vapour-liquid coexistence for the square-well mixture of monomers (1) and dimers (2) with $\lambda = 1.5$ for temperatures above the critical point of the pure monomer system. monomer. See Fig. 4.4 for details. The squares correspond to GEMC data for a system of $N = 1728$ particles.

Table 4.2: Vapour-liquid coexistence data obtained from NPT Gibbs ensemble Monte Carlo simulations for a mixture of square-well monomers and dimers at a reduced temperature of $T^* = 1.05$. See Table 4.1 for details.

P^*	η_v	η_l	$x_{2,v}$	$x_{2,l}$	E_v^*	E_l^*
0.005	0.004 ± 0.0003	0.388 ± 0.004	0.366 ± 0.020	0.892 ± 0.015	-0.12 ± 0.03	-5.17 ± 0.06
0.006	0.004 ± 0.0003	0.390 ± 0.005	0.371 ± 0.017	0.880 ± 0.017	-0.15 ± 0.03	-5.19 ± 0.08
0.011	0.007 ± 0.001	0.384 ± 0.004	0.159 ± 0.020	0.719 ± 0.017	-0.20 ± 0.04	-5.17 ± 0.07
0.017	0.010 ± 0.001	0.376 ± 0.004	0.083 ± 0.017	0.539 ± 0.012	-0.23 ± 0.05	-5.14 ± 0.07
0.020	0.012 ± 0.001	0.371 ± 0.005	0.067 ± 0.017	0.464 ± 0.017	-0.30 ± 0.05	-5.12 ± 0.08
0.027	0.018 ± 0.002	0.370 ± 0.004	0.057 ± 0.020	0.380 ± 0.010	-0.47 ± 0.10	-5.17 ± 0.07
0.031	0.020 ± 0.002	0.360 ± 0.006	0.032 ± 0.013	0.255 ± 0.014	-0.47 ± 0.08	-5.12 ± 0.09
0.034	0.022 ± 0.002	0.355 ± 0.006	0.018 ± 0.010	0.172 ± 0.011	-0.54 ± 0.09	-5.11 ± 0.09

Table 4.3: Vapour-liquid coexistence data obtained from NPT Gibbs ensemble Monte Carlo simulations for a mixture of square-well monomers and dimers at a reduced temperature of $T^* = 1.10$. See Table 4.1 for details.

P^*	η_v	η_l	$x_{2,v}$	$x_{2,l}$	E_v^*	E_l^*
0.009	0.006 ± 0.001	0.377 ± 0.004	0.322 ± 0.023	0.834 ± 0.017	-0.19 ± 0.04	-5.00 ± 0.08
0.017	0.010 ± 0.001	0.365 ± 0.005	0.117 ± 0.021	0.596 ± 0.015	-0.25 ± 0.05	-4.94 ± 0.07
0.026	0.016 ± 0.002	0.355 ± 0.006	0.069 ± 0.017	0.419 ± 0.013	-0.40 ± 0.07	-4.91 ± 0.09
0.033	0.022 ± 0.002	0.359 ± 0.006	0.067 ± 0.015	0.378 ± 0.013	-0.55 ± 0.09	-4.99 ± 0.09
0.038	0.021 ± 0.002	0.357 ± 0.006	0.045 ± 0.018	0.312 ± 0.010	-0.23 ± 0.07	-5.00 ± 0.09
0.047	0.038 ± 0.008	0.345 ± 0.007	0.030 ± 0.018	0.160 ± 0.009	-0.95 ± 0.26	-4.96 ± 0.11
0.052	0.050 ± 0.009	0.342 ± 0.006	0.040 ± 0.013	0.156 ± 0.008	-1.33 ± 0.28	-4.93 ± 0.09
0.058	0.051 ± 0.007	0.341 ± 0.013	0.007 ± 0.007	0.035 ± 0.003	-1.26 ± 0.22	-5.02 ± 0.18

Table 4.4: Vapour-liquid coexistence data obtained from NPT Gibbs ensemble Monte Carlo simulations for a mixture of square-well monomers and dimers at a reduced temperature of $T^* = 1.18$. See Table 4.1 for details.

P^*	η_v	η_l	$x_{2,v}$	$x_{2,l}$	E_v^*	E_l^*
0.008	0.007±0.001	0.368±0.005	0.790±0.015	0.966±0.008	-0.24±0.05	-4.80±0.07
0.013	0.011±0.001	0.370±0.005	0.547±0.017	0.900±0.015	-0.32±0.06	-4.89±0.08
0.018	0.012±0.001	0.361±0.005	0.317±0.024	0.778±0.017	-0.24±0.05	-4.77±0.08
0.032	0.019±0.002	0.368±0.006	0.139±0.022	0.539±0.017	-0.29±0.06	-4.71±0.09
0.036	0.022±0.002	0.348±0.007	0.124±0.018	0.491±0.016	-0.51±0.07	-4.66±0.10
0.045	0.032±0.004	0.343±0.007	0.131±0.019	0.429±0.018	-0.80±0.13	-4.70±0.11
0.060	0.047±0.005	0.328±0.010	0.072±0.013	0.258±0.020	-1.11±0.15	-4.61±0.14
0.076	0.077±0.012	0.306±0.010	0.039±0.014	0.108±0.008	-1.68±0.27	-4.45±0.14

Table 4.5: Vapour-liquid coexistence data obtained from NPT Gibbs ensemble Monte Carlo simulations for a mixture of square-well monomers and dimers at a reduced temperature of $T^* = 1.22$. See Table 4.1 for details.

P^*	η_v	η_l	$x_{2,v}$	$x_{2,l}$	E_v^*	E_l^*
0.016	0.013±0.001	0.357±0.006	0.513±0.044	0.827±0.018	-0.35±0.07	-4.67±0.08
0.022	0.015±0.002	0.354±0.006	0.368±0.028	0.788±0.017	-0.39±0.08	-4.65±0.08
0.027	0.016±0.002	0.336±0.007	0.209±0.028	0.644±0.018	-0.36±0.07	-4.48±0.09
0.032	0.022±0.002	0.345±0.007	0.236±0.029	0.642±0.022	-0.54±0.10	-4.59±0.10
0.043	0.029±0.004	0.333±0.008	0.155±0.023	0.488±0.023	-0.69±0.12	-4.51±0.11
0.054	0.036±0.005	0.316±0.010	0.099±0.022	0.345±0.021	-0.82±0.14	-4.38±0.13
0.065	0.052±0.007	0.314±0.009	0.091±0.019	0.274±0.016	-1.15±0.19	-4.40±0.13
0.076	0.067±0.018	0.299±0.010	0.066±0.022	0.183±0.010	-1.41±0.35	-4.26±0.13
0.081	0.071±0.010	0.285±0.014	0.046±0.018	0.125±0.010	-1.48±0.32	-4.14±0.17

Table 4.6: Vapour-liquid coexistence data obtained from NPT Gibbs ensemble Monte Carlo simulations for a mixture of square-well monomers and dimers at a reduced temperature of $T^* = 1.28$. See Table 4.1 for details.

P^*	η_v	η_l	$x_{2,v}$	$x_{2,l}$	E_v^*	E_l^*
0.022	0.023±0.005	0.353±0.005	0.753±0.050	0.931±0.011	-0.65±0.19	-4.56±0.07
0.027	0.023±0.003	0.346±0.006	0.561±0.032	0.850±0.016	-0.62±0.11	-4.50±0.09
0.032	0.023±0.002	0.331±0.008	0.336±0.029	0.715±0.019	-0.55±0.10	-4.36±0.10
0.043	0.031±0.003	0.327±0.009	0.266±0.032	0.619±0.018	-0.71±0.12	-4.35±0.12
0.054	0.041±0.005	0.320±0.009	0.230±0.025	0.523±0.023	-0.94±0.14	-4.30±0.12
0.065	0.046±0.005	0.304±0.011	0.159±0.022	0.407±0.019	-1.00±0.13	-4.15±0.14
0.076	0.062±0.011	0.294±0.012	0.136±0.026	0.322±0.018	-1.30±0.24	-4.08±0.15
0.085	0.080±0.020	0.277±0.015	0.114±0.030	0.241±0.014	-1.60±0.36	-4.93±0.18

Table 4.7: Vapour-liquid coexistence data obtained from NPT Gibbs ensemble Monte Carlo simulations for a mixture of square-well monomers and dimers at a reduced temperature of $T^* = 1.34$. See Table 4.1 for details.

P^*	η_v	η_l	$x_{2,v}$	$x_{2,l}$	E_v^*	E_l^*
0.027	0.025±0.003	0.329±0.008	0.713±0.028	0.907±0.012	-0.64±0.12	-4.23±0.10
0.032	0.028±0.003	0.325±0.008	0.577±0.030	0.842±0.016	-0.69±0.12	-4.21±0.10
0.038	0.033±0.005	0.324±0.007	0.514±0.034	0.793±0.017	-0.79±0.15	-4.21±0.10
0.043	0.035±0.004	0.316±0.009	0.420±0.027	0.723±0.020	-0.79±0.13	-4.13±0.11
0.054	0.040±0.006	0.296±0.010	0.294±0.036	0.590±0.018	-0.85±0.15	-3.95±0.12
0.065	0.051±0.006	0.299±0.012	0.292±0.028	0.555±0.020	-1.08±0.16	-3.99±0.14
0.076	0.066±0.011	0.280±0.015	0.221±0.033	0.426±0.019	-1.34±0.23	-3.83±0.17
0.086	0.077±0.012	0.266±0.018	0.201±0.030	0.364±0.018	-1.51±0.24	-3.71±0.20
0.097	0.088±0.025	0.235±0.039	0.177±0.034	0.297±0.003	-1.69±0.40	-3.43±0.41

Table 4.8: Vapour-liquid coexistence data obtained from NPT Gibbs ensemble Monte Carlo simulations for a mixture of square-well monomers and dimers at a reduced temperature of $T^* = 1.46$. See Table 4.1 for details. Results labeled with a † are obtained using $N = 1728$ particles.

P^*	η_v	η_l	$x_{2,v}$	$x_{2,l}$	E_v^*	E_l^*
0.043	0.056 ± 0.012	0.293 ± 0.011	0.914 ± 0.020	0.962 ± 0.007	-1.17 ± 0.26	-3.73 ± 0.13
0.049	0.071 ± 0.009	0.292 ± 0.012	0.861 ± 0.015	0.928 ± 0.012	-1.47 ± 0.17	-3.72 ± 0.14
0.054	0.056 ± 0.010	0.274 ± 0.012	0.681 ± 0.042	0.837 ± 0.013	-1.12 ± 0.22	-3.56 ± 0.13
0.065	0.060 ± 0.013	0.240 ± 0.016	0.563 ± 0.052	0.738 ± 0.014	-1.17 ± 0.26	-3.25 ± 0.16
0.065†	0.070 ± 0.004	0.250 ± 0.013	0.575 ± 0.015	0.731 ± 0.013	-1.40 ± 0.08	-3.35 ± 0.13
0.076†	0.077 ± 0.004	0.254 ± 0.010	0.573 ± 0.013	0.723 ± 0.011	-1.51 ± 0.08	-3.39 ± 0.10
0.081†	0.101 ± 0.012	0.235 ± 0.019	0.537 ± 0.024	0.651 ± 0.015	-1.86 ± 0.20	-3.23 ± 0.18
0.086†	0.122 ± 0.017	0.197 ± 0.034	0.519 ± 0.024	0.583 ± 0.027	-2.13 ± 0.22	-2.90 ± 0.32
0.092†	0.113 ± 0.011	0.212 ± 0.024	0.508 ± 0.020	0.595 ± 0.017	-2.01 ± 0.15	-3.04 ± 0.22

Table 4.9: Values of the reduced temperature $T^* = kT/\epsilon$, the reduced vapour pressure $P^* = P\sigma^3/\epsilon$ and the packing fractions η for the vapour-liquid coexistence of the pure square-well monomer fluid with a range $\lambda = 1.5$. The results are obtained by extrapolating the monomer-dimer mixture simulation data (see text for details). The vapour and liquid densities are denoted by v and l , respectively.

T^*	P^*	η_v	η_l
1.18	0.086	0.055	0.283
1.10	0.061	0.046	0.306
1.05	0.040	0.220	0.318
1.00	0.034	0.016	0.332

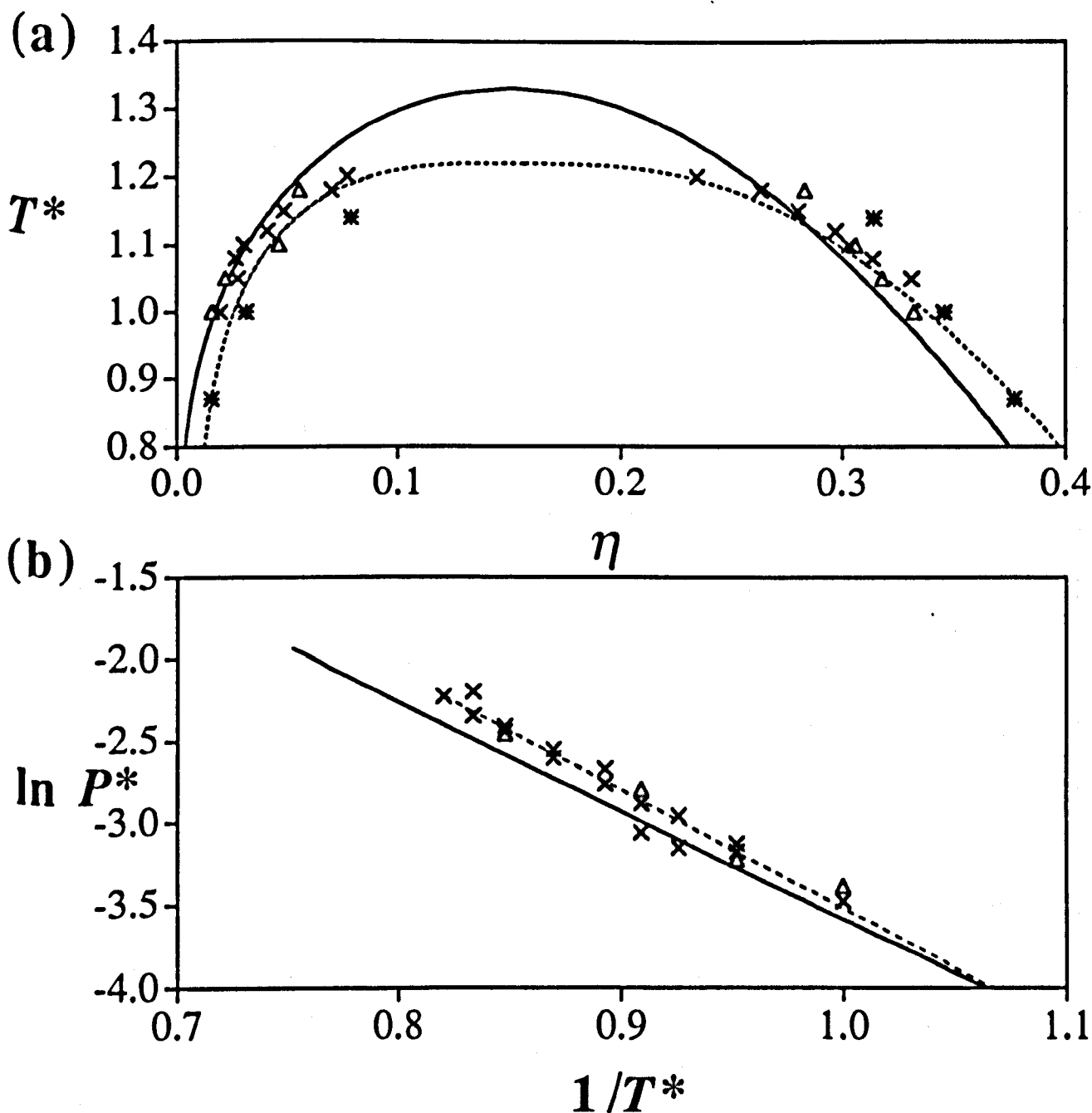


Figure 4.6: (a) Vapour-liquid coexistence densities for the monomer square-well system with $\lambda = 1.5$, where $T^* = kT/\epsilon$, and $\eta = \pi\rho_s\sigma^3/6$ is the packing fraction. The triangles correspond to the results obtained by extrapolating the mixture GEMC data, the crosses correspond to the GEMC data of Ref. [7], and the asterisks to the molecular dynamics data of Ref. [6]. The continuous curve represents the SAFT-VR prediction and the dashed curve to the Wegner expansion used in Ref. [7]. (b) Clausius-Clapeyron representation of the vapour pressures for the monomer fluid. The reduced pressure is defined as $P^* = P\sigma^3/\epsilon$. The continuous line is the SAFT-VR prediction and the dashed line corresponds to the fit obtained in Ref. [7].

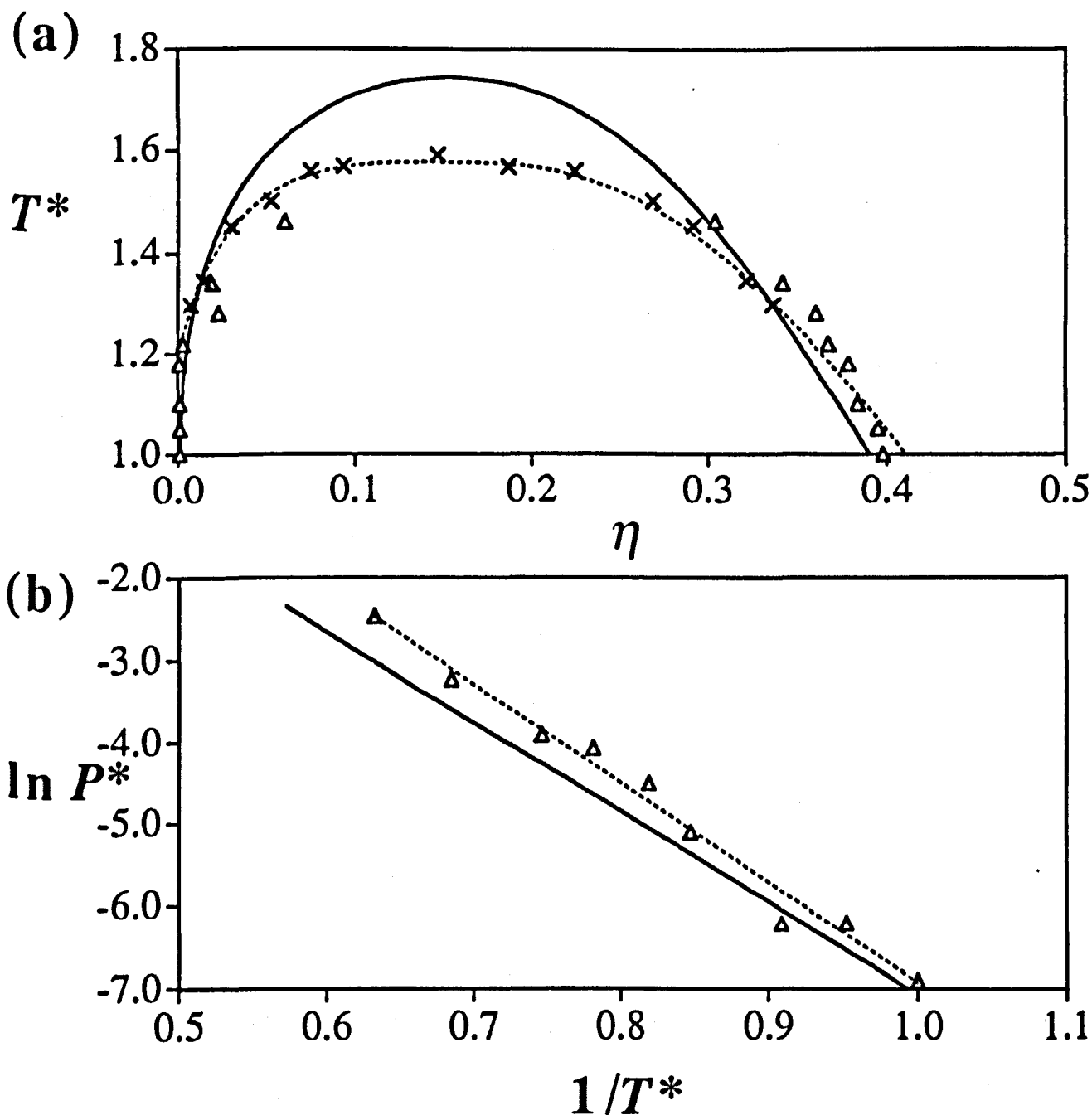


Figure 4.7: (a) Vapour-liquid coexistence densities for the dimer square-well system with $\lambda = 1.5$ (see Fig. 4.6 for details). The crosses correspond to the Monte Carlo simulation data of Ref. [8]. The dashed curve is obtained by fitting a Wegner expansion to the simulation data of Ref. [8]. (b) Clausius-Clapeyron representation of the vapour pressures for the dimer fluid. The continuous line is the SAFT-VR prediction and the dashed line corresponds to a linear fit of the simulation data.

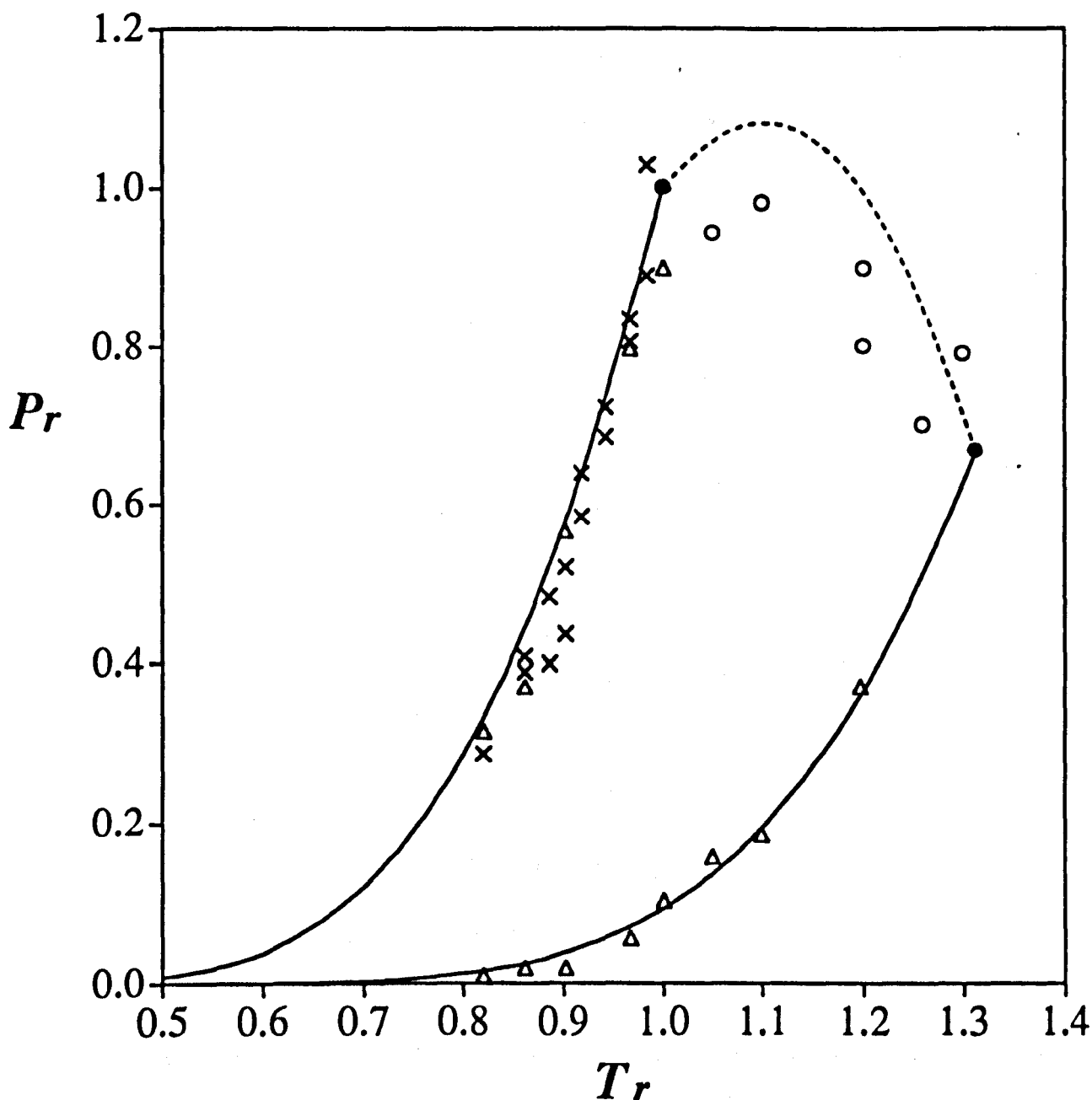


Figure 4.8: Pressure-temperature projection for the binary mixture of square-well monomers and dimers. The reduced pressure $P_r = P^*/P_{c,1}^*$ and temperature $T_r = T^*/T_{c,1}^*$ are defined in terms of the critical point of the monomers. The triangles are the vapour pressures obtained by extrapolating the mixture GEMC data, the crosses are the GEMC data of Ref. [7], the circles correspond to the estimated vapour-liquid critical points, and the filled circles are the pure component critical points. The continuous and dashed curves represent the SAFT-VR prediction for the pure component vapour pressures and the critical line of the mixture, respectively.

Table 4.10: Values of the reduced temperature $T^* = kT/\varepsilon$, the reduced vapour pressure $P^* = P\sigma^3/\varepsilon$ and the packing fractions η for the vapour-liquid coexistence of the pure square-well dimer fluid with a range $\lambda = 1.5$. The results are obtained by extrapolating the monomer-dimer mixture simulation data (see text for details). The vapour and liquid densities are denoted by v and l , respectively.

T^*	P^*	η_v	η_l
1.46	0.040	0.060	0.304
1.34	0.020	0.019	0.342
1.28	0.017	0.023	0.361
1.22	0.011	0.003	0.368
1.18	0.006	≤ 0.001	0.379
1.10	0.002	≤ 0.001	0.384
1.05	0.002	≤ 0.001	0.395
1.00	0.001	≤ 0.001	0.398

theoretical predictions and the exact simulation data are observed for all temperatures studied. The comparisons have been made in terms of the reduced pressure and temperature with respect to the pure square-well monomer, $P_r = P^*/P_{c,1}^*$ and $T_r = T^*/T_{c,1}^*$. As has been mentioned previously for the other mixtures studied, the vapour-liquid critical point of the pure monomer square-well fluid is overestimated by the theory. By viewing the phase behaviour of the monomer-dimer mixture in terms of reduced variables, we can again focus on the adequacy of the theoretical prediction for the mixture, without including the poor description of the pure component critical point.

Our monomer-dimer simulation data can be used to estimate the vapour-liquid coexistence of the individual components. We extrapolate the mixture Px data, using a linear Raoult's law dependence close to the $x_2 = 0$ and $x_2 = 1$ axes, to estimate values of the pure component vapour pressures for the monomer and dimer, respectively. An extrapolation of the temperature-density data for the mixture is used to estimate the coexisting densities of the pure components. The large curvature of the data close to the pure monomer axes ($x_2 = 0$) made a linear extrapolation unsuitable; the SAFT-VR theory for the mixture was used to guide the extrapolation in this case. The resulting estimates of the vapour-liquid equilibria for the pure component monomer and dimer systems are reported in Tables 4.9 and 4.10, respectively. The coexisting densities and vapour pressures (represented as Clausius-Clapeyron plots) are compared with the previous results in Figs. 4.6 and 4.7. It is gratifying to see that the extrapolation of the mixture data leads to values which are in close agreement with the previous data. As an

added bonus we can estimate the coexistence curve of the square-well dimer to much lower temperatures, and provide values for the vapour pressures which were not determined in the earlier work of Ref. [8]. Also shown on these figures are the SAFT-VR predictions of the vapour-liquid phase equilibria for both the pure components and the mixture. It has already been demonstrated that the SAFT-VR approach provides a good description of the phase envelope of the pure component monomer and dimer square-well systems [1], which is again apparent from an inspection of Figs. 4.6 and 4.7. In addition we show a comparison of the SAFT-VR predictions for the vapour pressures of the pure components with the simulated values: good agreement is again observed, although a slight underestimate is found. The SAFT-VR approach is known to overpredict the coexistence curve in the critical region, so that both the critical temperature and pressure of the model system occur at lower values than predicted by the SAFT-VR approach. The usual methodology for the determination of the critical parameters from Gibbs ensemble simulation data is from an appropriate critical expansion (e.g., see Refs. [7, 3] and Chapter 6). The coexistence curves obtained from a fit to the data using a Wegner expansion with a fixed critical exponent of $\beta = 0.325$, and the fit of the vapour-pressure curves using a Clausius-Clapeyron plot are also shown in Figs. 4.6 and 4.7. The corresponding estimates for the critical parameters are $T_{c,1}^* = 1.22$, $P_{c,1}^* = 0.108$, and $\eta_{c,1} = 0.157$ for the monomer of Ref. [7], and $T_{c,2}^* = 1.58$, $P_{c,1}^* = 0.085$, and $\eta_{c,1} = 0.147$ for the dimer; the latter are in good agreement with the estimates of $T_{c,2}^* = 1.59$ and $\eta_{c,2} = 0.14$ of Yethiraj and Hall in Ref. [8], but $P_{c,2}^* = 0.085$ is a new estimate for the critical pressure of the square-well dimer.

The critical points of mixtures can also be obtained by analysing the simulation data using a Wegner expansion (see Ref. [3] for details). In our case an expansion including the first extension to scaling term was used to estimate the critical points at constant temperature; and a simple extrapolation was used to obtain the critical temperature from the constant pressure slices. Due to the limited amount of simulation data close to the critical region only crude estimates of the vapour-liquid critical points could be made. The resulting vapour-liquid critical line of the monomer-dimer mixture is presented as a pressure-temperature PT projection in Fig. 4.8, together with the vapour-pressure curves of the two pure components. The vapour-liquid critical line is continuous and extends from the critical point of the pure component monomer to that of the dimer. There is no liquid-liquid immiscibility in this system due to the similarity in the attractive interactions. This type of vapour-liquid equilibria corresponds to type I in the classification of Scott and van Konynenburg [29, 30]. The vapour-liquid critical line of our monomer-dimer mixture obtained by extrapolation of the simulation data for the mixture also exhibits a maximum in pressure, a feature which is reproduced by the SAFT-VR predictions. As was mentioned earlier, the SAFT-VR theory is

seen to provide an excellent description of the vapour-pressure curves for both the monomers and dimers. The critical points estimated from the GEMC coexistence data are seen to deviate from the predicted critical line, although a large amount of scatter is evident.

4.4 Conclusions

The SAFT-VR equation of state is shown to be successful in its application to three mixtures of square-well monomers and dimers of equal diameter but with extreme values of the attractive interactions. The vapour-liquid equilibria of mixture of hard spheres and square wells, the liquid-liquid equilibria of a symmetrical mixture of square wells, and the vapour-liquid equilibria of a monomer-dimer square-well mixture predicted with the SAFT-VR equation of state are all shown to compare favourably with computer simulation data away from the critical region. The inadequacy of the SAFT-VR theory in describing the critical behaviour is a feature common to equations of state which are based on analytical expressions for the free energy, and near-critical corrections are possible although rather complex [31]. This work is essentially a test of the fundamental description of the range-dependence of the mixture expressions in terms of their pure-fluid counterparts, and of the adequacy of the SAFT-VR approach to describe the thermodynamics of model mixtures which consist of chain molecules. The pressure-composition slices of the phase diagram of the square-well monomer-dimer mixture obtained using the Gibbs ensemble technique indicate that there exists a small negative deviation from Raoult's law in this system. This non-ideality can be attributed entirely to the difference in chain length in this mixture since all the other intermolecular parameters such as the diameter and the range and depth of the square-well, are equal for both components. It is also shown that reasonable estimates of the pure component phase equilibria can be obtained by extrapolating the simulation data for the mixture.

Bibliography

- [1] A. Gil-Villegas, A. Galindo, P. J. Whitehead, S. J. Mills, G. Jackson, and A. N. Burgess, *J. Chem. Phys.*, **106**, 4168 (1997).
- [2] A. Galindo, L. A. Davies, A. Gil-Villegas, and G. Jackson, *Mol. Phys.*, in press (1997).
- [3] D. G. Green, G. Jackson, E. de Miguel, and L. F. Rull, *J. Chem. Phys.*, **101**, 3190 (1994).
- [4] J. R. Recht and A. Z. Panagiotopoulos, *Mol. Phys.*, **80**, 843 (1993).
- [5] E. de Miguel, *Phys. Rev. E*, **55**, 1347 (1997).
- [6] G. A. Chapela, S. E. Martínez-Casas, and C. Varea. *J. Chem. Phys.*, **86**, 5683 (1987).
- [7] L. Vega, E. de Miguel, L. F. Rull, G. Jackson, and I. A. McLure, *J. Chem. Phys.*, **96**, 2296 (1992).
- [8] A. Yethiraj and C. K. Hall, *Mol. Phys.*, **72**, 619 (1991).
- [9] L. L. Lee, *Molecular Thermodynamics of Nonideal Fluids* Butterworth Scientific, (1988).
- [10] J. A. Barker and D. Henderson, *J. Chem. Phys.*, **47**, 2856 (1967).
- [11] J. A. Barker and D. Henderson, *J. Chem. Phys.*, **47**, 4714 (1967).
- [12] J. A. Barker and D. Henderson, *Rev. Mod. Phys.*, **48**, 587 (1976).
- [13] T. Boublík, *J. Chem. Phys.*, **53**, 471 (1970).
- [14] G. A. Mansoori, N. F. Carnahan, K. E. Starling, and T. W. Leland, *J. Chem. Phys.*, **54**, 1523 (1971).
- [15] N. F. Carnahan and K. E. Starling, *J. Chem. Phys.*, **51**, 635 (1969).
- [16] T. M. Reed and K. E. Gubbins, *Applied Statistical Mechanics* McGraw-Hill, (1973).

- [17] W. H. Press, B. P. Flannery, S. A. Teukolsky, and W. T. Vetterling, *Numerical Recipes*, second edition Cambridge University Press, (1992).
- [18] A. Z. Panagiotopoulos, *Mol. Phys.*, **61**, 813 (1987).
- [19] A. Z. Panagiotopoulos, N. Quirke, M. R. Stapleton, and D. J. Tildesley, *Mol. Phys.*, **63**, 527 (1988).
- [20] M. Rigby, B. J. Alder, A. M. Sapse, and C. E. Hecht, *J. Chem. Phys.*, **52**, 3665 (1970).
- [21] G. Jackson, J. S. Rowlinson, and C. A. Leng, *J. Chem. Soc., Faraday Trans. 1*, **82**, 3461 (1986).
- [22] G. Jackson, *Mol. Phys.*, **72**, 1365 (1991).
- [23] H. E. Stanley, *Introduction to Phase Transitions and Critical Phenomena* Oxford University Press, (1987).
- [24] W. W. Wood, *J. Chem. Phys.*, **48**, 415 (1968).
- [25] M. P. Allen and D. J. Tildesley, *Computer Simulations of Liquids*, Clarendon Press, (1987).
- [26] B. Widom, *J. Chem. Phys.*, **39**, 2808 (1963).
- [27] B. Smit and D. Frenkel, *Mol. Phys.*, **68**, 951 (1989).
- [28] A. L. Archer and G. Jackson, *Mol. Phys.*, **73**, 881 (1991).
- [29] P. H. van Konynenburg and R. L. Scott, *Phil. Trans.*, **A298**, 495 (1980).
- [30] J. S. Rowlinson and F. L. Swinton, *Liquids and Liquid Mixtures*, third edition Butterworth Scientific, (1982).
- [31] A. Van Pelt, G. X. Jin, and J. V. Sengers, *Int. J. Thermophys.*, **15**, 687 (1994).

Chapter 5

Examination of the the phase behaviour of Yukawa and soft-core fluids using the SAFT-VR approach

5.1 Introduction

In the previous chapter we have shown that a version of the statistical associating fluid theory for spheres interacting via attractive wells of variable range (SAFT-VR) [1, 2], gives an accurate prediction of the thermodynamic properties of model fluid mixtures. More specifically, we have examined mixtures consisting of hard-spheres, square-well monomers, and square-well dimers. Within the SAFT-VR framework, the range of the interaction potential is a useful quantity in the description of experimental systems since it accounts for the non-conformal behaviour present in liquids and their mixtures [3]. In addition, the SAFT-VR theory comprises a compact representation of the monomer properties, in the framework of the Barker and Henderson perturbation theory for simple liquids [4]-[6]. Two major advantages of the SAFT approach are: that the equation of state is obtained from the properties of the constituent monomeric segments, and that each one of the terms can be directly compared with, and tested against, molecular simulation

results.

In this chapter we describe the application of the SAFT-VR methodology to the Yukawa and Sutherland potentials and also present a further extension of the SAFT-VR approach to describe the properties of chain molecules which are formed from soft-core segments with variable repulsive and attractive ranges. We illustrate the effectiveness of the SAFT-VR equation of state in the description of the properties of the Yukawa fluid via a comparison with integral equation theories. We demonstrate that the analytical expressions developed previously for the Sutherland potential [1] together with a Barker and Henderson effective hard-sphere diameter [6] can be used to account for potentials of variable attractive and repulsive ranges in the SAFT-VR framework. As specific applications, we present equations of state for Lennard-Jones chain (LJC) molecules. These system has been studied extensively in the past, and a number of accurate equations of state have been reported [7]-[11]. Our main goal is to show that the SAFT-VR methodology provides a simple and compact equation of state for systems interacting via more realistic potentials such as the Lennard-Jones model which is valid for ranges of density and temperature of practical interest.

We will first summarise the SAFT-VR equation of state for pure hard-core systems interacting with the Yukawa and the Sutherland- λ potentials. The Yukawa fluid is of particular theoretical interest since the nature of the potential allows for the exact solution of certain integral equations, such as the mean spherical approximation (MSA) of the model. These solutions can be readily used in a comparison of the adequacy of any other theoretical approach for the description of the Yukawa fluid properties. The SAFT-VR equation of state for the Sutherland potential is used as a model to obtain a general equation of state for the Mie $m - n$ family of potentials [12, 13], of which the Lennard-Jones potential is a specific case ($m = 6$ and $n = 12$). We also present a simple recipe for the calculation of the free energy due to chain formation, and the prediction of LJC properties are compared with simulation results.

5.2 SAFT-VR for pure fluids

As has been shown previously, the Helmholtz free energy of associating chain molecules is described in the SAFT-VR approach as

$$\frac{A}{NkT} = \frac{A^{IDEAL}}{NkT} + \frac{A^{MONO.}}{NkT} + \frac{A^{CHAIN}}{NkT} + \frac{A^{ASSOC.}}{NkT}, \quad (5.1)$$

where the different terms in this equation correspond to the contributions to the free energy due to the ideal fluid, the monomer segments, chain formation and intermolecular association, respectively. In this chapter will only present the SAFT-VR expressions for the pure fluid.

The free energy of an ideal gas is given by [14]

$$\frac{A^{IDEAL}}{NkT} = \ln(\rho\Lambda^3) - 1, \quad (5.2)$$

where $\rho = N/V$ is the number density of chain molecules and not of monomer segments. A separate treatment of this term renders all the other terms residual free energies.

The general form of the monomer-monomer interaction is given by a hard-sphere repulsive term plus an attractive well:

$$u^M(r; \sigma, \epsilon, \lambda) = \begin{cases} \infty & \text{if } r < \sigma \\ -\epsilon\phi(r; \lambda) & \text{if } r > \sigma, \end{cases} \quad (5.3)$$

where σ is the spherical hard-core diameter, while ϵ , ϕ and λ are, the depth, the shape and the range parameter of the attractive well, respectively.

The contribution to the free energy due to the monomers (m of which make up each chain molecule) interacting with a potential of the form given in Eq. (5.3) is

$$\begin{aligned} \frac{A^{MONO.}}{NkT} &= m_s \frac{A^M}{N_s kT} \\ &= m_s a^M, \end{aligned} \quad (5.4)$$

where N_s is the total number of spherical monomers, and $a^M = A^M/(N_s kT)$ is the excess Helmholtz free energy per monomer segment. An accurate description of a^M is obtained from the high-temperature expansion given by the Barker and Henderson perturbation theory for hard-core systems [4, 5, 6],

$$a^M = a^{HS} + \beta a_1 + \beta^2 a_2, \quad (5.5)$$

where $\beta = 1/kT$, and a_1 and a_2 are the first two perturbation terms associated with the attractive well. The mean-attractive energy a_1 is given by [6]

$$a_1 = -2\pi\rho_s\epsilon \int_{\sigma}^{\infty} r^2 \phi(r) g^{HS}(r) dr, \quad (5.6)$$

where $\rho_s = N_s/V$ is the density of monomers (segments) and $g^{HS}(r)$ is the radial distribution function of the hard-sphere reference system. By using the mean-value

theorem, $g^{HS}(r)$ can be factorised from the integral and written in terms of its contact value $g^{HS}(1; \eta_{eff})$, at an effective packing fraction η_{eff} , and the van der Waals mean-field term a_1^{VDW} [1]:

$$a_1 = a_1^{VDW} g^{HS}(1; \eta_{eff}), \quad (5.7)$$

where

$$g^{HS}(1; \eta_{eff}) = \frac{1 - \eta_{eff}/2}{(1 - \eta_{eff})^3}, \quad (5.8)$$

is obtained from the Carnahan and Starling expression [15]. The second-order term can be calculated in the local compressibility approximation [6],

$$a_2 = \frac{1}{2} \varepsilon K^{HS} \rho_s \frac{\partial a_1^*}{\partial \rho_s}, \quad (5.9)$$

where

$$a_1^* = -3\rho_s b^{VDW} \varepsilon \int_1^\infty x^2 [\phi(x)]^2 g^{HS}(x) dx, \quad (5.10)$$

and K^{HS} is the Percus-Yevick hard-sphere isothermal compressibility [6]

$$K^{HS} = \frac{(1 - \eta)^4}{1 + 4\eta + 4\eta^2}. \quad (5.11)$$

The Yukawa potential is given by

$$\phi^Y(r; \lambda) = \frac{e^{-\lambda(r/\sigma-1)}}{r/\sigma}. \quad (5.12)$$

By convention the range of the attractive forces in this model is characterised by λ^{-1} . The Yukawa model finds a particular use in the description of screened Coulombic interactions found in electrolytes and colloids. The van der Waals mean-field term for the Yukawa potential is given by

$$a_1^{VDW} = -12\eta\varepsilon(\lambda^{-1} + \lambda^{-2}), \quad (5.13)$$

and the parameterisation for $\eta_{eff}(\eta, \lambda)$ is obtained by using accurate values of a_1 obtained from the RIINC integral equation [1], as

$$\eta_{eff}(\eta, \lambda) = c_1\eta + c_2\eta^2, \quad (5.14)$$

with

$$\begin{pmatrix} c_1 \\ c_2 \end{pmatrix} = \begin{pmatrix} 0.900678 & -1.50051 & 0.776577 \\ -0.314300 & 0.257101 & -0.0431566 \end{pmatrix} \begin{pmatrix} 1 \\ \lambda^{-1} \\ \lambda^{-2} \end{pmatrix}. \quad (5.15)$$

The fluctuation term for the Yukawa fluid is obtained from

$$a_1^*(\lambda) = a_1^{VDW*} g^{HS}(1, \eta^*), \quad (5.16)$$

where

$$a_1^{VDW*} = -6\eta\varepsilon\lambda^{-1}, \quad (5.17)$$

and

$$g^{HS}(1, \eta^*) = \frac{1 - \eta^*/2}{(1 - \eta^*)^3}, \quad (5.18)$$

with the parameterisation

$$\eta^*(\eta, \lambda) = d_1\eta + d_2\eta^2, \quad (5.19)$$

where

$$\begin{pmatrix} d_1 \\ d_2 \end{pmatrix} = \begin{pmatrix} 0.989601 & -0.872203 & 0.320808 & 0.0 & 0.0 \\ -0.0119152 & -1.24029 & 2.41636 & -2.01922 & 0.647565 \end{pmatrix} \begin{pmatrix} 1 \\ \lambda^{-1} \\ \lambda^{-2} \\ \lambda^{-3} \\ \lambda^{-4} \end{pmatrix}. \quad (5.20)$$

The final expression for a_2 is

$$a_2^Y(\lambda) = \frac{1}{2} K^{HS} \eta \frac{\partial a_1^*(\lambda)}{\partial \eta}. \quad (5.21)$$

Thus for Yukawa fluids of variable range, the SAFT-VR EOS is obtained by substituting the expressions for a_1^Y and a_2^Y in Eq. (5.5) and then in Eq. (5.4). Although independent parameterisations are used for a_1 and a_1^* the thermodynamics of the Yukawa fluid can be recasted in terms of a_1^* only. By using the properties of Laplace transforms, it follows that

$$a_1 = \frac{\partial a_1^*}{\partial \lambda} - a_1^*. \quad (5.22)$$

This way of obtaining a_1 , however, makes the application of the Yukawa model to mixtures more complex.

We also examine systems interacting via the Sutherland potential which is given by

$$\phi^S(r; \lambda) = (\sigma/r)^\lambda. \quad (5.23)$$

The range parameter λ controls the decay of the interaction. By varying λ , different angle-averaged multipolar-like forces, such as the Mie m - n potentials can be modelled with this potential. For the Sutherland potential the van der Waals

mean-field term is given by

$$a_1^{VDW} = -4\eta\varepsilon \left(\frac{3}{\lambda - 3} \right), \quad (5.24)$$

where $\eta = \pi\sigma^3\rho_s/6$ is the packing fraction of the system, and

$$\eta_{eff}(\eta, \lambda) = c_1\eta + c_2\eta^2, \quad (5.25)$$

with

$$\begin{pmatrix} c_1 \\ c_2 \end{pmatrix} = \begin{pmatrix} -0.943973 & 0.422543 & -0.0371763 & 0.00116901 \\ 0.370942 & -0.173333 & 0.0175599 & -0.000572729 \end{pmatrix} \begin{pmatrix} 1 \\ \lambda \\ \lambda^2 \\ \lambda^3 \end{pmatrix}. \quad (5.26)$$

The fluctuation term a_2 for the Sutherland potential is given simply in terms of the mean-attractive energy of a Sutherland potential of inverse range 2λ

$$a_2^S(\lambda) = \frac{1}{2}\varepsilon K^{HS}\eta \frac{\partial a_1^S(2\lambda)}{\partial \eta}. \quad (5.27)$$

The contribution to the free energy due to the formation of a chain of m monomers is [7]

$$\frac{A^{CHAIN}}{NkT} = -(m_s - 1) \ln y^M(\sigma), \quad (5.28)$$

where $y^M(\sigma)$ is the monomer-monomer background correlation function evaluated at hard-core contact; if $g^M(r)$ is the monomer-monomer radial distribution function, then $y^M(r) = \exp[u^M(r)/kT]g^M(r)$. In the SAFT-VR approach a perturbation expansion is used for the monomer-monomer contact value of the radial distribution function [6],

$$g^M(\sigma^+) = g^{HS}(\sigma^+) + \beta\varepsilon g_1(\sigma^+), \quad (5.29)$$

and $g_1(\sigma^+)$ is obtained from a self-consistent calculation of the pressure, using the virial theorem of Clausius and the derivative of the free energy with respect to density. The contact value for the radial distribution function for Yukawa fluids can be expressed in terms of a_1 using the properties of Laplace transforms, giving a final expression for the contact value as,

$$g^Y(\sigma^+) = g^{HS}(\sigma^+) + \frac{1}{4}\beta \left[\frac{\partial a_1^Y}{\partial \eta} + \frac{\lambda}{3\eta} \frac{\partial a_1^Y}{\partial \lambda} - \frac{(1+\lambda)}{3\eta} a_1^Y \right]. \quad (5.30)$$

For the Sutherland potential we obtain an expression for the contact value of the

radial distribution function as [1]

$$g^S(\sigma^+) = g^{HS}(\sigma^+) + \frac{1}{4}\beta \left[\frac{\partial a_1^S}{\partial \eta} - \frac{\lambda}{3\eta} a_1^S \right]. \quad (5.31)$$

The value of $g^M(\sigma^+)$ is also required for the calculation of the contribution to the free energy due to association. It is important to stress that in order to obtain the complete equation of state all that is required is a hard-sphere equation of state together with the mean attractive energy a_1 , which is given in terms of the hard-sphere contact value of g .

The contribution to the Helmholtz free energy due to association for s sites on the chain molecules is obtained from the theory of Wertheim as [16]

$$\frac{A^{ASSOC.}}{NkT} = \left[\sum_{a=1}^s \left(\ln X_a - \frac{X_a}{2} \right) + \frac{s}{2} \right], \quad (5.32)$$

where the sum is over all s sites a on a molecule, and X_a is the fraction of molecules not bonded at site a . The latter quantity is obtained by a solution of the following mass action equation:

$$X_a = \frac{1}{1 + \sum_{b=1}^s \rho X_b \Delta_{a,b}}. \quad (5.33)$$

The function $\Delta_{a,b}$ characterises the association between site a and site b on different molecules. It can be written in terms of the contact value $g^M(\sigma)$ of the monomer-monomer radial distribution function, the Mayer function $f_{a,b} = \exp(-\phi_{a,b}/kT) - 1$ of the a - b site-site bonding interaction $\epsilon_{a,b}$, and the volume $K_{a,b}$ available for bonding as [17]

$$\Delta_{a,b} = K_{a,b} f_{a,b} g^M(\sigma). \quad (5.34)$$

The bonding volume $K_{a,b}$ can be determined from the parameters of the bonding site such as its position and range [17]. As for the chain contribution, $g^M(\sigma)$ is approximated by $g^M(\sigma^+)$.

5.3 Yukawa fluids

Interest in the Yukawa fluid arises due to the nature of the potential shown in Eq. (5.12), since it has the same form as the potential experienced by shielded ions in electrolyte solutions. Additionally, the exponential term in the attractive part of the potential allows for an exact solution of the mean-spherical approximation for this hard-core model. The MSA is an integral equation approach used to obtain the correlation functions and thermodynamic functions for a fluid, based on the

Ornstein-Zernike (OZ) relation:

$$h(\mathbf{r}_{12}) = c(\mathbf{r}_{12}) + \rho \int h(\mathbf{r}_{13})c(\mathbf{r}_{23})d\mathbf{r}_3. \quad (5.35)$$

Here, $h(\mathbf{r}_{ij})$ is the total correlation function between two particles with centres at \mathbf{r}_i and \mathbf{r}_j , at a distance $\mathbf{r}_{ij} = \mathbf{r}_i - \mathbf{r}_j$ apart, and $c(\mathbf{r}_{ij})$ is the corresponding direct correlation function. Given the general pair potential of Eq. (5.3) which is independent of the relative orientations of the particles, the correlation functions only depend on r which is the magnitude of the vector \mathbf{r}_{ij} , $r = |\mathbf{r}_{ij}| = |\mathbf{r}_i - \mathbf{r}_j|$. We know that the radial distribution function must obey the condition

$$g(r) = 0 \quad \text{if } r \leq \sigma. \quad (5.36)$$

Within the mean-spherical approximation the assumption is made that for all $r > \sigma$ we have

$$c(r) \simeq -\beta\epsilon\phi(r), \quad (5.37)$$

which simply indicates that the direct correlation between a pair of molecules is given by the pair interaction potential. Combining this approximation with the OZ relation between $c(r)$ and $h(r)$ of Eq. (5.35) allows for the determination of the radial distribution function $g(r)$ outside the hard core since

$$g(r) = h(r) - 1, \quad (5.38)$$

and also of the direct correlation function inside the core. Substitution of the Yukawa attractive well of inverse range λ given in Eq. (5.12) into the general expression of Eq. (5.37) yields the MSA exactly solvable [18].

The analytical solution of the MSA for the hard-core Yukawa fluid [18]-[20] consists of six nonlinear equations in six unknowns. However, this solution does not give explicit expressions for the free energy and other related functions of the system and several studies have been reported [21]-[32] which present versions of the MSA solution which can be written directly in term of the useful thermodynamic properties of the Yukawa fluid. One such route is the work of Ref. [32] following the work of Ginoza [29]-[31], where a high temperature expansion (HTE) is used within the original MSA to give expressions which depend explicitly on temperature, density and the range of the potential. The free energy of the Yukawa fluid is written as a first order expansion

$$a^Y = a^{HS} + \beta a_1^Y, \quad (5.39)$$

where a^{HS} is the free energy of the hard-sphere reference system, given by the Carnahan and Starling expression [15], and a_1^Y is the mean-attractive energy of

the Yukawa fluid, which is given by [32]

$$a_1^Y = -\frac{2\lambda L(\lambda)}{\exp(-\lambda)L(\lambda)S(\lambda)}. \quad (5.40)$$

The polynomials $L(\lambda)$ and $S(\lambda)$ are given by

$$L(\lambda) = 12\eta[(1 + \eta/2)\lambda + 1 + 2\eta] \quad (5.41)$$

and

$$S(\lambda) = (1 - \eta)^2\lambda^3 + 6\eta(1 - \eta)\lambda^2 + 18\eta^2\lambda - 12\eta(1 + 2\eta). \quad (5.42)$$

The contact value of the radial distribution function for the Yukawa fluid is also written as a first order expansion in Ref. [32]

$$g^Y(\sigma^+) = g_0(\sigma^+) + \beta g_1^Y(\sigma^+), \quad (5.43)$$

where g_0 is given by the Percus Yevick approximation for hard spheres [33]

$$g_0(\sigma^+) = \frac{1 + \eta/2}{(1 - \eta)^2}. \quad (5.44)$$

The first order term $g_1^Y(\sigma^+)$ is given by [32]

$$g_1^Y = \frac{1}{\Phi_0^2}, \quad (5.45)$$

where Φ_0 is defined

$$\Phi_0 = \frac{\exp(-\lambda)L(\lambda) + S(\lambda)}{\lambda^3(1 - \eta)^2}. \quad (5.46)$$

We can use these expressions as a means of testing the consistency of the SAFT-VR methodology for the thermodynamic properties of the Yukawa fluid. Previous results reported for this system include a Monte Carlo (MC) simulation study [34], which can be treated as 'exact' results, together with a full analytical solution of the mean-spherical approximation [34], and a more recent study using the truncated temperature expansions given above (Eqs. (5.40 and 5.43) within the MSA [32].

The values of the mean-attractive energy and the first fluctuation in energy for the Yukawa fluid with $\lambda = 1.8$ obtained with the SAFT-VR methodology are compared in Table 5.1 with those obtained with the MSA results of Ref. [34], for a series of reduced densities. No significant difference exists between the values for the mean-attractive energy obtained by either method, but the first fluctuation term a_2 is larger in the case of the SAFT-VR equation of state, indicating that the use of the local compressibility approximation results in a higher value of a_2 than the MSA. Comparing the values of a_2 obtained using the SAFT-VR equation of state with the perturbation theory results of Ref. [34], which are calculated

Table 5.1: Values of the mean-attractive energy a_1 and the first fluctuation term a_2 for the Yukawa fluid with $\lambda = 1.8$ obtained using the MSA [34] and SAFT-VR [1] approaches for a series of reduced densities $\rho^* = \rho\sigma^3$.

ρ^*	a_1		a_2	
	MSA	SAFT-VR	MSA	SAFT-VR
0.1	-0.566	-0.565	-0.054	-0.067
0.2	-1.175	-1.172	-0.065	-0.104
0.3	-1.824	-1.822	-0.057	-0.119
0.4	-2.513	-2.511	-0.044	-0.120
0.5	-3.237	-3.237	-0.030	-0.112
0.6	-3.995	-3.996	-0.019	-0.099
0.7	-4.784	-4.785	-0.011	-0.083
0.8	-5.602	-5.599	-0.006	-0.066
0.9	-6.446	-6.432	-0.003	-0.051
1.0	-7.314	-7.278	-0.001	-0.036

using MC techniques from exact expressions, also indicates that the fluctuation term is overestimated by the SAFT-VR approach. However, the fact that the values of a_2 obtained using the local compressibility approximation in the SAFT-VR methodology is less accurate than those obtained in the MSA does not have a significant influence on the accuracy of the overall SAFT-VR equation of state for the Yukawa fluid since for values of $\beta\varepsilon \leq 1$ the second-order contribution to the free energy is negligible with respect to a_1 .

The values of the Helmholtz free energies for the Yukawa fluid with $\lambda = 1.8$, obtained using the SAFT-VR equation of state up to first order, and including the second-order perturbation, are compared with the equivalent MSA expressions, for a series of reduced densities and temperatures in Table 5.2. Good agreement is observed between both theoretical approaches, and the contribution to the free energy from fluctuations is seen to be much smaller, in both cases, than that of the mean-attractive energy a_1 .

Values of the compressibility factor for the Yukawa fluid with $\lambda = 1.8$ obtained using the SAFT-VR equation of state are compared with the values obtained using the MSA of Ref. [34] and with the Monte Carlo results of Ref. [34] in Table 5.3, and in Figure 5.1. Results are presented for a series of reduced densities and temperatures and good agreement can be observed between both theoretical approaches and the simulation results, with neither theory giving results which are consis-

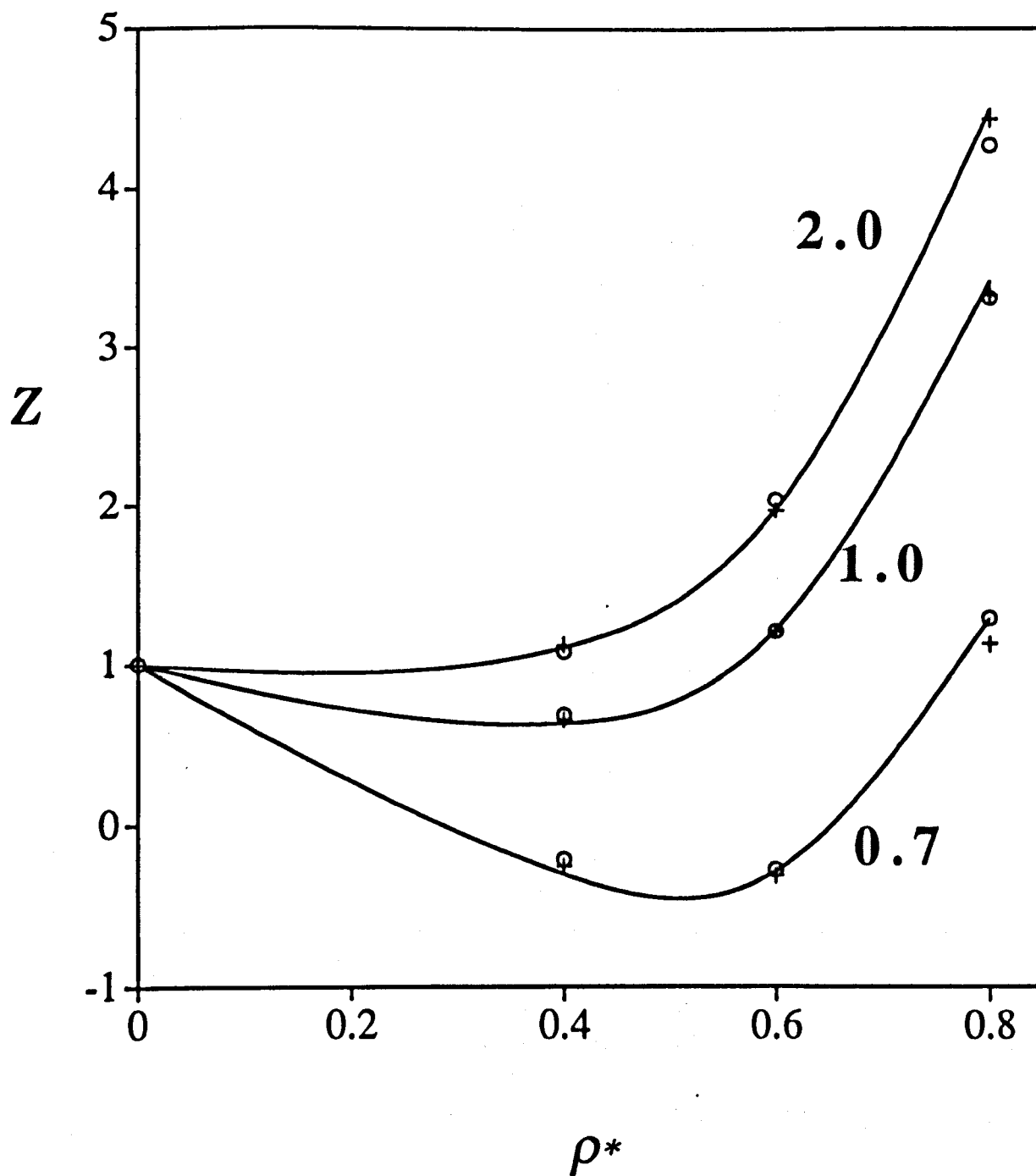


Figure 5.1: The compressibility factor $Z = PV/NkT$ for the Yukawa fluid with $\lambda = 1.8$ obtained from the SAFT-VR equation of state [1] (curves) compared with values obtained using the MSA (crosses) approach and from MC simulation (open circles) [34]. The reduced density is defined $\rho^* = \rho\sigma^3$, and the curves are labelled with the corresponding values of the reduced temperatures $T^* = kT/\epsilon$.

Table 5.2: Values of the Helmholtz free energy A/NkT for the Yukawa fluid with $\lambda = 1.8$ obtained using the MSA [34] and SAFT-VR [1] approaches to first and second order, for a series of reduced densities $\rho^* = \rho\sigma^3$ and temperatures $T^* = kT/\epsilon$.

ρ^*	T^*	1st order		2nd order	
		MSA	SAFT-VR	MSA	SAFT-VR
0.4	2.0	-0.137	-0.125	-0.139	-0.155
	1.5	-0.565	-0.549	-0.569	-0.597
	1.0	-1.426	-1.381	-1.443	-1.501
0.6	2.0	0.040	0.044	0.039	0.019
	1.5	-0.630	-0.622	-0.631	-0.666
	1.0	-1.972	-1.954	-1.976	-2.053
0.8	2.0	0.601	0.603	0.600	0.587
	1.5	-0.334	-0.330	-0.334	-0.359
	1.0	-2.205	-2.200	-2.206	-2.262
	0.7	-4.611	-4.595	-4.164	-4.731

tently the most accurate. The negative values of pressure at low temperatures correspond to metastable states within the coexistence region of the system.

An additional means of testing the adequacy of the MSA and SAFT-VR methods in their prediction of the properties of the Yukawa fluid is to compare the values of the radial distribution function evaluated at contact, obtained using both approaches. Within the MSA it is possible to obtain values of $g(\sigma^+)$ both from the full analytical solution of Ref. [34] and by using the truncated high temperature expansions of Ref. [32]. The contact value of the radial distribution function in the SAFT-VR approach is obtained using Eq. (5.30), where the mean-attractive energy is given by Eq. (5.7). It is interesting to note that a combination of both the SAFT-VR and the MSA approaches can be used to give an expression for the contact value of the radial distribution function of the Yukawa fluid, since the mean-attractive energy a_1 of the MSA methodology given by Eq. (5.40) can be used in the SAFT-VR expression for the radial distribution function Eq. (5.30). The values for the contact value of the radial distribution function obtained by each of these routes are compared directly with one another, and with the MC simulation results of Ref. [34], for a series of reduced densities and temperatures in Table 5.4. The values of $g(\sigma^+)$ obtained using the SAFT-VR equation of state are seen to be in better agreement with the simulation results than those obtained using either the full MSA of Ref. [34], or the truncated MSA of Ref. [32] (there is little difference

Table 5.3: Values of the compressibility factor $Z = PV/NkT$ for the Yukawa fluid with $\lambda = 1.8$ obtained using MC simulation [34] and both the MSA [34] and SAFT-VR [1] approaches, for a series of reduced densities $\rho^* = \rho\sigma^3$ and temperatures $T^* = kT/\epsilon$.

ρ^*	T^*	MC	MSA	SAFT-VR
0.4	2.0	1.08	1.119	1.106
	1.5	0.69	0.659	0.637
	1.0	-0.21	-0.251	-0.298
0.6	2.0	2.04	1.976	1.981
	1.5	1.21	1.213	1.223
	1.0	-0.27	-0.303	-0.277
0.8	2.0	4.27	4.432	4.486
	1.5	3.31	3.330	3.412
	1.0	1.29	1.131	1.287
	0.7	-1.63	-1.687	-1.401

between the values obtained using either MSA approach). However, the contact value of the radial distribution function obtained using the combination of the expression for a_1 from the MSA Eq. (5.40), and the expression for $g(\sigma^+)$ from the SAFT-VR approach Eq. (5.30) is seen to give values for $g(\sigma^+)$ which are in closest agreement with the simulation results. This indicates that use of the self-consistent route to obtain the radial distribution function, as given in the SAFT-VR approach by Eq. (5.30), results in a more accurate version of the MSA. The closed nature of the expression for $g(\sigma^+)$ enables it to be incorporated into the algebra of the analytical solution of the MSA, so that it can be evaluated exactly by an alternative and more accurate route.

It is clear that the SAFT-VR approach gives suitably accurate values for the contact value of the radial distribution function when compared with MC results and with the full analytical solution of the MSA for the Yukawa fluid.

The vapour-liquid phase equilibria of Yukawa chains of length $m_s=2, 4$ and 16 obtained using the SAFT-VR equation of state for inverse ranges of $\lambda=1.0, 1.8$ and 4.0 are shown in Figures 5.2, 5.3 and 5.4, respectively. The region of vapour liquid coexistence is seen to move to higher temperatures as the chain length increases, and extends as the range of the potential increases. In the case of the monomer Yukawa fluid with inverse range of $\lambda=1.8$ (Fig. 5.4) the SAFT-VR prediction is seen to compare favourably with the Gibbs ensemble simulation results of Ref. [35].

Table 5.4: Values of the contact value of the radial distribution function $g(\sigma^+)$ for the Yukawa fluid with $\lambda = 1.8$ obtained using MC simulation [34], the MSA equation of state, both analytically [34] and using a first order expansion [32], the SAFT-VR [1] approaches, and a combination of the MSA and SAFT-VR approaches, for a series of reduced densities $\rho^* = \rho\sigma^3$ and temperatures $T^* = kT/\epsilon$.

ρ^*	T^*	MC	MSA	HTE-MSA	SAFT-VR	SAFT-VR+MSA
0.4	2.0	2.128	1.963	1.944	2.106	2.124
	1.5	2.378	2.040	2.003	2.204	2.228
	1.0	2.943	2.222	2.121	2.401	2.436
0.6	2.0	2.921	2.561	2.555	2.821	2.846
	1.5	2.966	2.598	2.586	2.891	2.923
	1.0	3.205	2.681	2.649	3.029	3.079
0.8	2.0	4.109	3.629	3.628	4.177	4.191
	1.5	4.257	3.646	3.643	4.226	4.249
	1.0	4.490	3.681	3.674	4.325	4.359
	0.7	4.622	3.729	3.713	4.452	4.500

However, no simulation data currently exist for Yukawa chains so that we cannot make a direct comparison of the results obtained using the SAFT-VR approach for these systems.

5.4 Lennard-Jones chains

The expressions presented in the previous section can be used to develop an equation of state for chain molecules interacting via the Mie $m - n$ potentials [12], of which the Lennard-Jones ($m = 6$ and $n = 12$) is the most common example. The Mie $m - n$ potentials are given by

$$u^M = C\epsilon \left[\left(\frac{\sigma}{r} \right)^n - \left(\frac{\sigma}{r} \right)^m \right], \quad (5.47)$$

where

$$C = \frac{n}{n-m} \left(\frac{n}{m} \right)^{\frac{m}{n-m}}. \quad (5.48)$$

Systems interacting with binary potentials with soft repulsive interactions like Eq. (5.47) can be described within the Barker and Henderson perturbation theory,

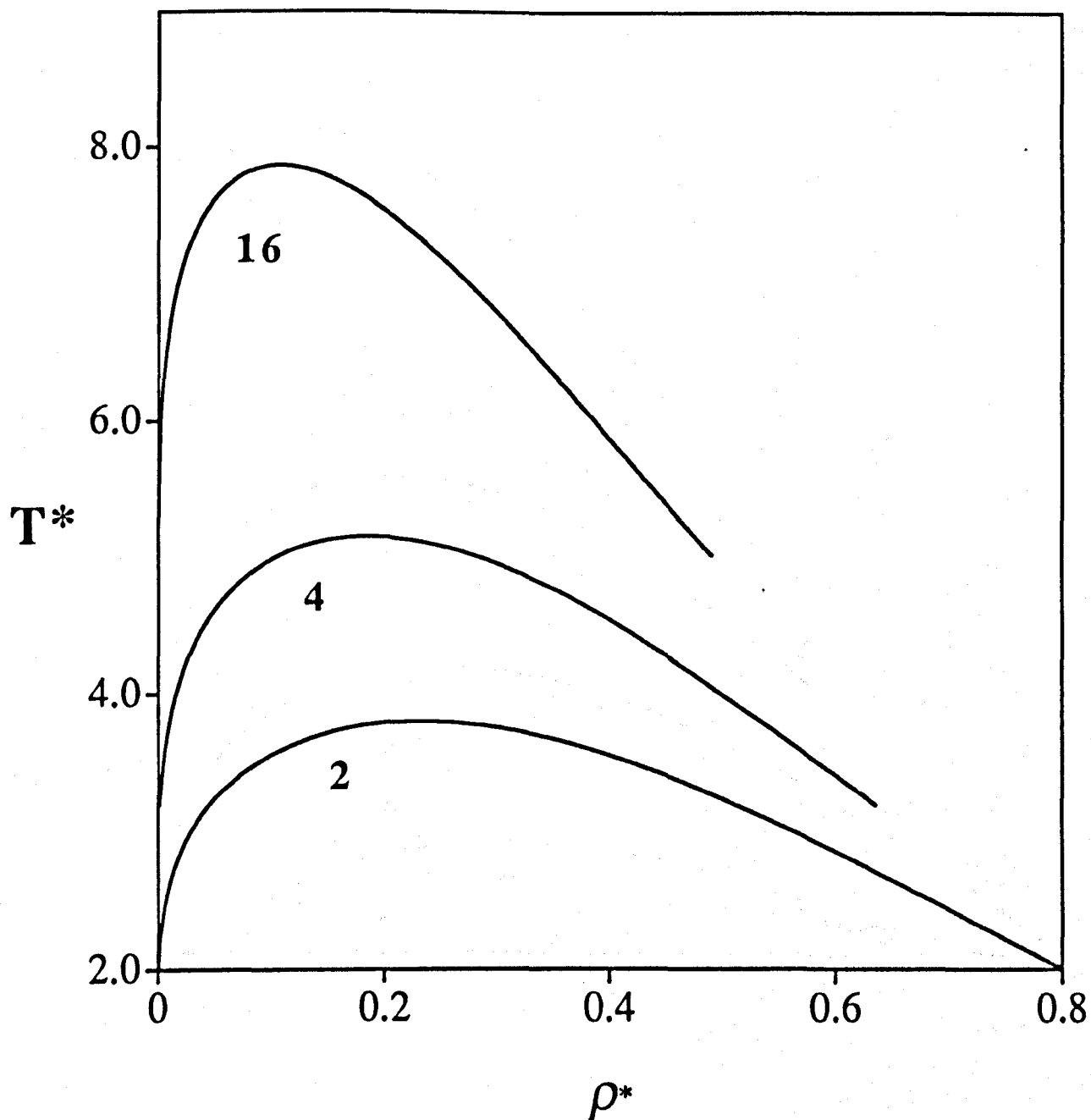


Figure 5.2: The vapour-liquid coexistence densities for Yukawa chains of length $m_s = 2, 4$ and 16 with inverse range of $\lambda = 1.0$. The curves are labelled with the values of the chain length m_s . The reduced parameters used are $T^* = kT/\epsilon$ and $\rho_s^* = \rho_s \sigma^3$.

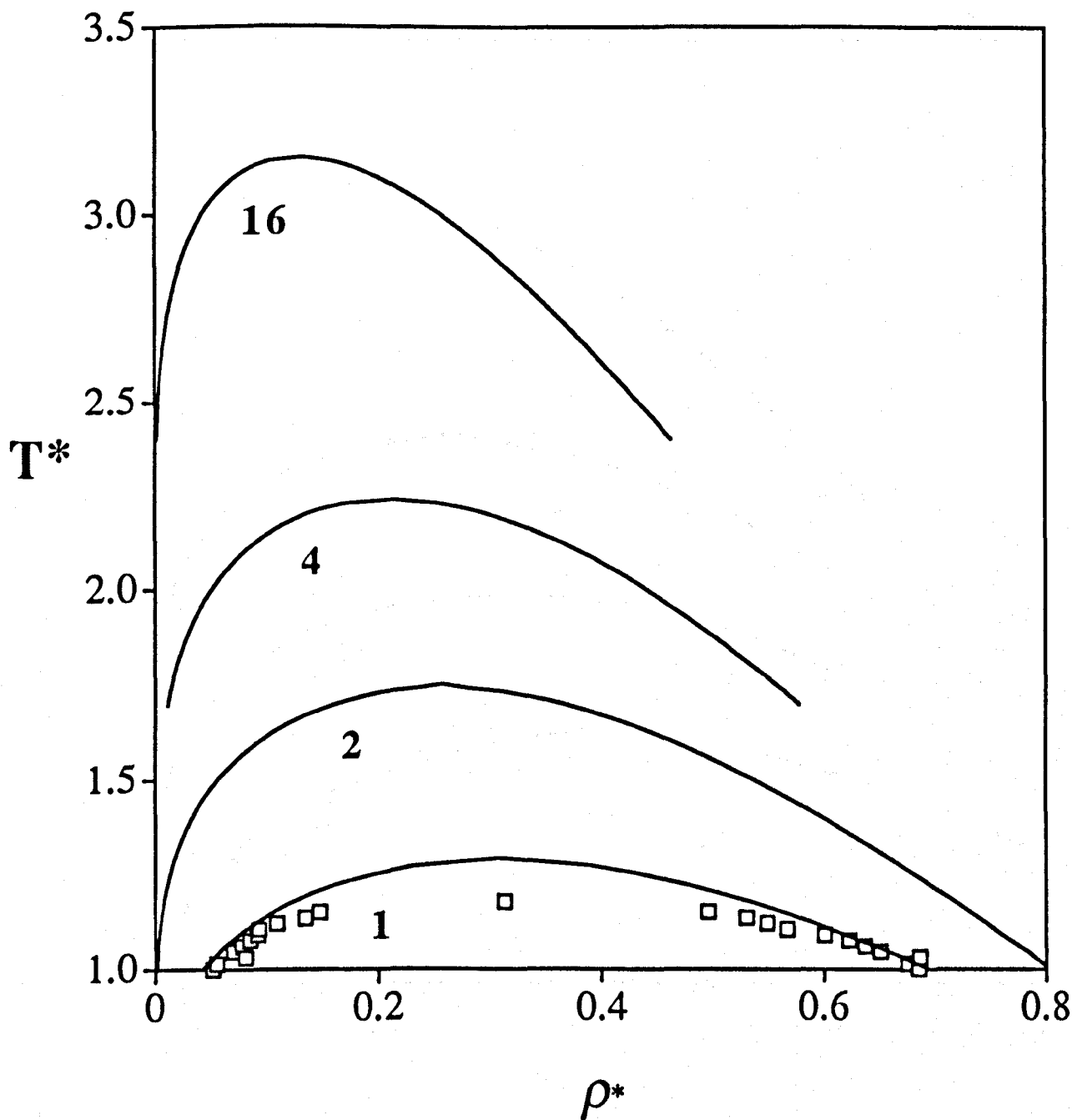


Figure 5.3: The vapour-liquid coexistence densities for Yukawa chains of length $m_s = 1, 2, 4$ and 16 with inverse range of $\lambda = 1.8$. The curves are labelled with the values of the chain length m_s . The reduced parameters used are $T^* = kT/\epsilon$ and $\rho_s^* = \rho_s \sigma^3$. The data points correspond to the Gibbs ensemble simulation data for Yukawa monomers of Lomba and Almarza [35].

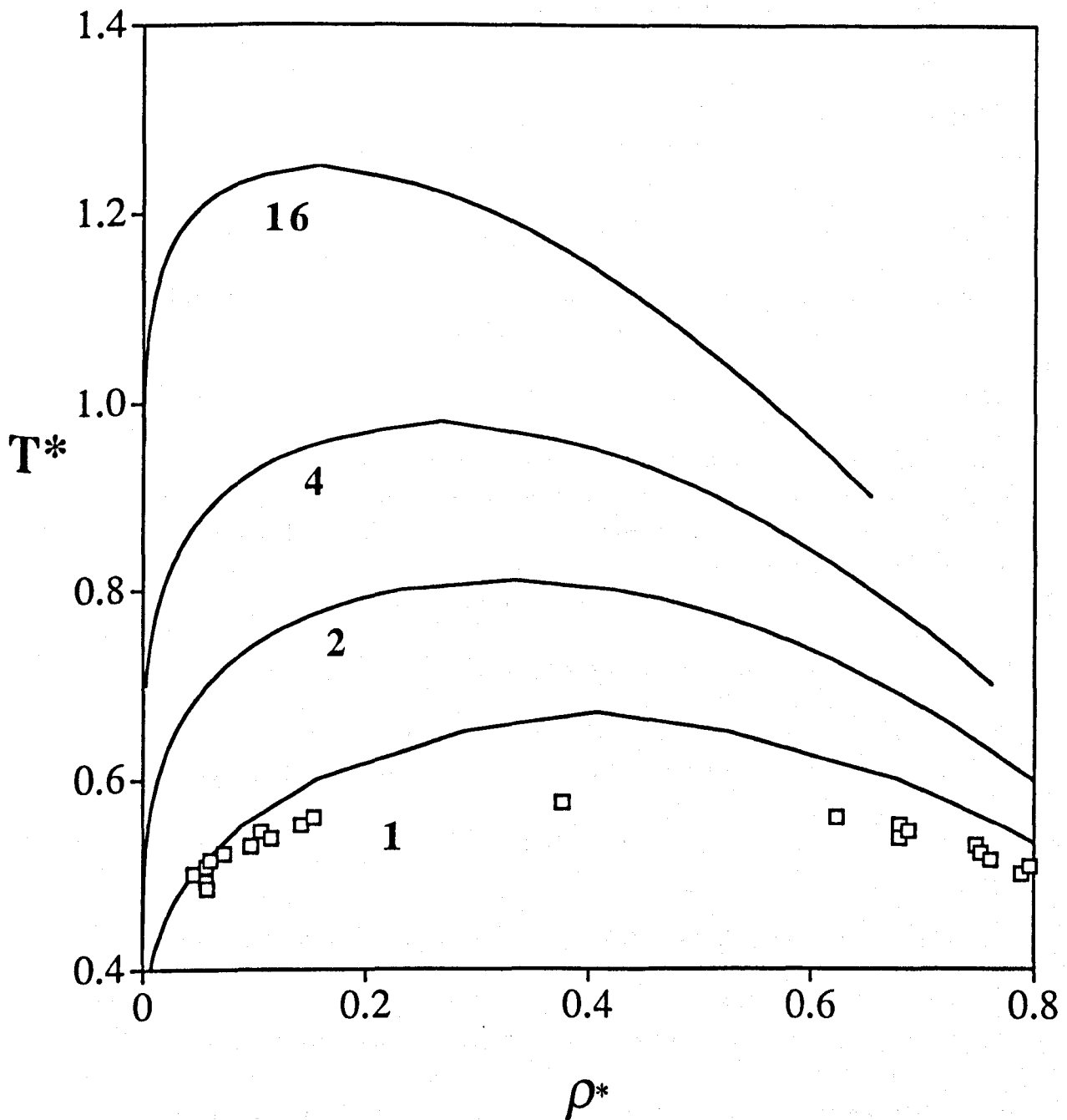


Figure 5.4: The vapour-liquid coexistence densities for Yukawa chains of length $m_s = 1, 2, 4$ and 16 with inverse range of $\lambda = 4.0$. The curves are labelled with the values of the chain length m_s . The reduced parameters used are $T^* = kT/\epsilon$ and $\rho_s^* = \rho_s \sigma^3$. The data points correspond to the Gibbs ensemble simulation data for Yukawa monomers of Lomba and Almarza [35].

by considering an equivalent potential with a hard-core temperature dependent diameter,

$$u_{BH}^M = \begin{cases} \infty & \text{if } r < \sigma_{BH}(T) \\ u^M & \text{if } r > \sigma_{BH}(T), \end{cases} \quad (5.49)$$

where

$$\sigma_{BH}(T) = \int_0^\sigma (1 - \exp(-\beta u^M)) dr, \quad (5.50)$$

and σ defines the position where u^M changes sign. The free energy is then calculated with the expansion of Eq. (5.5) using the packing fraction

$$\eta_{BH}(T) = \eta(\sigma_{BH}/\sigma)^3. \quad (5.51)$$

The expressions for a_1 , a_2 and $g(\sigma^+)$ for the Sutherland potential (Eqs. (5.7), (5.27) and (5.31)), can be used directly in the expressions for the soft-core systems. Since the family of Mie potentials can be represented by a sum of an attractive and of a repulsive Sutherland potential, the mean-attractive energy for such systems can be similarly expressed as the sum of two Sutherland a_1 terms,

$$a_1^{MIE} = C \left[-a_1^S(\eta_{BH}; \lambda = n) + a_1^S(\eta_{BH}; \lambda = m) \right], \quad (5.52)$$

where a_1^S corresponds to the mean-attractive energy for a Sutherland system with exponent λ . The second order term a_2 is given in terms of the attractive contribution only as

$$a_2^{MIE} = C a_2^S(\eta_{BH}; \lambda = m). \quad (5.53)$$

For the LJ fluid we can apply this recipe with the following parametrisation for σ_{BH} [1]:

$$\sigma_{BH}/\sigma = 0.995438 - 0.0259917T^* + 0.00392254T^{*2} - 0.000289398T^{*3}, \quad (5.54)$$

where $T^* = kT/\epsilon$. In order to calculate the contribution to the free energy due to chain formation, we require the monomer cavity function at the bonding distance, y_b^M . For systems interacting with soft repulsive interactions, the bond distance is σ , i.e., where the potential is zero. Since in the SAFT-VR approach the molecules are formed from effective hard-core segments with diameter σ_{HH} , the bond length is σ_{BH} and y_b^M can be calculated according to

$$y_b^M = y^{LJ}(\sigma_{BH}), \quad (5.55)$$

where y^{LJ} is the cavity function of the hard-core potential defined in the Barker and Henderson perturbation theory, which is given in Eq. (5.49). We have found

that a more accurate prediction of the properties of the Lennard-Jones chains is obtained with the approximation

$$y_b^M = y^{S6}(\sigma_{BH}) \quad (5.56)$$

where y^{S6} is the Sutherland-6 potential contact value, obtained directly from Eq. (5.31). With this approximation, the final expression for the chain free energy is

$$\frac{A^{CHAIN}}{NkT} = -(m_s - 1) \ln y^{S6}(\sigma_{BH}). \quad (5.57)$$

Here we only consider chains formed from segments with no association sites, hence there is no contribution to the Helmholtz free energy due to association, $A^{ASSOC.} = 0$.

The vapour-liquid phase equilibria of Lennard-Jones chains of length $m_s = 2, 4$ and 8 obtained using the SAFT-VR approach outlined in the previous section are compared with existing Gibbs ensemble Monte Carlo (GEMC) simulation results [11] in Figure 5.5. The SAFT-VR description for monomers ($m_s = 1$) given previously [1] and the corresponding GEMC simulation results [36] are also shown.

The SAFT-VR theory gives a good overall description of the coexistence region, and reproduces the effect of increasing the chain length. The theory's adequacy is, however, seen to decrease as the chain length increases, which can be rationalised in terms of an inaccurate description of molecular structure, such as folding, which occurs as the chain length increases [10]. It is well known that the SAFT approach accurately describes the behaviour of long-chain molecules up to $m_s = 8$ [37]. Versions of SAFT which account for higher body interactions have been proposed [37, 38], in order to be able to give a more accurate prediction of systems consisting of long chain molecules. Various super-critical isotherms calculated using the SAFT-VR approach for LJC with $m_s = 2, 4$ and 8 are presented in Figures 5.6, 5.7 and 5.8, respectively.

The SAFT-VR expressions are seen to compare favourably with results obtained with the equation of state proposed by Johnson *et al.* [10]; these authors used an accurate empirical representation for $g^{LJ}(\sigma)$. The approximation used in Eq. (5.57) gives an accurate prediction of the vapour-liquid envelope, as well as the pressure for the whole range of monomer densities ρ_s^* . The residual internal energy at a series of temperatures for LJC with $m_s = 2, 4$ and 8 are presented in Figures 5.9, 5.10 and 5.11, respectively. Our equation of state overpredicts the residual internal energy for densities $\rho_s^* > 0.7$.

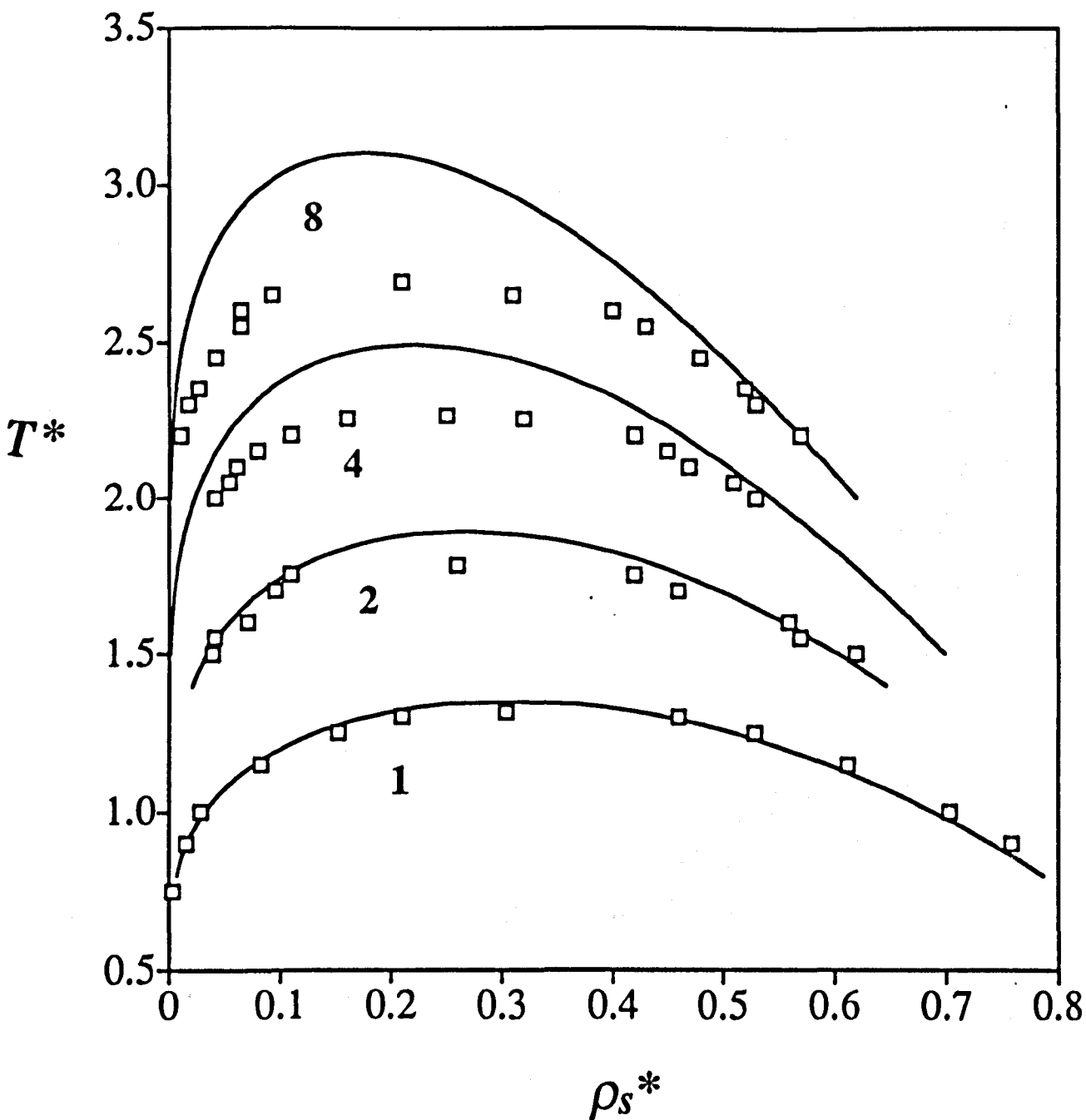


Figure 5.5: The vapour-liquid coexistence densities for Lennard-Jones chains of length m_s , compared with the Gibbs ensemble simulation data of Panagiotopoulos [36] ($m_s = 1$), and of Escobedo and de Pablo [11] ($m_s = 2, 4$ and 8). The continuous curves correspond to the SAFT-VR approach, and each is labelled with the values of the chain length m_s . The reduced parameters used are $T^* = kT/\varepsilon$ and $\rho_s^* = \rho_s\sigma^3$.

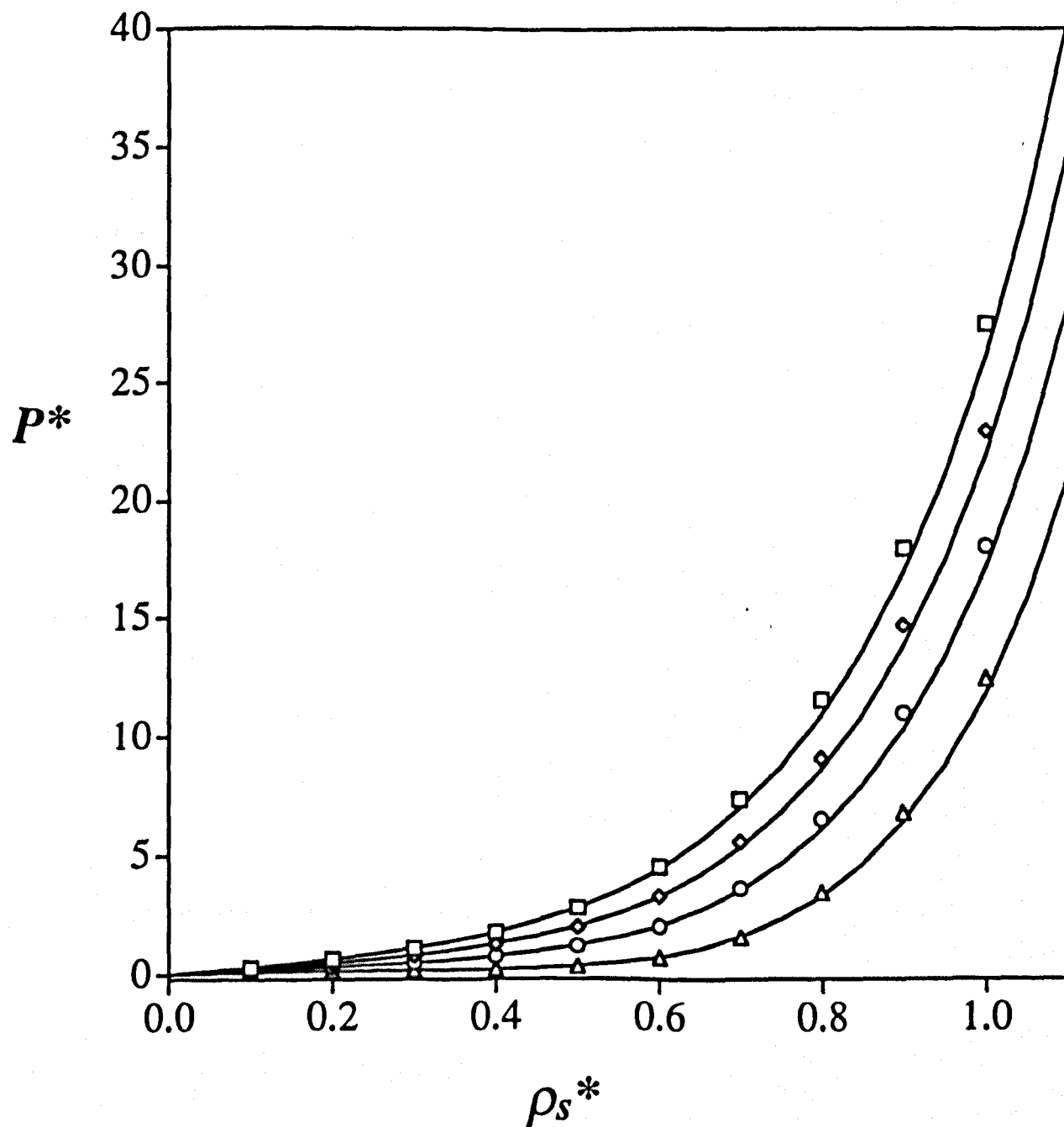


Figure 5.6: The reduced pressure $P^* = P\sigma^3/\epsilon$ of Lennard-Jones chains with $m_s = 2$ (diatomics) as a function of the reduced monomer density $\rho_s^* = \rho_s\sigma^3$. The squares, diamonds, circles and triangles are the molecular dynamics simulation results of Johnson *et al.* [10] for the reduced temperatures of $T^* = kT/\epsilon = 5, 4, 3$ and 2 , respectively. The continuous curves correspond to the SAFT-VR predictions.

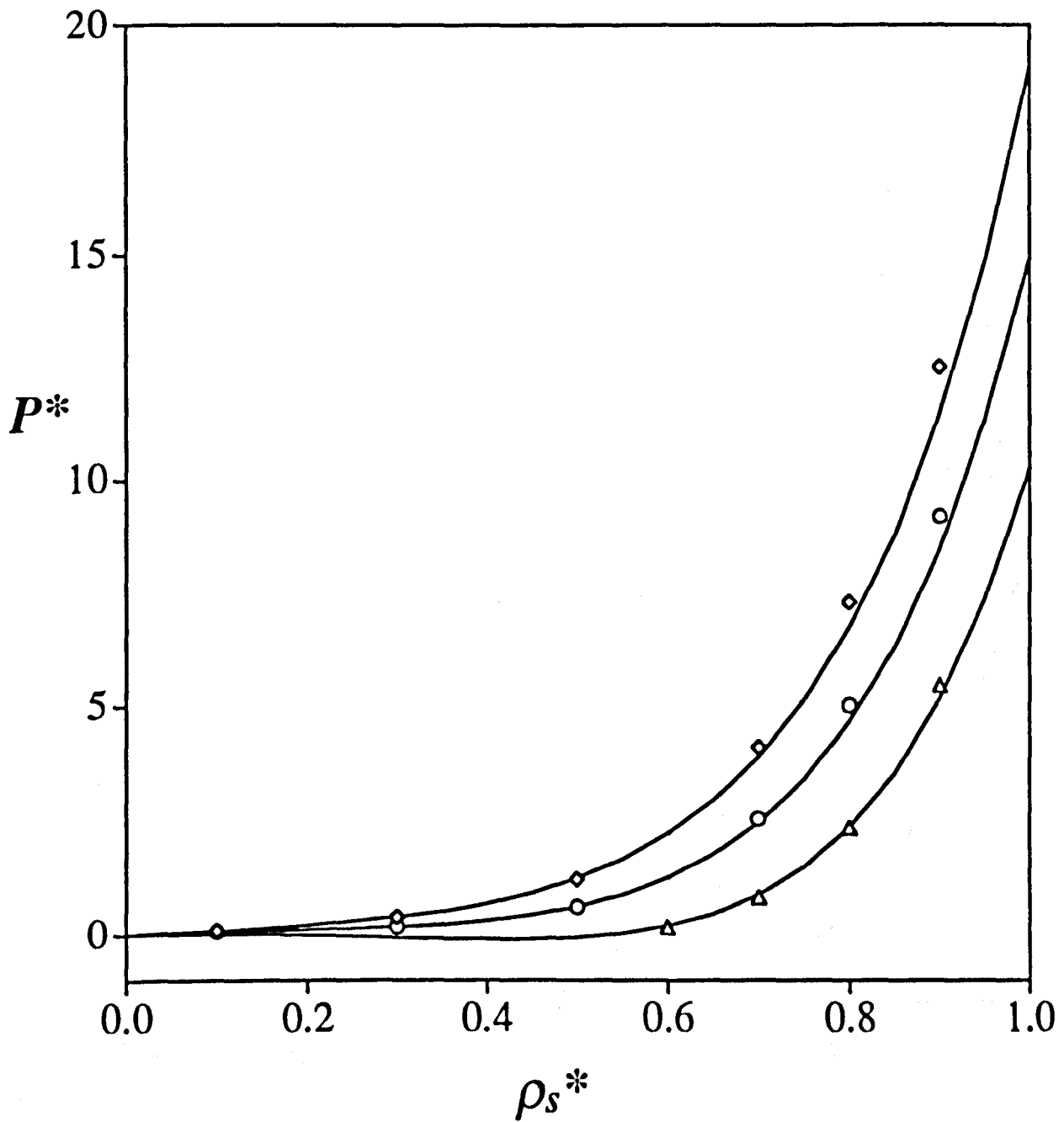


Figure 5.7: The reduced pressure $P^* = P\sigma^3/\epsilon$ of Lennard-Jones chains with $m_s = 4$ as a function of the reduced monomer density $\rho_s^* = \rho_s\sigma^3$. The diamonds, circles and triangles are the molecular dynamics simulation results of Johnson *et al.* [10] for the reduced temperatures of $T^* = kT/\epsilon = 4, 3$ and 2 , respectively. The continuous curves correspond to the SAFT-VR predictions.

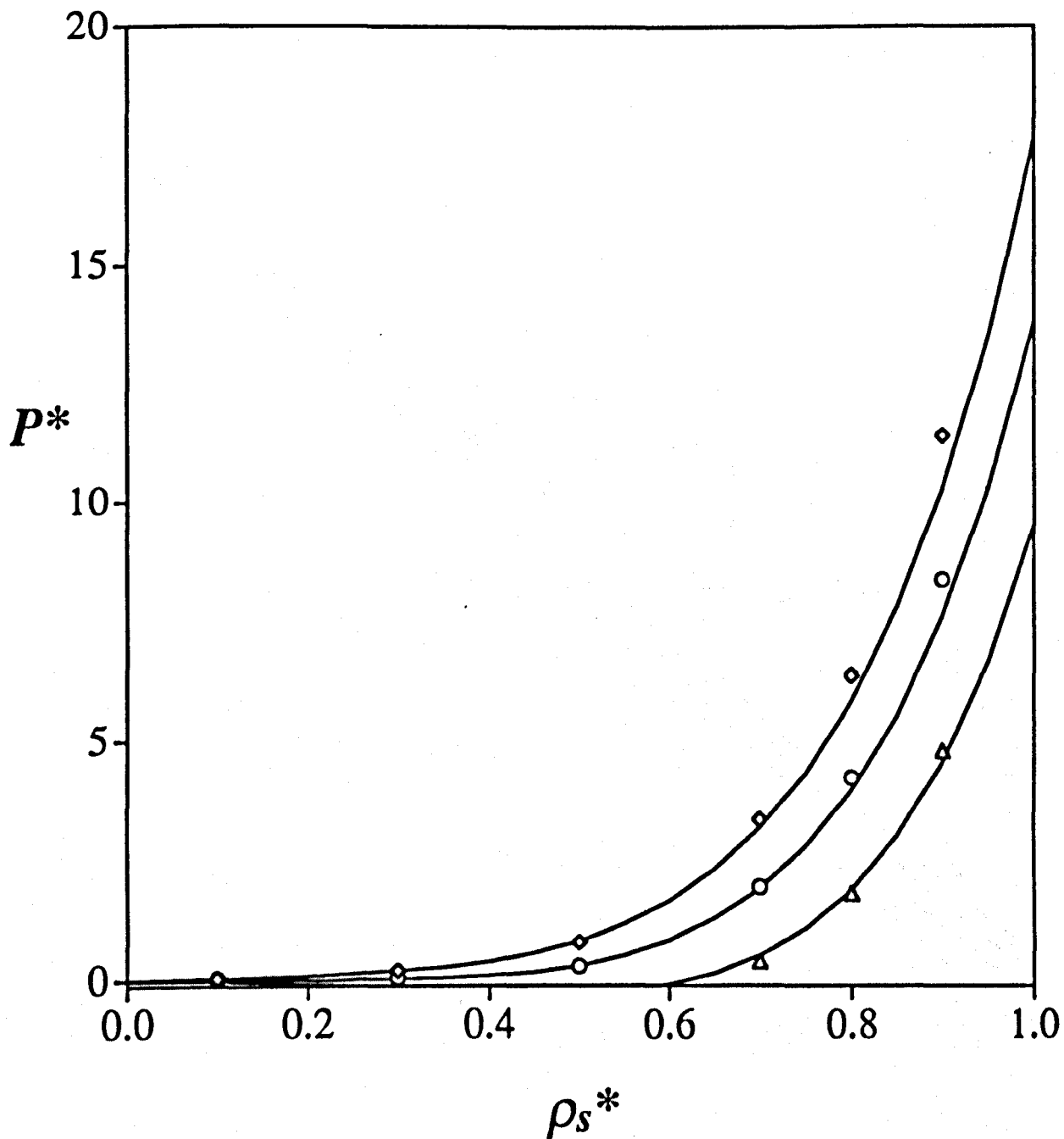


Figure 5.8: The reduced pressure $P^* = P\sigma^3/\epsilon$ of Lennard-Jones chains with $m_s = 8$ as a function of the reduced monomer density $\rho_s^* = \rho_s\sigma^3$. The diamonds, circles and triangles are the molecular dynamics simulation results of Johnson *et al.* [10] for the reduced temperatures of $T^* = kT/\epsilon = 4, 3$ and 2 , respectively. The continuous curves correspond to the SAFT-VR predictions.

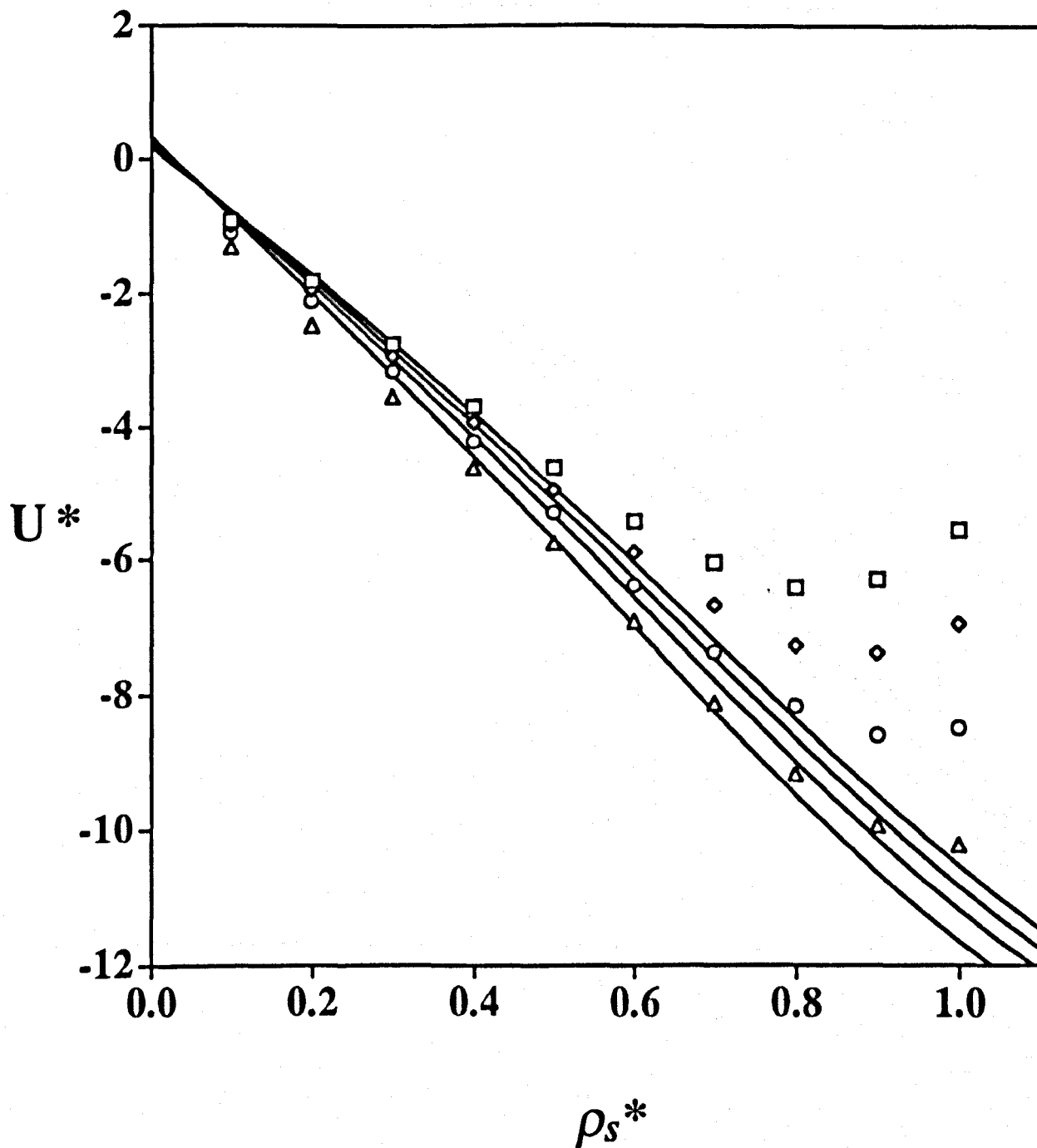


Figure 5.9: The residual internal energy $u^* = u/N\epsilon$ of Lennard-Jones chains with $m_s = 2$ (diatomics) and inverse range of $\lambda = 1.8$ as a function of the reduced monomer density $\rho_s^* = \rho_s \sigma^3$. The squares, diamonds, circles and triangles are the molecular dynamics simulation results of Johnson *et al.* [10] for the reduced temperatures of $T^* = kT/\epsilon = 5, 4, 3$ and 2 , respectively. The continuous curves correspond to the SAFT-VR predictions.

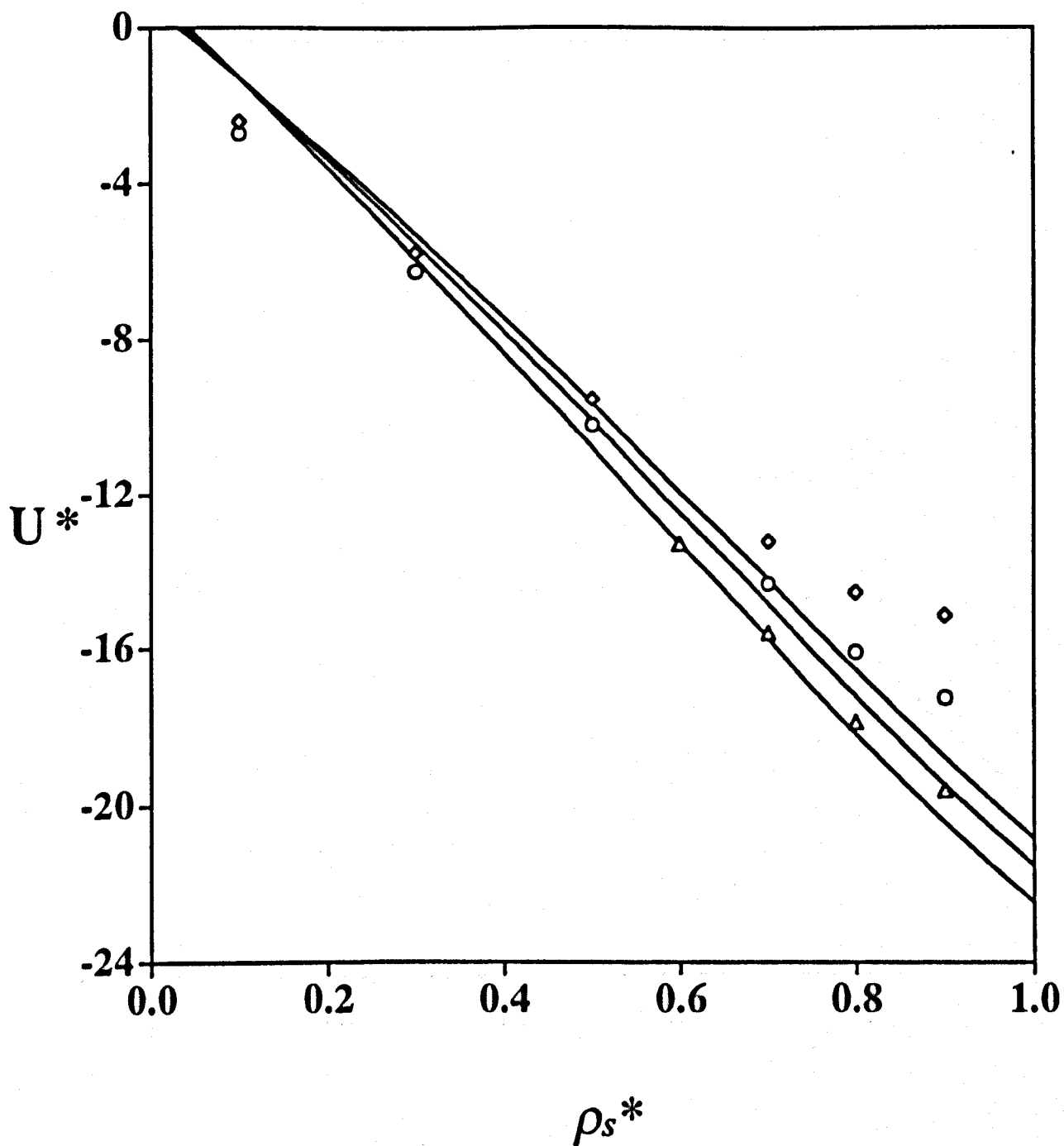


Figure 5.10: The residual internal energy $u^* = u/N\epsilon$ of Lennard-Jones chains with $m_s = 4$ and inverse range of $\lambda = 1.8$ as a function of the reduced monomer density $\rho_s^* = \rho_s\sigma^3$. The diamonds, circles and triangles are the molecular dynamics simulation results of Johnson *et al.* [10] for the reduced temperatures of $T^* = kT/\epsilon = 4, 3$ and 2 , respectively. The continuous curves correspond to the SAFT-VR predictions.

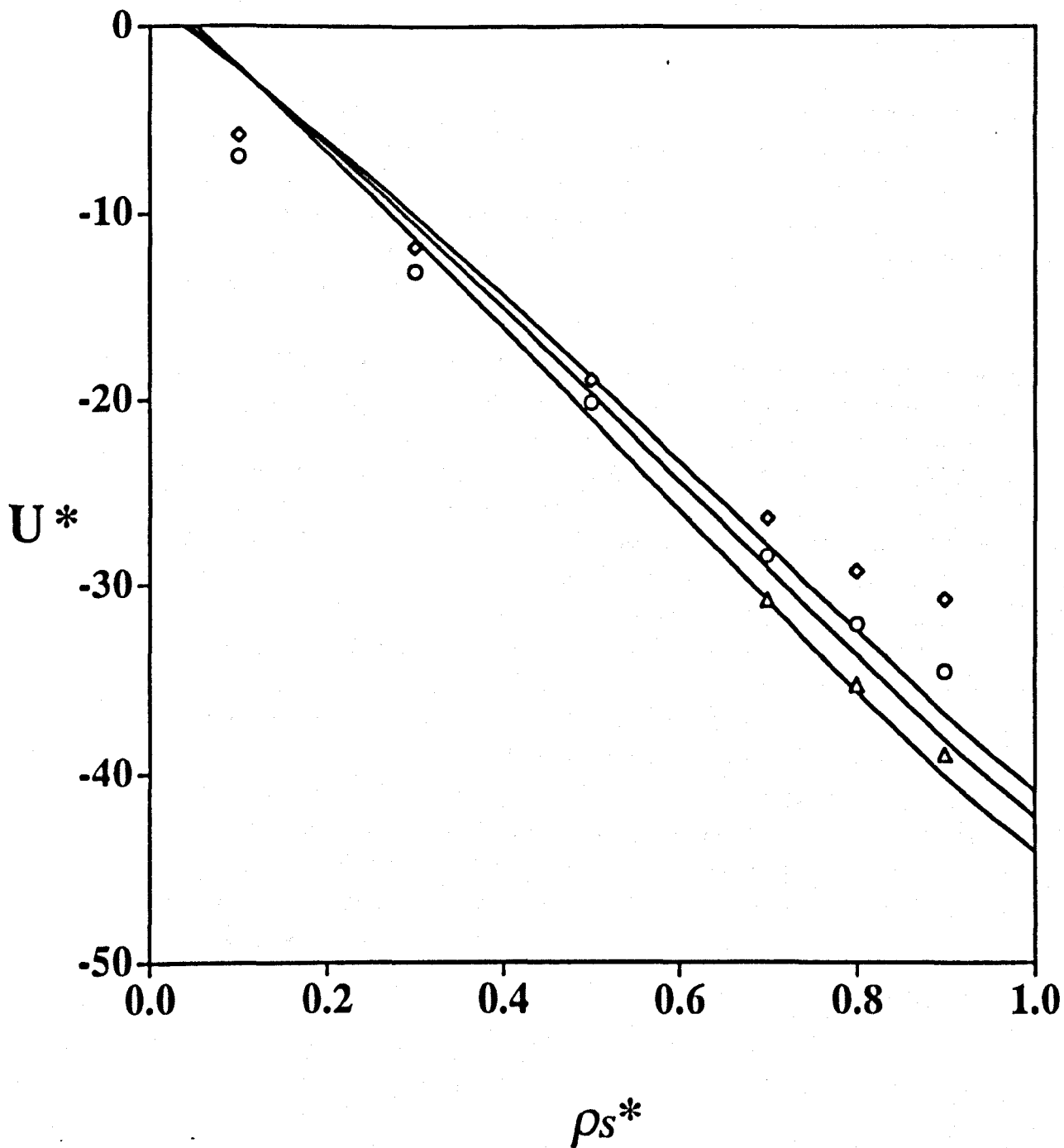


Figure 5.11: The residual internal energy $u^* = u/N\epsilon$ of Lennard-Jones chains with $m_s = 8$ and inverse range of $\lambda = 1.8$ as a function of the reduced monomer density $\rho_s^* = \rho_s \sigma^3$. The diamonds, circles and triangles are the molecular dynamics simulation results of Johnson *et al.* [10] for the reduced temperatures of $T^* = kT/\epsilon = 4, 3$ and 2 , respectively. The continuous curves correspond to the SAFT-VR predictions.

5.5 Conclusions

We have presented the SAFT-VR equations of state for the Yukawa and Sutherland potentials, and have illustrated how the expressions obtained for the Sutherland potential can be used to give a general equation of state for associating chain molecules interacting via potentials with soft-core repulsive interactions. In the case of Lennard-Jones chains, an accurate description is obtained for vapour-liquid coexistence properties using this approach.

The SAFT-VR expressions for the Yukawa fluid are seen to compare favourably with those obtained using the analytical solution of the mean spherical approximation. In the case of the contact value of the radial distribution function of the Yukawa fluid we obtain a recipe which combines both the MSA and the SAFT-VR approaches, which is seen to give results which are in closer agreement with simulation data than those obtained using either the individual MSA or SAFT-VR methods. As a result of the correspondence between the form of the Yukawa potential and the potential experienced by ions in solution, the expressions presented here can be used to describe the phase behaviour of fluids of industrial interest such as electrolytes. In addition, the extension of the SAFT-VR equation of state to systems interacting with potentials of variable repulsive range, leads to the possibility of the study of systems with interaction potentials which are more complex than those which can be modeled by hard-core potentials such as the square well. Furthermore, since the SAFT-VR methodology is easily applied to mixtures [1, 2] the expressions presented here for the pure fluid can find many applications in the prediction of the thermodynamics and phase behaviour of mixtures with specific intermolecular interactions.

Bibliography

- [1] A. Gil-Villegas, A. Galindo, P. J. Whitehead, S. J. Mills, G. Jackson, and A. N. Burgess, *J. Chem. Phys.*, **106**, 4168 (1997).
- [2] A. Galindo, L. A. Davies, A. Gil-Villegas, and G. Jackson, *Mol. Phys.*, accepted (1997).
- [3] C. M. McCabe, A. Galindo, A. Gil-Villegas, and G. Jackson, *Int. J. Thermophys.*, submitted (1997).
- [4] J. A. Barker and D. Henderson, *J. Chem. Phys.*, **47**, 2856 (1967).
- [5] J. A. Barker and D. Henderson, *J. Chem. Phys.*, **47**, 4714 (1967).
- [6] J. A. Barker and D. Henderson, *Rev. Mod. Phys.*, **48**, 587 (1975).
- [7] W. G. Chapman, *J. Chem. Phys.*, **93**, 4299 (1990).
- [8] D. Ghonasgi and W. G. Chapman, *Mol. Phys.*, **79**, 291 (1993).
- [9] M. Banaszak, Y. C. Chiew, R. Olenick, and M. Radosz, *J. Chem. Phys.*, **100**, 3803 (1994).
- [10] J. K. Johnson, E. A. Müller, and K. E. Gubbins, *J. Phys. Chem.*, **98**, 6413 (1994).
- [11] F. A. Escobedo and J. J. de Pablo, *Mol. Phys.*, **87**, 347 (1996).
- [12] T. M. Reed and K. E. Gubbins, *Applied Statistical Mechanics*, McGraw-Hill, (1973).
- [13] L. A. Davies, A. Gil-Villegas, and G. Jackson, *Int. J. Thermophys.*, submitted (1997).
- [14] L. L. Lee, *Molecular Thermodynamics of Nonideal Fluids*, Butterworth Publishers, (1988).
- [15] N. F. Carnahan and K. E. Starling, *J. Chem. Phys.*, **51**, 635 (1969).

- [16] W. G. Chapman, G. Jackson, and K. E. Gubbins, *Mol. Phys.*, **65**, 1057 (1988).
- [17] G. Jackson, W. G. Chapman, and K. E. Gubbins, *Mol. Phys.*, **65**, 1 (1988).
- [18] E. Waisman, *Mol. Phys.*, **25**, 45 (1973).
- [19] P. T. Cummings and E. R. Smith, *J. Chem. Phys.*, **42**, 241 (1979).
- [20] P. T. Cummings and E. R. Smith, *Mol. Phys.*, **38**, 997 (1979).
- [21] D. Henderson, G. Stell, and E. Waisman, *J. Chem. Phys.*, **62**, 4247 (1975).
- [22] P. T. Cummings and E. R. Smith, *Mol. Phys.*, **30**, 1505 (1975).
- [23] E. R. Smith, *Mol. Phys.*, **38**, 823 (1979).
- [24] P. T. Cummings and E. R. Smith, *Mol. Phys.*, **19**, 317 (1978).
- [25] J. S. Høye and G. Stell, *Mol. Phys.*, **32**, 195 (1976).
- [26] J. S. Høye and G. Stell, *J. Stat. Phys.*, **16**, 399 (1977).
- [27] L. Blum and J. S. Høye, *J. Stat. Phys.*, **19**, 17 (1978).
- [28] L. Blum and J. S. Høye, *J. Stat. Phys.*, **22**, 661 (1979).
- [29] M. Ginoza, *J. Phys. Soc. Jpn.*, **54**, 2783 (1985).
- [30] M. Ginoza, *J. Phys. Soc. Jpn.*, **55**, 95 (1985).
- [31] M. Ginoza, *Mol. Phys.*, **71**, 145 (1990).
- [32] D. Henderson, L. Blum, and J. P. Noworyta, *J. Chem. Phys.*, **102**, 4973 (1995).
- [33] J. K. Percus and G. J. Yevick, *Phys. Rev.*, **110**, 1 (1958).
- [34] D. Henderson, E. Waisman, J. L. Lebowitz, and L. Blum, *Mol. Phys.*, **35**, 241 (1978).
- [35] E. Lomba and N. G. Almarza, *J. Chem. Phys.*, **100**, 8367 (1994).
- [36] A. Z. Panagiotopoulos, *Mol. Phys.*, **61**, 813 (1987).
- [37] D. Ghonasgi and W. G. Chapman, *J. Chem. Phys.*, **100**, 6633 (1994).
- [38] F. W. Tavares, J. Chang, and S. I. Sandler, *Mol. Phys.*, **86**, 1451 (1995).

Chapter 6

Case Study: Closed-Loop Immiscibility in Fluids

6.1 Introduction

In this final chapter we present a detailed study of a specific class of phase behaviour, using a combination of the methods discussed previously. The experimentally observed phenomenon of closed-loop liquid-liquid immiscibility is examined; such behaviour is characterised by a closed region of two-phase immiscibility over a specific temperature range on the phase diagram of a system. A simple model system which incorporates the important features of mixtures which exhibit this re-entrant miscibility experimentally is examined with the SAFT-VR equation of state introduced in Chapter 2, and with the computer simulation techniques of Chapter 3. Particular attention is paid to the critical behaviour of this model, both at the high and low temperatures which bound the regions of immiscibility. The nature of the interactions which govern immiscibility in fluids are discussed as a means of introducing the energetic and thermodynamic concepts which lead to the existence of such closed-loop behaviour.

It is common for binary liquid mixtures with weak unlike interactions to have phase diagrams dominated by regions of immiscibility, as represented by the temperature-composition phase diagram shown in Figure 6.1. The two-phase coexistence re-

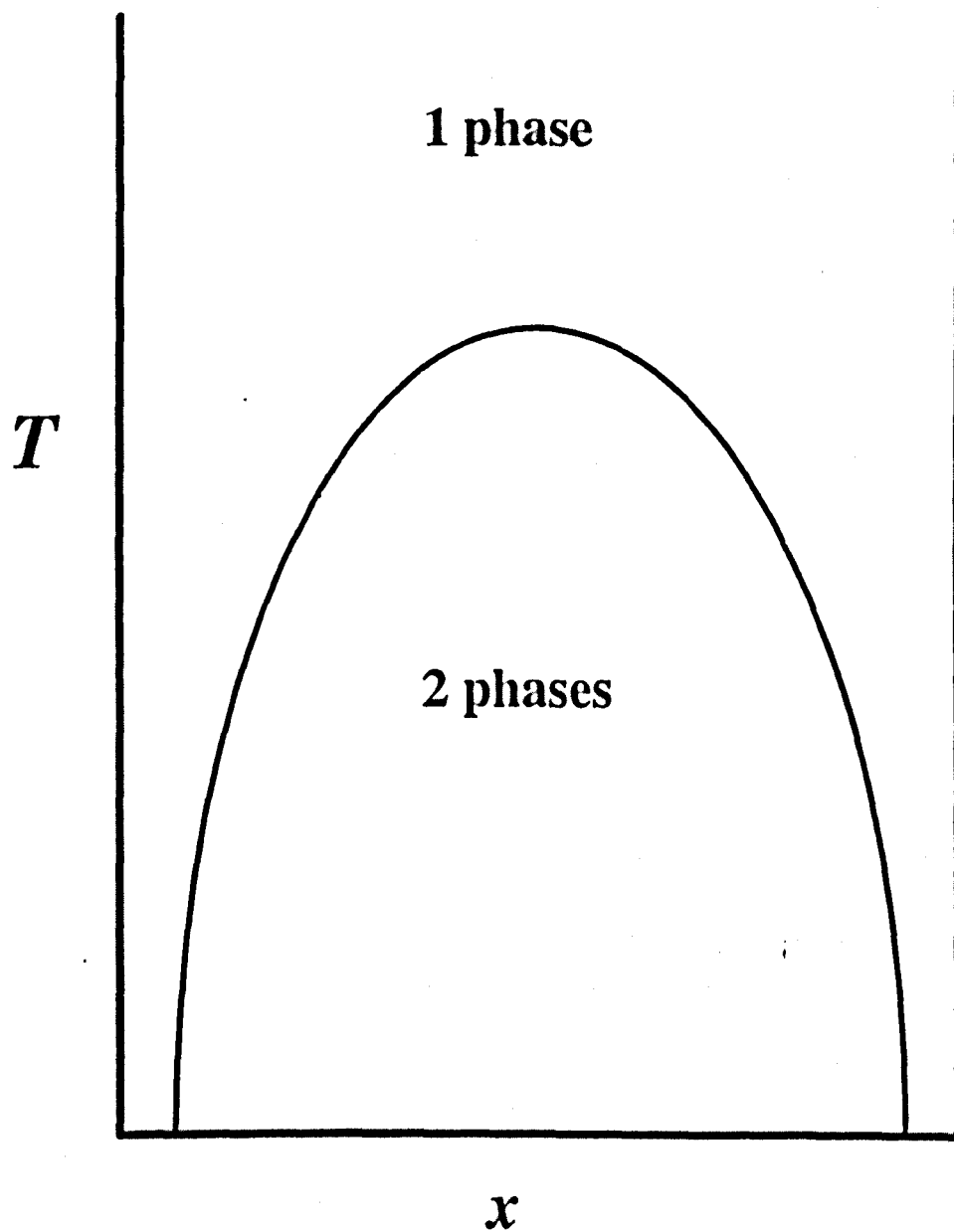


Figure 6.1: Schematic temperature composition phase diagram for a binary liquid mixture with weak unlike interactions.

gion is bounded at high temperatures by an upper critical solution temperature (UCST), the temperature at which the compositions of the two coexisting phases become identical, so that at temperatures above the UCST the system is completely miscible. The immiscibility of the fluid system at temperatures below the UCST is a result of the unfavourable energy which exists between unlike components in the mixture, so that like components have a high affinity for one another. This leads to clustering of particles of the same species, resulting in phase separation into an energetically favourable configuration, with one phase rich in one component and one phase rich in the other component. Precisely at the UCST the entropy of the system has increased sufficiently so that it is the dominant contribution to the Helmholtz free energy of the system. The free energy A is governed by the interplay between the internal energy U and the entropy S :

$$\Delta A = \Delta U - T\Delta S. \quad (6.1)$$

The temperature dependence in the above equation is responsible for the increase in the importance of the entropic contribution to the free energy with respect to the contribution due to the internal energy as temperature increases. At temperatures above the UCST the system no longer consists of regions which are rich in a particular component since the molecules are randomly distributed and the system is miscible. Specific examples of systems which exhibit such behaviour are methane+tetrafluoromethane, hexane+perfluorocyclohexane and methanol+cyclohexane [1].

A specific class of binary mixture which exhibits liquid-liquid immiscibility at temperatures below an UCST has a temperature-composition phase diagram similar to that shown in Figure 6.2. In this case, the region of immiscibility is also seen to decrease in size as temperature is decreased, and is bounded at lower temperatures by a lower critical solution temperature (LCST). Consequently the two phase region in such a system only exists over a specific temperature range between the LCST and the UCST. The system is hence said to possess a closed-loop of immiscibility. Within the classification of binary liquid mixtures proposed by Scott and van Konynenburg [2, 3] this type of phase behaviour is exhibited by type VI mixtures.

An understanding of the thermodynamics responsible for the existence of this LCST is, at first glance, difficult to obtain since the low temperature miscible phase appears to be more disordered and thus have a greater entropy than the immiscible phase. An examination of the common features of systems which exhibit such behaviour does however lead to a logical explanation for this re-entrant miscibility.

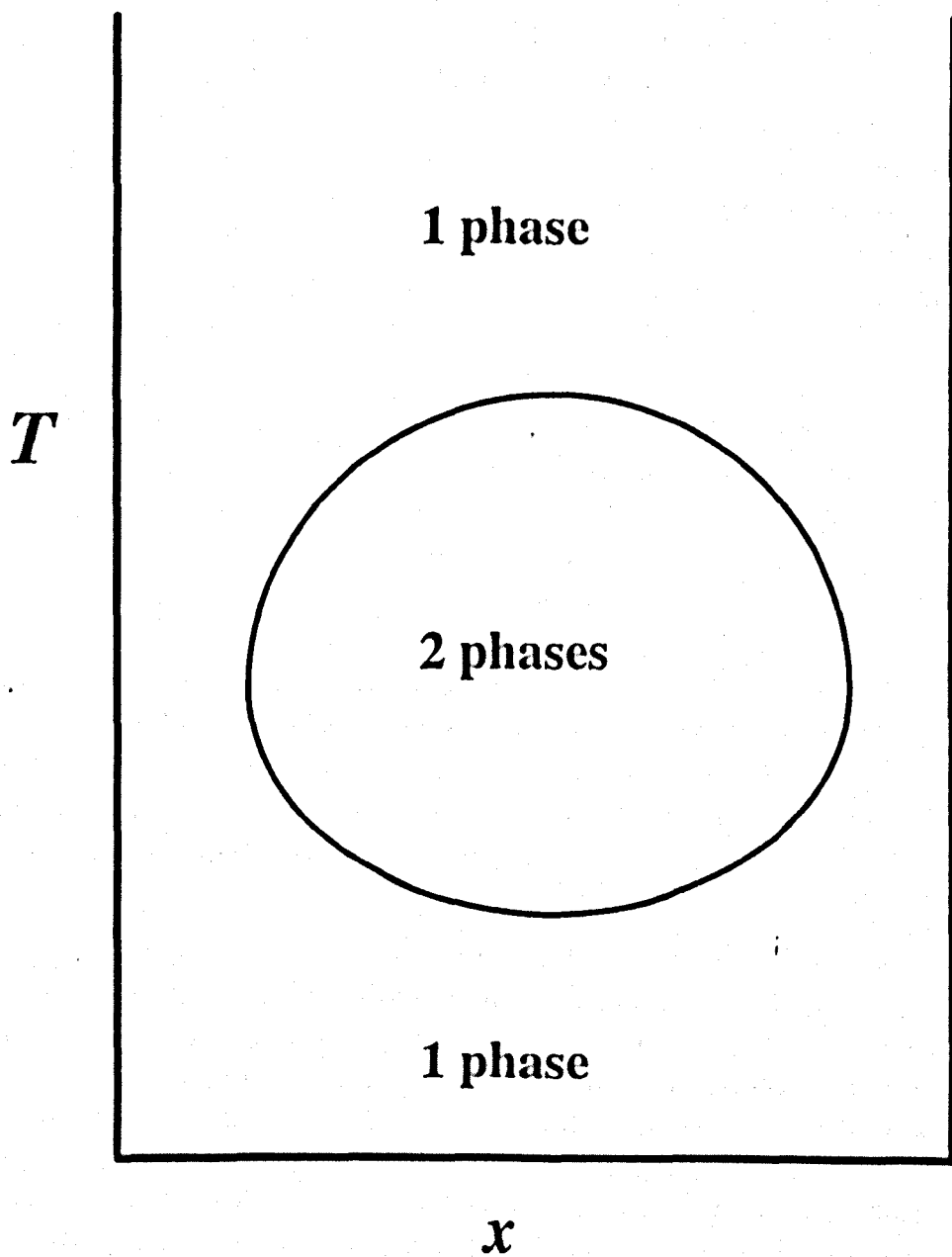


Figure 6.2: Schematic temperature composition phase diagram for a binary liquid mixture with weak unlike interactions and a strong association energy between unlike species which is dominant at low temperatures.

The first experimentally observed closed-loop of immiscibility was reported by Hudson in 1904 [4]. Whilst trying to crystallise nicotine from its aqueous solution in order to prove the existence of the hypothetical nicotine hydrate Hudson discovered the existence of a closed region of immiscibility for the nicotine+water system. Early studies which also report closed-loop behaviour are those of 2-butanol+water [5], 3-methylpyridine+heavy water [6] and guaiacol+glycerine [7]. The existence of re-entrance in the guaiacol+glycerine mixture is questioned in a second study [8] which reports that anhydrous guaiacol+glycerine are completely miscible at all temperatures. It is only in the presence of a small amount of water that the closed-loop of immiscibility appears, as the amount of water in the system is increased the loop also increases in size. Conversely, addition of water to the 3-methylpyridine+heavy water system leads to a decrease in the extent of the region of immiscibility. Considerable interest in the phase behaviour of these two ternary systems exists as a result of the critical role of the third component [6, 9], see Ref. [10] for a review.

The existence of the LCST in these systems was at first considered to be a result of the decomposition of one of the components in the mixture, or by the formation of new chemical compounds [11]. This is reflected in a comment by Hudson [4] with respect to his findings for the nicotine+water system: "It may be assumed that the presence of the hydrate is the cause for the miscibility of the otherwise insoluble liquids-more or less the same way as the addition of alcohol brings about the mixing of water and ether. The hydrate decomposes with increasing temperature and the two liquids, nicotine and water, separate because the quantity of their mutual solvent, namely the hydrate, is greatly reduced". However, no experimental evidence exists to confirm the existence of a different chemical species in these systems, so an alternative explanation must be sought.

A wide range of liquid mixtures are currently known to exhibit this re-entrant behaviour, including mixtures of aliphatic or aromatic alcohols, amines, ethers or ketones with water or alcohols. The common feature of all these systems which can be used to give an explanation of their unusual behaviour, is their ability to form hydrogen bonds. Hydrogen bonds can form between any electronegative atom, such as oxygen, nitrogen or fluorine, and a hydrogen atom via donation of lone pairs of electrons onto the electropositive hydrogen. Due to the short-ranged, directional nature of hydrogen bonds they can only form between two species when they approach one another closely and are in a specific orientation with respect to one another. The angular spread of a hydrogen bond is typically 10° , so that a small displacement of either species can lead to the destruction of the bond. Consequently hydrogen bonding is only observed in low-temperature configurations where molecules have a low mobility and hence remain in specific orientations for

relatively long timescales. However, in order to obtain a complete understanding of why hydrogen bonds are energetically favoured at low temperatures, one must consider the entropic consequences of the bonding process itself. The directional nature of the bond hinders the number of vibrational and rotational degrees of freedom available to a molecule when it is part of a hydrogen-bonded structure. This orientational constraint leads to a decrease in the randomness of the system upon the formation of such bonds, and hence a decrease in the orientational entropy, which is greater than the compositional entropy gained on mixing [12]. At low temperatures we know from Eq. (6.1) that entropic effects do not have a profound effect on the free energy of the system, but the combination of lowering the internal energy and an increase in the compositional entropy due to mixing leads to a favourable free energy for the overall system, despite the decrease in orientational entropy. Hence, for a mixture of two components which are both able to form hydrogen bonds, it is energetically favourable for such bonds to form. This results in the low temperature miscibility of the system since the bonds can occur between both the unlike and like components in the mixture. The unfavourable low orientational entropy of the hydrogen bond gives a more significant contribution to the free energy of the system as temperature increases, so that other configurations, such as those involving the clustering of like species become more energetically attractive. At higher temperatures the system hence moves from a miscible hydrogen-bonded phase to a two-phase system above a particular temperature (the LCST). This is the temperature at which the hydrogen bonded configuration becomes energetically unfeasible. Above this temperature the free energy of the system is dominated by the unfavourable internal energy contribution between unlike species, resulting in the clustering of like species. Hence, the compositional entropy is lowered with respect to that of the hydrogen bonded structure. This decrease, together with the increase in orientational entropy, favours the phase separation of the system for moderately high temperatures. This two-phase region is again bounded at high temperatures by an UCST, the temperature at which the entropic contribution to the free energy becomes greater than that of the internal energy in Eq. (6.1). At this temperature a random distribution of the species within the system is energetically favoured so that the system becomes miscible.

Having obtained a description of the thermodynamics involved in the phenomenon of closed-loop immiscibility it is also important to note that the strength of the hydrogen-bonding interaction plays a critical role in the determination of the extent of the immiscibility in a particular system. A 3-dimensional representation of the effect of a variation in strength of the hydrogen bond between unlike components on the temperature-composition phase diagram of a binary liquid mixture is shown in Figure 6.3. For a bonding strength of zero no LCST is observed and the system is immiscible at all temperatures below the UCST, which is the case shown in Fig.

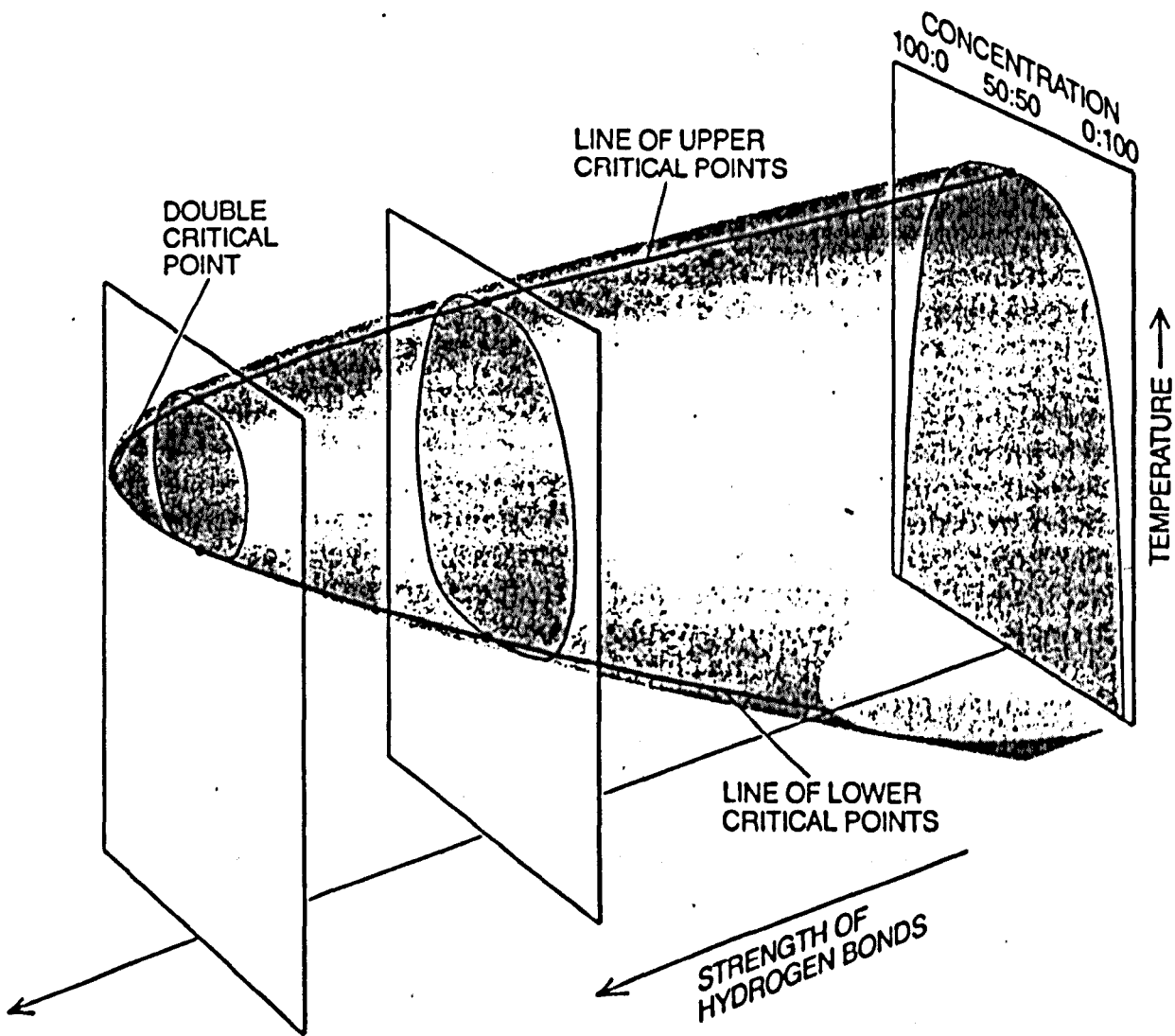


Figure 6.3: A three-dimensional representation of the effect of a variation in the strength of the hydrogen bond which can form between unlike components on the temperature composition phase diagram of the mixture. Each vertical 'slice' corresponds to the phase diagram for the system at that specific bonding strength.

6.1. As the strength of the bonding interaction is increased a LCST appears and a closed-loop of immiscibility is observed, corresponding to the phase diagram shown in Fig. 6.2. The extent of this region of immiscibility decreases as the bonding strength is increased further, until it vanishes completely at the point where the UCST and the LCST occur at the same temperature. Here the system becomes immiscible exactly at the point where it becomes miscible again, which corresponds to a double critical point (DCP) for the system. The effect of varying the strength of the hydrogen bonding interaction on the phase diagram of a system is equivalent to scaling the temperature of that system, and can be examined experimentally by several different routes:

- altering one of the components in the mixture, since different substances have different hydrogen bonding strengths.
- changing the pressure of the system. As the pressure increases the molecules are forced closer together, which leads to an effective increase in the bonding, so that the extent of the close-loop region decreases, vanishing completely at high enough pressures.
- adding a small quantity of a third component which is miscible in the binary mixture. The system continues to have all the essential features of a binary mixture, but (as for the guaiacol+glycerine system) the third component has a significant effect on the phase behaviour of the mixture. In the case of guaiacol+glycerine, addition of water leads to guaiacol forming hydrogen bonds with water, rather than with glycerine, hence decreasing the average bonding interaction between guaiacol and glycerine, which allows the appearance of the immiscible phase.

When hydrogen bonding is able to occur between like species, in addition to unlike, the system will tend to phase separate at temperatures below the LCST. In such cases, the sum of the directional and the non-directional interactions for a pair of like species is greater than for a pair of unlike molecules. The hydrogen bonding of like species to one another results in a decrease in both the compositional and orientational entropy of the mixture, resulting in phase separation at low temperatures. This effect is not generally seen experimentally since systems tend to freeze before the low-temperature miscibility can be observed. The 2-butanol+water mixture is an exception, where at high pressures (or on addition of *t*-butanol) two regions of immiscibility exist, the liquid-liquid immiscible phase bounded by the LCST and the UCST and a low-temperature immiscible phase, bounded by a UCST [13]. At atmospheric pressure the closed-loop merges with the low-temperature two-phase region, resulting in a so-called 'hour-glass' phase

diagram. The point at which the UCST of the low-temperature miscible region occurs at exactly the same temperature as the LCST of the closed-loop corresponds to a double critical point (DCP) for this system. The effect of varying the strength of the hydrogen-bonding interaction between unlike components on the phase diagram where bonding can occur between both unlike and like species, is shown in Figure 6.4. When the hydrogen bonds between unlike components are weak the system has a phase diagram with the form of Fig. 6.1. As the bonding strength increases the immiscible region splits into two separate regions, the closed-loop at higher temperatures and a second immiscible region bounded by an UCST at low temperatures.

Closed-loop behaviour is not only exhibited by simple liquid mixtures, a wide variety of other systems are known to undergo re-entrant phase transitions experimentally. The closed-loop behaviour of complex fluid systems such as microemulsions and polymer solutions [14, 15] and non-ionic surfactants [16, 17], can be discussed within the thermodynamic framework given previously; where the hydrogen bonds which are formed between unlike components are responsible for the low temperature miscibility. Furthermore, the phenomenon of re-entrance is not confined to liquid mixtures; it can be observed in a range of other systems, examples of which are given in Table 6.1.

Table 6.1: Examples of systems which exhibit re-entrant phase transitions together with the reappearing phases in each system (from Ref. [10]).

System	Example	Form of re-entrance
Binary gases	Ne-Kr [18]	Partial immiscibility
Liquid crystals	Octyloxycyanobiphenyl (80CB)+ hexalixycyanobiphenyl (60CB) [19]-[21]	Nematic phase
Ferroelectrics	Rochelle salt ($\text{NaKC}_4\text{H}_4\text{O}_6 \cdot 4\text{H}_2\text{O}$) [22]	non-polar phase
Superconductors	$\text{BaPb}_{0.75}\text{Bi}_{0.25}\text{O}_3$ [23]	Normal state (non-superconducting)
Gels	N,N-dimethacrylamide or N-isopropyl acrylamide gels in (water+dimethyl sulphoxide) [24]	Swollen state
Aqueous electrolytes	Tetra- <i>n</i> -butylammonium thiocyanate (Bu_4NSCN)+water [25]	Miscibility

It is obviously impossible to obtain an explanation of the physics of such diverse

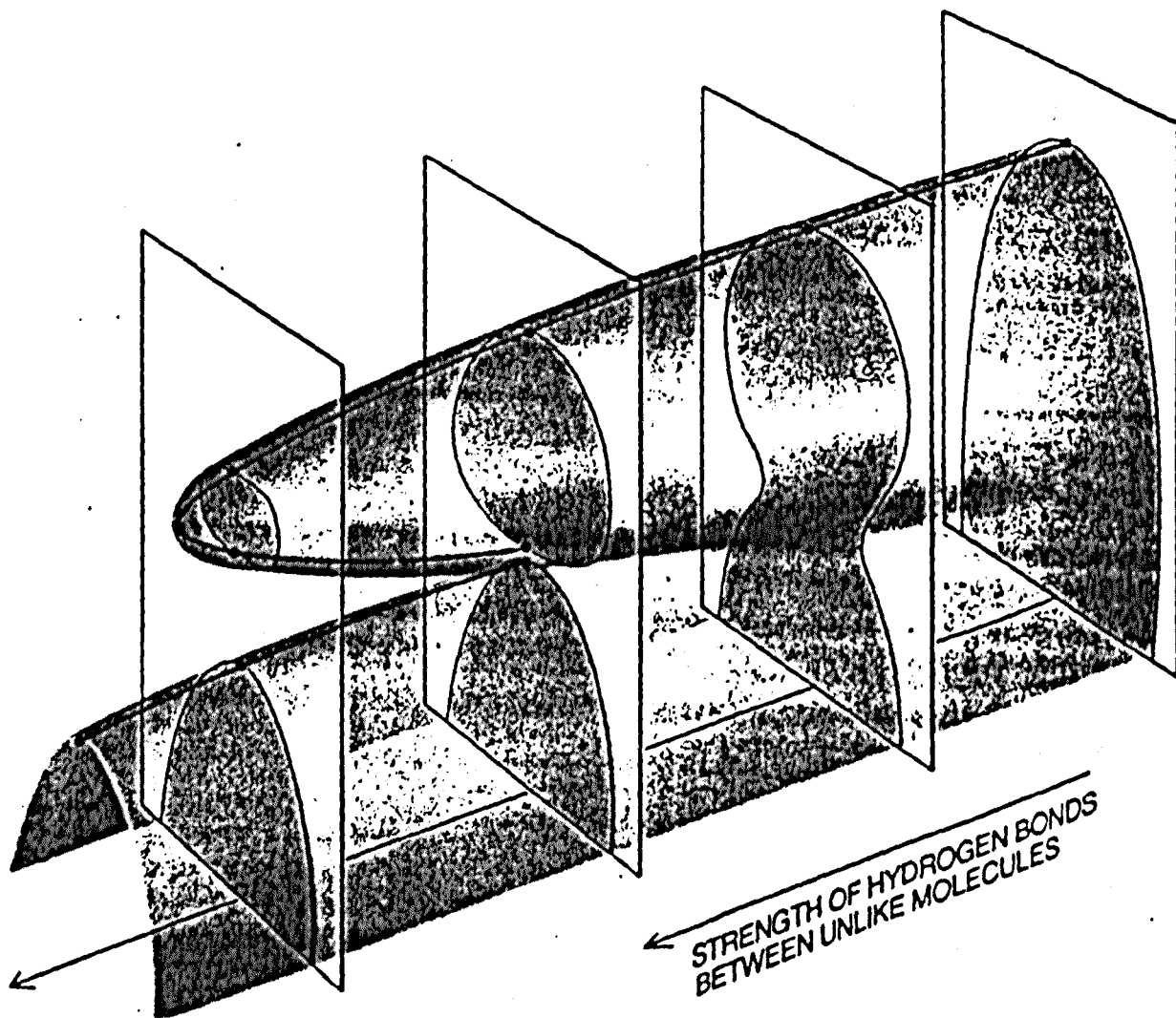


Figure 6.4: A three-dimensional representation of the effect of a variation in the strength of the hydrogen bond which can form both between unlike and like components on the temperature composition phase diagram of the mixture. The strength of the hydrogen bond between like components is constant.

systems using the same thermodynamic ideas as those used to rationalise closed-loop behaviour in liquid mixtures. However, it is possible to identify the competition between the entropy and the internal energy at low temperatures in the free energy expression of Eq. (6.1) as the driving force for the existence of re-entrance in all such systems. In this chapter we will concentrate on the study of the phenomenon of closed-loop immiscibility in binary liquid mixtures, and more specifically in a model mixture which is chosen due to its simplicity. The SAFT-VR equation of state and computer simulation techniques are used to provide a description of the phase behaviour of the model mixture in order to obtain an understanding of the interactions involved. Before describing the methods employed in this study in detail we review the other theoretical studies which have been performed previously for fluid systems which exhibit closed-loop immiscibility.

6.2 Theory of closed-loop behaviour

As a result of the novel nature of this re-entrant behaviour, together with its appearance in a wide variety of systems, theoretical studies of this type of phase behaviour are numerous. A detailed description of all the approaches is beyond the scope of this work. We give a brief review of the early studies and their findings but we are most interested in the use of continuum fluid theories to describe closed-loop immiscibility in mixtures. Early theoretical studies are based on the ideas proposed by Hirschfelder *et al.* [26], in the first study which appears in the literature where hydrogen bonds are cited as being the forces responsible for the existence of a LCST in binary liquid mixtures. Here the low temperature miscibility is explained in terms of the hindering of free rotation of molecules due to directional interactions between unlike components in the mixture. This description of the interactions can be incorporated into lattice model studies, the first of which to actually report a closed-loop of immiscibility for a specific model is the work by Barker and Fock [27]. Their model of a binary liquid mixture consists of a z co-ordinated lattice made up of two types of molecule, each of which has z contact points capable of interacting with the z contact points of the neighbouring molecules. One of the contact points on each molecule is specified as being distinct from all the others. Interactions between like molecules are taken to be zero, whilst interactions between unlike molecules are all considered to be repulsive, unless they exist between the distinct contact point on one molecule and the equivalent distinct contact point on the other molecule, in which case the interaction is considered to be attractive. The conditions of phase equilibria are solved for this model using Bethe-Guggenheim quasichemical approximation [28]. The resulting phase diagrams show both an upper and a lower critical solution temper-

ature, but the overall shape of the coexistence curves are very much narrower than those observed experimentally, and are parabolic at the critical point, whereas the experimental curves are cubic. These apparent failures of the Barker and Fock model can be rationalised in terms of the inadequacy of the quasichemical approximation, rather than as a consequence of the lattice model or the interaction potential used. The quasichemical approximation is a mean-field theory, so it will always predict parabolic behaviour at the critical point. Use of a higher order approximation for the same model [29], where the anisotropic interactions in the model are better accounted for gives results which are in closer agreement with the experimental findings.

After this initial breakthrough, a series of lattice studies were performed on more complex model systems. The first of these is the study by Wheeler [30] which introduces a decorated lattice model, which can be exactly mapped onto a spin $\frac{1}{2}$ Ising model, for which exact solutions are known, and which also predicts the correct cubic (universal) critical behaviour. The known solutions for the Ising magnet are used to predict the phase behaviour of a model system with highly anisotropic interactions, yielding closed-loop regions for a specific choice of interaction parameters. Despite a reasonable agreement between the results obtained from these lattice model studies and their experimentally observed counterparts [31], further studies have been undertaken in order to obtain closer agreement. One of the shortcomings of the use of such lattice models is that they yield inherently symmetrical results, which is obviously not mirrored by real systems. A number of studies have been performed which produce asymmetrical coexistence curves [32]-[34] by including interactions between unlike species. Another series of investigations using the Potts model report closed-loop regions for appropriate interaction parameters [35]-[38], where the interaction potential has a directional component and the system is examined using the Migdal-Kadanoff approximation via renormalisation group theory (known as the Walker and Vause model).

The underlying feature common to all of these lattice-based approaches which is thought to be responsible for the re-entrant behaviour observed is that the interaction potential used in the description of the model fluid is always anisotropic. Despite the basic oversimplification involved in using a lattice to represent the structure of a liquid such studies give a useful qualitative description of the shape of the closed-loop and also illustrate which features of the interaction potential are responsible for the existence of closed-loop immiscibility.

An alternative approach for the description of closed-loop behaviour in mixtures is the use of continuum fluid theories, which account for the structure of the liquid in a more complete manner than lattice models. Such theories consist of the

proposal of an equation of state for a model system which is used to predict the phase behaviour and thermodynamics of the fluid. The large number of continuum studies which currently exist in the literature indicate the importance of such predictive work to theoreticians and experimentalists alike. The most significant early work in this field is that of van Konynenburg and Scott [2, 3], where the van der Waals equation of state [39] is used to obtain the phase diagrams of binary mixtures. The systems examined by van Konynenburg and Scott are assumed to obey the van der Waals mixing rules and the phase behaviour of all but one of the types of phase equilibria are successfully predicted by varying the intermolecular parameters. The failure of this approach to predict the phase behaviour of type VI binary mixtures which possess the closed regions of immiscibility can be understood by examining the nature of the intermolecular interactions described by the van der Waals equation of state. Since re-entrant miscibility is only observed in lattice models which contain short-ranged, directional interactions, one expects that the equivalent criterion should hold in the case of continuum theories. The van der Waals equation has no provision for such temperature dependent interactions, so that its failure to predict the re-entrant behaviour of the type VI mixture is not unexpected. Numerous studies have subsequently been performed in order to obtain an equation of state which can predict the low-temperature miscibility of such systems. The SAFT equation of state has been used successfully in this context.

A simplified version of the SAFT-VR equation of state is known to predict the closed-loop phase behaviour of a model system [40]. The model examined in Ref. [40] consists of a binary mixture of equal sized-spheres with one off-centre association site per sphere, these sites are included to account for the directional nature of the hydrogen-bond. The version of SAFT used in Ref. [40] differs from the SAFT-VR equation of state given in Chapter 2 in the nature of the dispersive interactions, in the simplified SAFT-IIS approach they are given by the van der Waals equation. The SAFT-IIS equation of state is also used in a global study of model binary mixtures of water+alkanols [41]. The effect of chain length and association on the phase equilibria are presented in Ref. [41], where closed-loop regions are observed for intermediate chain lengths and bonding energies. A recent application of this simplified SAFT approach is in the prediction of the closed-loop phase behaviour of binary aqueous solution of 1-butanol, *n*-butoxyethanol and *n*-decylpentoxyethylenether ($C_{10}E_5$) [42]. The extent of the immiscibility in real mixtures is seen to be accurately predicted using the SAFT-IIS equation of state, via the fitting of a specific number of interaction parameters. In this work we re-examine the phase behaviour of the symmetrical binary mixture introduced in Ref. [40] using the SAFT-VR equation of state.

Before presenting the specific SAFT-VR expressions for the model system it is important to discuss other recent continuum theory studies which also examine the phenomenon of closed-loop immiscibility. By combining the results obtained from lattice studies and the knowledge that the van der Waals equation of state is unable to predict closed-loop behaviour, it is not over-presumptuous to state that a short-ranged directional interaction must be included in the potential model, in order for a given model system to exhibit re-entrant miscibility. It is also widely believed that the appearance of the LCST experimentally in systems is a direct result of hydrogen-bonding between the two components in the mixture, so that the directional nature and the temperature dependence of such bonding must be accounted for in any theoretical studies of such associating fluids. However, certain continuum fluid studies present results which contradict the above statements, that is, they predict closed-loop immiscibility for systems with isotropic potentials. We will discuss the findings of each of these studies in turn.

The global study of the phase diagram of a model mixture interacting via the Lennard-Jones potential by Boshkov *et al.* [43]-[45] is one such study. A closed-loop of immiscibility is reported for a system with only spherically symmetrical interactions, where the model does not account for low temperature directional interactions. By taking a closer look at the methods by which they arrive at their results one can uncover possible sources of error. The configurational part of the free energy is calculated in the work of Refs. [43]-[45] using a solution for the pure component Lennard-Jones fluid obtained using the Ree equation of state [46]. This equation of state is obtained by performing a fitting to computer simulation data points over a temperature range of $0.54 < T/T_c < 1.93$. The closed-loop of immiscibility presented in the work by Boshkov *et al.* has a temperature range of $0.45 < T/T_c < 0.50$ [40], indicating that the Ree equation of state has been used outside its range of validity. Another important observation, mentioned in the original Ree paper (Ref. [46]) is that the equation should not be used below the triple point of the system, which for the Lennard-Jones fluid occurs at $T/T_c = 0.49$ [46]. This indicates that the results presented by Boshkov *et al.* should be viewed with caution.

A series of studies by van Pelt *et al.* [47]-[49] also predicts closed-loop immiscibility for an isotropic potential model, in this case for the simplified perturbed hard chain theory (SPHCT) [50]. Within the SPHCT equation the attractive part of the partition function is written in terms of the temperature and density dependence of the co-ordination number, which is a function of the Boltzmann factor of the the interaction potential. The results obtained using this attractive term compare favourably with computer simulation results in the one-phase region of the phase diagram, but the agreement decreases rapidly in the gas-liquid, two-phase region.

This indicates that such an attractive term within the SPHCT equation should not be relied upon to give accurate predictions below the gas-liquid critical point. However, the work van Pelt *et al.* reports the existence of closed-loop regions in the temperature range $T/T_c \leq 1.0$, which is exactly the region in which the attractive term is considered to be invalid. The occurrence of closed-loop regions for the SPHCT equation at these low temperatures is believed to be a result of the inverse exponential temperature dependence in the expression for the co-ordination number [41], rather than a consequence of the true phase behaviour of the system.

A recent study of the topology of the type VI phase diagram attempts to illustrate which features of an equation of state are important in order for it to be able to predict the existence of closed-loop regions on the global phase diagram for a model system [51]. A version of the SAFT equation of state where the repulsive interactions are given by a van der Waals description is used in Ref. [51]. The occurrence of critical saddle points in the binary liquid-gas critical line are reported to be responsible for the appearance of both an upper and a lower critical point on the phase diagram. The investigation presented in Ref. [52] concludes that type VI behaviour can be rationalised for simple, non-directional equations of state, but that these theoretical findings cannot be considered as being experimentally observable since they occur for highly un-physical models with un-realistic interactions.

The confusion which currently exists in the literature with respect to the nature of the interaction potential of an equation of state which is either able or unable to predict closed-loop immiscibility for a model system provides the motivation for the work presented in this chapter. Within theoretical descriptions of systems the most 'exact' results are those obtained from computer simulation studies. We undertake a Gibbs ensemble Monte Carlo (GEMC) simulation study of a model mixture. The system examined consists of monomeric segments with short-ranged directional interaction sites, and is shown to exhibit closed-loop immiscibility for a specific choice of interaction parameters using the SAFT-VR equation of state. The results obtained from a computer simulation study of this model system can be presented as substantial evidence that anisotropic interactions are required in order for a model system to exhibit a closed region of immiscibility. To date no simulation results have been reported for a specific potential model where both an upper and a lower critical solution temperature can be observed on the phase diagram.

In the following section we briefly summarise the SAFT-VR equation of state for the binary mixture of interest, illustrating the prediction of phase behaviour. The GEMC simulation technique used to give comparable results is subsequently presented. Additionally, simulations performed in the semigrand canonical ensemble

are used to estimate both the upper and lower critical temperatures of the system using finite-size scaling (FSS) methods.

6.3 SAFT-VR prediction

The phase behaviour of a two-component model mixture consisting of square-well monomer segments with equal diameter $\sigma = \sigma_{11} = \sigma_{12} = \sigma_{22}$, no unlike interactions $\epsilon_{12} = 0$, and $\epsilon = \epsilon_{11} = \epsilon_{22}$ with fixed interaction range $\lambda = \lambda_{11} = \lambda_{22} = 1.5$, has been examined previously using the SAFT-VR equation of state in Chapter 4. By specifying that there is no attraction between unlike components, we induce the system to phase separate leading to the existence of a large region of liquid-liquid immiscibility, which is bounded at high temperature by an UCST. Gibbs ensemble computer simulations for this system have also been reported [53, 54], where the phase diagrams presented confirm the SAFT-VR prediction in showing no regions of low-temperature miscibility and no LCST. In order for such a model to be able to associate at low temperatures a short-ranged square-well interaction site is placed at an off-centred position on each sphere. In order for bonding to occur between two sites on adjacent particles in the mixture the sites must be in a specific orientation with respect to one another and are also required to be within a distance shorter than the range of the site-site interaction. Such constraints mimic the physical constraints of hydrogen bonding within an experimental system. This model system has been examined previously [40].

As discussed in Chapter 2 the Helmholtz free energy for a mixture of chain molecules within the general SAFT-VR approach can be written as a sum of individual contributions [55, 56]

$$\frac{A}{NkT} = \frac{A^{IDEAL}}{NkT} + \frac{A^{MONO.}}{NkT} + \frac{A^{CHAIN}}{NkT} + \frac{A^{ASSOC.}}{NkT}. \quad (6.2)$$

The SAFT-VR expressions for the ideal and monomeric contributions to the Helmholtz free energy for the associating mixture are identical to those presented for the symmetrical mixture of square-well monomers in Chapter 4. Since the mixture examined here also only consists of monomer segments, there is no contribution to the Helmholtz free energy due to chain formation, so that $A^{CHAIN} = 0$.

The contribution to the free energy due to the association mediated by the s_i sites on molecules of species i can be described within the framework of the theory of

Wertheim as [57]

$$\frac{A^{ASSOC.}}{NkT} = \sum_{i=1}^n x_i \left[\sum_{a=1}^{s_i} \left(\ln X_{a,i} - \frac{X_{a,i}}{2} \right) + \frac{s_i}{2} \right]. \quad (6.3)$$

The first sum is over the number of species i in the mixture and the second sum is over all sites a on a molecule of type i . The fractions of molecules of species i not bonded at a particular site a , $X_{a,i}$, is given by solution of the simultaneous equations:

$$X_{a,i} = \frac{1}{1 + \sum_{j=1}^n \sum_{b=1}^{s_j} \rho x_j X_{b,j} \Delta_{a,b,i,j}}, \quad (6.4)$$

where

$$\Delta_{a,b,i,j} = K_{a,b,i,j} f_{a,b,i,j} g_{ij}^{SW}(\sigma_{ij}) \quad (6.5)$$

is specific for each a - b site-site interaction, and incorporates the volume available for bonding $K_{a,b,i,j}$, and the strength of the association via the Mayer function $f_{a,b,i,j} = \exp(\varepsilon_{ij}/kT) - 1$ of the square-well potential. The contact value of the radial distribution function for the square-well interaction, $g_{ij}^{SW}(\sigma_{ij})$ is evaluated within the SAFT-VR approach for mixtures [55, 56] using a first order perturbation expansion

$$g_{ij}^{SW}(\sigma_{ij}) = g_{ij}^{HS}(\sigma_{ij}) + \beta \varepsilon_{ij} g_1(\sigma_{ij}). \quad (6.6)$$

The contact value of the radial distribution function for the hard-sphere reference system $g_{ij}^{HS}[\sigma_{ij}; \zeta_3^{eff}]$ is evaluated at an effective packing fraction ζ_3^{eff} , using the expression of Boublík [58] and Mansoori *et al.* [59]

$$g_{ij}^{HS}[\sigma_{ij}; \zeta_3^{eff}] = \frac{1}{1 - \zeta_3^{eff}} \quad (6.7)$$

$$+ 3 \frac{\sigma_{ii}\sigma_{jj}}{\sigma_{ii} + \sigma_{jj}} \frac{\zeta_2^{eff}}{(1 - \zeta_3^{eff})^2} + 2 \left(\frac{\sigma_{ii}\sigma_{jj}}{\sigma_{ii} + \sigma_{jj}} \right)^2 \frac{\zeta_2^{eff^2}}{(1 - \zeta_3^{eff})^3}. \quad (6.8)$$

The first order perturbation term, $g_1(\sigma_{ij})$ is obtained from a self-consistent calculation of the pressure using the Clausius virial theorem, as explained in Chapter 2.:

$$g_{ij}^{SW}[\sigma_{ij}; \zeta_3] = g_{ij}^{HS}[\sigma_{ij}; \zeta_3] + \beta \varepsilon_{ij} \left[g_{ij}^{HS}[\sigma_{ij}; \zeta_3^{eff}] + (\lambda_{ij}^3 - 1) \left(\frac{\lambda_{ij}}{3} \frac{\partial g_{ij}^{HS}[\sigma_{ij}; \zeta_3^{eff}]}{\partial \lambda_{ij}} - \rho_s \frac{\partial g_{ij}^{HS}[\sigma_{ij}; \zeta_3^{eff}]}{\partial \rho_s} \right) \right]. \quad (6.9)$$

The components in the mixture are of equal diameter and each sphere only has one interaction site. Bonding is only permitted between unlike components in the mixture, i.e., between site a on component 1 and site b on component 2 when the two sites are within a distance τ_c . The expression for the contribution to the

Helmholtz free energy due to association of Eq. (6.3) thus simplifies to

$$\frac{A^{ASSOC.}}{NkT} = x_1 \left(\ln X_a - \frac{X_a}{2} + \frac{1}{2} \right) + x_2 \left(\ln X_b - \frac{X_b}{2} + \frac{1}{2} \right). \quad (6.10)$$

The fractions X_a and X_b of molecules of species 1 and 2 not bonded at sites a and b , respectively, are given by

$$X_a = \frac{1}{1 + \rho x_2 X_b \Delta_{a,b}}, \quad (6.11)$$

and

$$X_b = \frac{1}{1 + \rho x_1 X_a \Delta_{a,b}}, \quad (6.12)$$

where

$$\Delta_{a,b} = K_{a,b} f_{a,b} g^{SW}(\sigma). \quad (6.13)$$

The volume available for bonding between two sites a and b which are positioned at a distance r_d from the centre of spheres with diameter σ and have an interaction range r_c is given by [40]

$$K_{a,b} = 4\pi^2 \sigma \{ \ln[(r_c + 2r_d)/\sigma] (6r_c^3 + 18r_c^2 r_d - 24r_d^3) \quad (6.14)$$

$$+ (r_c + 2r_d - \sigma)(22r_d^2 - 5r_c r_d - 7r_d \sigma - 8r_c^2 + r_c \sigma + \sigma^2) \} / (72r_d^2). \quad (6.15)$$

The contact value of the square-well distribution function simplifies to

$$g^{SW}[\sigma; \eta] = g^{HS}[\sigma; \eta] \quad (6.16)$$

$$+ \beta \epsilon \left[g^{HS}[\sigma; \eta^{eff}] + (\lambda^3 - 1) \frac{\partial g^{HS}[\sigma; \eta^{eff}]}{\partial \eta^{eff}} \left(\frac{\lambda}{3} \frac{\partial \eta^{eff}}{\partial \lambda} - \eta \frac{\partial \eta^{eff}}{\partial \eta} \right) \right],$$

where $g^{HS}[\sigma_{ij}; \zeta_3]$ and $g^{HS}[\sigma_{ij}; \zeta_3^{eff}]$ become the Carnahan and Starling equation [60, 61] with the total and effective packing fractions, respectively

$$g^{HS}[\sigma; \eta] = \frac{1 - \eta/2}{(1 - \eta)^3}, \quad (6.17)$$

and

$$g^{HS}[\sigma; \eta^{eff}] = \frac{1 - \eta^{eff}/2}{(1 - \eta^{eff})^3}, \quad (6.18)$$

with $\eta^{eff} = \zeta_3^{eff}$. The parameterisation for η^{eff} obtained for the pure square-well fluid in Ref. [55] is used.

The thermodynamic properties of this mixture used in the determination of phase equilibria are obtained from the expressions for the Helmholtz free energy using the standard thermodynamic relations given earlier. In the discussion of the pre-

diction of phase behaviour obtained using the SAFT-VR equation of state for this associating system a number of reduced variables are used. The strength of the site square-well interaction is reduced with respect to the magnitude of the square-well interaction of the monomeric segments $\epsilon_{a,b}^* = \epsilon_{a,b}/\epsilon$. The reduced temperatures and pressures are defined in terms of the van der Waals parameters α , which is given for the square-well potential by $\alpha = -4\epsilon(\lambda^3 - 1)$ and $b = 2/3\pi\sigma^3$. The pressure is given by $P^* = pb^2/\alpha = pb/\epsilon$ and the temperature by $T^* = kTb/\alpha$. These values for the pressure and temperature are also reduced with respect to the critical pressure and temperatures of the pure component square-well monomer, so that $P_r = P^*/P_c^*$ and $T_r = T^*/T_c^*$. Where the critical values are $P_c^* = 0.00792563199$ and $T_c^* = 0.139942105$.

The PT projection for the binary square-well mixture with a site-site interaction energy of $\epsilon_{AB}^* = 15$ obtained using the SAFT-VR equation of state is shown in Figure 6.5. The vapour pressure curves of the pure components are represented by the solid curve, both curves lie on the same line due to the symmetry of the mixture studied here. The dashed curve which originates at the vapour-liquid critical point of the pure component and moves to higher pressures and temperatures represents the gas-liquid critical line. The distinction between gas and liquid phases is arbitrary at high pressures and temperatures. In this discussion we use the term gas to describe a phase which has its origins in the vapour phase of the pure component. This gas-liquid critical line goes through a minimum in temperature close to the critical point of the pure component. This critical line then moves to higher pressures, reaching a maximum before ending at a double critical point DCP, where it connects with the three-phase line. The bold curve which originates at high pressures is the three-phase line for the mixture, along which two liquid phases and one gas phase coexist. The three-phase line ends at the double critical point, which corresponds to the point at which three phases simultaneously vanish. The dashed curve which extends from the DCP to higher temperatures going through a minimum in pressure, is the liquid-liquid critical line. This line forms the boundary of the closed-loop region for this mixture, for pressures between that of the DCP and of the minimum in the liquid-liquid critical line. In this region the system is seen to possess two liquid-liquid critical points, the LCST at lower temperatures and the UCST at higher temperatures. A third critical point is observed at lower temperatures, where the gas-liquid critical line is crossed.

The effect of varying the strength of the site-site interaction on the phase behaviour of this model system is shown in Figure 6.6. Decreasing the association strength from $\epsilon_{a,b}^* = 15$ to $\epsilon_{a,b}^* = 14$ shrinks the the minimum in the liquid-liquid critical line, and hence the extent of closed-loop immiscibility exhibited by the system. A further decrease of the magnitude of the interaction energy to $\epsilon_{a,b}^* = 13$ leads to the

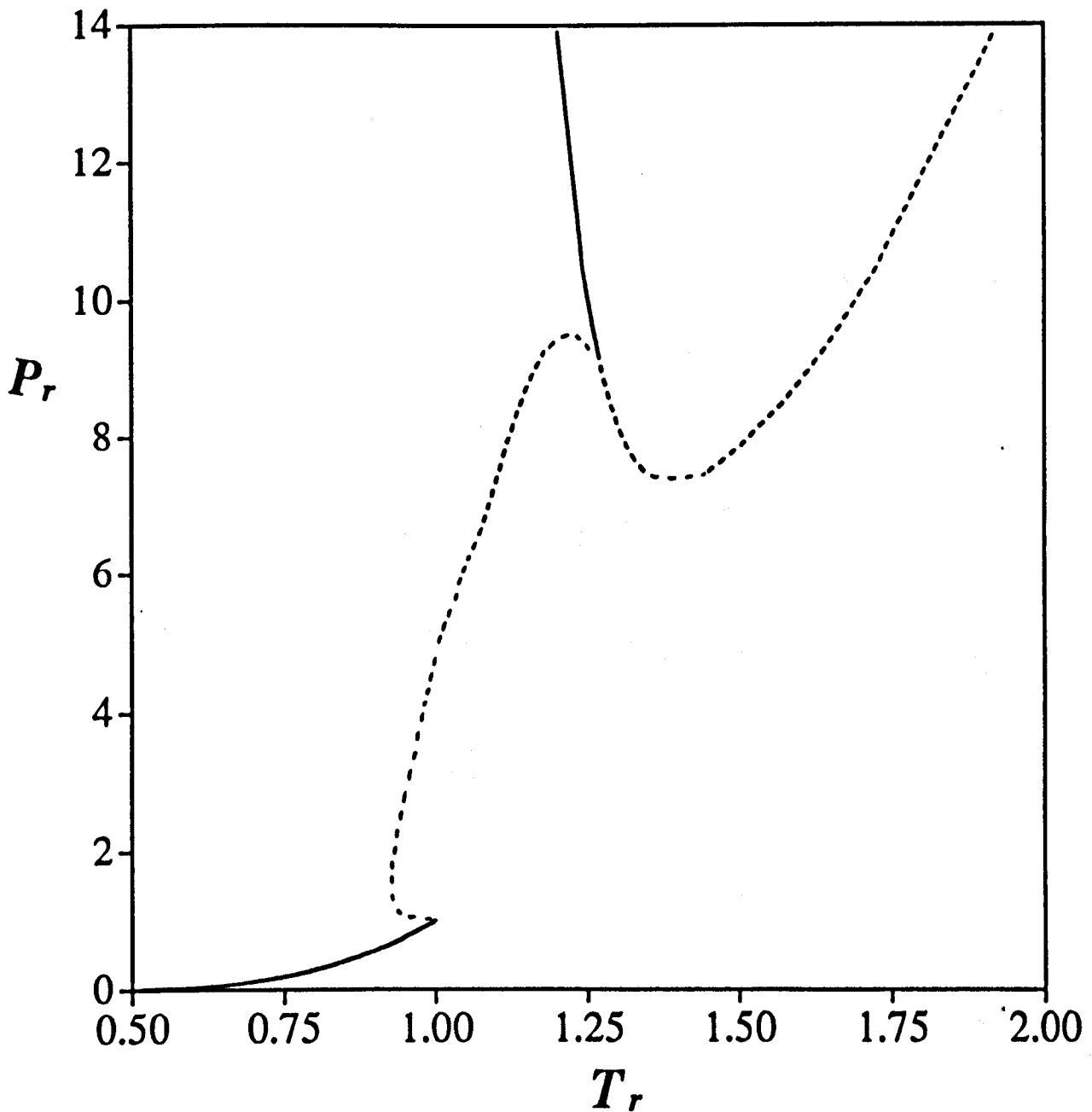


Figure 6.5: Pressure-temperature projection for the binary associating square-well mixture with a bonding strength of $\epsilon_{a,b}^* = 15$ obtained using the SAFT-VR equation of state. The reduced pressure $P_r = P^*/P_c^*$ and reduced temperature $T_r = T^*/T_c^*$ are defined in terms of the pure component values, given in the text. The solid curve at low pressures and temperatures corresponds to the vapour-liquid curve of the pure component, whilst the solid curve at high pressures and temperatures corresponds to the three-phase line of the mixture. The dashed curves correspond to the critical lines, gas-liquid at low pressures and temperatures, and liquid-liquid at high pressures and temperatures.

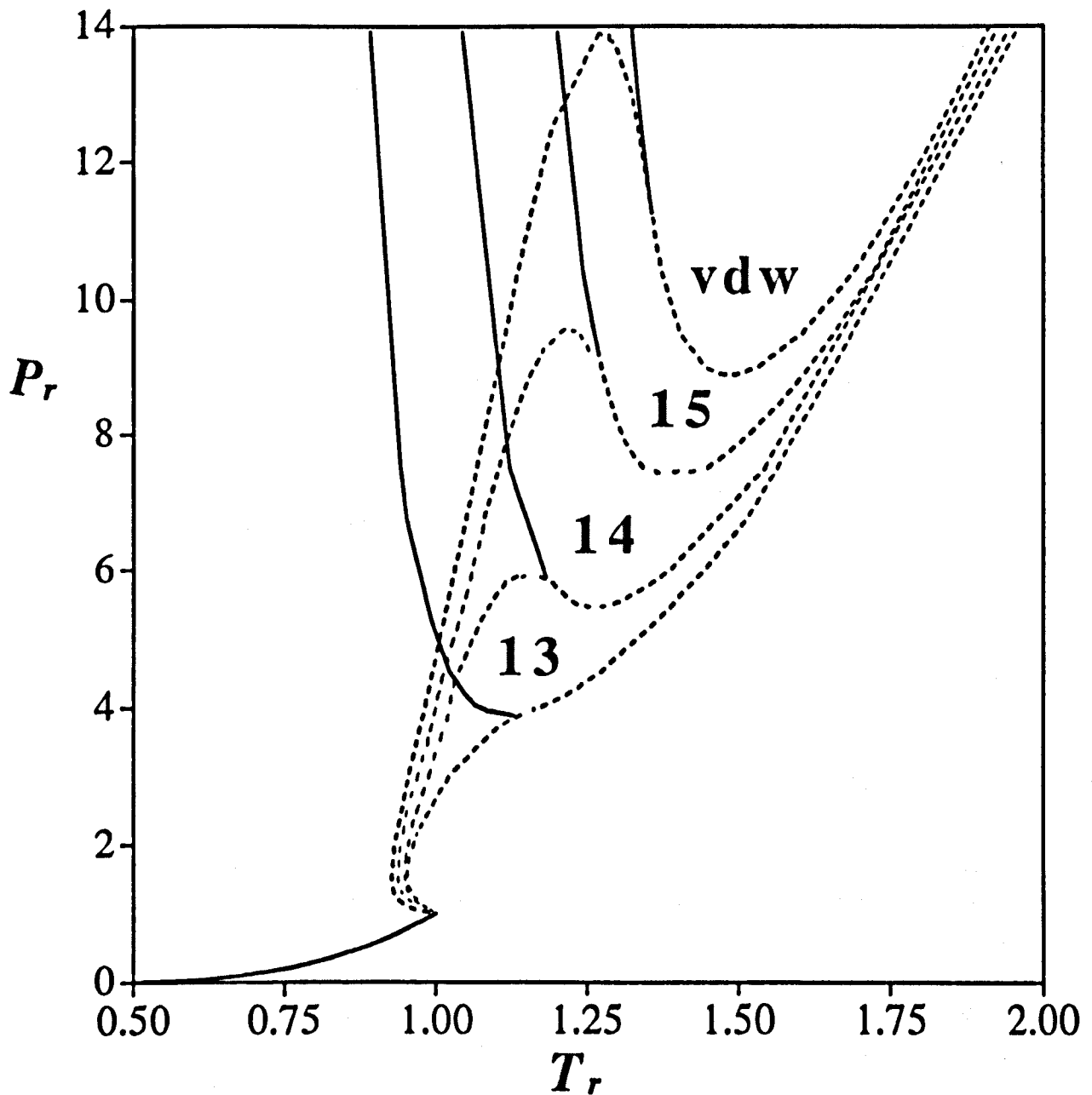


Figure 6.6: Pressure-temperature projection for the binary associating square-well mixture with a range of bonding strengths of $\epsilon_{a,b}^* = 13, 14$ and 15 obtained using the SAFT-VR equation of state, see Figure 6.5 for details. The curves are labelled with the corresponding value of the site-site interaction energy. Also shown (labelled vdw) is the equivalent prediction obtained using the SAFT-IIS equation of state given in Ref. [40].

disappearance of the minimum in the liquid-liquid critical line, so that the three-phase line meets the gas-liquid and the liquid-liquid critical lines before either go through a maximum or minimum in pressure. In this case the system only possesses a single critical point at any given pressure or temperature. Decreasing the strength of the bonding interaction further, eventually to zero, leads to the gas-liquid and liquid-liquid critical lines becoming one continuous curve originating from the vapour-liquid critical point of the pure component. Additionally the three-phase line curves so that its origins are moved to low temperatures and pressures. This corresponds to the situation observed for a binary mixture with no bonding sites in Ref. [40]. Conversely, increasing the strength of the site-site interaction beyond $\epsilon_{a,b}^* = 15$, leads to the displacement of the DCP and hence the end of the three-phase line and the origin of the liquid-liquid critical line, to higher temperatures and pressures, so that the system only exhibits a single critical point, corresponding to the gas-liquid critical line. The PT projection obtained using the SAFT-HS equation of state as given in Ref. [40] is also shown in Fig. 6.6, with a corresponding reduced site-site interaction energy of $\epsilon_{a,b}^* = 13$. It is hence possible to conclude that use of the SAFT-VR approach to evaluate the mean-attractive energy and its derivatives, as opposed to treating the attractive interactions at the van der Waals level, decreases the relative strength of the reduced site-site interaction $\epsilon_{a,b}^*$.

The effect of a variation in pressure on the extent of the closed-loop region of the binary square-well mixture is illustrated in Figure 6.7, via a series of constant pressure slices of the PT projection for a system with $\epsilon_{a,b}^* = 15$. The symmetry of the phase diagram about $x_2 = 0.5$ is a result of the symmetry of the model system. For a reduced pressure of $P_r = 6.8$ the system is seen to be miscible at all temperatures above $T_r = 1.1$, indicating that we are well below the minimum in pressure of the liquid-liquid critical line. The closed-loop region appears when the pressure of the system is increased above that of the minimum of the liquid-liquid critical line to $P_r = 8.2$, and a further increase in pressure to $P_r = 9.3$ gives rise to the appearance of the gas+liquid+liquid three-phase line. At higher pressures of $P_r = 10.4$ the three-phase line merges with the low temperature gas-liquid critical lines, so that the system only possesses a single critical point at these pressures.

The SAFT-VR equation of state can also be used to give information about the degree of association present in the system at any given temperature, via X_a , the fraction of molecules of component 1 not bonded at site a . An understanding of the mechanism of closed-loop immiscibility can be hence obtained by considering the intermolecular association exhibited by the system. The total fraction of not-bonded molecules are shown as a function of temperature in Figure 6.8, this corresponds to the temperature-composition slice at pressure $P_r = 10.9$ of Fig. 6.7.

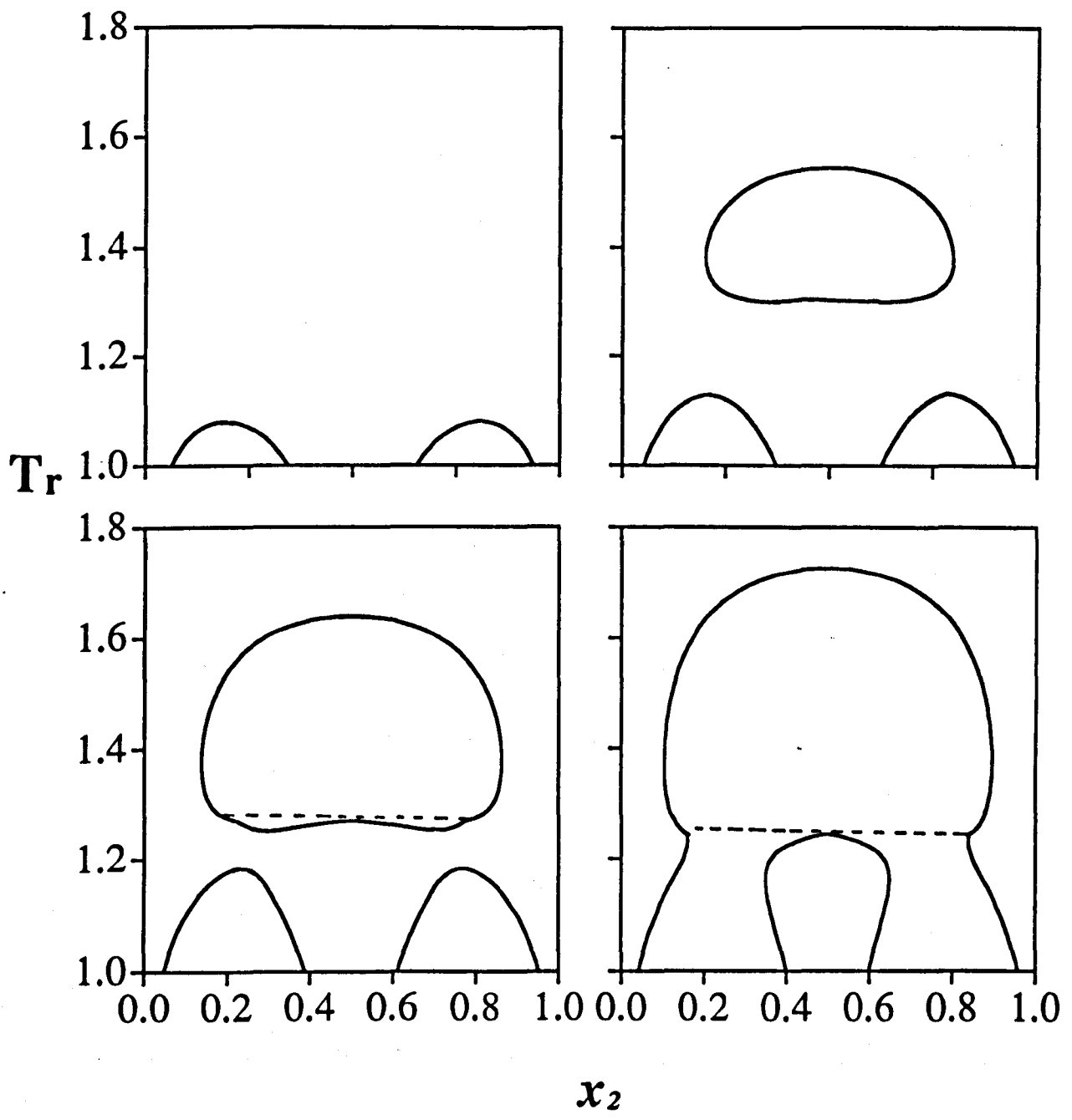


Figure 6.7: Temperature-composition slices of the coexistence region for the symmetrical square-well mixture with $\epsilon_{a,b}^* = 15$ at a series of reduced pressures $P_r = 6.8, 8.2, 9.3$ and 10.4 , obtained using the SAFT-VR equation of state. The pressure of the slices increases from left to right and from top to bottom. See Figure 6.5 for details.

The degree of association is the same in both components so that $X_a = X_b$, since bonding is only permitted between unlike species. Hence, the total fraction of molecules bonded in the coexisting liquid phases is represented by a single solid line. The extent of association increases rapidly as the temperature of the system approaches that of the LCST. This confirms that the low temperature miscibility of the system is observed due to the formation of bonds between unlike components in the mixture. The total fraction of molecules bonded at low temperatures corresponds to the association in the coexisting gas-liquid regions, each of which have the same fraction of molecules bonded. The degree of association is greater in the gas phase than in the liquid phase since the composition of the two components in the gas phase are more similar than those in the liquid phase, which favours bonding between unlike species.

In summary, the extent of closed-loop immiscibility as predicted by the SAFT-VR equation of state for a model system of a binary mixture of square-well monomers with no unlike interactions and with a single bonding site per sphere is governed by the interplay of several factors. Most importantly, the ability of the system to associate at low temperatures via directional interaction sites is found to be responsible for the existence of the closed-loop of immiscibility. An increase in the relative strength of the site-site interaction initially leads to an increase in the temperature range of the closed-loop region. A very large site-site interaction results in the system becoming miscible at all temperatures, at the expense of the loss of the closed-loop of immiscibility. An increase in pressure similarly leads to the initial appearance of the closed-loop region, but a large increase in pressure increases the temperature difference between the LCST and the UCST, until the LCST merges with the three-phase line, upon which the closed-loop region is lost.

6.4 Gibbs ensemble Monte Carlo simulation results

As has been discussed previously, the Gibbs ensemble Monte Carlo technique was first introduced in 1987 by Panagiotopoulos [62, 63], and is a highly effective direct simulation technique used for the determination of phase equilibria in fluid systems. The method discussed in detail in Chapter 3, consists of a simulation performed in two distinct regions which are in thermodynamic equilibrium, but not in physical contact. Three distinct Monte Carlo moves are performed in order to satisfy the conditions of equilibrium: particle displacements within either subsystem, to maintain equality of temperature; volume changes of either subsystem, to maintain equality of pressure; and particle interchanges between the two subsystems, to maintain equality of chemical potential. As a consequence, the energy E^j , volume

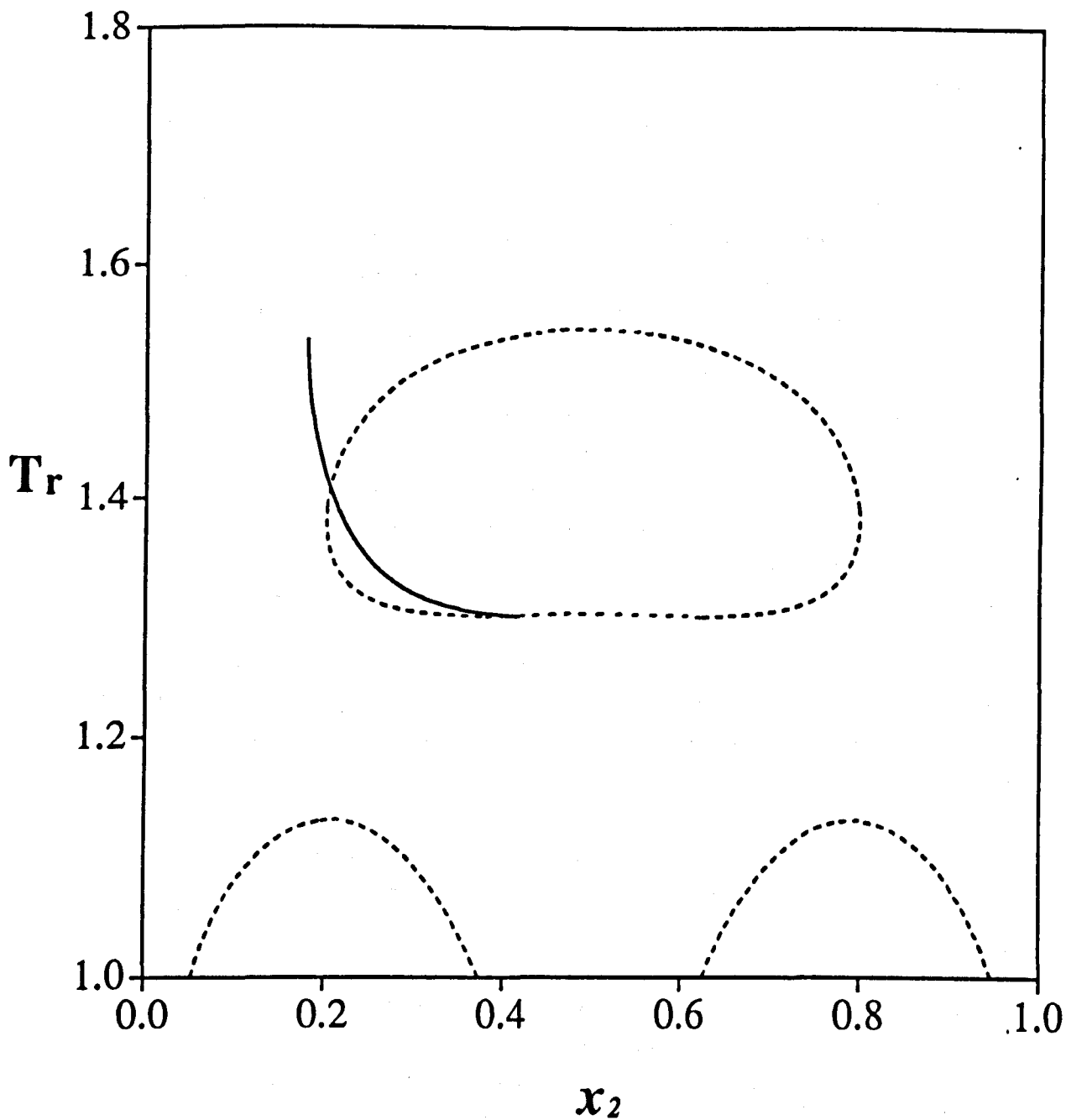


Figure 6.8: Total fraction of molecules bonded in the coexisting phases for the symmetrical square-well mixture with $\epsilon_{a,b}^* = 15$ at a constant reduced pressure of $P_r = 8.2$ as a function of reduced temperature. The dashed curve corresponds to the temperature-composition phase diagram for this system at this pressure (shown in Fig. 6.7).

V^j , and composition $x_i^j = N_i^j/N^j$ of particles of type i in subsystem j vary during the course of the simulation.

We perform GEMC simulations at constant number of particles, pressure and temperature (NPT) for the symmetrical square-well mixture with a single off-centre bonding site per sphere, with interactions defined in the previous section. We aim to confirm the theoretical results obtained using the SAFT-VR equation of state, where the addition of a bonding site onto the monomer segments is sufficient to lead to the appearance of a LCST for the system. Simulations are performed in cubic boxes, the particles are initially arranged on a face-centred-cubic (fcc) lattice. The usual periodic boundary conditions and minimum image convention are used [64]. Initial guesses for the coexisting densities and compositions at each pressure and temperature state point are made by using the corresponding SAFT-VR solutions. The chemical potential is evaluated using the Widom test-particle method as adapted for the Gibbs ensemble [65, 66]. One simulation cycle consists of N displacements in each box, one volume change for either box, and a specific number of particle interchanges. The maximum displacement and the maximum volume change are controlled in order to give corresponding acceptance ratios of between 30 and 40%, the number of insertions is adjusted so that between 1 and 3% of particles are interchanged each cycle. We use the particle transfer algorithm originally proposed for mixtures by Panagiotopoulos *et al.* [63]. Simulations consisting of systems with $N=512$, $N=1000$ and $N=1728$ particles are performed at a series of different coexisting pressures, for different strength of the site-site interaction energy. An initial equilibration simulation of 50,000 cycles is performed before averaging for between 150,000 and 250,000 cycles.

The reduced thermodynamic variables, temperature, $T^* = kT/\varepsilon$, pressure $P^* = P\sigma^3/\varepsilon$, and site-site interaction energy $\varepsilon_{a,b}^* = \varepsilon_{a,b}/\varepsilon$ are used in the following discussion. It is convenient to reduce the pressure and temperature with respect to the critical point of one of the components, such that $T_r = T^*/T_c^*$ and $P_r = P^*/P_c^*$, where the subscript c denotes the critical value of a variable. We use the critical values of $T_c^* = 1.219 \pm 0.008$ and $P_c^* = 0.108 \pm 0.016$ as estimated in Ref. [73] for the pure-component square-well system with range $\lambda = 1.5$.

The GEMC results obtained for the mixture of square wells are presented in Tables 6.2 to 6.12 and the corresponding constant pressure temperature-composition Tx slices of the coexistence regions are shown in Figures 6.9 to 6.12 and 6.14. The pressure of $P^* = 0.756$ of Figure 6.9 is approximately seven times the critical pressure of the pure square-well system with $\lambda = 1.5$. The Gibbs ensemble simulation data with $\varepsilon_{a,b}^* = 13$ for three system sizes are shown, with a negligible system size effect. The region of liquid-liquid immiscibility bound by an UCST at

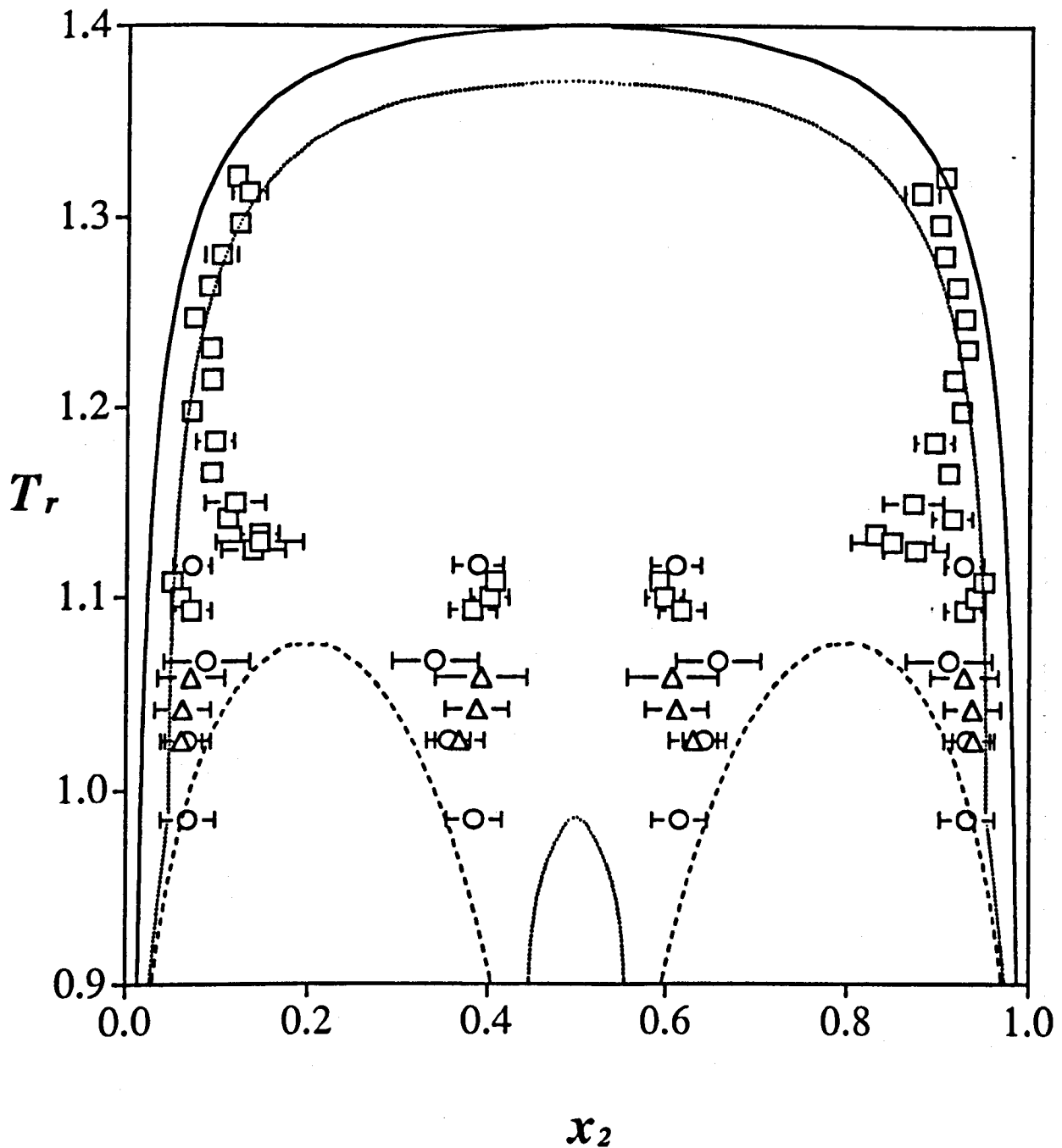


Figure 6.9: Temperature-composition slice of the coexistence region for the symmetrical square-well mixture at a reduced pressure of $P^* = P\sigma^3/\epsilon = 0.756$ with a bonding interaction of $\epsilon_{a,b}^* = 13$. The triangles correspond to the GEMC data for a system of $N=512$ particles, the circles to a system of $N=1000$ particles, and the squares to a system of $N=1728$ particles. The continuous, dotted and dashed curves correspond to the SAFT-VR prediction for the same model with bonding strengths of $\epsilon_{a,b}^* = 12, 13$ and 14 , respectively.

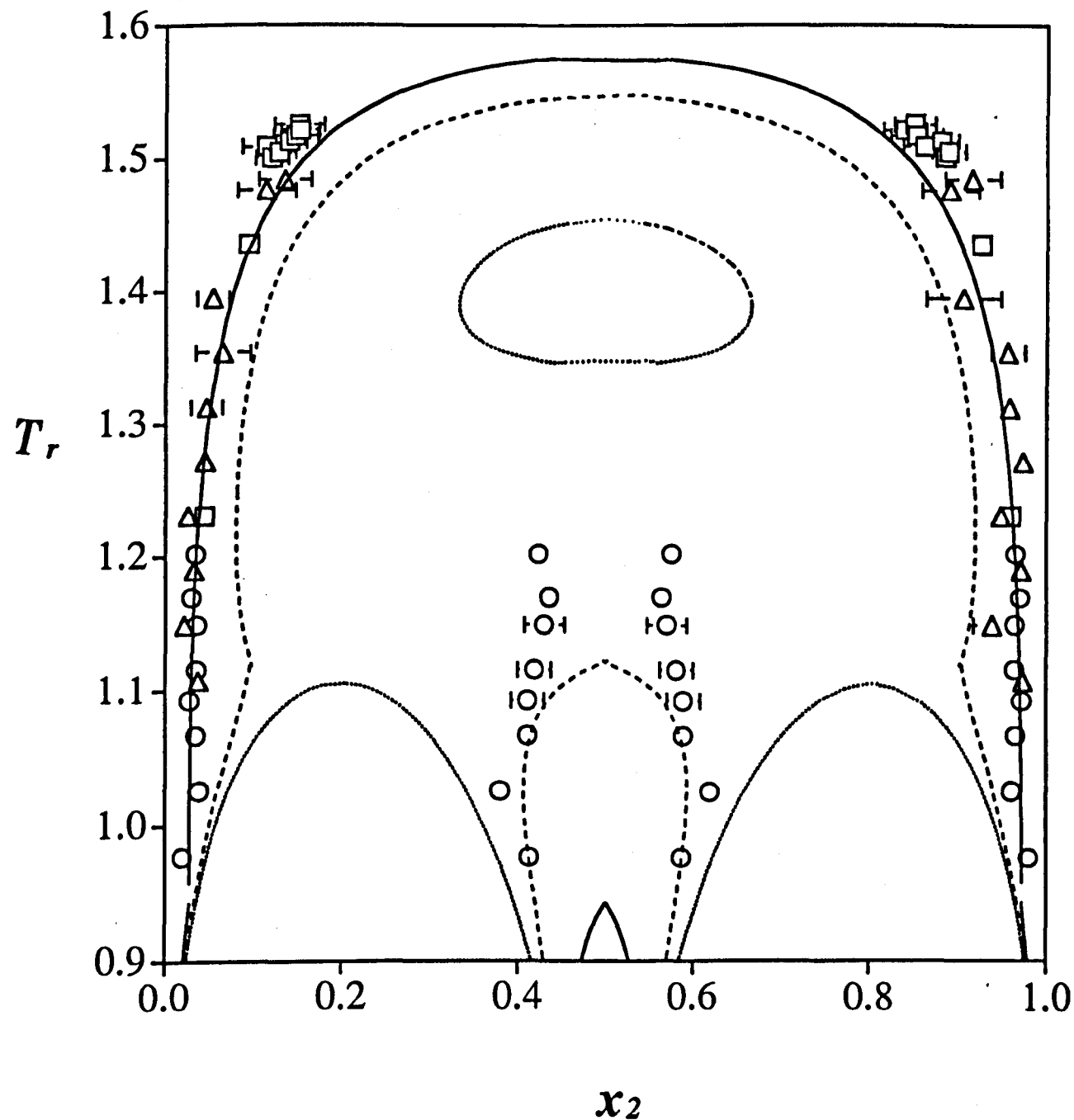


Figure 6.10: Temperature-composition slice of the coexistence region for the symmetrical square-well mixture at a reduced pressure of $P^* = P\sigma^3/\varepsilon = 1.08$ with a bonding interaction of $\varepsilon_{a,b}^* = 13$. The triangles correspond to the GEMC data for a system of $N=512$ particles, the circles to a system of $N=1000$ particles, and the squares to a system of $N=1728$ particles. The continuous, dotted and dashed curves correspond to the SAFT-VR prediction for the same model with bonding strengths of $\varepsilon_{a,b}^* = 13, 14$ and 15 , respectively.

high temperatures is clearly shown, together with low temperature regions of gas-liquid immiscibility below a three-phase line. The curves represent the SAFT-VR prediction for the equivalent model, with three different strengths of the site-site interaction energy. For a value of $\epsilon_{a,b}^* = 12$ the theory predicts immiscibility of the system at all temperatures below an USCT, as the site-site interaction is increased in to $\epsilon_{a,b}^* = 13$ the prediction includes regions of low temperature gas-liquid immiscibility, and the three-phase line can be observed at a temperature close to the critical temperature of the pure component. Increasing the strength of the bonding interaction further to $\epsilon_{a,b}^* = 14$, leads to a complete change in the nature of the Tx slice, now the theory predicts a large region of miscibility above two low temperature regions of gas-liquid immiscibility, indicating that increasing the site-site interaction energy from $\epsilon_{a,b}^* = 13$ to $\epsilon_{a,b}^* = 14$ has resulted in both the formation and the loss of a region of closed-loop immiscibility at this pressure. The low-temperature regions of gas-liquid immiscibility obtained from simulation appear at slightly higher temperatures than those predicted by the SAFT-VR equation of state for $\epsilon_{a,b}^* = 13$.

The equivalent temperature-composition Tx slice for a higher pressure of $P^* = 1.08$, which is approximately ten times the critical pressure of the pure component, is given in Figure 6.10. The simulation results again show a region of liquid-liquid immiscibility bounded at high temperatures by an UCST, and low temperature regions of gas-liquid immiscibility. The region of liquid-liquid immiscibility is seen to be larger than in the lower pressure case of Fig. 6.9, but no closed-loop of immiscibility is observed. For a site-site interaction energy of $\epsilon_{a,b}^* = 13$ the SAFT-VR approach predicts a region of liquid-liquid immiscibility bounded by an UCST and small regions of low temperature gas-liquid immiscibility below the three phase line. The SAFT-VR prediction for a site-site interaction energy of $\epsilon_{a,b}^* = 14$, the low temperature, gas-liquid immiscible regions are larger than in the $\epsilon_{a,b}^* = 13$ case, so that the onset of a closed-loop region can be observed. For an association energy of $\epsilon_{a,b}^* = 15$ the SAFT-VR equation of state predicts the existence of a small closed-loop of immiscibility at temperatures between $T_r = 1.35$ and $T_r = 1.45$, together with low-temperature regions of gas-liquid immiscibility.

At this stage, one can conclude that increasing the pressure from $P^* = 0.756$ to $P^* = 1.08$ for a system with an interaction energy of $\epsilon_{a,b}^* = 13$, does not bring about a sufficient change in the phase diagram of the system, in order for a closed-loop of immiscibility to be observed by GEMC simulation. An increase in strength of the bonding interaction, together with a slight increase in pressure, is shown to give more pleasing results. The temperature-composition slice for a pressure of $P^* = 1.28$ is shown in Figure 6.11. Here, the Gibbs ensemble simulation data is obtained for a mixture with a site-site interaction energy of $\epsilon_{a,b}^* = 14.5$, for two system

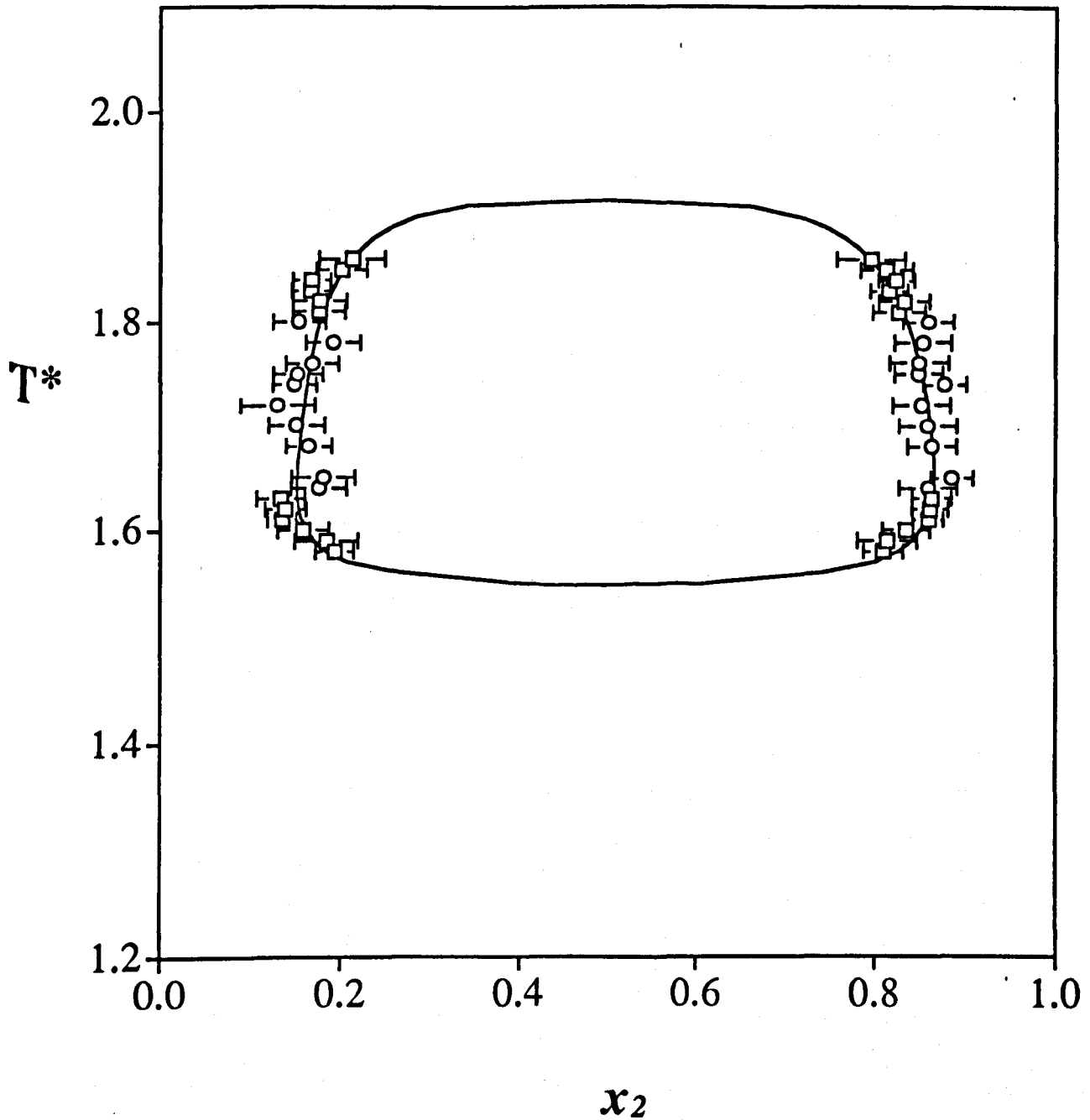


Figure 6.11: Temperature-composition slice of the coexistence region for the symmetrical square-well mixture at a reduced pressure of $P^* = P\sigma^3/\epsilon = 1.28$ with a bonding interaction of $\epsilon_{a,b}^* = 14.5$. The circles correspond to the GEMC data for a system of $N=1000$ particles, and the squares to a system of $N=1728$ particles. The continuous curve corresponds to the Wegner expansion of Eq. (6.30) which is fitted to the simulation data and includes a first correction to scaling.

sizes. The region of closed-loop immiscibility can be clearly observed, bounded at $T^* \approx 1.56$ by a LCST and at $T^* \approx 1.92$ by an UCST. No low-temperature regions of gas-liquid immiscibility were observed for this system. The curve fitted through the GEMC results is obtained using a Wegner expansion, using a method which is described later. As a means of monitoring the association present in the system, the fraction of molecules bonded is calculated during the simulation. The extent of association as a function of temperature for the system at a pressure of $P^* = 1.28$ with $\epsilon_{a,b}^* = 14.5$ is shown in Fig. 6.12. The association is again seen to increase dramatically as the temperature of the system approaches that of the LCST (cf. Fig. 6.8), indicating that association of the system is responsible for the low-temperature miscibility. The SAFT-VR predictions at a pressure of $P^* = 1.28$ with site-site interactions of $\epsilon_{a,b}^* = 14.5$ and $\epsilon_{a,b}^* = 15$ are shown in Fig 6.13. For $\epsilon_{a,b}^* = 14.5$ the theory predicts a region of liquid-liquid immiscibility bounded by an UCST and regions of low-temperature gas-liquid immiscibility for certain compositions at temperatures below the three-phase line. Increasing the strength of the site-site interaction to $\epsilon_{a,b}^* = 15$ leads to the prediction of a closed-loop of immiscibility, which has upper and lower boundaries which are similar to those obtained using Gibbs ensemble simulation. It is encouraging to observe the existence of a closed-loop of immiscibility for this system with a single association site, both by simulation and by using the SAFT-VR equation of state.

A temperature-composition slice obtained at a higher pressure of $P^*=1.48$ by Gibbs ensemble simulation is shown in Figure 6.14. As for the case of the $P^*=1.28$ slice, the strength of the site-site interaction is fixed at $\epsilon_{a,b}^* = 14.5$, and the region of closed-loop immiscibility is clearly observed, with no low-temperature immiscible regions. For this higher pressure case the closed loop is bounded at higher temperatures by an UCST at $T^* \approx 2.07$ and at low temperatures by a LCST at $T^* \approx 1.47$. This indicates that the extent of the closed-loop region has increased from that of the $P^* = 1.28$ state, which is in line with the theoretical prediction of the effect of pressure on the closed-loop. The degree of association at this higher pressure is shown, as a function of temperature in Figure 6.15, the extent of association is again seen to increase rapidly at temperatures close to the LCST. The prediction of SAFT-VR for two different interaction energies $\epsilon_{a,b}^* = 14.5$ and $\epsilon_{a,b}^* = 15$ is shown in Figure 6.16, where the simulation and theoretical results both predict regions of miscibility for temperatures below the LCST.

These GEMC simulation results confirm the theoretical predictions that the extent of closed-loop behaviour has a critical dependency on the pressure, temperature, composition and the strength of the site-site interaction of the model system. The existence of closed regions of immiscibility for simulations performed for the model with a specific choice of interaction energy confirms that the existence of

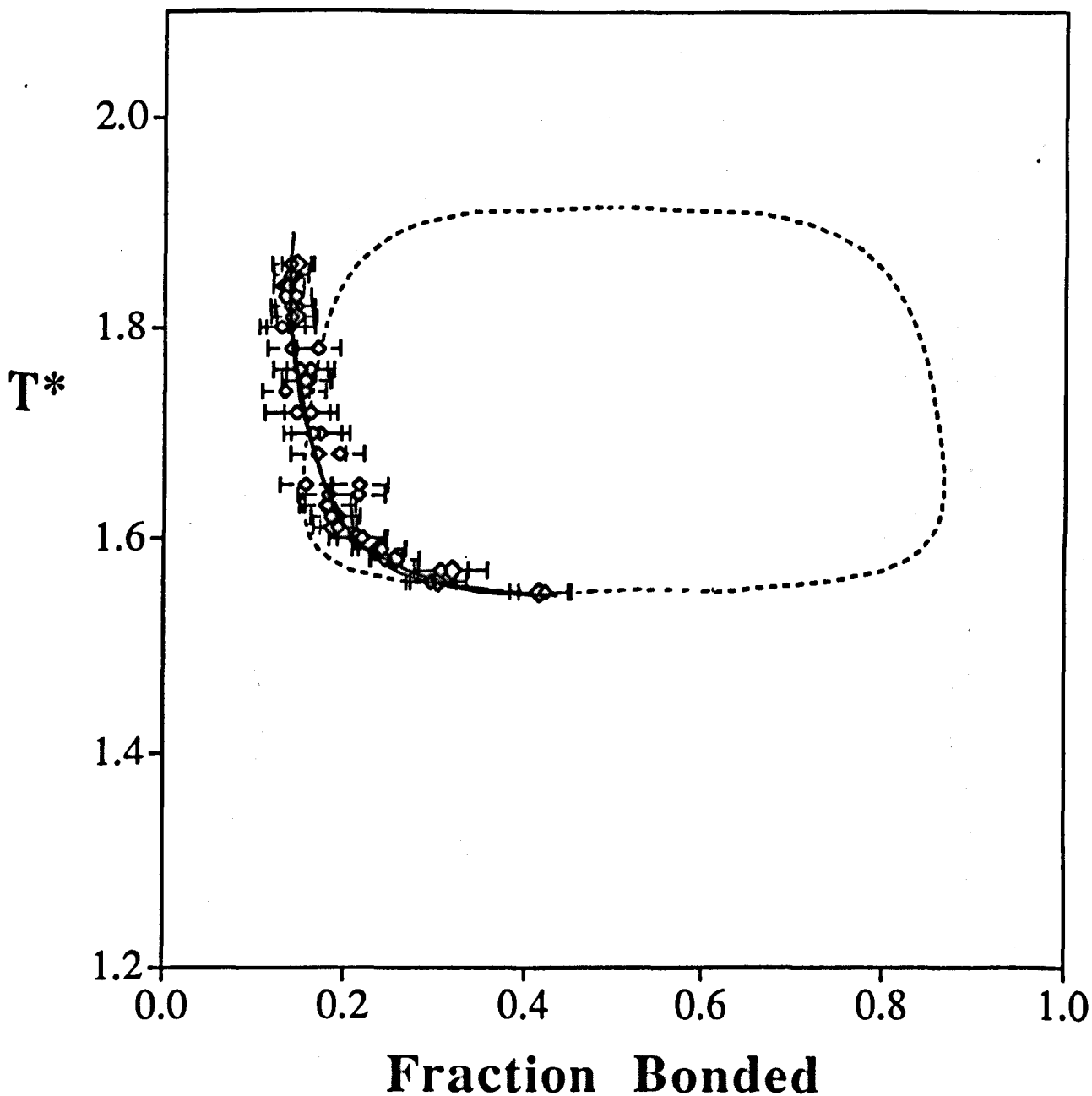


Figure 6.12: Total fraction of molecules bonded in the symmetrical binary mixture as a function of temperature, obtained using GEMC simulation at a reduced pressure of $P^* = P\sigma^3/\varepsilon = 1.28$ with a bonding interaction of $\varepsilon_{a,b}^* = 14.5$. The dashed curve corresponds to the Wegner expansion of Eq. (6.30) which is fitted to the simulation data and includes a first correction to scaling.

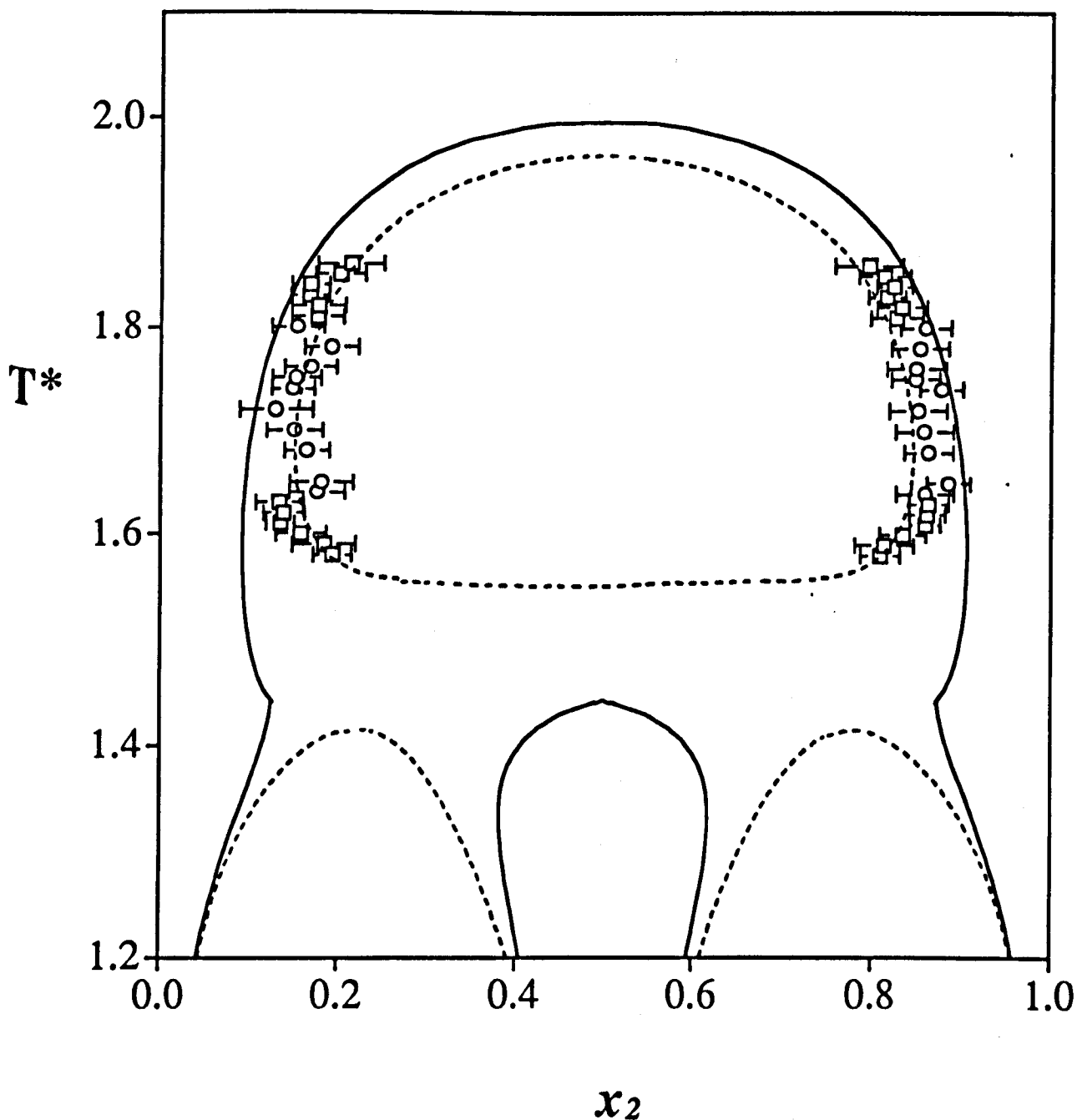


Figure 6.13: Temperature-composition slice of the coexistence region for the symmetrical square-well mixture at a reduced pressure of $P^* = P\sigma^3/\varepsilon = 1.28$ with a bonding interaction of $\varepsilon_{a,b}^* = 14.5$. The data points correspond to the GEMC data. The bold and dashed curves correspond to the SAFT-VR prediction for the same model with bonding strengths of $\varepsilon_{a,b}^* = 14.5$ and 15, respectively. See Figure 6.11 for details.

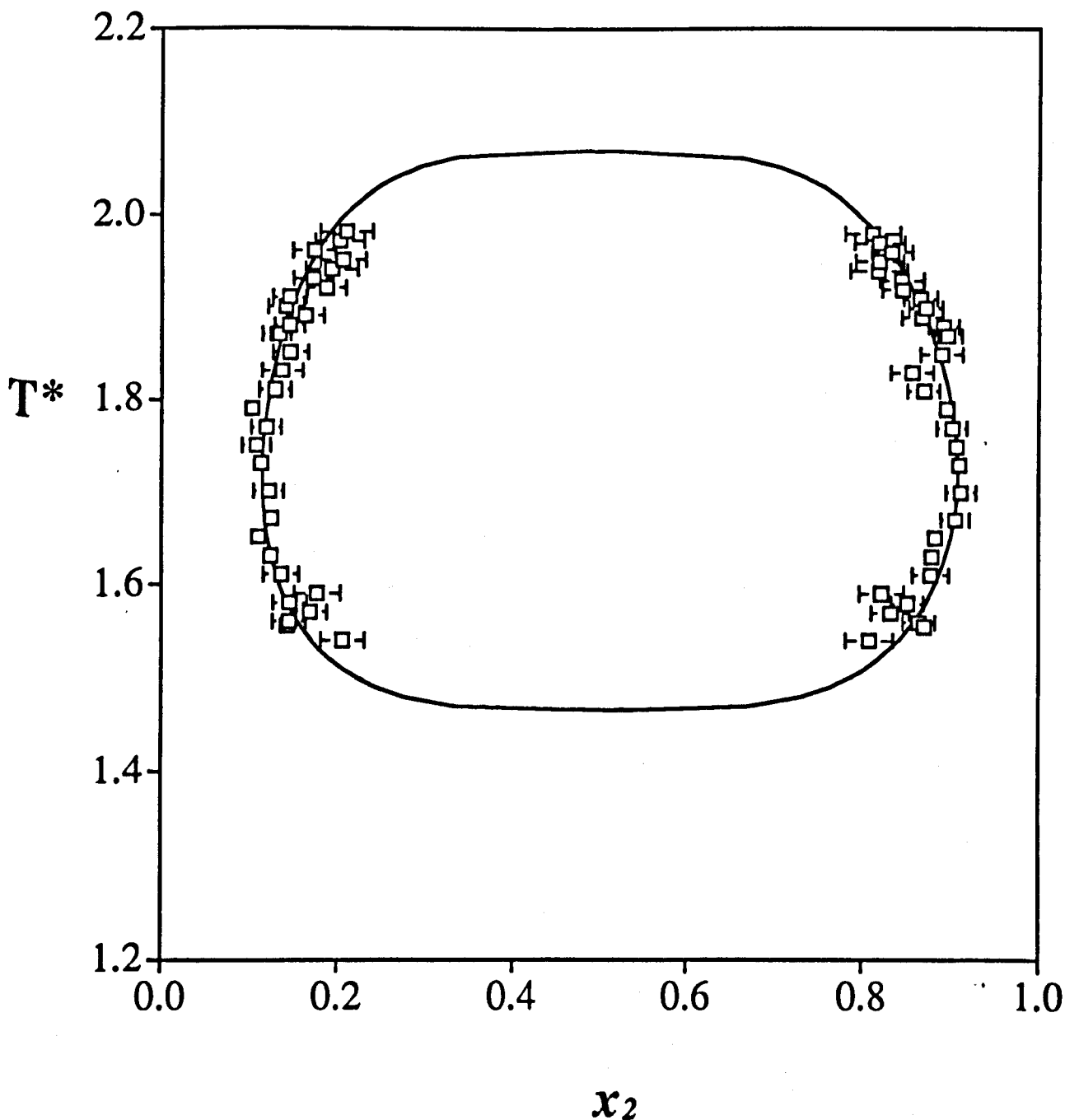


Figure 6.14: Temperature-composition slice of the coexistence region for the symmetrical square-well mixture at a reduced pressure of $P^* = P\sigma^3/\epsilon = 1.48$ with a bonding interaction of $\epsilon_{a,b}^* = 14.5$. The squares correspond to the GEMC data for a system of $N=1728$ particles. The continuous curve corresponds to the Wegner expansion of Eq. (6.30) which is fitted to the simulation data and includes a first correction to scaling.

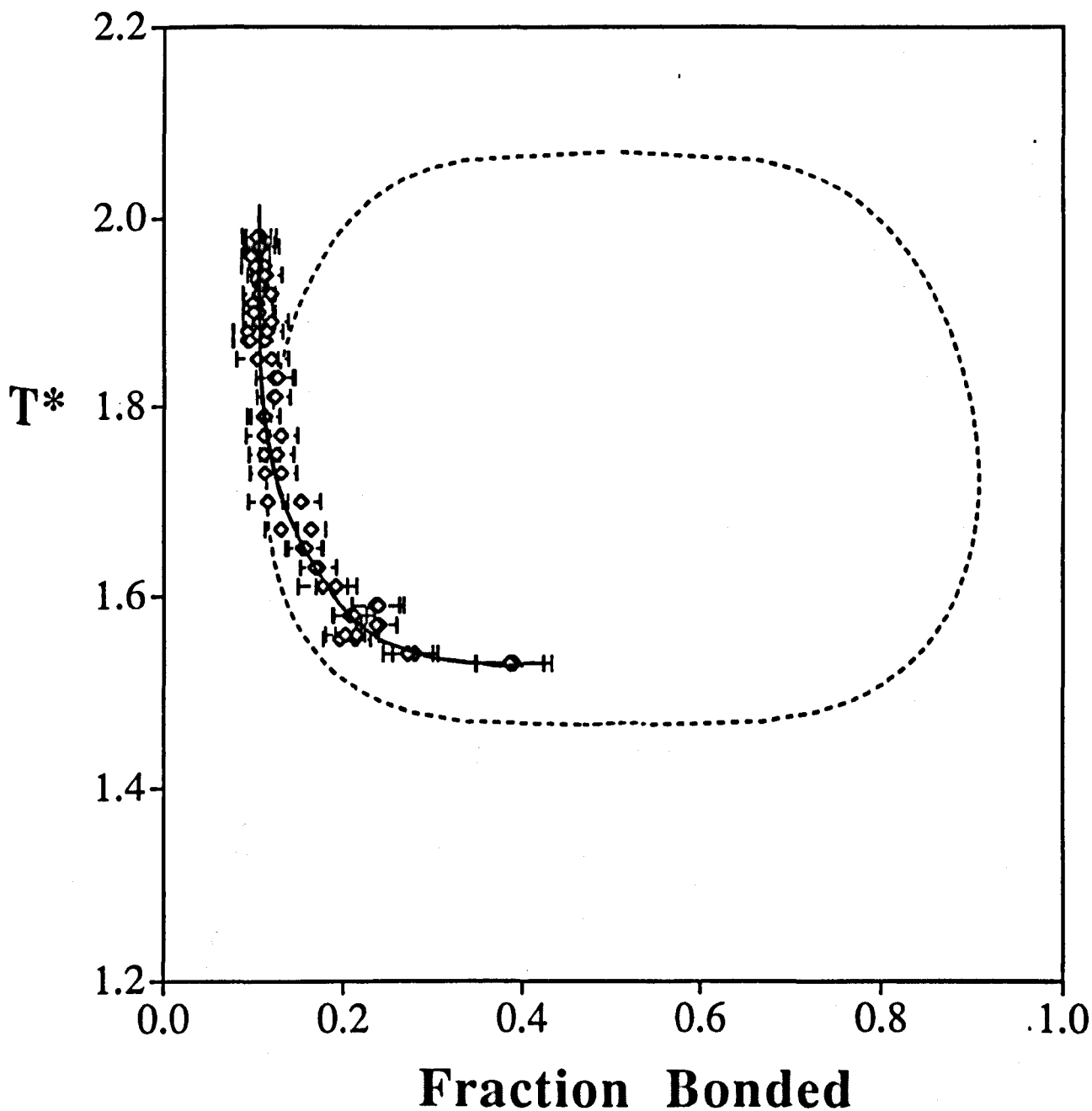


Figure 6.15: Total fraction of molecules bonded in the symmetrical binary mixture as a function of temperature, obtained using GEMC simulation at a reduced pressure of $P^* = P\sigma^3/\epsilon = 1.48$ with a bonding interaction of $\epsilon_{a,b}^* = 14.5$. The dashed curve corresponds to the Wegner expansion of Eq. (6.30) which is fitted to the simulation data and includes a first correction to scaling.

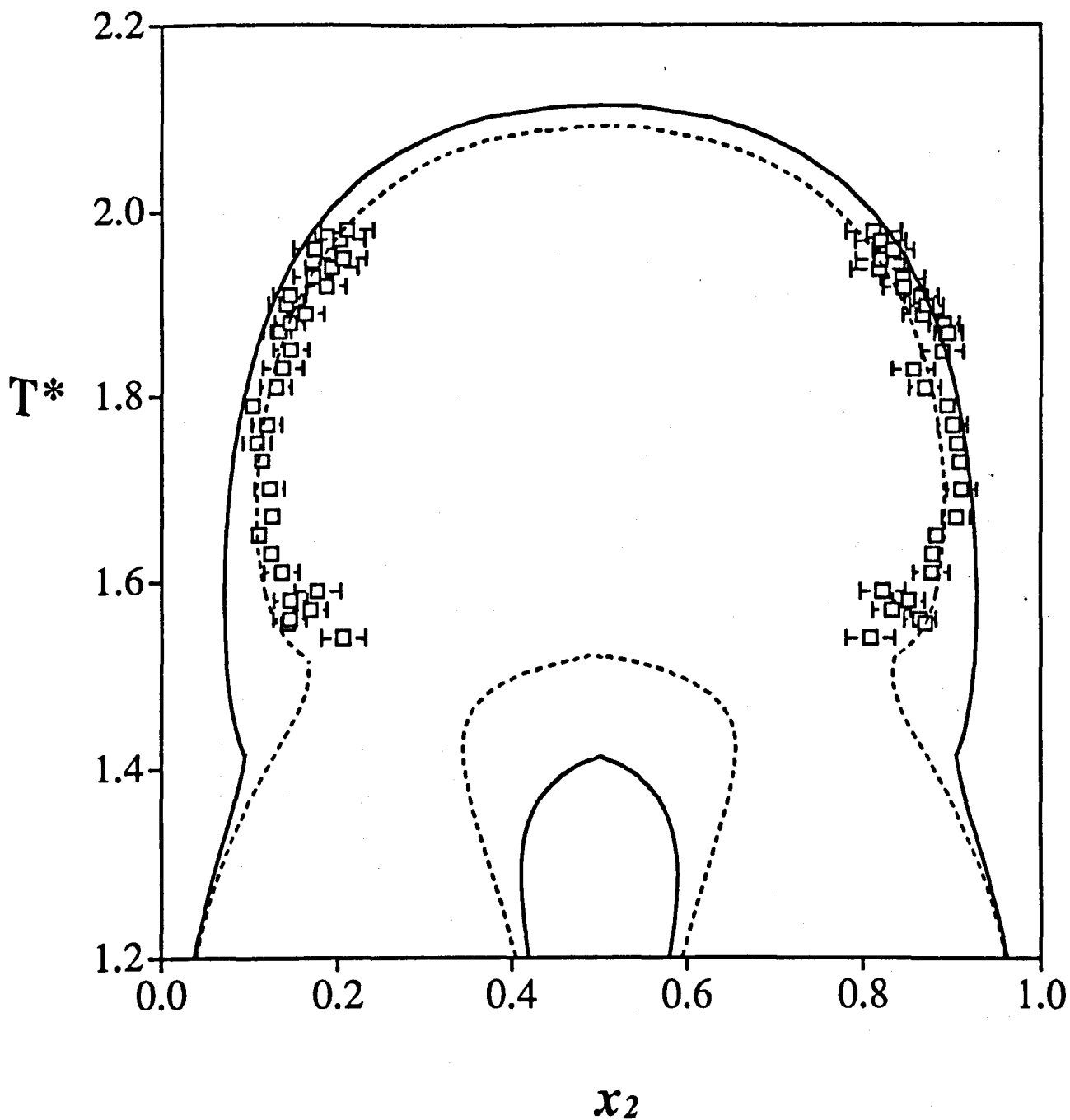


Figure 6.16: Temperature-composition slice of the coexistence region for the symmetrical square-well mixture at a reduced pressure of $P^* = P\sigma^3/\varepsilon = 1.48$ with a bonding interaction of $\varepsilon_{a,b}^* = 14.5$. The data points correspond to the GEMC data. The bold and dashed curves correspond to the SAFT-VR prediction for the same model with bonding strengths of $\varepsilon_{a,b}^* = 14.5$ and 15, respectively. See Figure 6.14 for details.

a low temperature region of miscibility is a direct result of the inclusion of the association sites in the potential model of the system. It is gratifying to observe the parallels which exist between the results obtained using the SAFT-VR approach and the Gibbs ensemble simulation technique, especially in their ability to predict the extent of the region of immiscibility for the model examined. By monitoring the effect of association in the model system, both using the SAFT-VR approach and by computer simulation methods the low-temperature miscibility of the system is confirmed to be a direct result of the formation of directional bonds between unlike species. Such bonds can be considered to be representative of the hydrogen bonds which form between components in a real fluid mixture.

Table 6.2: Vapour-liquid coexistence data obtained from NPT Gibbs ensemble Monte Carlo simulations for a mixture of square-well monomers with a range $\lambda = 1.5$, and a single interaction site of reduced depth $\epsilon_{a,b}^*/\epsilon = 13$. The fixed variables during the simulation are the number of particles N , the reduced pressure $P^* = P\sigma^3/\epsilon = 0.756$ and the reduced temperature $T^* = kT/\epsilon$. The packing fractions η and mole fractions x_2 in the coexisting vapour and liquid phases are labeled v and l , respectively; the uncertainties correspond to one standard deviation.

T^*	N	η_v	η_l	$x_{2,v}$	$x_{2,l}$
1.20	1000	0.335±0.006	0.316±0.005	0.932±0.030	0.615±0.031
1.25	1000	0.331±0.006	0.313±0.005	0.932±0.025	0.643±0.024
1.30	1000	0.316±0.010	0.295±0.005	0.912±0.047	0.658±0.047
1.36	1000	0.299±0.006	0.272±0.007	0.928±0.022	0.611±0.028
1.332	1728	0.308±0.006	0.283±0.005	0.929±0.022	0.617±0.026
1.34	1728	0.308±0.005	0.283±0.005	0.941±0.016	0.598±0.021
1.35	1728	0.307±0.005	0.281±0.008	0.950±0.014	0.592±0.015
1.29	512	0.317±0.008	0.287±0.011	0.929±0.037	0.607±0.051
1.27	512	0.323±0.008	0.296±0.009	0.938±0.031	0.612±0.035
1.25	512	0.322±0.008	0.295±0.009	0.939±0.023	0.631±0.027

6.5 Critical behaviour and finite-size effects

The existence of both an upper and a lower critical solution temperature in this particular system allows the study of the differences or the similarities between the two critical regions. The inadequacy of mean-field equations of state such as the SAFT-VR approach in the description of the critical region has been discussed previously. A means of obtaining critical point parameters from computer simulation data is an alternative approach which gives more satisfactory results. However,

Table 6.3: Liquid-liquid coexistence data obtained from NPT Gibbs ensemble Monte Carlo simulations for a mixture of square-well monomers with a single interaction site of reduced depth $\varepsilon_{a,b}^*/\varepsilon = 13$, at a reduced pressure of $P^* = P\sigma^3/\varepsilon = 0.756$ for $N = 1728$ particles. The packing fractions η and mole fractions x_2 in the coexisting liquid phases are labeled l_1 and l_2 . See Table 6.2 for details.

T^*	η_{l_1}	η_{l_2}	x_{2,l_1}	x_{2,l_2}
1.37	0.276±0.009	0.271±0.007	0.875±0.035	0.139±0.028
1.375	0.272±0.008	0.273±0.009	0.849±0.045	0.146±0.048
1.38	0.263±0.005	0.265±0.006	0.831±0.016	0.146±0.021
1.39	0.278±0.009	0.272±0.006	0.915±0.022	0.111±0.017
1.40	0.269±0.008	0.271±0.008	0.872±0.033	0.119±0.033
1.42	0.274±0.005	0.275±0.006	0.911±0.014	0.093±0.014
1.44	0.268±0.005	0.270±0.007	0.895±0.021	0.097±0.021
1.46	0.275±0.004	0.276±0.005	0.925±0.014	0.071±0.013
1.48	0.264±0.006	0.262±0.005	0.916±0.016	0.093±0.014
1.50	0.270±0.005	0.262±0.004	0.931±0.015	0.092±0.014
1.52	0.267±0.004	0.267±0.004	0.928±0.011	0.073±0.011
1.54	0.262±0.003	0.260±0.004	0.919±0.014	0.090±0.016
1.56	0.250±0.004	0.248±0.004	0.905±0.017	0.103±0.018
1.58	0.246±0.003	0.241±0.003	0.900±0.014	0.123±0.014
1.60	0.238±0.004	0.235±0.004	0.880±0.019	0.133±0.019
1.61	0.246±0.003	0.241±0.003	0.906±0.013	0.120±0.014

Table 6.4: Vapour-liquid coexistence data obtained from NPT Gibbs ensemble Monte Carlo simulations for a mixture of square-well monomers with a single interaction site of reduced depth $\varepsilon_{a,b}^*/\varepsilon = 13$, at a reduced pressure of $P^* = P\sigma^3/\varepsilon = 1.08$ for $N = 1000$ particles. See Table 6.2 for details.

T^*	η_v	η_l	$x_{2,v}$	$x_{2,l}$
1.465	0.313±0.005	0.284±0.006	0.965±0.011	0.573±0.016
1.425	0.320±0.005	0.291±0.006	0.970±0.009	0.564±0.015
1.400	0.319±0.005	0.290±0.007	0.964±0.014	0.570±0.023
1.360	0.326±0.005	0.303±0.005	0.964±0.015	0.581±0.019
1.332	0.335±0.005	0.307±0.006	0.972±0.012	0.589±0.019
1.300	0.335±0.006	0.313±0.008	0.965±0.012	0.589±0.016
1.250	0.339±0.005	0.318±0.005	0.961±0.013	0.620±0.013
1.190	0.359±0.004	0.343±0.005	0.980±0.006	0.587±0.009

Table 6.5: Liquid-liquid coexistence data obtained from NPT Gibbs ensemble Monte Carlo simulations for a mixture of square-well monomers with a single interaction site of reduced depth $\varepsilon_{a,b}^*/\varepsilon = 13$, at a reduced pressure of $P^* = P\sigma^3/\varepsilon = 1.08$ for $N = 512$ particles. See Table 6.2 for details.

T^*	η_1	η_2	x_{2,l_1}	x_{2,l_2}
1.35	0.331±0.009	0.325±0.008	0.973±0.013	0.038±0.017
1.40	0.311±0.008	0.326±0.008	0.938±0.021	0.022±0.011
1.45	0.313±0.008	0.312±0.008	0.971±0.013	0.033±0.012
1.50	0.294±0.007	0.307±0.009	0.948±0.015	0.026±0.013
1.55	0.303±0.008	0.295±0.008	0.973±0.011	0.045±0.015
1.60	0.288±0.009	0.285±0.009	0.958±0.017	0.047±0.018
1.65	0.281±0.010	0.272±0.011	0.956±0.019	0.065±0.030
1.70	0.258±0.012	0.269±0.008	0.906±0.042	0.054±0.018
1.80	0.242±0.010	0.242±0.009	0.891±0.034	0.114±0.033
1.81	0.249±0.011	0.238±0.008	0.916±0.031	0.135±0.030

Table 6.6: Liquid-liquid coexistence data obtained from NPT Gibbs ensemble Monte Carlo simulations for a mixture of square-well monomers with a single interaction site of reduced depth $\varepsilon_{a,b}^*/\varepsilon = 13$, at a reduced pressure of $P^* = P\sigma^3/\varepsilon = 1.08$ for $N = 1728$ particles. See Table 6.2 for details.

T^*	η_1	η_2	x_{2,l_1}	x_{2,l_2}
1.50	0.298±0.011	0.297±0.008	0.959±0.015	0.044±0.012
1.75	0.257±0.004	0.251±0.003	0.926±0.012	0.094±0.013
1.83	0.242±0.004	0.241±0.005	0.885±0.016	0.120±0.019
1.835	0.243±0.005	0.240±0.004	0.889±0.019	0.128±0.019
1.84	0.238±0.005	0.242±0.007	0.862±0.024	0.114±0.027
1.845	0.239±0.005	0.236±0.004	0.881±0.019	0.140±0.019
1.85	0.233±0.005	0.233±0.005	0.853±0.029	0.147±0.025
1.855	0.231±0.003	0.232±0.004	0.840±0.024	0.152±0.023
1.86	0.233±0.005	0.232±0.005	0.851±0.023	0.151±0.028

Table 6.7: Liquid-liquid coexistence data obtained from NPT Gibbs ensemble Monte Carlo simulations for a mixture of square-well monomers with a single interaction site of reduced depth $\varepsilon_{a,b}^*/\varepsilon = 14.5$, at a reduced pressure of $P^* = P\sigma^3/\varepsilon = 1.28$ for $N = 1000$ particles. See Table 6.2 for details.

T^*	η_1	η_2	x_{2,l_1}	x_{2,l_2}
1.64	0.284±0.006	0.279±0.006	0.860±0.032	0.177±0.031
1.65	0.292±0.007	0.285±0.007	0.886±0.026	0.176±0.036
1.68	0.282±0.007	0.277±0.006	0.864±0.027	0.166±0.025
1.70	0.275±0.007	0.273±0.007	0.859±0.032	0.152±0.031
1.72	0.272±0.007	0.274±0.010	0.852±0.032	0.131±0.041
1.74	0.271±0.005	0.267±0.005	0.878±0.024	0.150±0.024
1.75	0.266±0.004	0.266±0.004	0.849±0.027	0.154±0.027
1.76	0.264±0.006	0.261±0.005	0.850±0.033	0.170±0.029
1.78	0.262±0.007	0.257±0.006	0.854±0.032	0.193±0.030
1.80	0.262±0.005	0.260±0.004	0.860±0.028	0.154±0.029

Table 6.8: Reduced energies per segment $E^* = E/\varepsilon$ and chemical potentials μ_i^j of component i in subsystem j obtained from NPT Gibbs ensemble Monte Carlo simulations for a mixture of square-well monomers with a single interaction site of reduced depth $\varepsilon_{a,b}^*/\varepsilon = 14.5$, at a reduced pressure of $P^* = P\sigma^3/\varepsilon = 1.28$ for $N = 1000$ particles. See Table 6.7 for details.

T^*	$E_{l_1}^*$	$E_{l_2}^*$	μ_1^a	μ_2^a	μ_1^b	μ_2^b
1.64	-4.602±0.154	-4.649±0.155	-0.869	-0.833	-0.867	-0.850
1.65	-4.621±0.148	-4.694±0.148	-0.759	-0.741	-0.753	-0.759
1.68	-4.487±0.173	-4.500±0.171	-0.793	-0.759	-0.781	-0.770
1.70	-4.349±0.156	-4.347±0.169	-0.811	-0.787	-0.827	-0.803
1.72	-4.267±0.150	-4.257±0.149	-0.761	-0.771	-0.774	-0.800
1.74	-4.148±0.135	-4.148±0.135	-0.793	-0.764	-0.783	-0.759
1.75	-4.136±0.148	-4.146±0.138	-0.787	-0.783	-0.770	-0.770
1.76	-4.063±0.154	-4.054±0.151	-0.799	-0.795	-0.798	-0.797
1.78	-3.989±0.151	-3.992±0.150	-0.779	-0.761	-0.774	-0.764
1.80	-3.934±0.137	-3.926±0.144	-0.713	-0.718	-0.718	-0.729

Table 6.9: Liquid-liquid coexistence data obtained from NPT Gibbs ensemble Monte Carlo simulations for a mixture of square-well monomers with a single interaction site of reduced depth $\varepsilon_{a,b}^*/\varepsilon = 14.5$, at a reduced pressure of $P^* = P\sigma^3/\varepsilon = 1.28$ for $N = 1728$ particles. See Table 6.2 for details.

T^*	η_{l_1}	η_{l_2}	x_{2,l_1}	x_{2,l_2}
1.58	0.289±0.004	0.289±0.004	0.810±0.021	0.195±0.020
1.59	0.289±0.004	0.290±0.003	0.814±0.033	0.185±0.035
1.60	0.291±0.003	0.292±0.004	0.835±0.026	0.159±0.028
1.61	0.292±0.003	0.292±0.003	0.860±0.017	0.136±0.017
1.62	0.289±0.004	0.290±0.004	0.862±0.020	0.140±0.023
1.63	0.290±0.005	0.290±0.005	0.864±0.022	0.135±0.027
1.81	0.254±0.004	0.254±0.004	0.827±0.029	0.177±0.029
1.82	0.256±0.003	0.255±0.003	0.833±0.028	0.178±0.030
1.83	0.254±0.003	0.255±0.003	0.816±0.021	0.168±0.021
1.84	0.254±0.003	0.254±0.003	0.824±0.020	0.169±0.021
1.85	0.251±0.004	0.249±0.004	0.813±0.029	0.202±0.028
1.86	0.247±0.005	0.247±0.005	0.796±0.038	0.214±0.037

Table 6.10: Reduced energies per segment $E^* = E/\varepsilon$ and chemical potentials μ_i^j of component i in subsystem j obtained from NPT Gibbs ensemble Monte Carlo simulations for a mixture of square-well monomers with a single interaction site of reduced depth $\varepsilon_{a,b}^*/\varepsilon = 14.5$, at a reduced pressure of $P^* = P\sigma^3/\varepsilon = 1.28$ for $N = 1000$ particles. See Table 6.9 for details.

T^*	$E_{l_1}^*$	$E_{l_2}^*$	μ_1^a	μ_2^a	μ_1^b	μ_2^b
1.58	-4.962±0.122	-5.020±0.128	-0.870	-0.898	-0.912	-0.922
1.59	-4.939±0.131	-4.948±0.144	-0.881	-0.873	-0.879	-0.874
1.60	-4.866±0.131	-4.863±0.136	-0.872	-0.819	-0.850	-0.863
1.61	-4.777±0.110	-4.747±0.116	-0.836	-0.797	-0.830	-0.812
1.62	-4.682±0.096	-4.739±0.112	-0.852	-0.842	-0.823	-0.825
1.63	-4.676±0.114	-4.694±0.106	-0.805	-0.812	-0.793	-0.828
1.81	-3.826±0.124	-3.845±0.117	-0.802	-0.780	-0.754	-0.771
1.82	-3.843±0.120	-3.826±0.112	-0.718	-0.708	-0.723	-0.756
1.83	-3.811±0.102	-3.803±0.099	-0.720	-0.712	-0.712	-0.698
1.84	-3.772±0.105	-3.762±0.108	-0.731	-0.682	-0.710	-0.718
1.85	-3.720±0.118	-3.696±0.107	-0.711	-0.706	-0.707	-0.715
1.86	-3.647±0.126	-3.658±0.110	-0.708	-0.713	-0.699	-0.695

Table 6.11: Liquid-liquid coexistence data obtained from NPT Gibbs ensemble Monte Carlo simulations for a mixture of square-well monomers with a single interaction site of reduced depth $\varepsilon_{a,b}^*/\varepsilon = 14.5$, at a reduced pressure of $P^* = P\sigma^3/\varepsilon = 1.48$ for $N = 1728$ particles. See Table 6.2 for details.

T^*	η_1	η_2	x_{2,l_1}	x_{2,l_2}
1.54	0.307±0.003	0.305±0.003	0.808±0.027	0.206±0.025
1.555	0.312±0.003	0.310±0.003	0.870±0.015	0.143±0.015
1.56	0.306±0.004	0.305±0.004	0.863±0.018	0.145±0.019
1.57	0.302±0.003	0.303±0.004	0.832±0.021	0.169±0.019
1.58	0.299±0.003	0.300±0.004	0.851±0.018	0.146±0.017
1.59	0.295±0.004	0.295±0.004	0.822±0.025	0.177±0.026
1.61	0.301±0.005	0.300±0.004	0.877±0.020	0.136±0.020
1.63	0.295±0.006	0.295±0.006	0.878±0.014	0.124±0.015
1.65	0.292±0.003	0.294±0.003	0.882±0.014	0.110±0.014
1.67	0.296±0.007	0.292±0.005	0.905±0.016	0.125±0.015
1.70	0.292±0.005	0.289±0.004	0.911±0.017	0.122±0.017
1.73	0.287±0.004	0.282±0.003	0.909±0.014	0.113±0.015
1.75	0.286±0.004	0.284±0.004	0.906±0.014	0.108±0.016
1.77	0.282±0.004	0.279±0.003	0.901±0.017	0.119±0.016
1.79	0.280±0.004	0.280±0.004	0.895±0.015	0.103±0.014
1.81	0.268±0.004	0.268±0.004	0.869±0.018	0.129±0.019
1.83	0.264±0.005	0.265±0.004	0.856±0.024	0.137±0.023
1.85	0.271±0.005	0.265±0.004	0.889±0.024	0.146±0.020
1.87	0.272±0.004	0.268±0.004	0.896±0.016	0.131±0.016
1.88	0.269±0.004	0.264±0.004	0.891±0.017	0.145±0.019
1.89	0.262±0.004	0.258±0.003	0.867±0.023	0.163±0.021
1.90	0.263±0.003	0.261±0.003	0.871±0.019	0.141±0.020
1.91	0.260±0.004	0.259±0.004	0.865±0.019	0.145±0.019
1.92	0.255±0.005	0.252±0.003	0.845±0.023	0.187±0.022
1.93	0.256±0.004	0.254±0.004	0.844±0.025	0.172±0.022
1.94	0.250±0.004	0.249±0.004	0.818±0.032	0.193±0.030
1.95	0.247±0.003	0.248±0.003	0.819±0.027	0.206±0.026
1.96	0.252±0.003	0.251±0.004	0.833±0.023	0.173±0.024
1.97	0.250±0.004	0.248±0.004	0.819±0.028	0.202±0.028
1.98	0.248±0.004	0.246±0.004	0.811±0.031	0.210±0.030

Table 6.12: Reduced energies per segment $E^* = E/\varepsilon$ and chemical potentials μ_i^j of component i in subsystem j obtained from NPT Gibbs ensemble Monte Carlo simulations for a mixture of square-well monomers with a single interaction site of reduced depth $\varepsilon_{a,b}^*/\varepsilon = 14.5$, at a reduced pressure of $P^* = P\sigma^3/\varepsilon = 1.28$ for $N = 1000$ particles. See Table 6.11 for details.

T^*	$E_{i_1}^*$	$E_{i_2}^*$	μ_1^a	μ_2^a	μ_1^b	μ_2^b
1.54	-5.363±0.122	-5.365±0.142	-0.715	-0.810	-0.736	-0.800
1.555	-5.111±0.101	-5.143±0.106	-0.835	-0.654	-0.721	-0.649
1.56	-5.043±0.108	-5.076±0.102	-0.799	-0.758	-0.801	-0.750
1.57	-5.112±0.118	-5.140±0.122	-0.806	-0.783	-0.765	-0.718
1.58	-4.972±0.117	-4.971±0.118	-0.803	-0.805	-0.787	-0.813
1.59	-5.015±0.132	-5.014±0.130	-0.821	-0.794	-0.830	-0.819
1.61	-4.841±0.128	-4.881±0.122	-0.679	-0.695	-0.710	-0.705
1.63	-4.706±0.107	-4.716±0.123	-0.751	-0.737	-0.721	-0.763
1.65	-4.612±0.109	-4.637±0.102	-0.721	-0.734	-0.694	-0.704
1.67	-4.556±0.103	-4.627±0.094	-0.668	-0.611	-0.672	-0.607
1.70	-4.437±0.101	-4.507±0.112	-0.621	-0.599	-0.624	-0.594
1.73	-4.334±0.091	-4.300±0.089	-0.675	-0.609	-0.633	-0.631
1.75	-4.297±0.091	-4.306±0.101	-0.556	-0.556	-0.568	-0.555
1.77	-4.216±0.101	-4.223±0.101	-0.610	-0.561	-0.581	-0.571
1.79	-4.166±0.094	-4.156±0.120	-0.595	-0.548	-0.550	-0.559
1.81	-3.989±0.101	-3.987±0.106	-0.623	-0.634	-0.628	-0.610
1.83	-3.918±0.097	-3.929±0.104	-0.635	-0.618	-0.610	-0.640
1.85	-3.953±0.109	-3.870±0.107	-0.560	-0.536	-0.578	-0.545
1.87	-3.925±0.105	-3.898±0.100	-0.481	-0.470	-0.481	-0.450
1.88	-3.854±0.096	-3.825±0.109	-0.496	-0.488	-0.505	-0.474
1.89	-3.774±0.099	-3.731±0.107	-0.531	-0.528	-0.559	-0.533
1.90	-3.743±0.093	-3.729±0.102	-0.519	-0.508	-0.512	-0.518
1.91	-3.693±0.102	-3.684±0.109	-0.525	-0.516	-0.522	-0.502
1.92	-3.613±0.110	-3.574±0.103	-0.565	-0.548	-0.550	-0.556
1.93	-3.622±0.104	-3.563±0.104	-0.513	-0.513	-0.531	-0.507
1.94	-3.509±0.120	-3.484±0.104	-0.545	-0.545	-0.541	-0.544
1.95	-3.410±0.098	-3.393±0.100	-0.565	-0.563	-0.560	-0.573
1.96	-3.467±0.093	-3.476±0.112	-0.494	-0.510	-0.490	-0.489
1.97	-3.467±0.104	-3.424±0.101	-0.483	-0.492	-0.497	-0.483
1.98	-3.397±0.109	-3.366±0.117	-0.504	-0.491	-0.496	-0.499

it is important to understand the differences between the coexistence and critical regions before such an analysis can be performed. In this section we give a detailed description of the nature of the critical region in fluids. Two procedures which can be used to obtain accurate estimates for the critical parameters of model systems using computer simulation are discussed in subsequent sections.

It is known from statistical mechanics that a true phase transition, that is, a singularity in the free energy of a system, can only occur in the thermodynamic limit $L \rightarrow \infty$, where L is the linear system size [67]. The free energy surface of a finite-sized system is regular, it has no singularities. Hence a phase transition in a finite system is smeared or rounded over a particular temperature region, the centre of which corresponds to the critical temperature of the finite system, $T_c(N)$. This temperature is shifted from the critical temperature of the infinite system, $T_c(\infty)$. Various critical exponents such as λ , the shift exponent and θ , the rounding exponent, control the dependence of the critical region on the system size N , whilst other exponents control the size dependence of critical properties. In finite fluid systems the order parameter Δx , which can be given in terms of either density or composition, is defined

$$\Delta x = x_{phase1} - x_{phase2}. \quad (6.19)$$

In the infinite system limit Δx vanishes at the critical point, but for finite system it obeys the scaling relationship [68]

$$\langle |\Delta x| \rangle_{T_c, L} \sim L^{-\beta/\nu}, \quad (6.20)$$

which is controlled by the critical exponents β and ν . Finite-size effects are important in experimental systems, which are homogeneous only for finite-sized regions, and in computer simulation studies, where small system sizes are used to obtain the thermodynamic properties of model systems.

In order to understand the nature of the critical region, we must introduce the correlation length ζ_a of a specific property a . This property a is a well defined function of the positions \mathbf{r}_i and the momenta \mathbf{p}_i of all the i particles, such as an energy per particle, and is intensive, that is, does not scale with system size. This correlation length is characteristic of the critical point and is defined [69]

$$\zeta_a = \int_0^\infty dr \frac{\langle \partial a(0) \partial a(r) \rangle}{\langle \partial a^2 \rangle}, \quad (6.21)$$

where $\langle \partial a(0) \partial a(r) \rangle$ is the spatial correlation function of the property a . This correlation function becomes $\langle \partial a^2 \rangle$ for an infinitesimally small system, i.e. $r = 0$. As r increases to infinity the correlation function decays to zero since

$\langle \partial a(0) \rangle$ and $\langle \partial a(r) \rangle$ become uncorrelated, so that $\langle \partial a(0) \partial a(r) \rangle \rightarrow \langle \partial a(0) \rangle \langle \partial a(r) \rangle$. Away from the critical point the correlation length ζ_a is small (only a few molecular units in magnitude). In order to ensure good statistical sampling, the simulation box size L should be larger than ζ_a for all a properties studied in the simulation. The continuous nature of the phase transition which occurs in fluids can be characterised by the divergence of the correlation length and by the increase of the order parameter to macroscopic dimensions. This divergence can be used as a means of signaling the approach to criticality of a specific fluid system. In the vicinity of the critical point the correlation length may hence exceed the simulation box length, resulting in a shift and a rounding of the singularities and the discontinuities which characterise critical behaviour in the thermodynamic limit [70, 69], which in turn lead to finite-size effects. The shift in the phase transition caused by finite-sized simulation cells is a result of the correlation length ζ_a only having to reach a value of L in finite systems, to reach critical behaviour, rather than its divergent value in infinite systems. The rounding of the phase transition is caused by the partition function of a finite system being analytic, whereas in the limit $L \rightarrow \infty$ it has the singularities which lead to discontinuous or divergent properties [69].

The increase of the correlation length beyond the linear dimensions of the simulation box, leads to the critical point of a finite sized system $T_c(N)$ usually being an overestimation of the infinite volume critical point $T_c(\infty)$. The difference between $T_c(N)$ and $T_c(\infty)$ as $N \rightarrow \infty$ is given by [68]

$$T_c(N) - T_c(\infty) \propto N^{1/d\nu} \quad (6.22)$$

where d is the spatial dimensionality of the system and ν is the correlation length critical exponent.

Much theoretical interest lies in the accurate determination of the infinite system-size critical point, as a result of the universal nature of fluids precisely at that temperature. The most important of the theoretical studies in this area are finite-size scaling (FSS) techniques [67]. Such techniques have been developed in order to give an understanding of the relationship between properties obtained for finite systems and their counterparts in the thermodynamic limit of $L \rightarrow \infty$. Before presenting the details of such methods we examine the finite-size dependence of simulations performed in the Gibbs ensemble. We also illustrate how the GEMC simulation data for the closed-loop coexistence regions presented in the previous section can be extrapolated to give initial estimates for the critical parameters of the system. The results obtained are subsequently compared with equivalent results obtained using FSS methods.

6.6 Finite-size effects in the Gibbs ensemble

The large density fluctuations which appear as the critical point is approached prevent the direct study of the critical region using conventional simulation techniques. Hence, simulations performed in standard ensembles such as the canonical or the isothermal-isobaric ensembles, give estimates for the critical point of a particular system which are an overestimate of the infinite system critical temperature, $T_c(\infty)$. Conversely, for the Gibbs ensemble it was initially proposed, via a study of the surface contributions to the free energy in Ref. [71] that values for the critical point could be obtained which would slightly underestimate $T_c(\infty)$. The work of Ref. [71] illustrates that close to but below $T_c(N)$ no coexistence is observed in the Gibbs ensemble. At temperatures well below $T_c(N)$ the densities of the individual phases in the Gibbs ensemble are obtained by sampling the individual subsystem densities at regular intervals. Closer to $T_c(N)$, the subsystems may continuously change identity from being rich in one of the coexisting densities (or compositions) to the other. Hence, in order to obtain an estimate for the density in one of the two phases it is necessary to construct a probability distribution for the observed order parameter in a particular subsystem, which samples the density in both subsystems. This distribution function is not affected when the identity of the subsystems is interchanged. At low temperatures the surface tension of the system is high so that the two phases present will not tend to coexist within the same subsystem. This results in a density distribution function for the overall system which has two sharp peaks, representing each of the coexisting phases. As the temperature of the system increases, the surface tension decreases and becomes similar in magnitude to the enthalpy of formation of the interface [72]. This leads to the formation of a third peak on the density distribution function which exists at a density corresponding to the average overall density of the system. A further increase in temperature leads to the dominance of the entropic contribution, so that the central, average density, peak becomes more pronounced. This leads to the disappearance of the two individual phase density peaks in the probability distribution at temperatures close to, but below $T_c(N)$. The system hence appears to have undergone a phase transition at a temperature below the critical temperature of the finite system. These theoretical findings are confirmed by simulation studies of the Lennard-Jones fluid [71]. However, the study of finite-size effects in the Gibbs ensemble reported in Ref. [68] indicate that no such third central peak is observed in the probability distribution function for the 2D lattice gas model. In this case, the double peaked structure of the probability distribution function merges directly into a single peak at the average system density as the temperature of the system approaches $T_c(N)$. It is shown in Ref. [68] that for any model system, providing that the linear size of the simulation cell, L , is greater than the correlation function of the density fluctuations ζ_a , the height of the third peak, if

it occurs, is exponentially smaller than the height of the two peaks corresponding to the coexisting phases. Additionally, they indicate that in order to study the density probability distribution function close to the critical temperature, when $L \leq \zeta_a$, the finite-size rounding of the interfacial free energy must be accounted for, a fact which was ignored in the analysis of [71]. It is also important to note that finite-size effects in lattice models are significantly greater than those observed for continuum models, such as the Lennard-Jones fluid, hence they may be more difficult to detect in the latter [72].

Numerous studies of the finite-size dependence of the Gibbs ensemble exist which report small or negligible finite-size effects; examples include studies of three-dimensional systems interacting via the square-well potential [73, 54] and [74] and via the Lennard-Jones potential [62, 71]. Two studies which are a source of particular interest in this area are the examination of the lattice gas model in 2-D presented in Ref. [68] and that of the symmetrical square-well mixture with no association sites given in Ref. [53]. In the work of Ref. [68] a critical temperature for a finite system of a 10×10 lattice is reported which is 20% greater than the known infinite system critical temperature. However, the simulations reported in Ref. [68] are performed in the so-called 'restricted' Gibbs ensemble, where no volume exchanges between the two subsystems occur, and the authors concede that use of the 'restricted' Gibbs ensemble for simulation of real fluids could lead to "a behaviour rather different from the full Gibbs ensemble". Large finite size effects for both the two- and the three-dimensional systems are also reported for the square-well mixture in Ref. [53]. In this case simulations are performed in the 'restricted' Gibbs ensemble at constant NVT , so that the density of the system remains constant. The estimated critical temperatures of the finite systems studied are all significantly greater than the estimated infinite-volume critical temperature for the square-well system, even for systems of greater than $N = 1000$ particles. It is noted in Ref. [54] that the suppression of volume changes (allowed due to the system's symmetry) in the version of the Gibbs ensemble used in the work of Ref. [53] is responsible for this large finite size effect. Since the simulations are performed at constant density, the additional constraint of not performing any volume changes leads to the suppression of both the density and volume fluctuations in the work of Ref. [53]. Such fluctuations are known to influence the properties of a system as the critical point is approached. By means of illustrating that the lack of volume change steps does not affect the results of Ref. [53], a system of $N = 3200$ particles in 2-D is simulated in the 'full' Gibbs ensemble and no significant difference is observed between the results and those obtained when no volume changes are performed. This is not surprising due to the large system size studied, the difference between the two sets of results is expected to increase as the system size decreases [54]. A similar system size dependence is observed in the canonical

(*NVT*) ensemble where the system volume is kept constant, lending further evidence to support the idea that the absence of volume fluctuations in simulations performed at constant density, leads to a large finite size effect. Other results in Ref. [53], for the pure Lennard-Jones fluid in 3-D, where simulations are performed in the ‘full’ Gibbs ensemble (where volume changes are performed), show little or no system size dependence, which is in agreement with the studies of Refs. [62] and [71]. However, a recent study [74] indicates that the system-size effect observed in Ref. [53] is merely a result of the means by which the equilibrium compositions are defined. This point will be discussed in greater detail later.

Generally, finite size effects in the Gibbs ensemble are considered to be negligible in regions away from the critical point, so that simulation data from these regions can be used as experimental data and lead to an estimate of $T_c(N)$ via extrapolation of a Wegner expansion which includes scaling corrections. This method has been used successfully to predict the critical parameters of the pure Lennard-Jones fluid [75], the pure square-well fluid [73], and also for the square-well mixture of Ref. [54]. Before such a fitting can be performed it is necessary to identify to which universality class [76] the phase transitions occurring at the UCST and the LCST belong in the symmetrical associating mixture of interest here. As the critical point is approached the critical exponent β is defined in terms of the critical temperature of the finite system as, [77]

$$\Delta x(N) = B_0(N) \left| 1 - \frac{T}{T_c(N)} \right|^\beta. \quad (6.23)$$

Here, $B_0(N)$ is the leading amplitude term. We assume that the phase transitions occurring at the LCST and at the UCST both belong to the Ising universality class, so that the critical exponent takes the universal value of $\beta = 0.325$ in both cases. The coexistence curve thus has a cubic form in the critical region. Providing that the correlation length ζ_a remains less than the linear box length L , the value of $\beta = 0.325$ can be assumed to be valid over the entire duration of the simulation. The cross-over of the value of the critical exponent from universal to mean-field, where $\beta = 0.5$, only occurs when the correlation length becomes greater than L [68]. A value of $\beta = 0.5$ results in a quadratic coexistence curve close to the critical point. This type of behaviour has been observed in Gibbs ensemble simulation studies of a 2-D lattice gas [68] and in a 2-D square-well mixture [53]. A plot of the square of the order parameter Δx^2 with temperature in this case, is linear, whereas in the case where $\beta = 0.325$, a plot of Δx^3 with temperature is linear. Simulation studies of the the square-well fluid in 3-D [53] and [74], show no sign of this cross-over behaviour. This can be explained by considering the relationship between the dimensionality of the system and the temperature dependence of the

correlation length,

$$\zeta_a \propto \left| 1 - \frac{T}{T_c(N)} \right|^{-\nu} \quad (6.24)$$

The exponent ν takes a value of unity in 2-D and of 0.63 in 3-D, so that the correlation length grows more rapidly with temperature as $T \rightarrow T_c(N)$ in two dimensions than in three [78]. Hence the cross-over from universal to classical (mean-field) exponents occurs further away from $T_c(N)$ in 2-D than in 3-D, making it more easily observed in simulations of 2-D systems. It is generally agreed that this type of cross-over behaviour cannot be observed in 3-D systems using regular simulation techniques [79]. The other critical exponents can hence also be attributed their universal values, $\alpha = 0.11$ for the heat capacity, $\gamma = 1.24$ for the compressibility on the critical isochore, and $\delta = 4.8$ for the critical isotherm [80]. Away from the critical region the power law of Eq. (6.23) fails to accurately describe the shape of the coexistence curve. It is hence necessary to include corrections to the renormalisation group (RG) based scaling laws in order to obtain more accurate results. Such corrections can be written as an expansion in $t = 1 - T/T_c(N)$ [80], in a so-called Wegner expansion [81]

$$|x_1 - x_2| = B_0|t|^\beta + B_1|t|^{\beta+\Delta_1} + B_2|t|^{\beta+2\Delta_1} + \dots, \quad (6.25)$$

where Δ_1 is a RG gap exponent, equal to 0.5 in the case studied here, and the B_i terms are the correction amplitudes. This expansion leads to the estimation of the critical temperature whilst assuming a universal value for the critical exponent. A similar expansion can be written for the diameter of the coexistence curve [80]

$$\frac{(x_1 + x_2)}{2} = \zeta_c + C_1|t|^\psi + C_2|t| + C_3|t|^{\psi+\Delta_1} + \dots, \quad (6.26)$$

where ζ_c is the critical composition, the C_i terms are the coefficients of the expansion, and ψ is an exponent which characterises the anomaly in the diameter of the curve. These two expansions can be combined to give one expression for the coexisting compositions

$$x_{\pm} = x_c + C_1|t|^\psi + C_2|t| + C_3|t|^{\psi+\Delta_1} + \dots \\ \pm \frac{1}{2} \left(B_0|t|^\beta + B_1|t|^{\beta+\Delta_1} + B_2|t|^{\beta+2\Delta_1} + \dots \right), \quad (6.27)$$

where x_- and x_+ represent the smaller and larger coexistence compositions, respectively. Similar expressions can be written in terms of the coexistence densities.

For the symmetrical square-well mixture studied here this expression can be simplified due to the symmetry of the system. The critical composition is known to be equal to 0.5, and the non-linear C_i coefficients can be disregarded, since the diameter is symmetrical about 0.5. Additionally, only the first correction to scaling

term B_1 is required in order to give an adequate description of the liquid-liquid coexistence region. Hence the expression for the compositions of the coexisting phases becomes

$$x_{\pm} = 0.5 + C_2|t| \pm \frac{1}{2} \left(B_0|t|^{\beta} + B_1|t|^{\beta+\Delta_1} \right). \quad (6.28)$$

Assuming values of $\beta = 0.325$ and $\Delta_1 = 0.5$ the above equation can be fitted to the simulation data using a standard least-squares procedure [82] to give estimates of the critical temperature. Since the coexistence curves obtained by GEMC simulation in Figs. 6.11 and 6.14 have two critical points it is possible to use two such power laws, one to estimate the UCST, and one to estimate the LCST. These two expressions can be combined to give a complete description of the region of closed-loop immiscibility. A hyperbolic tangent function of the form:

$$\tanh(x) = \frac{\exp(x) - \exp(-x)}{\exp(x) + \exp(-x)} \quad (6.29)$$

is used as a switching function between the expression for the UCST and that for the LCST. Hence, only the expansion fitted to data close to the UCST is used above a certain temperature T_{switch} , and the expansion fitted to data close to the LCST is used at temperatures below this point. The compositions of the coexisting liquid phases in the closed-loop region are obtained as

$$x_{\pm}^{loop} = F(T)x_{\pm}^{UCST} + (1 - F(T))x_{\pm}^{LCST}, \quad (6.30)$$

where $F(T)$ is given by

$$F(T) = \frac{1}{2} + \frac{1}{2} \tanh(y), \quad (6.31)$$

with

$$y = \frac{T - T_{switch}}{2\lambda_{fix}}. \quad (6.32)$$

The parameter λ_{fix} controls the steepness of the tanh function. In order to describe the coexistence curves in Figs. 6.11 and 6.14 we assume $\lambda_{fix} = 0.1$. This procedure is seen to provide an excellent description of the shape of the closed-loop of immiscibility at the two pressures in question (see Figs. 6.11 and 6.14). The estimated critical temperatures, together with the values of the coefficients B_0 , B_1 and C_2 are given in Table 6.13 for the temperature-composition slice at a reduced pressure of $P^* = 1.28$ and in Table 6.14 for a pressure of $P^* = 1.48$.

As with all ensembles, data obtained in close proximity to the critical point has to be treated with care, especially in systems of low dimensionality. This is due to the cross-over from universal to mean-field critical exponents which occurs as the critical temperature is approached. However, the selection of data which can be considered far enough away from the critical region to be included in the ex-

Table 6.13: Estimated critical constants for the symmetrical square-well mixture with $\lambda = 1.5$ with a single bonding site of reduced energy $\varepsilon_{a,b}^* = 14.5$ at a reduced pressure of $P^* = 1.28$. The errors represent the maximum possible error which is estimated from the reported errors in the compositions obtained from the simulation data.

	UCST	LCST
$T_c^*(N)$	1.915 ± 0.689	1.557 ± 0.009
B_0	2.32 ± 1.85	3.00 ± 0.21
B_1	-2.61 ± 3.20	-4.94 ± 0.54
C_2	0.067 ± 0.095	0.17 ± 0.42

Table 6.14: Estimated critical constants for the symmetrical square-well mixture with $\lambda = 1.5$ with a single bonding site of reduced energy $\varepsilon_{a,b}^* = 14.5$ at a reduced pressure of $P^* = 1.48$. The errors represent the maximum possible error which is estimated from the reported errors in the compositions obtained from the simulation data.

	UCST	LCST
$T_c^*(N)$	2.068 ± 1.038	1.466 ± 0.239
B_0	2.01 ± 2.27	2.03 ± 0.89
B_1	-1.45 ± 3.01	-1.51 ± 1.12
C_2	0.078 ± 0.056	0.051 ± 0.038

trapolation is an arbitrary process. An alternative and more rigorous route to the estimation of critical point parameters is via finite-size scaling methods.

6.7 Finite-size scaling theory

It is well-known that finite-size effects can lead to serious errors in computer simulation estimates of critical point parameters, and FSS techniques have been developed in order to overcome such problems [67]. Application of these techniques to finite systems which are close to criticality, allow the infinite system-size quantities to be estimated accurately. The basic FSS hypothesis states that for sufficiently large values of the correlation length ζ_a and of the linear simulation cell L , the coarse-grained properties of a specific system close to criticality are universal [76] and only depend on the length scale L and on the appropriate scaling fields. These fields measure deviations from criticality [81] and are quantities which are specific to each universality class. Exactly at the critical point the probability distribution functions of certain observable quantities such as the density or composition, do not vary with system size: they are said to be scale invariant [83]-[85]. Another feature of these critical distribution functions, which is central to the FSS analysis, is that they are all identical for systems which belong to the same universality class, that is, they are universal functions. These concepts of scale invariance and universality provide the basis of the way in which FSS methods are used to estimate the infinite volume critical parameters of specific, finite, systems.

It is well known experimentally [86]-[80], theoretically [88, 89], and from computer simulation studies [90], that simple fluids belong to the Ising universality class. This enables the matching of the (easily measured) critical distribution function for the Ising model with those obtained from simulation studies of fluid systems, due to their universal equivalence. This matching allows the infinite system size critical properties for fluid systems to be estimated.

Here, we will only give a brief outline of the FSS analysis method; more details can be found in Ref. [91] (see also Ref. [92] for a review). For the Ising universality class, the critical point is characterised by two scaling fields: τ the thermal scaling field, and h the ordering scaling field. For systems which possess the so-called particle-hole symmetry, such as the Ising magnet, τ is the reduced temperature and h is the reduced magnetic field [67]. Fluid systems have a reduced symmetry with respect to the Ising model, so that the scaling fields τ and h take a different form [93]; they consist of linear combinations of the potential well-depth ω and of

the chemical potential μ [91]:

$$\tau = \omega_c - \omega + s(\mu - \mu_c), \quad h = \mu - \mu_c + \tau(\omega_c - \omega) \quad (6.33)$$

where s and τ are system specific quantities which control the degree of field mixing. In the case of the Ising model, $s = 0$ and $\tau = 0$. This field mixing does not affect the universal properties of fluids, it only has an observable effect on non-universal properties close to criticality. The most familiar effect of field mixing is that of the failure of the law of rectilinear diameters due to the weak, energy-like singularity in the coexistence diameters at criticality [94]. Conjugate to the the scaling fields τ and h there are two scaling operators \mathcal{E} and \mathcal{M} [91], which are linear combinations of the particle density ρ and the energy density u ,

$$\mathcal{M} = \frac{1}{1 - s\tau}[\rho - su], \quad \mathcal{E} = \frac{1}{1 - s\tau}[u - \tau\rho]. \quad (6.34)$$

\mathcal{M} is the ordering operator (conjugate to h) and \mathcal{E} is the energy-like operator (conjugate to τ). For the Ising model \mathcal{M} is simply the magnetisation and \mathcal{E} is the energy density. The symmetry of the square-well system studied here leads to the simplification of these scaling expressions. The fact that the critical composition of this system is fixed at $x_c = 0.5$ together with the symmetrical nature of the square-well interactions between species, leads to the absence of field mixing, between the thermal and ordering scaling fields τ and h in Eq. (6.33). Hence, the field mixing parameters s and τ are zero, and we are effectively examining the critical behaviour of a system which had an equivalent symmetry to that of the Ising magnet. In this case, the ordering operator \mathcal{M} is equal to the density (or composition) of the individual species, and the energy-like operator \mathcal{E} is equal to the energy density. Hence, a study of the distribution of the order parameter for this system is equivalent to a study of the distribution function of the Ising magnet, which is considered to be a hallmark of this universality class.

Finite-size scaling methods [91] which are based on the renormalisation group theories [83], predict that the concentration distribution of the symmetrical square-well system of linear dimensions L exactly at criticality scales with system size as

$$P_L(m) \approx a_m^{-1} L^{\beta/\nu} \tilde{P}_m(L^{\beta/\nu} a_m^{-1} \delta m), \quad (6.35)$$

where $m = x - x_c$ and $\delta m = m - m_c$. a_m is a non-universal scale factor which can be assigned a specific value in order to ensure the universality of $\tilde{P}_m(y)$, which is a universal function of the scaling variable $y = L^{\beta/\nu} a_m^{-1} \delta m$. Performing simulations close to the critical points of the symmetrical square-well mixture at a series of different system sizes should therefore result in universal concentration distributions at two specific temperatures; corresponding to the UCST and the LCST of

the infinite system. The observation of these size-independent distributions enable the accurate estimation of infinite system critical temperatures for this system. An initial estimate for $T_c(\infty)$ is obtained from the linear relationship between the critical temperature of the finite system $T_c(N)$ and the system size N given in Eq. (6.22). This relies on the prior estimation of critical temperatures for a series of finite-size systems. This is achieved using the relationship given in Eq. (6.23). Such results rely on the successful simulation of the system in regions close enough to the critical point so that Eq. (6.23) is valid. This in turn relies on the choice of a suitable ensemble.

The majority of FSS studies have been implemented in the grand canonical (GC) ensemble with μVT fixed. The main advantage of this ensemble over other common ensembles is that it allows the total number of particles to fluctuate during the simulation, via particle insertion steps. This allows the fluctuation in the order parameter (density or composition) to be observed over the full length scale of the system itself, hence minimising corrections to scaling. FSS ideas have also been applied to systems in the canonical ensemble NVT fixed [95, 96]. In this case the simulation box is divided into sub-sections of length l , within which the density is allowed to fluctuate. Use of FSS techniques in the canonical ensemble has been found to be less successful than those in the GC ensemble, which is partly due to the introduction of an additional length scale l into the FSS analysis. The magnitude of this length has to be significantly larger than the individual particle diameter σ , and significantly smaller than the total simulation box length L . This leads to the situation where prohibitively large simulations are necessary in order to obtain satisfactory results [92]. A study of the FSS properties of the Lennard-Jones fluid at constant pressure P , within the isothermal-isobaric (NPT fixed) ensemble has also been reported [97]. Here, the number of particles is fixed, as in the canonical ensemble, but the overall density is allowed to fluctuate by means of volume changes of the simulation box. This leads to complications for the application of FSS ideas since these are based on the concept of comparing the correlation length of fluctuations with the linear dimensions (L) of the simulation box. In the NPT ensemble L is varied during the simulation, however, it has been shown that the critical scaling distribution functions in the NPT ensemble are equivalent to those in the GC ensemble [97]. This equivalence can be rationalised by considering that either ensemble only has one extensive variable, N in the grand canonical ensemble and V in the isothermal-isobaric ensemble. Other statistical ensembles, such as the microcanonical (NVE fixed) or the canonical, have different characteristic scaling functions, which are in turn different to those in the GC ensemble, since they have two extensive variables; N and V . However, use of the NPT ensemble is not preferred over the GC ensemble, since in the NPT ensemble, the correlation time (the time equivalent of the correlation length) is much longer,

hence making it less efficient. One advantage of the NPT ensemble over the μVT ensemble, is that no particle insertions have to be performed, so that the NPT ensemble is favoured in simulations of high density systems.

No method currently exists to implement FSS methods within the Gibbs ensemble, which is mainly due to the fact that the two subsystems in the Gibbs ensemble both undergo volume fluctuations during the simulation, so that there is no length scale which remains constant over the whole course of the simulation. It is only in simulations of symmetrical fluid systems (such as the square-well system studied here) or the Ising lattice gas [98], where volume fluctuations can be excluded due to symmetry, that accurate results can be obtained via a full FSS analysis in the Gibbs ensemble [92]. Use of the Gibbs ensemble to provide estimates of the critical point and its associated phenomena is hence currently restricted to extrapolation of data obtained well away from the critical region itself.

The semigrand canonical ensemble (SGC) [99, 100], described in Chapter 3, is an ensemble which can be used to obtain data which can be analysed using FSS methods. The total number of particles N is kept constant, but the concentration of the individual species is permitted to fluctuate by enforcing that the difference in chemical potentials $\Delta\mu = \mu_1 - \mu_2$ is kept constant, together with the variables NVT . The symmetrical square-well mixture with no interaction sites has recently been examined using FSS ideas in the SGC ensemble [74]. As a result of the symmetry of this binary mixture, the SGC ensemble can be used to simulate two-phase coexistence in a single simulation but by performing the simulation in a single subsystem. Additionally, as mentioned previously, the symmetry of the system results in the simplification of the complex FSS expressions involved in the description of the critical behaviour of the mixture. The combination of a single box simulation and particle identity changes, lead to the efficiency of simulations in the SGC ensemble being much higher than that of simulations performed in either the Gibbs or the GC ensembles. This is advantageous since a full FSS analysis for a specific model system is very time consuming, for example, in the FSS study of Ref. [91] the simulations are performed on 4096 distributed array processors (DAPS) for runs up to 2×10^6 Monte Carlo cycles.

6.8 Semigrand canonical ensemble simulation results

The binary mixture of square-well molecules with one off-centre bonding site is examined by simulations performed in the semigrand canonical ensemble at constant $\Delta\mu NVT$, where a simulation cycle consists of N trial displacements and

a fixed number of trial particle identity changes, following the acceptance rules given Chapter 3. Displacements are performed in such a way to give a 30% to 40% acceptance rate, and the number of identity changes is controlled so that between 1% and 3% of the particles are given a new identity. A smaller number of identity changes are required as the critical point of the system is approached. The strength of the site-site interaction energy is fixed at $\varepsilon_{a,b}^* = 14.5$ and simulations are performed at a constant packing fraction of $\eta = 0.287$ and $\eta = 0.247$, which correspond to the packing fractions of the UCST and the LCST, respectively, of the $P^* = 1.28$ closed-loop GEMC simulations reported in the previous section (cf. Fig 6.11). Simulations are performed for systems with $N = 108, 256$ and 864 particles, for a range of temperatures at both densities.

For the symmetrical square-well mixture it is possible to guarantee equilibrium between a single liquid phase and its symmetrical counterpart by fixing $\Delta\mu^0 = 0$ [74]. Hence the two coexisting phases need not be simulated individually. The liquid-liquid phase equilibria of a system with equivalent symmetry can be therefore be obtained by fixing $\Delta\mu^0 = 0$ at constant NVT in the semigrand canonical ensemble, and allowing composition fluctuations to occur by performing identity changes. For the square-well system studied here, simulation of the region of liquid-liquid coexistence between the upper and the lower critical solution temperatures will yield equilibrium compositions of the individual phases. As a result of the ability of the simulation box to change identity during the simulation, from being rich in component 1 to being rich in component 2, it is necessary to use histograms to monitor the relative frequency at which specific compositions of either component appear in the distribution function. Away from the critical region, the histograms are singly peaked, since the simulation samples either phase a , rich in component 1, or phase b , rich in component 2. As the critical region is approached the histograms are double peaked, indicating that the system is sampling both coexisting phases. Above the critical temperature, for the UCST, below for the LCST, the histograms display a broad peak centred at the critical composition. This variation in the shape of the concentration distribution functions with temperature is shown in Figure 6.17 for simulations performed at $\eta = 0.287$, and in Figure 6.18 for the simulations performed at $\eta = 0.247$. The average concentration of species i in each phase is given by an average over the distribution function, $\bar{x} = \sum x P_N(x)$. When the histograms exhibit two peaks, the total histogram may be approximated by $P_N(x) \approx P_N^a(x) + P_N^b(x)$, where $P_N^a(x)$ is the concentration distribution of a component in phase a , and $P_N^b(x)$ is the distribution in phase b . In this case the average concentration of species i in each phase can be written as a sum over the corresponding distribution function,

$$\bar{x}^a = \sum x P_N^a(x), \quad \bar{x}^b = \sum x P_N^b(x), \quad (6.36)$$

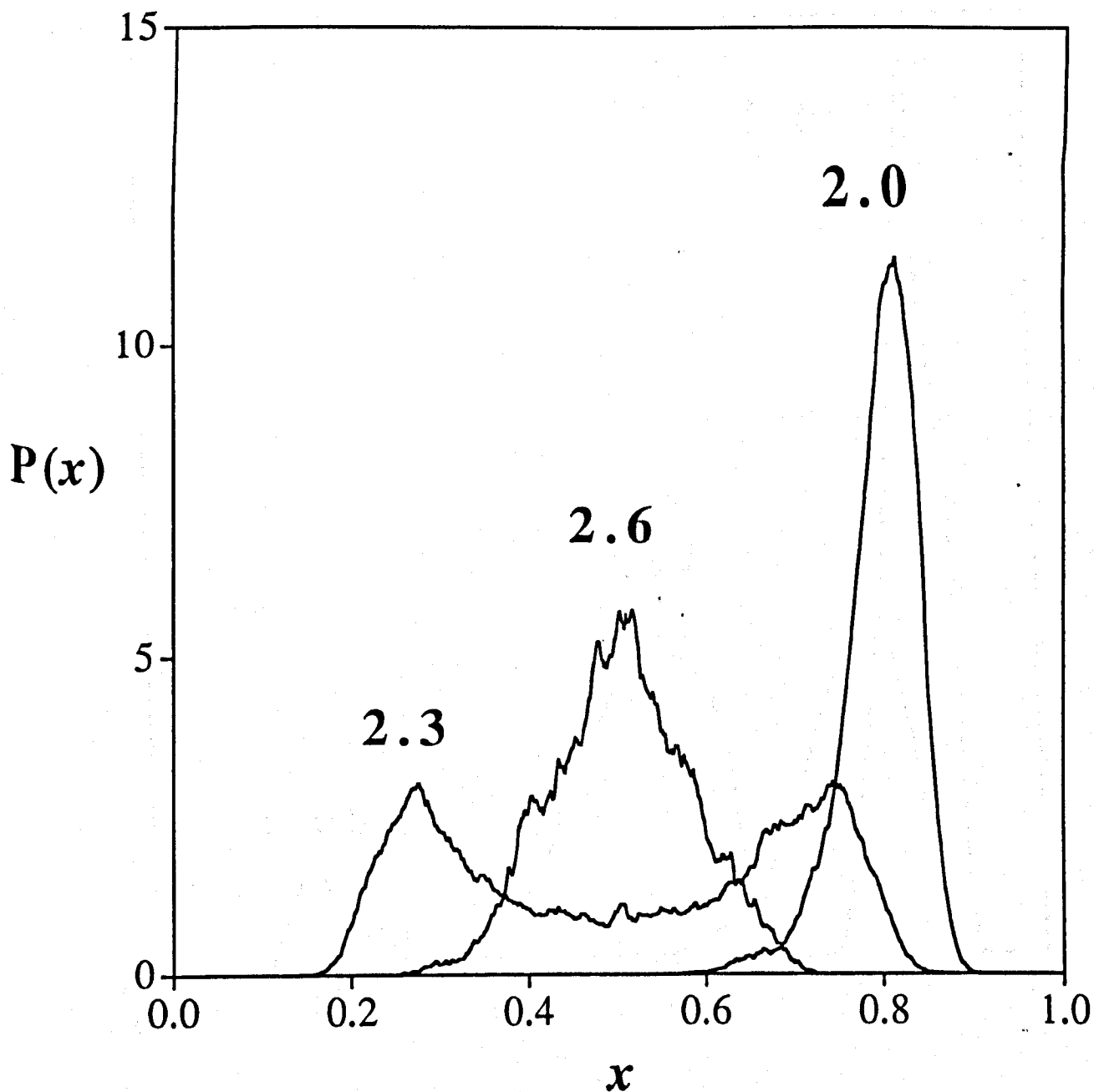


Figure 6.17: Concentration distribution functions $P_N(x)$ of a component in the symmetrical square-well mixture with $\epsilon_{a,b}^* = 14.5$. Simulations are performed in the semigrand ensemble at a constant packing fraction of $\eta = 0.287$ with $N = 864$ particles. The curves are labelled with the corresponding values of the reduced temperatures $T^* = kT/\epsilon$. The estimated UCST for this finite system is $T_c^*(N) = 2.382$.

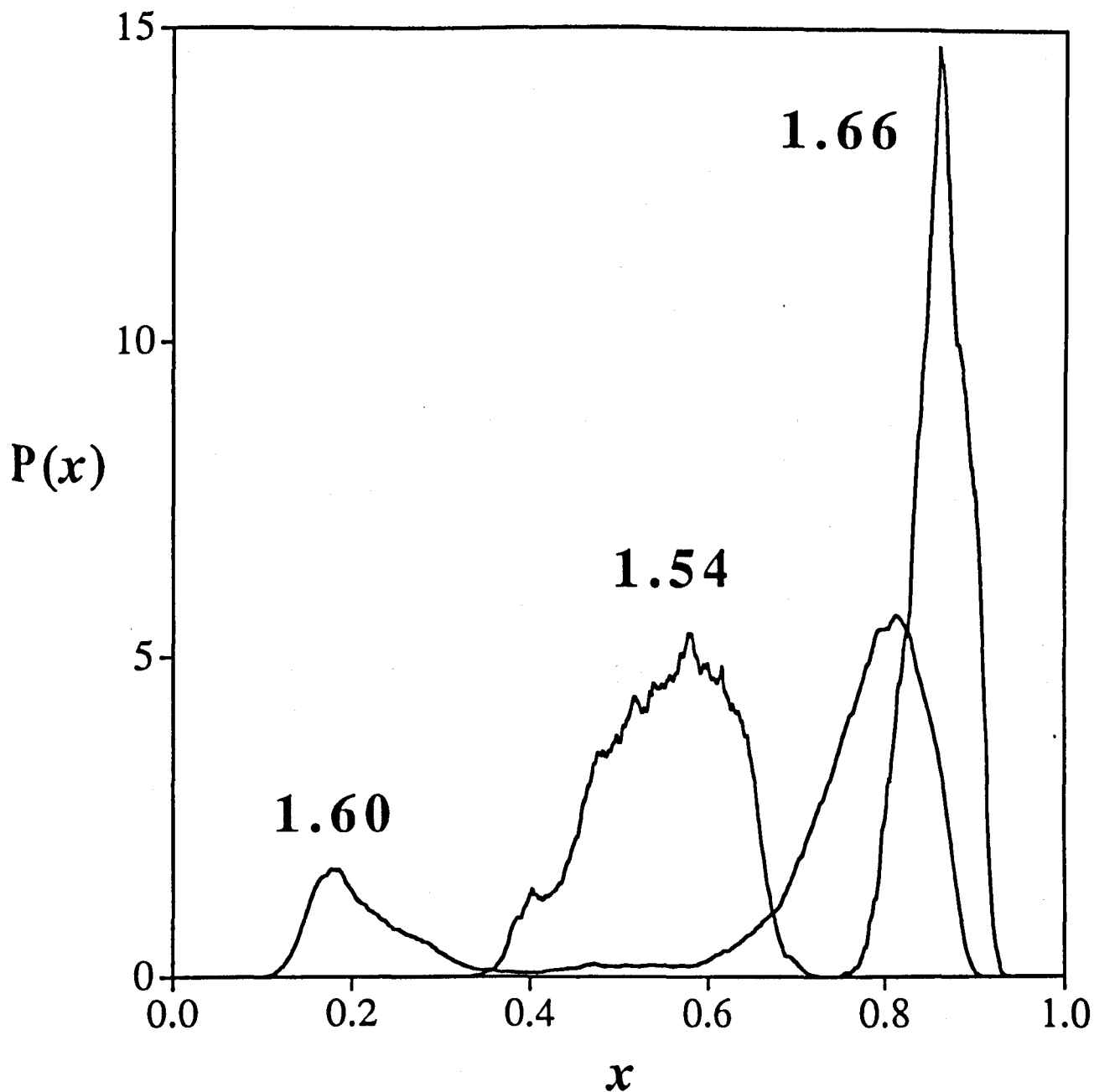


Figure 6.18: Concentration distribution functions $P_N(x)$ of a component in the symmetrical square-well mixture with $\varepsilon_{a,b}^* = 14.5$. Simulations are performed in the semigrand ensemble at a constant packing fraction of $\eta = 0.247$ with $N = 864$ particles. The curves are labelled with the corresponding values of the reduced temperatures $T^* = kT/\varepsilon$. The estimated LCST for this finite system is $T_c^*(N) = 1.570$.

where $P_N^a(x)$ and $P_N^b(x)$ are normalised to unity. Due to symmetry, $\bar{x}^a = 1 - \bar{x}^b$. The importance of correctly identifying the equilibrium value x_{eq} of the concentration of a given species with the average value of x taken over the whole distribution function \bar{x} , as in Eq. (6.36), rather than with the most probable value is discussed in Ref. [74]. The assumption that the concentration distribution functions can be approximated by symmetrical Gaussians in regions close to the critical temperature of the system, as used in Ref. [53] is found to be invalid. The large finite-size effect observed in the critical temperatures estimated for the symmetrical square-well system in the work of Ref. [53] are explained in terms of the use of this incorrect assumption in Ref. [74].

The effect of varying the system size on the form of the composition distribution function for the simulations performed at a packing fraction of $\eta = 0.287$ is shown in Figure 6.19, at a temperature well below that of the UCST. The curves are seen to become more asymmetric as the system size decreases. A similar comparison is made in Figure 6.20, now at a temperature close to the estimated UCST. Here the distributions are asymmetric for all system sizes and the peak heights are seen to approach the thermodynamic limit of $\bar{x} = 0.5$ as the system size increases. The equivalent curves for the system at a packing fraction of $\eta = 0.247$, away from the LCST and close to the LCST are given in Figures 6.21 and 6.22, respectively. In this case, the trends exhibited by the curves are not as clear as those for the UCST, nevertheless the shift of the maxima of the distributions to the thermodynamic limit as the system size increases can be observed.

In this work we follow the methodology of Ref. [74], and fit the doubly-peaked concentration distribution functions to two asymmetric Gaussians [82], in order to obtain \bar{x} . We assume that the distribution function $P_N(x)$ can be written as a sum $P_N(x) = P_N^a(x) + P_N^b(x)$, where

$$P_N^a(x) = \begin{cases} A_1^a \exp[-A_2^a(x - \bar{x}^a)^2], & \text{if } x < \bar{x}^a, \\ A_1^a \exp[-A_3^a(x - \bar{x}^a)^2], & \text{if } x \geq \bar{x}^a \end{cases} \quad (6.37)$$

$$P_N^b(x) = \begin{cases} A_1^b \exp[-A_2^b(x - \bar{x}^b)^2], & \text{if } x < \bar{x}^b, \\ A_1^b \exp[-A_3^b(x - \bar{x}^b)^2], & \text{if } x \geq \bar{x}^b \end{cases} \quad (6.38)$$

For sufficiently large system sizes the asymmetry coefficients A_i^j become equal in each phase, since the Gaussians become symmetrical as the system size increases, so that $A_2^a = A_3^a$ and $A_2^b = A_3^b$. A typical fit to one of the doubly-peaked concentration distributions is shown in Figure 6.23. The values obtained for the equilibrium compositions \bar{x} using this fitting procedure are given in Table 6.15, for three system sizes of $N = 108, 256$ and 864 particles for the simulations performed

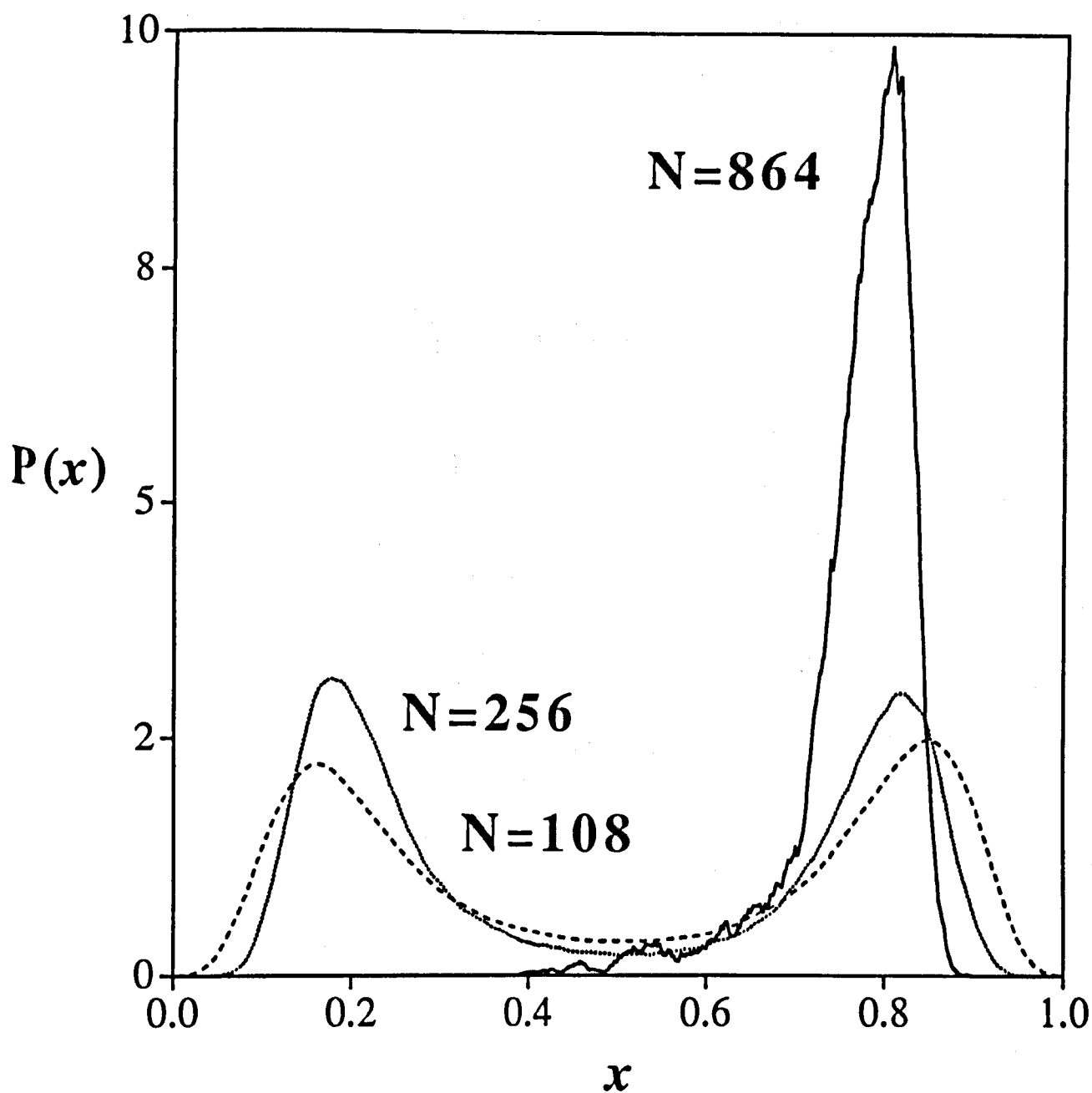


Figure 6.19: Effect of a variation in system size on the concentration distribution function $P_N(x)$ for a component in the symmetrical square-well mixture with $\epsilon_{a,b}^* = 14.5$ at a constant packing fraction of $\eta = 0.287$, at a reduced temperature of $T^* = kT/\epsilon = 1.80$, which is well below the estimated UCST for the system. The dashed curve corresponds to simulations of $N = 108$ particles, the dotted curve to simulations of $N = 256$ particles and the bold curve to simulations of $N = 864$ particles.

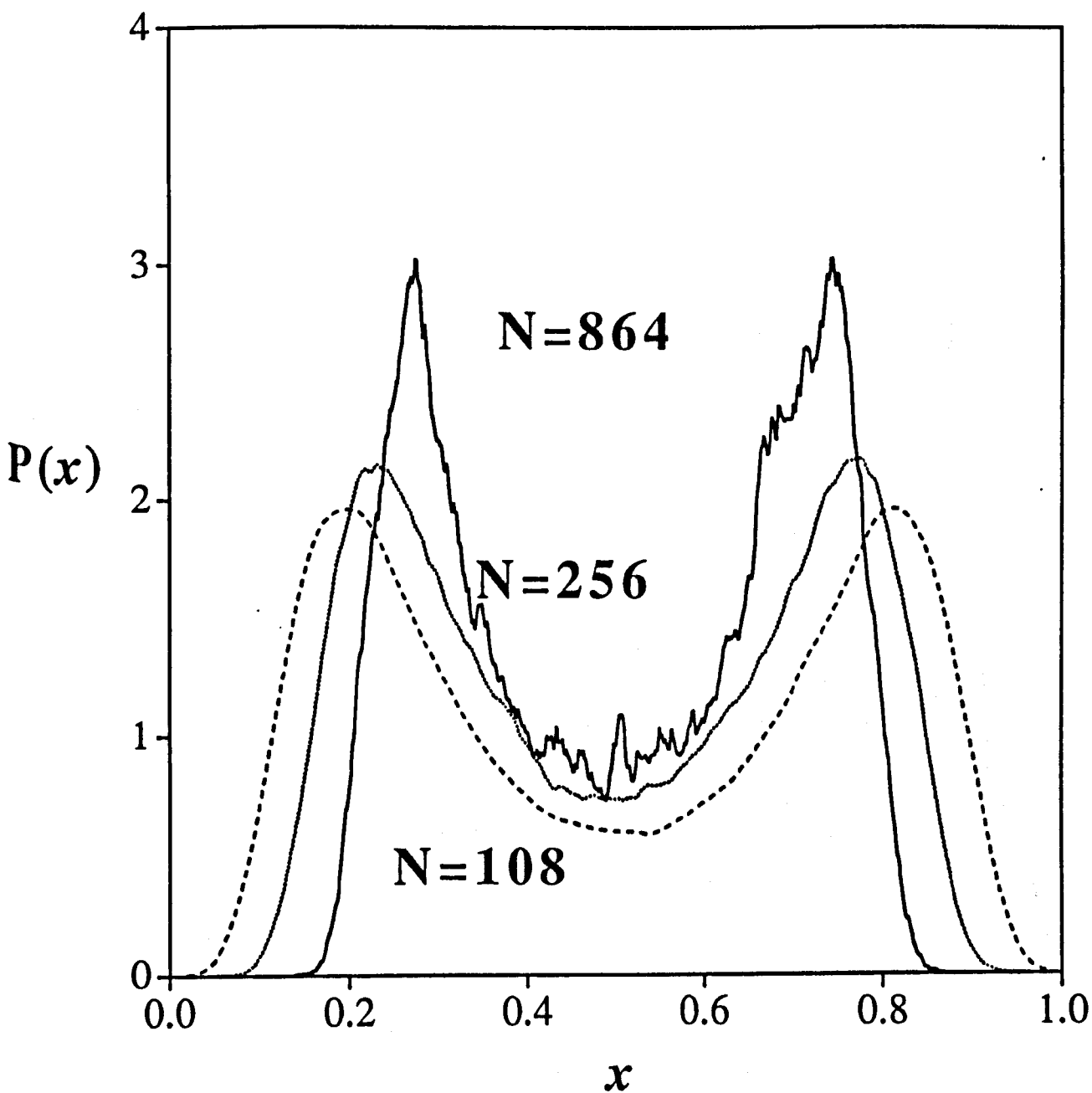


Figure 6.20: Effect of a variation in system size on the concentration distribution function $P_N(x)$ for a component in the symmetrical square-well mixture with $\epsilon_{a,b}^* = 14.5$ at a constant packing fraction of $\eta = 0.287$, at a reduced temperature of $T^* = kT/\epsilon = 2.30$, which is close to the estimated UCST for the finite, $N = 864$ system. The dashed curve corresponds to simulations of $N = 108$ particles, the dotted curve to simulations of $N = 256$ particles and the bold curve to simulations of $N = 864$ particles.

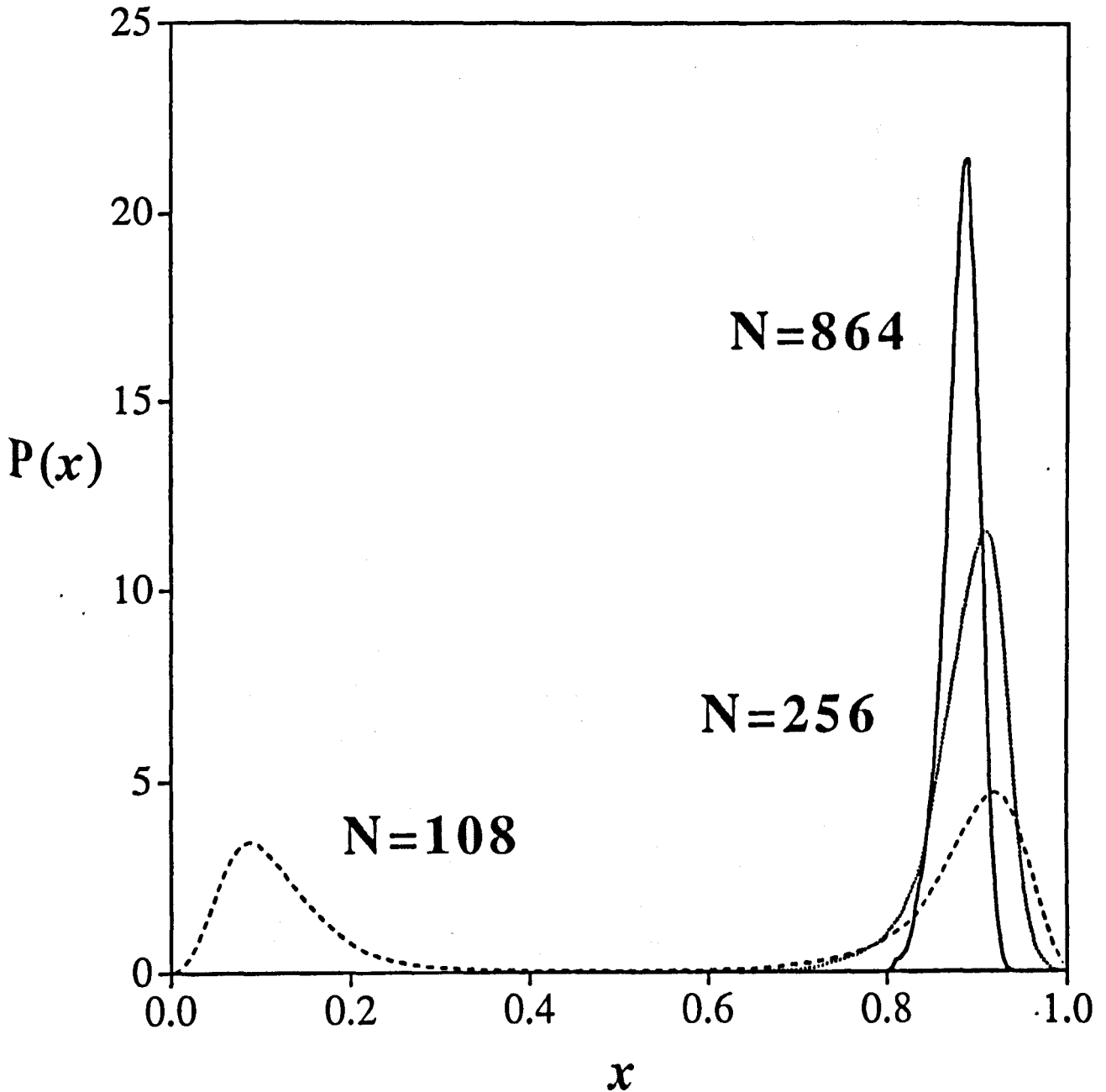


Figure 6.21: Effect of a variation in system size on the concentration distribution function $P_N(x)$ for a component in the symmetrical square-well mixture with $\epsilon_{a,b}^* = 14.5$ at a constant packing fraction of $\eta = 0.247$, at a reduced temperature of $T^* = kT/\epsilon = 1.68$, which is well below the estimated LCST for the system. The dashed curve corresponds to simulations of $N = 108$ particles, the dotted curve to simulations of $N = 256$ particles and the bold curve to simulations of $N = 864$ particles.

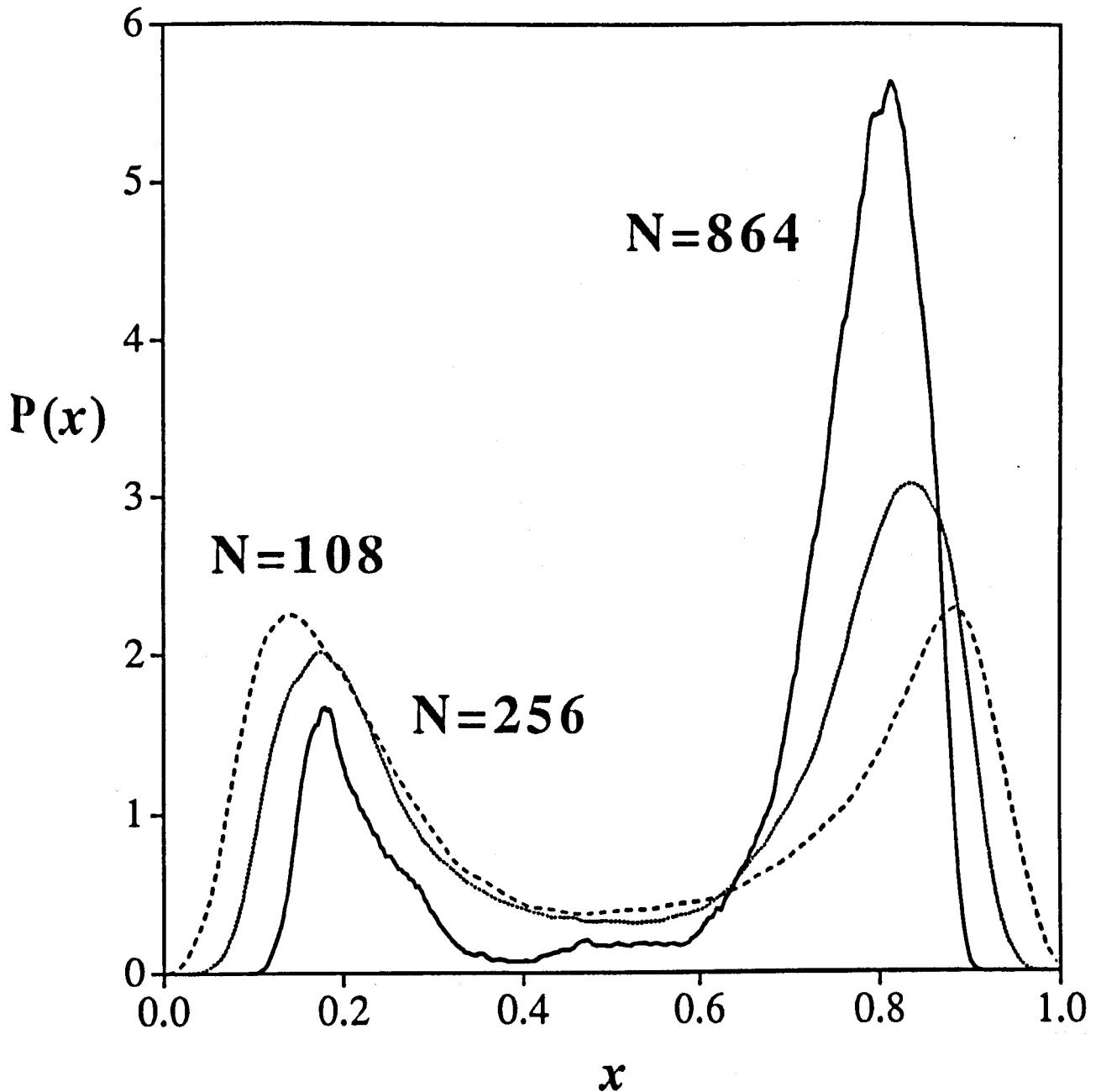


Figure 6.22: Effect of a variation in system size on the concentration distribution function $P_N(x)$ for a component in the symmetrical square-well mixture with $\varepsilon_{a,b}^* = 14.5$ at a constant packing fraction of $\eta = 0.247$, at a reduced temperature of $T^* = kT/\varepsilon = 1.60$, which is close to the estimated LCST for the finite, $N = 864$ system. The dashed curve corresponds to simulations of $N = 108$ particles, the dotted curve to simulations of $N = 256$ particles and the bold curve to simulations of $N = 864$ particles.

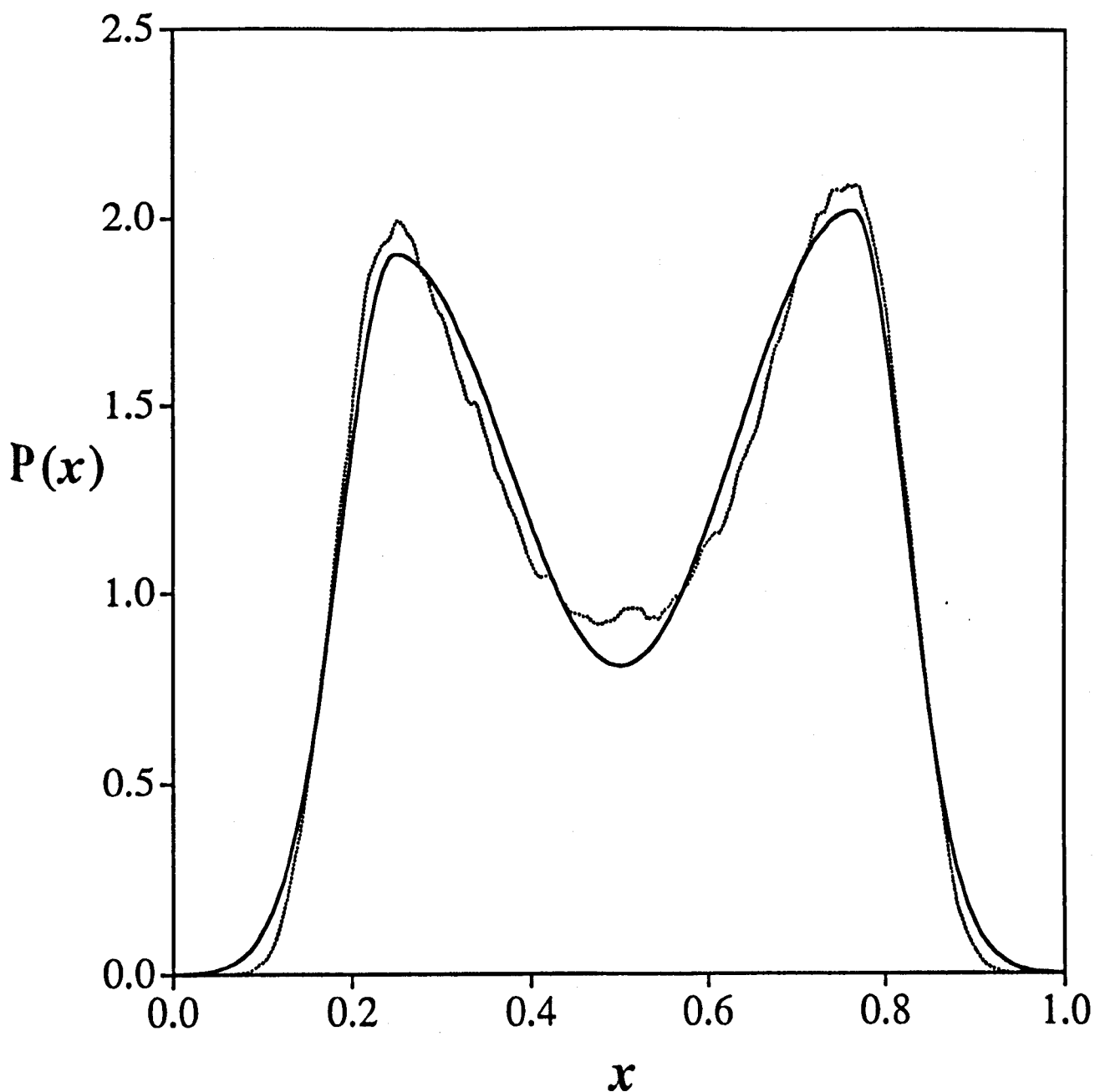


Figure 6.23: Typical fit of the composition distribution function $P_N(x)$ obtained from simulation (dotted curve) to the sum of two asymmetric Gaussians (bold curve). The simulation is performed at a constant packing fraction of $\eta = 0.287$ at a reduced temperature $T^* = kT/\varepsilon = 2.35$ for a system of $N = 256$ particles.

at $\eta = 0.287$. The equivalent values for the simulations performed at a packing fraction of $\eta = 0.247$ are given in Table 6.16.

Table 6.15: Liquid-liquid coexistence data obtained from semigrand canonical ensemble simulations at constant packing fraction $\eta = 0.287$ for the symmetrical square-well system with $\lambda = 1.5$ and with a single interaction site of depth $\epsilon_{a,b}^* = 14.5$. The data for the concentration of component 1 were obtained as averages over the distribution function for three different system sizes. Due to symmetry the composition of component 2 is given by $1 - x$. The reduced temperature is defined as $T^* = kT/\epsilon$.

T^*	$x(N = 108)$	$x(N = 256)$	$x(N = 864)$
2.35	0.314	0.282	0.234
2.30	0.259	0.293	0.313
2.25	0.239	0.268	0.276
2.20	0.230	0.238	0.253
2.15	0.210	0.217	0.231
2.10	0.194	0.202	0.216
2.00	0.183	0.188	0.203
1.90	0.188	0.195	0.201

Table 6.16: Liquid-liquid coexistence data obtained from semigrand canonical ensemble simulations at constant packing fraction $\eta = 0.247$ for the symmetrical square-well system with $\lambda = 1.5$ and with a single interaction site of depth $\epsilon_{a,b}^* = 14.5$. See Table 6.15 for details.

T^*	$x(N = 108)$	$x(N = 256)$	$x(N = 864)$
1.58	-	-	0.294
1.60	0.199	0.218	0.211
1.62	0.157	0.153	0.177
1.64	0.133	0.144	0.146
1.66	0.120	0.126	0.140
1.68	0.108	0.117	0.118
1.70	0.096	0.108	0.082

These values of the equilibrium compositions can be used to give an estimate of the respective critical temperature for each system size at a fixed packing fraction. This is achieved by assuming the linear relationship between temperature and the order parameter given in Eq. (6.23) and fixing $\beta = 0.325$. The estimates of $T_c(N)$

obtained by this mechanism can, in turn be used to estimate the value of $T_c(\infty)$ for both the LCST and UCST of the symmetrical square-well system. In this case, the shift of the infinite system critical point is given by the linear relationship between $T_c(N)$ and the size of the system given in Eq. (6.22). The dimensionality of the system is given as $d=3$ and the correlation length critical exponent is assumed to take the value $\nu=0.63$. The estimated critical temperature for each of the system sizes are given in Table 6.17 for both the UCST and the LCST.

Table 6.17: Estimations for the critical temperatures obtained from the semi-grand ensemble simulation data at a constant packing fraction of $\eta=0.287$ (for the UCST), and $\eta=0.247$ (for the LCST). $T_c(N)$ is the estimated critical temperature of a system of N particles, obtained by extrapolation of Eq. (6.23) assuming a value of $\beta=0.325$. The infinite system-size critical point is obtained by extrapolation of Eq. (6.22), see text for details.

N	$T_c^*(N)$ UCST	$T_c^*(N)$ LCST
108	2.523	1.528
256	2.451	1.549
864	2.382	1.570
∞	2.314	1.590

In order to check the validity of the estimations of $T_c(\infty)$ for the upper and lower critical solution temperatures, we turn to the finite-size scaling analysis described earlier. The order parameter distribution function exactly at criticality for a system belonging to the Ising universality class is known not to scale with system size. The form of the distribution function is given in Eq. (6.35). Simulations are therefore also performed for the three system sizes at the estimated infinite system-size critical temperature of $T^*=2.31$ with a packing fraction of $\eta=0.287$. The resulting concentration distribution functions are plotted in Figure 6.24 in terms of the scaling variable $y = L^{\beta/\nu} a_m^{-1} \delta m$, where the non-universal scaling factor a_m^{-1} is chosen so that each of the distribution functions has unit variance. The fact that the individual functions for each system size lie on the same curves is an indication that the estimate of $T_c(\infty)$ for the UCST is consistent with the results of a finite-size scaling analysis. This estimate of the critical temperature is significantly greater than that obtained by the Wegner fitting using a first correction to scaling term, where $T_c^*(N)=1.915$, however the estimate does fall within the error bars of the fitted critical temperature. Similarly, simulations are performed at the estimated infinite system-size critical temperature of $T^*=1.59$ for the system with a packing fraction of $\eta=0.247$. The distributions obtained are plotted as a function of the scaling variable y in Figure 6.25, and in this case the universal

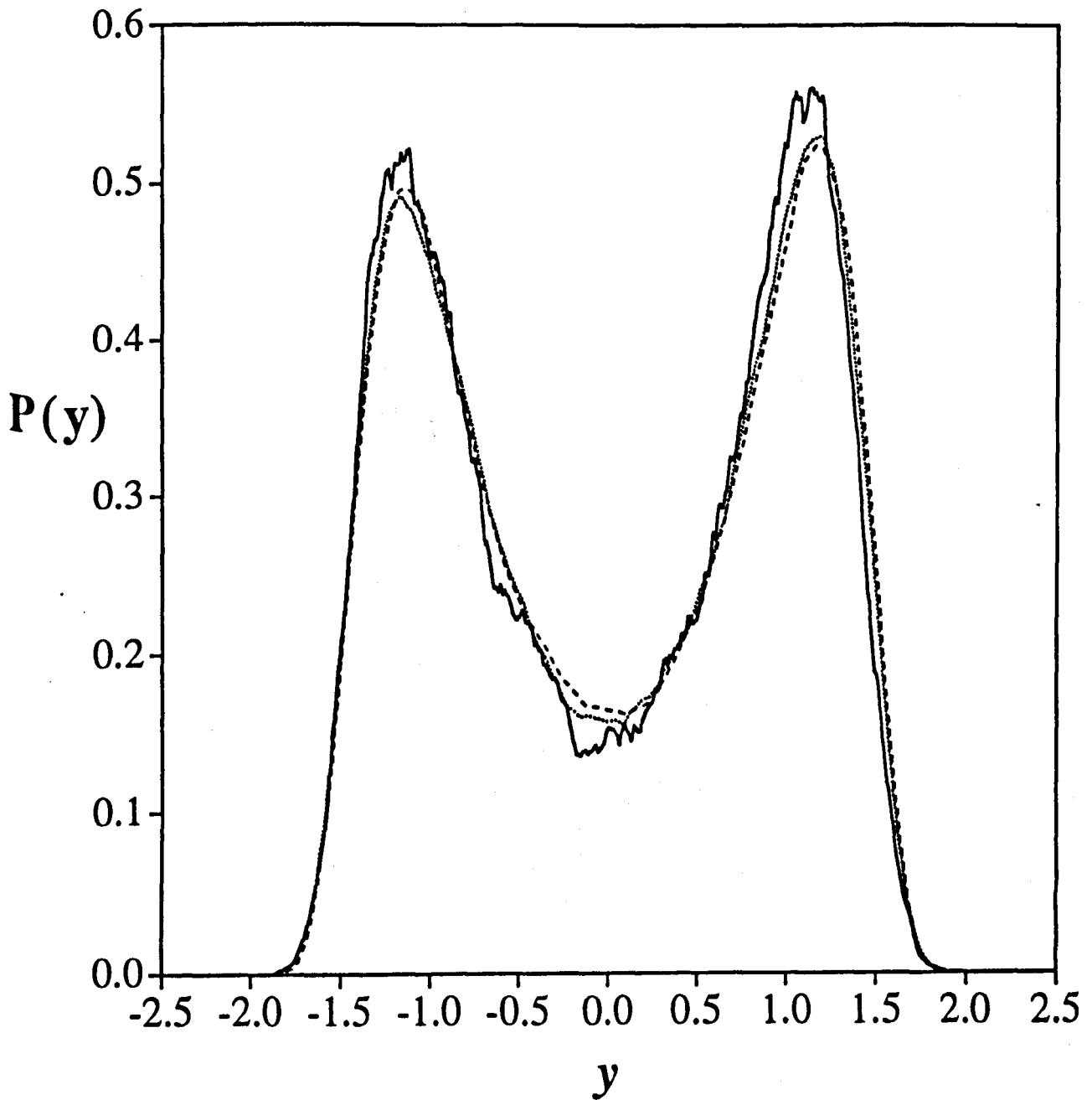


Figure 6.24: Scaled composition distribution function $P_N(y)$ at the estimated infinite system-size UCST of $T^* = 2.31$ plotted in terms of the scaling variable $y = a_M^{-1} L^{\beta/\nu} \delta m$. The distributions for each system size ($N = 108$ -dashed, $N = 256$ -dotted and $N = 864$ -bold) are obtained in the semigrand canonical ensemble at a constant packing fraction of $\eta = 0.287$.

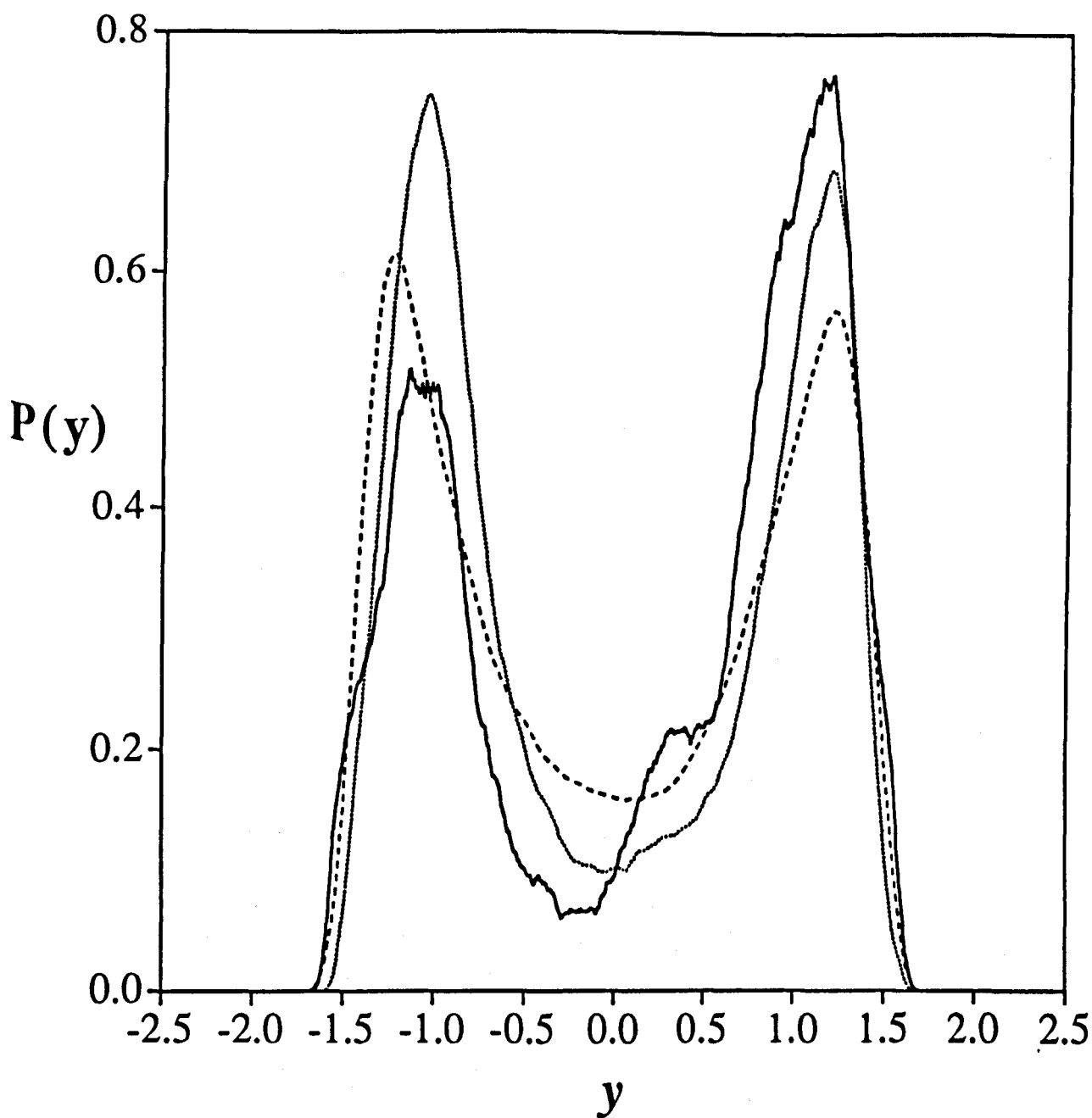


Figure 6.25: Scaled composition distribution function $P_N(y)$ at the estimated infinite system-size LCST of $T^* = 1.59$ plotted in terms of the scaling variable $y = a_M^{-1} L^{\beta/\nu} \delta m$. The distributions for each system size ($N = 108$ -dashed, $N = 256$ -dotted and $N = 864$ -bold) are obtained in the semigrand canonical ensemble at a constant packing fraction of $\eta = 0.247$.

nature of the curves for each system size is not so clear. It is expected that better agreement will be observed after completing longer simulations. However, the agreement between this FSS estimate of the LCST and that obtained using the Wegner expansion with a first correction to scaling, $T_c^*(N) = 1.557$, is much better than that of the UCST.

6.9 Conclusions

This chapter has formed a case study of the phenomenon of closed-loop immiscibility in mixtures. A specific model system is examined using both a theoretical equation of state and computer simulation methods. The SAFT-VR approach is seen to predict re-entrant miscibility for a range of pressures and temperatures; the extent of which also depends on the strength of the site-site interaction potential. We present the first simulation results which display a closed-loop region of liquid-liquid immiscibility for a specific model system. The Gibbs ensemble simulation results are shown to have a dependency similar to the SAFT-VR prediction on the pressure, temperature and the strength of the association energy of the system. The closed-loop of immiscibility for this system only exists for a narrow range of temperatures at specific pressures and at a relatively large value of the site-site interaction energy. The existence of both an UCST and a LCST for this model system in results obtained by computer simulation confirms that the short-ranged directional interaction site which is responsible for the low-temperature miscibility of the system. Previous GEMC simulation studies of square-well mixture with no association sites [53, 54] and [74], only report regions of liquid-liquid immiscibility below an UCST with no low temperature features on the phase diagram of the system. An examination of the extent of association present in the system, using both the SAFT-VR equation of state and the simulation results, indicates that the amount of inter-molecular association increases dramatically as the temperature of the system approaches that of the LCST. This endorses the idea that the low-temperature miscibility is a direct result of the bonding which occurs at low temperatures between unlike species in the mixture. The experimental observation of closed regions of immiscibility only in systems which have the ability to form hydrogen bonds between unlike components adds to the validity of our findings. As a general conclusion it is possible to state that any theoretical approach which intends to predict closed-loop immiscibility, must include a directional, temperature dependent interaction in order to give physically reasonable results.

Additionally, simulations performed in the semigrand canonical ensemble are used to estimate the finite system critical temperatures at both the UCST and the

LCST. These estimates are found to differ from those obtained by a Wegner expansion which includes corrections to scaling. These finite system values can be used to estimate the infinite system critical temperature. The validity of these estimates are confirmed by the use of finite-size scaling methods. Further work in this area is required in order to obtain a complete description of the critical behaviour of the system in the vicinity of the LCST.

Bibliography

- [1] J. S. Rowlinson, and F. L. Swinton, *Liquids and Liquid Mixtures*, (3rd ed.), Butterworth Scientific, (1982).
- [2] R. L. Scott and P. H. van Konynenburg, *Discuss. Faraday Soc.*, **49**, 87 (1970).
- [3] P. H. van Konynenburg and R. L. Scott, *Phil. Trans. R. Soc. A*, **298**, 495 (1980).
- [4] C. S. Hudson, *Z. Phys. Chem.*, **47**, 113 (1904).
- [5] W. Dolgolenko, *Z. Phys. Chem.*, **62**, 499 (1908).
- [6] R. J. L. Andon and J. D. Cox, *J. Chem. Soc.*, **1952**, 4601 (1952).
- [7] B. C. McEwan, *J. Chem. Soc.*, **123**, 2284 (1923).
- [8] G. Poppe, *Bull. Soc. Chim. Belg.*, **44**, 640 (1935).
- [9] G. M. Schneider, *Ber. Bunsenges. Phys. Chem.*, **76**, 325 (1972).
- [10] T. Narayanan and A. Kumar, *Phys. Rep.*, **249**, 135 (1994).
- [11] S. Glasstone, *Textbook of Physical Chemistry*, Van Nostrand, (1971).
- [12] J. S. Walker and C. A. Vause, *Scient. Am.*, **256** Num. 5, 90 (1987).
- [13] C. M. Sorensen, *Int. J. Thermophys.*, **9**, 703 (1988).
- [14] F. F. Nord, M. Bier, and S. N. Timasheff, *J. Am. Chem. Soc.*, **73**, 289 (1951).
- [15] G. N. Malcolm and J. S. Rowlinson, *Trans. Faraday Soc.*, **53**, 921 (1957).
- [16] J. C. Lang, R. D. and Morgan, *J. Chem. Phys.*, **73**, 5849 (1980).
- [17] K. L. Mittal and B. Lindman, *Surfactants in Solution* Vols. 1-3 Plenum, (1984).
- [18] R. J. Tufeu, P. H. Keyes, and W. B. Daniles, *Phys. Rev. Lett.*, **35**, 1004 (1975).
- [19] D. Guillon, P. E. Cladis, and J. Stamatoff, *Phys. Rev. Lett.*, **41**, 1598 (1978).

- [20] A. R. Kortan, H. V. Känel, R. J. Birgeneau, and J. D. Litster, *Phys. Rev. Lett.*, **47**, 1206 (1981).
- [21] A. R. Kortan, H. V. Känel, R. J. Birgeneau, and J. D. Litster, *J. Phys. (Paris)*, **45**, 529 (1984).
- [22] G. B. Kozlov, E. B. Kryukova, S. P. Lebedev, and A. A. Sobyenin, *Sov. Phys. JETP*, **67**, 1689 (1988).
- [23] T. H. Lin, X. Y. Shao, M. K. Wu, P. H. Hor, X. C. Jin, C. W. Chu, N. Evans, and R. Bayuzick, *Phys. Rev. B*, **29**, 1493 (1984).
- [24] S. Katayama, Y. Hirokawa, and T. Tanaka, *Macromolecules*, **17**, 2649 (1984).
- [25] H. Glasbrenner, and H. Weingaärtner, *J. Phys. Chem.*, **93**, 3378 (1989).
- [26] J. Hirschfelder, D. Stevenson, H. Eyring, *J. Chem. Phys.*, **5**, 896 (1937).
- [27] J. A. Barker and W. Fock, *Discuss. Faraday Soc.*, **15**, 188 (1953).
- [28] E. A. Guggenheim, *Mixtures*, Oxford University Press (1952).
- [29] E. Bodegom and P. H. E. Meijer, *J. Chem. Phys.*, **80**, 1617 (1984).
- [30] J. C. Wheeler, *J. Chem. Phys.*, **62**, 433 (1975).
- [31] G. R. Andersen and J. C. Wheeler, *J. Chem. Phys.*, **69**, 2082 (1978).
- [32] G. R. Andersen and J. C. Wheeler, *J. Chem. Phys.*, **69**, 3403 (1978).
- [33] J. C. Wheeler and G. R. Andersen, *J. Chem. Phys.*, **73**, 5778 (1980).
- [34] J. M. Romero Enrique, I. Rodriguez Ponce, L. F. Rull and U. Marini Bettolo Marconi, *Mol. Phys.*, submitted (1997).
- [35] J. S. Walker and C. A. Vause, *Phys. Lett.*, **A79**, 421 (1980).
- [36] C. A. Vause and J. S. Walker, *Phys. Lett.*, **A90**, 419 (1982).
- [37] R. E. Golstein and J. S. Walker, *J. Chem. Phys.*, **78**, 1492 (1983).
- [38] R. E. Golstein, *J. Chem. Phys.*, **79**, 4439 (1983).
- [39] J. D. van der Waals, Ph.D. Thesis, University of Leiden (1873); English translation edited by J. S. Rowlinson in *Studies in Statistical Mechanics*, Vol. **14**, North Holland (1988).
- [40] G. Jackson, *Mol. Phys.*, **72**, 1365 (1991).
- [41] D. G. Green and G. Jackson, *J. Chem. Phys.*, **97**, 8672 (1992).

- [42] M. N. Garcia-Lisbona, A. Galindo, G. Jackson, and A. N. Burgess, *Mol. Phys.*, in press (1997).
- [43] V. A. Mazur, L. Z. Boshkov, V. B. Fedorov, *Dokl. Acad. Nauk. SSSR*, **282**, 137 (1985).
- [44] L. Z. Boshkov and V. A. Mazur, *Russ. J. phys. Chem.*, **60**, 16 (1986).
- [45] L. Z. Boshkov, *Dokl. Acad. Nauk. SSSR*, **294**, 901 (1987).
- [46] F. H. Ree, *J. Chem. Phys.*, **73**, 5401 (1980).
- [47] A. van Pelt, C. J. Peters, and J. de Swaan Arons, *J. Chem. Phys.*, **95**, 7569 (1991).
- [48] A. van Pelt, C. J. Peters, J. de Swaan Arons, and P. H. E. Meijer, *J. Chem. Phys.*, **99**, 9920 (1993).
- [49] A. van Pelt, C. J. Peters, J. de Swaan Arons, and U. K. Deiters, *J. Chem. Phys.*, **102**, 3361 (1995).
- [50] C. H. Kim, P. Imalchand, M. D. Donohue, and S. I. Sandler, *AIChE J.*, **32**, 1726 (1986).
- [51] T. Kraska, *Berichte der Bunsen-Gesellschaft*, **100**, 1318 (1996).
- [52] M. Gencaslan, P. H. E. Meijer, M. Keskin, and A. H. L. Levelt, *J. Supercritical Fluids*, **7**, 107 (1994).
- [53] J. R. Recht and A. Z. Panagiotopoulos, *Mol. Phys.*, **80**, 843 (1993).
- [54] D. G. Green, G. Jackson, E. de Miguel and L. F. Rull, *J. Chem. Phys.*, **101**, 3190 (1994).
- [55] A. Gil-Villegas, A. Galindo, P. J. Whitehead, S. J. Mills, G. Jackson, and A. N. Burgess, *J. Chem. Phys.*, **106**, 4168 (1997).
- [56] A. Galindo, L. A. Davies, A. Gil-Villegas, and G. Jackson, *Mol. Phys.*, in press (1997).
- [57] W. G. Chapman, G. Jackson, and K. E. Gubbins, *Mol. Phys.*, **65**, 1057 (1988).
- [58] T. Boublík, *J. Chem. Phys.*, **53**, 471 (1970).
- [59] G. A. Mansoori, N. F. Carnahan, K. E. Starling, and T. W. Leland, *J. Chem. Phys.*, **54**, 1523 (1971).
- [60] N. F. Carnahan, and K. E. Starling, *J. Chem. Phys.*, **51**, 635 (1969).
- [61] L. L. Lee, *Molecular Thermodynamics of Nonideal Fluids*, Butterworth Publishers (1988).

- [62] A. Z. Panagiotopoulos, *Mol. Phys.*, **61**, 813 (1987).
- [63] A. Z. Panagiotopoulos, N. Quirke, M. R. Stapleton, and D. J. Tildesley, *Mol. Phys.*, **63**, 527 (1988).
- [64] M. P. Allen and D. J. Tildesley, *Computer Simulation of Liquids*, Clarendon, (1987).
- [65] B. Widom, *J. Chem. Phys.*, **39**, 2802 (1963).
- [66] B. Smit and D. Frenkel, *Mol. Phys.*, **68**, 951 (1989).
- [67] V. Privman (Editor), *Finite Size Scaling and Numerical Simulation of Statistical Systems*, World Scientific, (1990).
- [68] K. K. Mon and K. Binder, *J. Chem. Phys.*, **96**, 6989 (1992).
- [69] M. P. Allen, *Computer Simulation in Chemical Physics*, edited by M. P. Allen and D. J. Tildesley Kluwer Academic, (1993), pp. 49-92.
- [70] K. Binder, *Computational Methods in Field Theory*, edited by H. Gausterer and C. B. Lang Springer-Verlag, (1992), pp. 59-125.
- [71] B. Smit, Ph. de Smedt, and D. Frenkel, *Mol. Phys.*, **68**, 931 (1989).
- [72] B. Smit, *Computer Simulation in Chemical Physics*, edited by M. P. Allen and D. J. Tildesley Kluwer Academic, (1993), pp. 173-209.
- [73] L. Vega, E. de Miguel, L. F. Rull, G. Jackson, and I. A. McLure, *J. Chem. Phys.*, **96**, 2296, (1992).
- [74] E. de Miguel, E. M. del Río, and M. M. Telo da Gamma, *J. Chem. Phys.*, **103**, 6188 (1995).
- [75] R. R. Singh and K. S. Pitzer, *J. Chem. Phys.*, **90** 5742 (1989).
- [76] L. P. Kadanoff, *Phase Transitions and Critical Phenomena*, Vol. 5A, edited by C. Domb and M. S. Green Academic (1976), pp. 1-34.
- [77] H. E. Stanley, *Introduction to Phase Transitions and Critical Phenomena*, Oxford University Press, (1971).
- [78] A. Z. Panagiotopoulos, *Observation and Prediction of Phase Transitions in Complex Fluids*, Enrico Fermi Course CXXIX-NATO ASI, edited by M. Baus, L. F. Rull and J. P. Ryckaert, Kluwer (1995), pp. 463-501.
- [79] A. Z. Panagiotopoulos, *Int. J. Thermophys.*, **10**, 447 (1989).
- [80] J. V. Sengers and J. M. H. Levelt Sengers, *Ann. Rev. Phys. Chem.*, **37**, 189 (1986).

- [81] F. J. Wegner, *Phys. Rev. B*, **5**, 4529 (1972).
- [82] W. H. Press, B. P. Flannery, S. A. Teukolsky, and W. T. Vetterling, *Numerical Recipes*, 2nd ed, Cambridge University Press, (1992).
- [83] A. D. Bruce, *J. Phys. C*, **14**, 3667 (1981).
- [84] K. Binder, *Z. Phys. B*, **43**, 119 (1981).
- [85] R. Hilfer, *Z. Phys. B*, **96**, 63 (1994).
- [86] M. W. Pestak and M. H. W. Chan, *Phys. Rev. B*, **30**, 274 (1984).
- [87] U. Närgler and D. A. Balzarani, *Phys. Rev. B*, **42**, 6651 (1990); U. Närgler, J. R. de Bruyn, M Stein, and D. A. Balzarani, *Phys. Rev. B*, **39**, 11914 (1989).
- [88] Q. Zhang and J. P. Badiali, *Phys. Rev. Lett.*, **67**, 1598 (1991); *Phys. Rev. A*, **45**, 8666 (1992).
- [89] J. F. Nicoll, *Phys. Rev. A*, **24**, 2203 (1981); J. F. Nicoll and R. K. P. Zia, *Phys. Rev. B*, **23**, 6157 (1981).
- [90] A. D. Bruce and N. B. Wilding, *Phys. Rev. Lett.*, **68**, 193 (1992).
- [91] N. B. Wilding and A. D. Bruce, *J. Phys. Condens. Matter*, **4**, 3087 (1992).
- [92] N. B. Wilding, *Annual Reviews of Computational Physics IV*, edited by D. Stauffer, World Scientific, (1996) pp. 37-73.
- [93] J. J. Rehr and N. D. Mermin, *Phys. Rev. A*, **8**, 472 (1973).
- [94] M. Müller and N. B. Wilding, *Phys. Rev. E*, **51**, 2079 (1995).
- [95] M. Rovere, D. W. Heermann, and K. Binder, *Europhys. Lett.*, **6**, 585 (1988).
- [96] M. Rovere, D. W. Heermann, and K. Binder, *J. Phys. Condens. Matter*, **2**, 7009 (1990).
- [97] N. B. Wilding and K. Binder *Physica A*, **231**, 439 (1996).
- [98] K. K. Mon, *Phys. Rev. B*, **47**, 5497 (1993).
- [99] D. A. Kofke and E. D. Glandt, *Mol. Phys.*, **64**, 1105 (1988).
- [100] D. Frenkel, *Computer Simulation in Chemical Physics*, edited by M. P. Allen and D. J. Tildesley Kluwer Academic, (1993), pp. 93-152.
- [101] N. B. Wilding, *Phys. Rev. E*, **52**, 602 (1995).

Chapter 7

Concluding Remarks

The ultimate aim of theoretical studies of the liquid state is to obtain an understanding of the interactions which govern the phase behaviour in real systems. In this work we illustrate how the phase behaviour of even simple model mixtures can be made surprisingly complex by varying the size, the chain length and the nature of the intermolecular interactions of the system.

Specifically, we have examined the mixing rules involved in the application of the SAFT-VR equation of state to mixtures. The vapour-liquid and liquid-liquid coexistence regions of a series of model mixtures have been investigated using the SAFT-VR approach. The predictions obtained are seen to compare favourably with corresponding molecular simulation results. The extension of the SAFT-VR methodology to incorporate systems which interact via soft-core potentials is presented. The proposed recipe is shown to give an accurate description of chain molecules interacting with the Lennard-Jones potential.

The effect of the addition of an anisotropic interaction site, which mimics hydrogen bonding in real systems, on the phase diagram of a specific model system is carefully monitored. For a specific association strength the SAFT-VR equation of state predicts that the system exhibits a region of low-temperature miscibility, a finding which is confirmed by a computer simulation study performed for the same model system. This re-entrant phase behaviour is a phenomenon which is exhibited experimentally for a range of aqueous solutions of many organic molecules, such as alcohols and surfactants. It is satisfying that a simple model system, con-

taining the essential physical features of the experimental systems can be used within a theoretical approach to give a qualitative representation of this kind of novel phase behaviour. Accurate results have been reported for mixtures of alkanes, perfluoroalkanes, refrigerants, alcohols and the more complex polyoxyethylene surfactants.

An advantage of a molecular based approach such as the SAFT-VR equation of state is that it can be easily applied to a range of model systems of various diameters, chain length and number of associating sites. Additionally, the non-conformal properties of the model can be accounted for in the approach, since the range of the interaction potential can be used as a variable. Hence, the application of the SAFT-VR methodology to more realistic model systems than those considered is a straightforward process. The phase behaviour of mixtures of real systems using the SAFT-VR approach (and the simpler SAFT-HS version) is currently a source of interest both theoretically and industrially.

As a closing statement, it is important to note that the work presented here is by no means an exhaustive study of the phase behaviour of these type of model systems. Routes of future research include the study of multicomponent systems, simulation studies of more complex models and the study of systems with long-range interactions such as electrolytes.